NANOSTRUCTURED THERMOELECTRIC MATERIALS AND OPTICAL METHOD FOR THERMAL CONDUCTIVITY MEASUREMENT

By

ZAHRA ZAMANIPOUR

Bachelor of Science in Applied Physics
Amirkabir University of Technology
Tehran, Iran
1996

Master of Science in Physics
Sharif University of technology
Tehran, Iran
1998

Submitted to the Faculty of the
Electrical and Computer Engineering
Graduate College of the
Oklahoma State University
in partial fulfillment of
the requirements for
the Degree of
DOCTOR OF PHILOSOPHY
July, 2013

COPYRIGHT ©
By
Zahra Zamanipour

NANOSTRUCTURED THERMOELECTRIC

MATERIALS AND OPTICAL METHOD FOR

THERMAL CONDUCTIVITY MEASURMENT

Dissertation Approved:

Dr. Daryoosh Vashaee

Dissertation Adviser

Dr. Jerzy Krasinski

Committee Member

Dr. Reza Abdolvand

Committee Member

Dr. Kenneth F. Ede

Outside Committee Member

ACKNOWLEDGEMENTS

First of all, I would like to express the deepest appreciation to my advisor, Professor Daryoosh Vashaee. His knowledge, perfect thought, and supervision gave me this opportunity to progress in my education and research program. His patience and dedication to his students create a great enthusiasm and encouragement leading to fruitful research.

I am grateful to Professor Jerzy Krasinski, who had always unique ideas, and supported my research especially in the development of the optical experiments.

I owe special thanks to my dissertation committee members, Professor Kenneth F. Ede, and Professor Reza Abdolvand for their support and guidance through my education and graduation process.

I am grateful for the support from the Air Force Office of Scientific Research (AFOSR) High Temperature Materials program (Grant No. FA9550-10-1-0010) and the National Science Foundation (NSF) (Grant No. 0933763).

Acknowledgements reflect the views of the author and are not endorsed by committee members or Oklahoma State University.

Name: ZAHRA ZAMANIPOUR

Date of Degree: JULY, 2013

Title of Study: NANOSTRUCTURED THERMOELECTRIC MATERIALS AND OPTICAL METHOD FOR THERMAL CONDUCTIVITY MEASURMENT

Major Field: ELECTRICAL ENGINEERING

Abstract: A good thermoelectric material has large electrical conductivity, large Seebeck coefficient, and small thermal conductivity. Among the different techniques to achieve small thermal conductivity is the nanostructuring method. In a nanostructured material the thermal conductivity decreases due to the increased interfacial scattering of phonons. In most thermoelectric materials, due to the larger mean free path of phonons compared with electrons, the effect of interfaces on phonon scatterings is more than on carrier scattering. Therefore, reduction of the thermal conductivity becomes possible with almost no or small change in the electrical conductivity via nanostructuring.

The materials that have shown large power factor but have small efficiency due to their large thermal conductivity are good candidates for nanostructuring. For high temperature applications, several transition metal silicides have shown high power factor while they have large thermal conductivity. While silicides have been investigated in crystalline and polycrystalline form in the past, their nanostructuring had not been pursued extensively at the time that this research started. In this PhD dissertation, we have developed several nanostructured materials based on transition metal silicides.

In the path to develop high temperature thermoelectric materials, synthesis, structural characterizations, thermoelectric properties measurements, and analysis of the nanostructured bulk $Si_{1-x}Ge_x$, Higher Manganese Silicide (HMS), $Si_{0.8}Ge_{0.2}$ structures with $CrSi_2$ nanocrystallite inclusions, and nanocomposites of SiGe-$FeSi_2$ were completed. The synthesis process parameters including powder processing and sintering parameters were derived for each material system. Model calculations for electron and phonon transport were performed in detail to explain the measured data and direct the experiments. Boron precipitation effect on thermoelectric properties of $Si_{0.8}Ge_{0.2}$ was also studied by analyzing the experimental data and through theoretical calculations.

At the device level, in order to find the optimum metal contact for HMS, an extensive study was performed to find the best electrical contact for HMS thermoelectric devices.

Along with thermoelectric material development, a novel ultrafast optical characterization method for thermal properties measurement and ultrafast carrier dynamics study was also developed. The designed optical system is a new pump-probe arrangement to perform both thermal properties measurement and ultrafast carrier dynamics study in one set up. The existing radial heat flow analysis for thermal properties measurement was extended to three-dimensional heat flow, which is applicable for distinguishing the xyz thermal conductivity of the anisotropic material.

TABLE OF CONTENTS

LIST OF TABLES

LIST OF FIGURES

Chapter 1: Introduction

As the world energy demand and costs increases, sustainable energy technologies are developing significantly. The fossil fuel sources are not sufficient for world energy consumption. The first concern is energy production and conversion in universal form and convenient for practical applications. Renewable energy sources such as wind, solar and geothermal energies not only expensive costs, but also they provide only small fraction of the needed energy. The other concern is environmental issues. Huge greenhouse gas emissions from organic fuel power plants are changing the global climate. However, a huge source of low-cost sustainable energy is heat. Nearly 60% of the world's useful energy is wasted as heat. Enormous amount of energy are wasted in industrial processes, home heating and vehicles. In the U.S. alone, fuel for vehicles costs billions of dollars a year, with most of the power wasted as heat due to low efficiency of combustion engines. Using an efficient and cost-effective technology to convert waste heat to electricity is becoming vital subject of research and development among all variety of energy conversion technologies. Solid state thermoelectric devices using waste heat energy generates electricity. Their advantages over traditional electric generators are simplicity, no moving parts, low noise performance, high reliability and miniaturization. In addition, these bidirectional energy convertors are used in cooling systems. However, the operational efficiencies of thermoelectric (TE) systems are not high enough to be used in broad range of applications. Nevertheless, there exit many applications including spacecraft, wrist watches, portable household refrigerators, thermal cycles for DNA synthesizers, car seat cooler/heaters, electronic, medical, and research equipment such as cooling infrared detectors and optoelectronic devices. Improving the efficiencies of TE

materials and optimizing the TE devices are two important directions led to extend their application areas.

Temperature gradient imposed on a thermoelectric material produces a voltage gradient via Seebeck effect which is first observed by Seebeck in 1821[1]. Similarly, a current flow across a thermoelectric material produces temperature difference between two ends of the material. This phenomena is known as Peltier effect and it is discovered by Peltier in 1834 [2].

The field of thermoelectric materials advanced in the 1950s when the basic science of thermoelectrics became well-established. The enhancement in figure of merit of thermoelectric materials (ZT) was initiated by Ioffe and his colleagues [11] who developed the theory of thermoelectric conversion. Figure of merit in thermoelectric materials is defined as $ZT = \frac{S^2\sigma}{\kappa}T$, where S is Seebeck coefficient, σ is electrical conductivity, κ is thermal conductivity, and T is the absolute temperature [2,3]. The $S^2\sigma$ is called power factor. A lot of research was done in order to improve ZT of many semiconductors. However, the highest achievable ZT values of all materials remained below value of one. The only traditional way to optimize the ZT in a given semiconductor was changing the doping concentration. Increasing the doping concentration would increase the electrical conductivity; but this also decreases Seebeck coefficient. This trade-off is the main challenge in producing compound material with high ZT. During 1960-1990 periods, the thermoelectric conversion received little attention from the worldwide scientific research community. In the early 1990's, the US research community started to re-examine research for thermoelectric materials to a point that they could be efficiently used for power generation and cooling applications [4]. As a result of this stimulation, two different research approaches were taken for developing the next generation of new thermoelectric materials: One using new families of advanced bulk thermoelectric materials, and the other using low-dimensional materials. During the 1990's these two approaches developed independently and mostly in different directions but it seems that both are coming together again. Firstly, the most successful new bulk thermoelectric materials with a nanoscale crystalline. Secondly, low-dimensional materials systems are

now being assembled as nanocomposite containing a coupled assembly of nanoclusters showing short-range low dimensionality embedded in a host material, thereby producing a bulk material with nanostructures and many interfaces that scatter phonons more effectively than electrons.

1.1. Role of Nanostructuring

One of the directions to improve the ZT is to reduce the thermal conductivity. In this direction different techniques have been utilized to increase phonon scatterings. For a long time alloying technique was one of the methods to reduce the thermal conductivity of crystalline or polycrystalline bulk thermoelectric materials for a long time. Making alloys generates atomic-scale defects and scatter phonons resulting in thermal conductivity reduction [5]. However, this method reaches a limit which is called alloying limit of thermal conductivity. Phonon rattler concept is another approach [6,7]. Metal atoms can be interspersed into Skutterudite thermoelectrics such as $IrSb_3$, $CoSb_3$ and $RhSb_3$, which have low open crystal structure and act as rattlers scattering phonons and reducing the thermal energy transport. Therefore, the material is glass like respect to phonon transport while crystalline with respect to electrical carrier transport. This concept has been applied to other open structures such as clathrates and defect structured compounds.

The low dimensional nanostructuring was introduced in the 1990s [4]. An improvement in power factor and a reduction in lattice thermal conductivity are possible via nanostructuring. It is indicated that thermal conductivity reduction can be achieved in nanometer-size low-dimensional structures as well as bulk nanostructured materials. In both structures phonon scatterings is increased at boundaries and interfaces. Many theoretical and experimental studies have shown that nanostructuring is an effective way to improve ZT. Some examples are bulk lead telluride (PbTe) based materials, BiTe/SbTe superlattices, PbTe/PbSeTe quantum dot superlattices (QDSL), and more recently BiSbTe composite structure and Si nanowires [4,8,9,10,11,12]. It is believed that the significant enhancement of ZT is due to the reduction of the thermal conductivity by scattering

phonons more effectively than electrons at interfaces in superlattices or at grain boundaries of nanostructured materials.

1.2. Bulk versus thin film thermoelectrics

With the increasing demand on new applications of TE materials both for power generation and cooling functions, a cost effective approach to make highly efficient TE materials is strongly needed. Although, in recent years there has been significant development of high ZT materials based on superlattice structures, these materials made with thin film deposition techniques are too expensive to make. Moreover, many of these structures are not thermally stable over thermal cycling, or are very sensitive to defects in the structure. Defects induced by thermal or mechanical stress can significantly affect their performance.

However, nanostructured thermoelectric materials made with mechanical alloying are potentially inexpensive to make and appropriate for batch processing [13,14]. They increase the figure of merit based on the same principle as in superlattices that the scattering of phonons should be enhanced relative to electrons. Hence, prior theoretical and experimental studies on quantum-well superlattice and quantum-wire samples have now evolved into studies on bulk samples containing nanostructured constituents prepared by chemical or physical approaches.

1.3. Recent advances in Thermoelectric materials

In the last 8 years, there have been several reports by Harman [15], Venkatasubramanian [16], Kanatzidis [17] [18], Heremans [19**]**, Zeng/Chen [20][21][13], etc. showing ZT in 1.3-2.4 range. However, the recent more careful measurements of the Harman samples have revealed that their ZT values are actually closer to 1.0[15]. The measurements on bulk sample are less controversial and the Boston College/MIT group has demonstrated a unicouple with maximum cooling capability of ~100C near room temperature, which matches their ZT~1.5 [13]. Almost all of these approaches benefit from a reduction in

lattice thermal conductivity without degrading the electronic performance. Until some years ago, a quantitative theory for thermal transport in nanostructured material was missing. With the recent work of Majumdar [22], and Chen [23] now we understand the importance of blocking mid-long wavelength phonons to beat the alloy limit. Hereman's paper [19] on resonant energy level in TlPbTe is an exception to the previous work. Here the improvement comes from the TE power factor and a ZT ~ 1.5 at 773K was measured. A roadmap does not seem to exist which would suggest how to implement the resonant energy levels to reach ZT>2.5 at room temperature. Recent ZT enhancements in thermoelectric materials are shown in Figure 1-1.

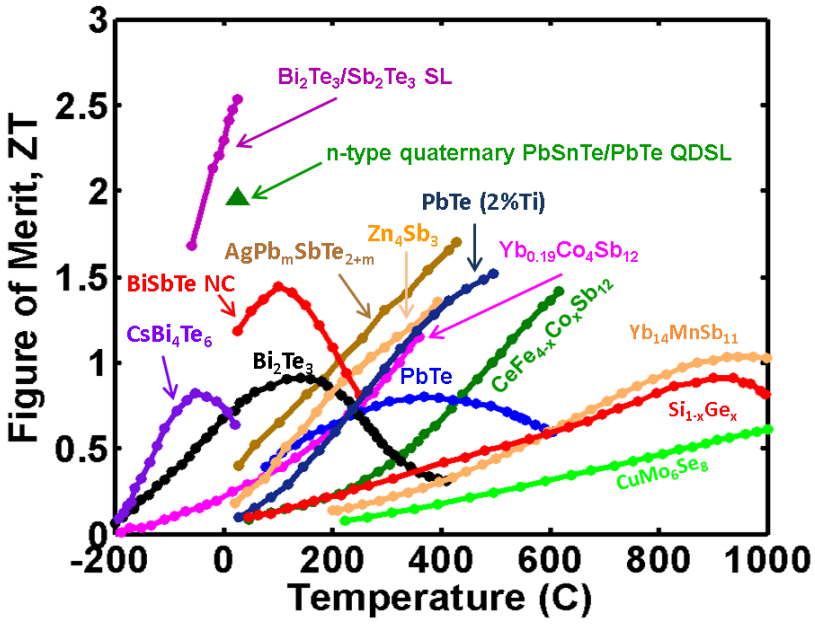

Figure 1-1 ZT enhancement in Thermoelectric materials

Despite all of the advances in materials, TE modules with cooling or coefficient of performance (COP) significantly better than the commercial BiTe ones have not been demonstrated (at least in the refereed literature). With thin films, there are significant challenges due to electrical and thermal resistances of the interfaces, which could be alleviated if the leg thickness could be increased to 50-100 microns. In nanostructured bulk materials, the problems seem to be in non-uniform material properties, mechanical

robustness and parasitic electrical resistances. A unique manufacturing technique has been developed to sputter BiTe elements directly on Silicon substrates [24]. In this work, they have commercialized thin film modules with 100s of elements 20-50 microns thick and demonstrated cooling power density ~100W/cm^2. However, the achievable temperature difference produced by these devices is limited to ~60-65°C due to inherently low material ZT~0.6.

1.4. Transition metal silicides

Nanostructuring approach provides means to reduce the thermal conductivity (κ) without significantly affecting the thermoelectric power factor ($S^2\sigma$). For this reason, materials with high power factor would be best candidates. We can reduce the thermal conductivity in the nanostructured bulk material to reach a large ZT by maintaining the power factor. For the temperature range of 500-1000°C, several transition metal silicides have large power factor, but they are not very good thermoelectrics because of their large thermal conductivity. For example, chromium and tungsten silicides have shown a power factor times temperature ($S^2\sigma T$) over 10 W/mK, which would result in ZT of over 2 if the thermal conductivity was reduced to 5 W/mK in the nanostructured form.

In fact, compounds of silicon with transition metal silicides have been interesting for thermoelectric applications for several distinct characteristics. In addition to high efficiency, they are inexpensive, mechanically robust, non-toxic, and resistive to oxidation and degradation when operated in high temperature in air without any protection. They have also lower density than Bismuth and Chalcogenide based alloys owing to the small density of Silicon (lighter than Aluminum).

Among silicide compounds, SiGe and higher manganese silicides (HMS: $MnSi_{1.71\text{-}1.75}$) [25] are two candidates with promising thermoelectric properties. The efficiency of these alloys even in crystalline or polycrystalline form is comparable with that of conventional chalcogenide TE materials. Moreover, they can work to higher temperature range (as opposed to chalcogenides which are generally good only up to 500C), have superior

physicochemical, mechanical, and cost parameters [26]. Such collective properties makes them specially promising for large scale high temperatures applications.

1.5. **Motivation**

There have been significant efforts in generating thermoelectric materials based on BiTe, PbTe, and SiGe alloys in the past. While each material system covers certain range of working temperature (BiTe 0-200°C, PbTe 300-500°C, and SiGe 800-1100°C), there is a gap for temperature range of 500-1000C. While the efficiency of energy conversion for low temperature range is small (due to small Carnot efficiency), one can have significant enhancement in efficiency at high temperature, which urges to develop materials for this range of temperature.

The objective in this research is to develop efficient nanostructured thermoelectric materials suitable for the entire temperature range of 500-1000°C in a combined theoretical and experimental effort. As it is mentioned several transition metal silicides have shown large power factor in this range of temperature, but due to their large thermal conductivity have not been efficient thermoelectrics. While silicides have been investigated in crystalline and polycrystalline form before, their nanostructuring has not been pursued precisely yet. In order to achieve our goal we will develop nanostructured materials based on transition metal silicides.

In this approach the enhancement in ZT is attributed mainly to the reduced lattice and bipolar thermal conduction due to strong interface scattering of phonons and charge carriers, respectively via synthesizing nanostructured materials.

In the path to realization of the promised high-performance TE materials the following tasks were performed:

1. Synthesis, characterization, thermoelectric properties measurements, and analysis of nanostructured silicides including $Si_{1-x}Ge_x$, Higher Manganese Silicide (HMS), and $CrSi_2$ inclusion embedded in $Si_{0.8}Ge_{0.2}$. Thermal/thermoelectric properties of the synthesized nanostructured materials were measured.

2. Optimization of synthesis process parameters for bulk p-type SiGe alloys including nanostructuring and sintering were done in order to attain the desired nanoscale features for each synthesized bulk nanostructured materials.
3. A detailed combined electron and phonon transport modeling was applied to study and analyze the data and to guide the experiments. A code for carrier and phonon transport calculations was recently developed in our group. Using this code, the theoretical parameters were fitted to the experimental data and more parameters were extracted to further analyze the synthesized structures.
4. Boron Precipitation effect on thermoelectric properties of $Si_{0.8}Ge_{0.2}$ has been studied. By analyzing the experimental data as well as theoretical fitting, boron precipitation process and its effect on electric properties of p-type bulk nanostructured silicon germanium ($Si_{0.8}Ge_{0.2}$) was compared with that of large grain polycrystalline $Si_{0.8}Ge_{0.2}$.
5. Different metal and silicides were investigated to determine a proper electrical contact for HMS. An extensive study has been accomplished to find the best electrical contact for thermoelectric devices using HMS. In this study, several contact structures with various contact materials were synthesized, characterized and analyzed.
6. A novel ultrafast optical characterization method for electrical and thermal transport properties analysis was developed. Design, fabrication, set up, instrumentation, theoretical calculation, modeling, debugging the system, and data analyzing are the main accomplished steps of this study. The optical pump-probe system of a new design was utilized to study thermal properties of strong anisotropic low dimensional structures such as planar nanowire superlattices. The optical system is based on a femtosecond laser was designed such that the ultrafast carrier dynamics can be investigated as well.

1.6. Organization of the Dissertation

This dissertation consists of two main parts. In the first part, the thermoelectric materials development is discussed. In this part, experimental material search and optimizations are

explained and the results and discussions of the study are given in detail. In the second part, a novel design for optical characterization of low dimensional material systems is described. The new pump-probe technique for thermal properties measurement and carrier dynamics studies is analyzed. In addition, existing heat flow and theoretical calculation for thermal properties measurement of thin films is extended to 3D heat transfer that can be applied for thermal properties measurement of nanowires.

Chapter 2 comprises thermoelectrics fundamental concepts. The thermoelectric effects are explained conceptually and transport properties equation are derived based on Boltzman equation under relaxation time approximation. The experimental procedure, characterizations and measurements process are introduced in chapter 3 in detail. The resulted experimental data are compared to theoretical data which are extracted from transport calculation. The transport calculation code was developed in Nano Science Engineering Group to evaluate properties of thermoelectric materials. In Chapter 3, the calculation flow chart is explained.

In Chapter 4, a systematic study of p-type bulk nanostructured SiGe is presented. The synthesis procedure including powder process and sintering are explained in detail. The whole process is optimized to maximize figure of merit of SiGe alloy. The result and discussion section shows the experimental and theoretical data analysis.

Boron is used as a dopant for all bulk nanostructured SiGe alloys in this research study. The effect of boron precipitation on thermoelectric properties is studied both experimentally and theoretically in Chapter 5.

The nanostructured bulk $Si_{0.80}Ge_{0.20}$ alloy is studied in Chapter 6. A detail of phase identification off this structure using Differential thermal analysis (DTA) and compare to x-ray diffraction (XRD) analysis is explained. Using model calculation, existence of two phases in the synthesized structure which was revealed with the DTA analysis is confirmed and thermoelectric properties are analyzed in detail.

In Chapter 7, the results of study on thermoelectric properties of $Si_{0.8}Ge_{0.2}$ embedded with $CrSi_2$ nano-crystallite inclusions are presented. The effect of $CrSi_2$ nano-inclusions on

electrical and thermal characteristics of composite structure are analyzed theoretically using experimental data.

Study on nanostructured bulk p-type higher manganese silicide is presented in Chapter 8. In this investigation, different composite of $MnSi_x$ were synthesized, and the result of structural characterization and thermoelectric properties are discussed.

Chapter 9 is devoted to experimental studies on electrical contacts for higher manganese silicide thermoelectric devices. Electrical contacts are very critical in thermoelectric devices. Different metals and silicides were tested to find an optimum contact material for higher manganese silicide.

In the second part of this dissertation, we focus on development of a new design of optical pump-probe method. Chapter 10 describes the method, theoretical background and previous works. Our new experimental set up for pump-probe method and our approach to correct the errors in optical design and instrumentation is presented in Chapter 11.

In Chapter 12, the thermal transport modeling of one dimensional heat flow and radial heat flow are presented from previous works and the equations for thermal properties measurement is derived. The thermal transport calculations are extended to 3 dimensional heat flow to extract thermal properties in systems with strong anisotropic properties respect to thermal flow.

1.7. **Reference**

1 TJ. Seebeck, "Magnetische Polarisation der Metalle und Erzedurch Temperatur Differenz", Abhand Deut. Akad. Wiss. Berlin; 265 (1822).

2 CRC Handbook of Thermoelectrics, edited by D. M. Rowe, CRC Press, Boca Raton, FL, 1995, 157.

3 H. Julian Goldsmid, "Introduction to thermoelectricity", Springer, 2009.

4 M.S.Dresselhaus, G. Chen, M.Y. Tang, R. Yang, H. Lee, D. Wang, Z. Ren, J. fleurial, P. Gogna, Advanced Materials, vol. 19, pp.1043-1053, 2007.

5 Nolas G. S., Sharp J. W., Goldsmid H J. 2001. "Thermoelectrics: Basic Principles and New Materials Developments", Berlin/Heidelberg: Springer.

6 Nolas GS, Slack GA, Morelli DT, Tritt TM, Ehrlich AC. 1996. The effect of rare-earth filling on the lattice thermal conductivity of skutterudites. J. Appl. Phys. 79:4002–8

7 P. Pichanusakorn, P. Bandaru, Materials Science and Engineering, R 67,2010, 19–63.

8 T. Koga, S. B. Cronin, M. S. Dresselhaus, J. L. Liu, K. L. Wang, Appl. Phys. Lett., 2000, 77, 1490.

9 X. B. Zhao, S. H. Yang, Y. Q. Cao, J. L. Mi, Q. Zhang, T. J. Zhu, J. Electron. Mater., 2009, 38, 1017.

10 R. Venkatasubramanian, E. Siivola, T. Colpitts, B. O'Quinn, Nature2001, 413, 597.

11 Q. Zhang, J. He, X. B. Zhao, S. N. Zhang, T. J. Zhu, H. Yin, T. M. Tritt, J. Phys. D: Appl. Phys., 2008, 41, 185103.

12 W. Kim, J. Zide, A. Gossard, D. Klenov, S. Stemmer, A. Shakouri, A. Majumdar, Phys. Rev. Lett., 2006, 96.

13 B. Poudel, Q. Hao, Y. Ma, Y. Lan, A. Minnich, B. Yu, X. Yan, D. Wang, A. Muto, D. Vashaee, X. Chen, J. Liu, M. S. Dresselhaus, G. Chen, Z. Ren, Science, Vol. 320. no. 5876, pp. 634 – 638 (2008).

14 M. S. Dresselhaus, G. Chen, M. Y Tang, R. Yang, H. Lee, D. Wang, Z. Ren, J-P Fleurial, P. Gogna, Advanced Materials, v 19, n 8, Apr 20, p 1043-1053 (2007).

15 T. C. Harman, P. J. Taylor, M. P. Walsh, B. E. LaForge, Science 27 September 2002: Vol. 297. no. 5590, pp. 2229 – 2232.

16 Rama Venkatasubramanian, Edward Siivola, Thomas Colpitts & Brooks O'Quinn, Nature 413, 597-602 (11 October 2001).

17 J. Androulakis, K. F. Hsu, R. Pcionek, H. Kong, C. Uher, J. J. D'Angelo, A. Downey, T. Hogan, M. G. Kanatzidis, Advanced Materials, Volume 18 Issue 9, Pages 1170 – 1173, 2006

18 Kuei Fang Hsu, Sim Loo, Fu Guo, Wei Chen, Jeffrey S. Dyck, Ctirad Uher, Tim Hogan, E. K. Polychroniadis, Mercouri G. Kanatzidis, Science 2004, Vol. 303. no. 5659, pp. 818 - 821.

19 Joseph P. Heremans, Vladimir Jovovic, Eric S. Toberer, Ali Saramat, Ken Kurosaki, Anek Charoenphakdee, Shinsuke Yamanaka, G. Jeffrey Snyder, Science 321, 554 (2008).

20 X.W. Wang, H. Lee, Y.C. Lan, G.H. Zhu, G. Joshi, D.Z. Wang, J. Yang, A.J. Muto, M.Y. Tang, J. Klatsky, S. Song, M.S. Dresselhaus, G. Chen, and Z.F. Ren, Applied Physics Letters, Vol. 93, 193121 (1-3), 2008.

21 Yi Ma, Qing Hao, Bed Poudel, Yucheng Lan, Bo Yu, Dezhi Wang, Gang Chen, and Zhifeng Ren, Nano Letters, Vol. 8, No. 8, pp. 2580-2584 (2008).

22 Woochul Kim, Joshua Zide, Arthur Gossard, Dmitri Klenov, Susanne Stemmer, Ali Shakouri, and Arun Majumdar, PRL 96, 045901, 2006.

23 G.H. Zhu, H. Lee, Y.C. Lan, X.W. Wang, G. Joshi, D.Z. Wang, J. Yang, D. Vashaee, H. Guilbert, A. Pillitteri, M.S. Dresselhaus, G. Chen, and Z.F. Ren, Physical Review Letters, Vol. 102, 196803, 2009.

24 H. Bottner, The Proceeding of the 24th International Conference on Thermoelectrics (ICT), 19-23 June 2005, Clemson, SC, USA.

25 Ivanova, L.D., Abrikosov, N. Kh., Elagina, E. I., and Khostikova, V. D., Izv. Akhad. Nauk SSSR Neorg. Mater., 5, 1933, 1969.

26 M. I. Fedorov, E. A. Gurieva, L. V. Prokof'eva, and V. K. Zaitsev, Proceedings of the 14th International Conference on Thermoelectrics, St. Petersburg, 1995, pp. 254–258.

Chapter 2: Basics of Thermoelectricity

When a temperature gradient is applied to a material, an electrical field is generated. On the contrary, when an electrical field is applied through a material, a temperature gradient is created between two ends of material. These effects are called thermoelectric effects. The origin of these effects is that charge carriers can transport heat while they carry charge in metals and semiconductors. The fundamental concepts of thermoelectric effects, use of these concepts to find new advanced materials and enhance their thermoelectric properties, and also their relation to develop thermoelectric generators and refrigerators will be discussed in this chapter.

9.1.Thermoelectric effects

From 1821 to 1851, the three thermoelectric effects (Seebeck, Peltier and Thomson) were discovered and understood from macroscopic point of view. Later on, from 1930 to the beginning of the 1960s, there has been important progress both in the understanding of phenomena at a microscopic scale and in the discovery and optimization of presently used thermoelectric materials. The physical concepts of these effects were explained in this section.

2.2.1. Seebeck effect

Thermoelectric power generation is based on Seebeck effect in thermoelectric materials which is discovered by Seebeck in 1821. When there is a temperature difference between two ends of a material, electrical potential which is proportional to temperature difference is generated (Figure 2-1 (a)).

Seebeck observed that temperature gradient between two junctions of dissimilar conductor yields to an electrical field. This principle has been used for temperature measurements for a long time.

The generated electrical potential is proportional to the temperature difference. Seebeck coefficient (S) is then the ratio of Seebeck voltage to the temperature difference [1,2]:

$$S = -\Delta V/\Delta T \qquad (1)$$

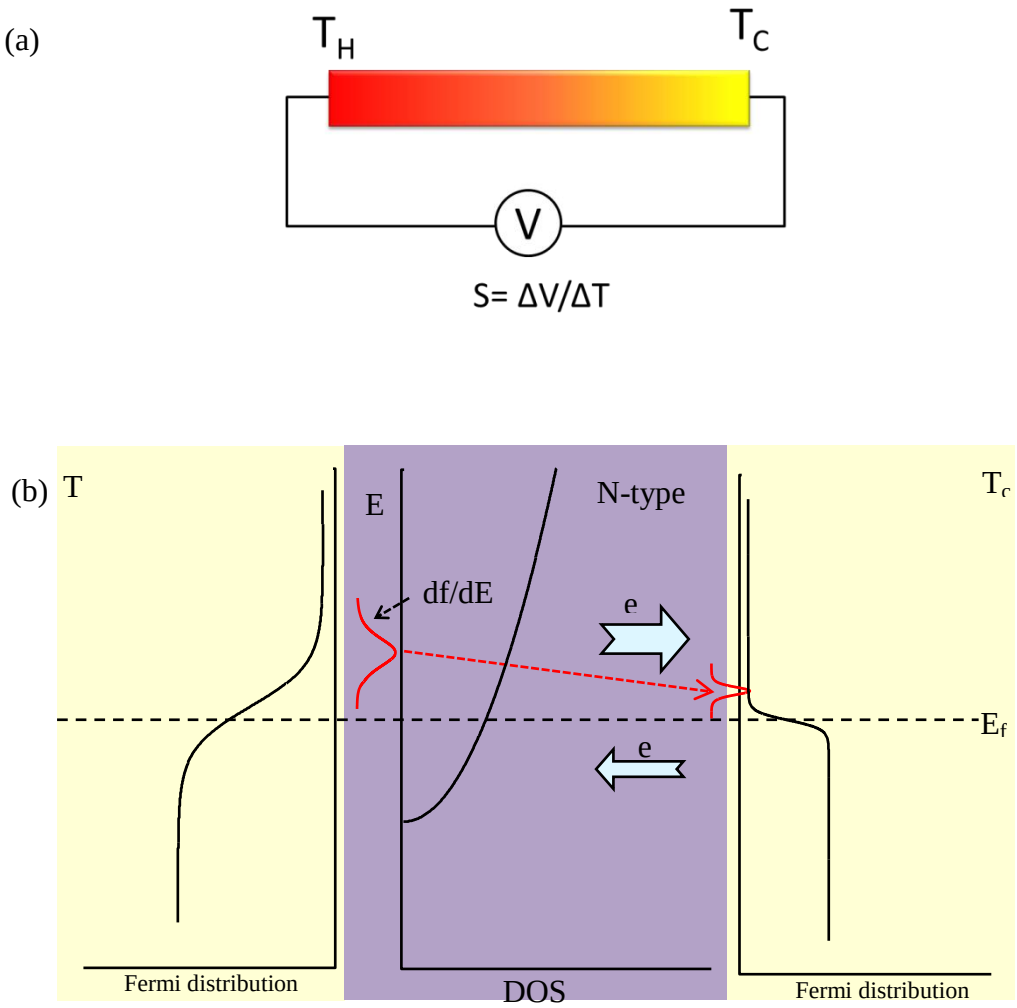

Figure 2-1 Seebeck effect: (a) A temperature difference between two ends of the material generates a voltage (b) Microscopic phenomenon for n-type semiconductor.

Microscopic principle of Seebeck effect is shown schematically in Figure 2-1 (b) for an n-type semiconductor. It is noted that the carrier distribution depending on the temperature is different

for the hot and cool junctions. At the hot side, the carriers will have higher energy and the density of carriers above Fermi energy level is higher. Consequently, there will be a net diffusion of the carriers from hot side to cold side generating an electric field. The excess energy of transported carriers is given to the lattice due to Thompson effect which will be discussed in the next section. This transport will be continued until the generated electric field is sufficient to stop the further diffusion. The majority carriers in both p-type (holes) and n-type (electrons) semiconductors move from T_h to T_c and create electric voltage, but the direction of generated field is opposite. Therefore, Seebeck coefficient has positive sign in p-type semiconductors and it has negative sign in n-type semiconductors.

2.2.2. Peltier effect

The Peltier effect was recognized by Peltier in 1934. In this phenomenon, a temperature difference is generated between two ends of a material when an electrical current passes through the material (Figure 2-2 (a)).

There is absorption of heat Q at one junction and rejection of heat Q at the other junction, the Peltier coefficient is defined as:

$$\Pi = Q / I \qquad (2)$$

The Peltier effect was considered as an interface effect. In this view, an energy transfer happens in the interface and causes cooling the junction [3]. Recent Studies on microscopic process of Peltier effect have shown that the Peltier effect happens mostly inside the metal contacts rather than inside the semiconductor which is the main thermoelectric material [4].

When an electrical current passes through the semiconductor, the energy levels change. As it is shown in Figure 2-2 (b), for an n-type semiconductor E_f and conduction band move downward by qv, where q is the carrier charge and v is the applied voltage. The curvature of the density of state (DOS) in metal and semiconductor are different. The DOS curve in metal is almost vertical due to high density of free electrons, whereas it has a sharp slope in semiconductor. Consequently, carriers (electrons) feel this difference at the interface and tend to go to higher energy level. Therefore electrons absorb energy (Q) from the lattice and cool the lattice

temperature down which is shown by step1→ step 2 in Figure 2-2 (b). Since the lattice temperature change, electrons energy distribution becomes narrower and the average energy level of the electrons shifts down toward Fermi level (step2→ step 3) which is change in Seebeck effect. The effect of temperature change on Seebeck effect (which is originated from the difference of the average energy of the electrons and Fermi energy level) is called Thompson effect. From step 3 to step 4 electrons transport through the lattice and the only phenomena is the joule heating during this transport which drops the energy of electrons. Once more when the electrons reach to the interface, they feel the DOS

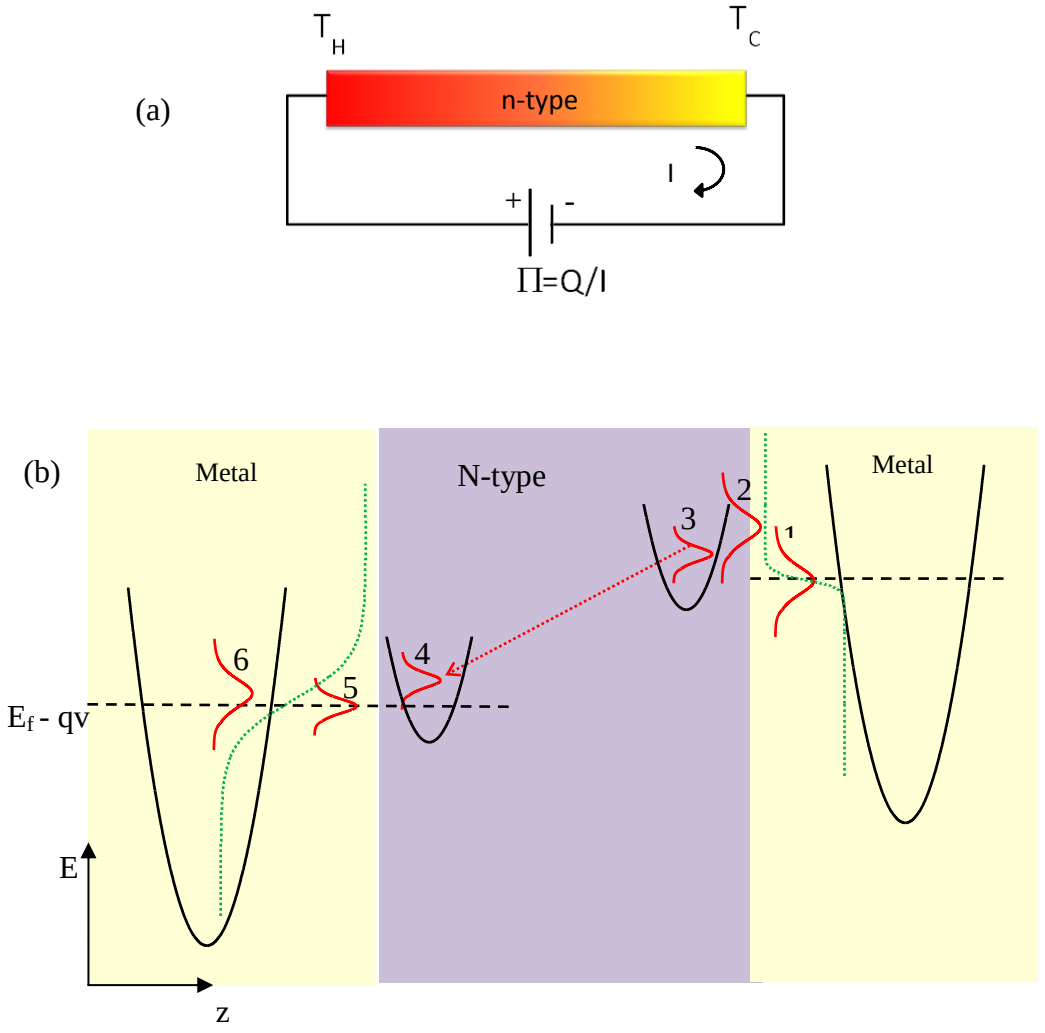

Figure 2-2 Peltier effect: (a) temperature gradient is generated by flow of current through a material, (b) microscopic origin of Peltier effect.

curvature difference between semiconductor and metal. In this location, electrons give up their energy (Q) to the lattice and heat it up (step4→ step 5). Due to temperature change the electron distribution becomes broaden in metal. This phenomenon shifts the distribution slightly up which is shown in step 4→ step 5 (Thompson effect). This change is very small, because the DOS of metal is not changing much. In overall, one junction of the semiconductor cooled while the other junction heated. This effect is base of Peltier coolers which has been used cooling microelectronic devices.

2.2.3. Thomson effect

The third thermoelectric effect is called Thompson effect. The Thomson effect was predicted and subsequently observed by Lord Kelvin in 1851[1]. Suppose electrical current (I)flows through a material which is exposed to a temperature gradient. In this case, heat is generated at a rate proportional to the electrical current and temperature gradient:

$$\dot{Q} = \tau I(-\nabla T) \quad (3)$$

where τ is Thompson coefficient. It was shown that the Thompson coefficient was related to the temperature dependence of the Seebeck coefficient:

$$\tau = T\frac{d\alpha}{dT} \quad (4)$$

In fact, the origin of the Thompson generated heat is temperature change of the Peltier heat [5]. Unlike Peltier which is at interface, Thompson heat dissipates in whole device such as joule heat.

2.1. Transport properties

2.1.1. Electronic properties

The semi classical Boltzmann equation under the relaxation time approximation describes the charge carrier and phonon transport processes in thermoelectric materials. Following Boltzman equation to derive thermoelectric parameters, Fermi level along with carrier concentration was calculated for each doping level. Different types of scattering mechanism can be considered for

each material system such as ionized impurities, acoustic phonons, and crystallite boundaries. The Mathiessen's rule is used to calculate the total scattering rate as the sum of the individual scattering rates:

$$\frac{1}{\tau_{tot}} = \sum \frac{1}{\tau_i} \tag{2.1}$$

where τ_i is the relaxation time for each scattering mechanism and τ_{tot} is total relaxation time.

According to Boltzman equation, for each band, the carrier concentration is given by the following equation

$$n = \frac{(2m_{DOS}k_B T)^{3/2}}{3\pi^2 h^3} \; {}_0\zeta_0^{3/2} \tag{2.2}$$

where

$${}_k^n\zeta_y^m = \int_0^\infty (-\frac{\partial f}{\partial x})\, x^n (x + \beta x^2)^m \tau(x)^k (1 + 2\beta x)^y \, dx \tag{2.3}$$

$$x = \frac{E}{k_B T} \tag{2.4}$$

$$\beta = (k_B T)\alpha \tag{2.5}$$

$$f(x) = \frac{1}{e^{(x-\eta)}+1} \tag{2.}$$

$$\eta = \frac{E_f}{k_B T} \tag{2.7}$$

k_B is the Boltzmann constant, α and β are the non-parabolicity parameters, η is the reduced Fermi energy, and f(x) is the Fermi-Dirac distribution function. The factor (1+2βx) is introduced due to the energy dependency of the effective mass to the non-parabolic band. The non-parabolicity of the band structure is considered in dispersion relation

$$E(1 + \alpha E) = \frac{\hbar^2 k^2}{2m_{DOS}} \tag{2.8}$$

where m_{DOS} is the density of states mass.

The mobility is derived by:

$$\mu = \frac{e\ll\tau\gg}{m} = \frac{e}{m}\frac{{}^{0}\zeta_{-1}^{3/2}}{{}_{0}\zeta_{0}^{3/2}} \quad (2.9)$$

The electrical conductivity can be calculated independently for each band [6]:

$$\sigma_i = en\mu = e\frac{(2m_{DOS}k_B T)^{\frac{3}{2}}}{3\pi^2h^3}\,{}_{0}\zeta_{0}^{3/2}\,\frac{e}{m^*}\frac{{}^{0}\zeta_{0-1}^{3/2}}{{}_{0}\zeta_{0}^{3/2}}$$

$$= \frac{e^2}{m^*}\frac{(2m_{DOS}k_B T)^{\frac{3}{2}}}{3\pi^2h^3}\int_0^\infty\left(-\frac{\partial f}{\partial z}\right)\tau(z)\frac{(z+\beta z^2)^{\frac{3}{2}}}{1+2\beta z}dz \quad (2.10)$$

where m^* is the conduction band effective mass which is taken to be equal to $m_{DOS}(m^* = m_{DOS})$ in modeling as an approximation.

The total electrical conductivity is given by:

$$\sigma = \sum_i \sigma_i \quad (2.11)$$

where σ_i is the electrical conductivity of each band.

Seebeck coefficient is calculated by the following equation for each band:

$$S = \pm\frac{k_B}{e}\left(\frac{{}^{1}\zeta_{-1}^{3/2}}{{}_{0}\zeta_{-1}^{3/2}} - \eta\right) \quad (2.12)$$

and then the total Seebeck coefficient can be computed by:

$$S_{tot} = \frac{\sum_i \sigma_i S_i}{\sum_i \sigma_i} \quad (2.13)$$

For p-type materials in thermal equilibrium, the electric field generated by the Seebeck effect and temperature gradient should point in the same direction, therefore S>0 and in case of n-type materials, we have S<0.

2.1.2. Thermal conductivity

Thermal conductivity can be calculated based on Steigmeier [7] approach. The theory of electron-phonon scattering which was developed by Ziman [8] is extended to high temperatures using the formalism of Klemens and Callaway [9]. Phonon-phonon scattering, electron-phonon scattering, and point defect scattering mechanisms with separate relaxation times were taken into accounted for in the calculation of the thermal conductivity.

The formalism introduced by Callaway [9] is used to calculate the lattice thermal conductivity

$$k_l = 4.67\times10^{-2}\left(\theta^2/\delta\right)\left\{I_1 + I_2{}^2 / I_3\right\} \tag{2.14}$$

$$I_1 = \int_0^1 \tau_c x^2 \frac{\nu^2 x^2 e^{\nu x}}{(e^{\nu x}-1)^2}\,dx \tag{2.15}$$

$$I_2 = \beta\int_0^1 (\tau_c/\tau_u) x^2 \frac{\nu^2 x^2 e^{\nu x}}{(e^{\nu x}-1)^2}\,dx \tag{2.16}$$

$$I_3 = \beta\int_0^1 (1/\tau_u)(1-\beta\frac{\tau_c}{\tau_u}) x^2 \frac{\nu^2 x^2 e^{\nu x}}{(e^{\nu x}-1)^2}\,dx \tag{2.17}$$

where

$$\tau_C{}^{-1} = \tau_N^{-1} + \tau_U^{-1}$$
$$\nu = (\theta/T)^{\kappa}$$
$$x = \omega/\omega_D$$
$$\beta = \frac{\tau_U}{\tau_N}$$
$$\rho = \frac{M}{\delta^3 N_A}$$

and δ is the cube root of the atomic volume, M is the atomic mass, ω_D is the Debye frequency, τ_C, τ_N and τ_U represent total, normal and Umklapp relaxation time respectively. κ is a factor to incorporate the effect of higher order phonon scattering. β is the ratio of Umklapp to normal mode scattering. We set κ=1and $\beta = 0.2$ in our model.

Total thermal conductivity is given by

$$k = k_l + k_e + k_b \tag{2.18}$$

where k_l represents the lattice part of thermal conductivity, k_e indicates the electronic part of it and k_b is the bipolar contribution to the total thermal conductivity.

The contribution of charge carriers to the thermal conductivity is given by Wiedemann-Franz law and by considering different bands [6], we have

$$k_e = \sum_i L_i T \sigma_i \tag{2.19}$$

$$L_i = \left(\frac{k_B}{e}\right)^2 \left\{ \frac{{}^{2}\zeta^{3/2}_{1}\zeta_{-1}}{{}^{0}\zeta^{3/2}_{1}\zeta_{-1}} - \left[\frac{{}^{1}\zeta^{3/2}_{1}\zeta_{-1}}{{}^{0}\zeta^{3/2}_{1}\zeta_{-1}}\right]^2 \right\} \tag{2.20}$$

which the summation is done over all involved bands.

According to Ravich [10], the bipolar Lorenz number is given by:

$$L_b = \frac{\sum_{i<j} \frac{\sigma_i \sigma_j}{\sigma_i + \sigma_j} (S_i - S_j)^2}{\sum \sigma} \tag{2.21}$$

where i and j are the valley indices.

2.2. **Figure of merit**

Thermoelectric materials are characterized by the dimensionless figure-of-merit, ZT. It is defined as:

$$\mathrm{ZT} = \frac{\mathrm{S}^2 \sigma}{\kappa} \mathrm{T} \tag{2.22}$$

Here, S is Seebeck coefficient, σ is electrical conductivity κ is total thermal conductivity, and T is the absolute temperature. ZT determines the maximum energy generation efficiency in generators, as well as the maximum cooling temperature in Peltier coolers.

As it is expressed in ZT equation, the thermoelectric efficiency is increased by square of the generated voltage (S^2) and electrical conductivity. The reduction of thermal conductivity will decrease the heat transfer through the sample, so the temperature difference can be remained constant. It must be considered that all of the three thermoelectric parameters are related to each

other. In order to illustrate the tradeoff between Seebeck coefficient, electrical conductivity, and thermal conductivity all parameters as a function of carrier concentration are shown in Figure 2-3 schematically. All materials have thermoelectric (TE) properties, but degenerate semiconductors have the best thermoelectric properties which are indicated in the Figure 2-3. Metals have high electrical conductivity as well as high thermal conductivity. Because the electronic part of the thermal conductivity which is the dominant part in total thermal conductivity in metals, is proportional to the electrical conductivity due to Wiedsmann-Frantz law. The Seebeck coefficients of metal are very low. In contrary, insulators have high Seebeck coefficient and low thermal conductivity, but they are not conductive electronically. The semiconductor which are located in the medium carrier concentration region, have shown the best thermoelectric properties. The free carriers in semiconductors are made by doping procedure. Their electrical conductivity can be changed by doping type and doping concentration. In addition, the lattice part of the thermal conductivity which is the dominant part in semiconductors can be reduced via some methods such as alloying without a significant effect on electrical conductivity. Therefore, by tuning the doping concentration, and lattice thermal conductivity reduction, thermoelectric properties of degenerate semiconductors would be optimized to have maximum figure-of-merit.

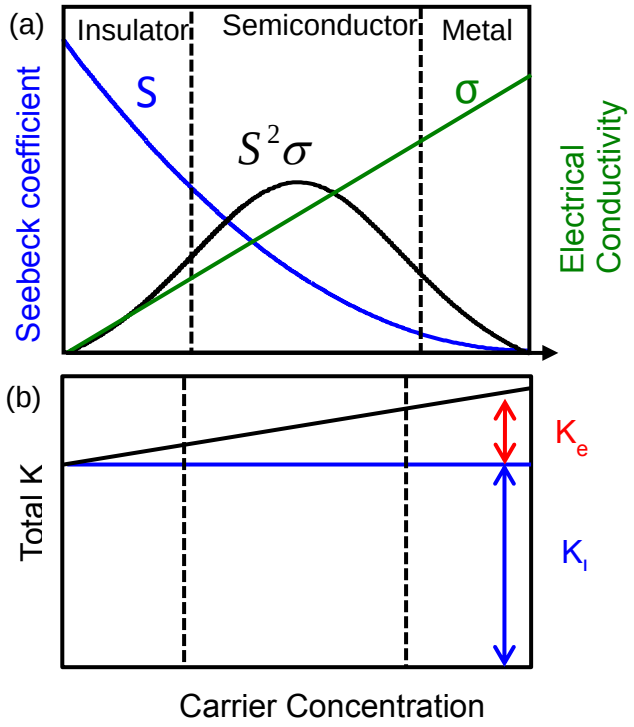

Figure 2-3 Thermoelectric properties as a function of carrier concentration

2.3. **Efficiency of thermoelectric devices**

The limiting value for the efficiency of energy conversion from the waste heat depends on the temperature of the hot (T_H) and cold (T_c) junctions and is given by the well-known Carnot efficiency: $\eta_{carnot} = 1 - T_C/T_H$. This is the ideal efficiency, which indicates that the larger the ratio of the hot to cold side temperature, the larger the efficiency. The theoretical efficiency of a thermoelectric device η_{TE} depends on the Carnot efficiency and thermoelectric material efficiency which expresses with material figure of merit (ZT) [1]:

$$\eta_{TE} = \eta_{carnot} \times \frac{\sqrt{ZT+1}-1}{\sqrt{ZT+1}+T_C/T_H} \quad (33)$$

Figure 2-4 depicts the efficiency of the thermoelectric energy conversion versus the figure-of-merit at two cases of low and high temperatures. The cold side temperature for both cases is assumed to be 10 °C. The efficiency at 90 °C remains below 5% even with relatively large ZT of 1.5.

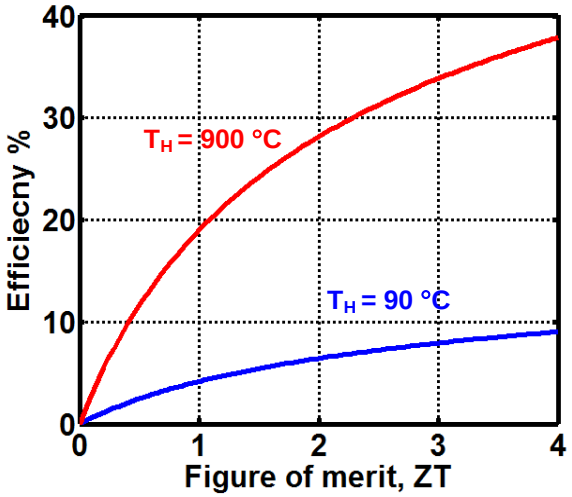

Figure 2-4 Efficiency of thermoelectric energy conversion versus figure of merit for two cases of low (90C) and high (900C) temperatures.

However, the efficiency at 900 °C is above 20% for ZT>1.1 and approaches to ~28% for ZT of 2. The enhanced efficiency at higher temperature is due to the fundamental limit of the Carnot efficiency and indicates the benefit of having good TE materials that can work at higher temperature range.

2.4. **References**

1 D.M Rowe, Thermoelectrics Handbook : Macro to Nano,CRC press, BocaRaton, FL,2005.

2 H. Julian Goldsmid, Springer, 2009.

3 Ali Shakouri, Annu. Rev. Mater.Res. 2011.

4 Zebarjadi M, Shakouri A, Esfarjani K, Phys. Rev. B, 74: 195331, 2006.

5 C. B. Vining, SCT- 93, 1993.

6 Ravich, Semiconducting Lead Chalcogenides, 1970, pp349.

7 E.F.Steigmeier and B.Abeles, Physical Review Volume 136, Number 4A 16 NOV. 1964.

8 J.M.Ziman, Philos. Mag. 1, 191 (1955).

9 J.Callaway, Phys. Rev.113, 1046 (1959).

10 Yu. I. Ravich et al., Semiconducting Lead Chalcogenides, Plenum, New York, pp189 (1970).

Chapter 3: Methodology

Presented research studies have been pursued in a combined theoretical and experimental approach. Different materials synthesis have been accomplished with similar experimental procedure of ball milling and hot press sintering developed for making bulk nanostructured thermoelectric materials [1]. The theoretical calculations were used for the further analysis of experimental data and utilized as guidance in optimizing the experimental parameters. In this chapter, a brief description of the experimental process and theoretical procedure are presented.

3.1. Experimental Procedure

In order to obtain a nanostructured thermoelectric material with the desired composition, the high energy ball milling was used for all different processed materials. Mechanical ball milling was utilized for two purposes. First, making alloys from constituent materials and also for composition of two different alloys. The second purpose was grinding the alloyed structures into nano-scale crystallites. The obtained grains usually were in the order of micrometer and the crystallite sizes several of nano meters. The next common step was sintering process of desired alloys. The hot press technique was applied in all the material sintering. Electrical and thermal properties of synthesized samples were measured as a function of temperature.

3.1.1. Mechanical milling

Powders with desired stoichiometric ratio were loaded in Tungsten Carbide bowls. All different types of processed powders in this project were milled in a planetary mill (Fritsch P7 PL) under Argon atmosphere with different milling parameters. The milling parameters are specifically optimized for different materials to obtain the nanostructured alloys. The details of optimum milling parameters were explained for each material structure in the related chapters.

The mechanical alloying process was explained in details in other reports [2,3]. The milling parameters definition is described briefly here:

The milling time is the total run time excluding the pause durations. Pause time was introduced after each run time to prevent overheating of the bowl. The effectiveness of the mechanical alloying to produce a specific structure depends on the ball-to-powder ratio. The bigger ball-to-powder ratio leads to more efficient formation of alloy and nanostructuring. The optimum ball-to-powder ratio required for each material structure was obtained experimentally for different processed powders. The centrifugal factor is defined as: $F=R\omega^2/g$, where R is the distance from the center of the disk to the center of the bowl, ω is the angular frequency of the sun-disk, and g is the gravitational acceleration. The other critical value for the milling condition is the ratio of the speed of the bowls (n) and sun-disk (N), i.e., n/N. This ratio sets the milling regime of impact, attrition, or combined. The mills had ratio of $n/N \cong 2$ which set a combined regime suitable for simultaneous mechanical alloying and crystallite size reduction [4].

In order to study the alloying progress, crystallite size, and contaminations, small amount of powders were collected at different milling times for X-ray diffraction characterization.

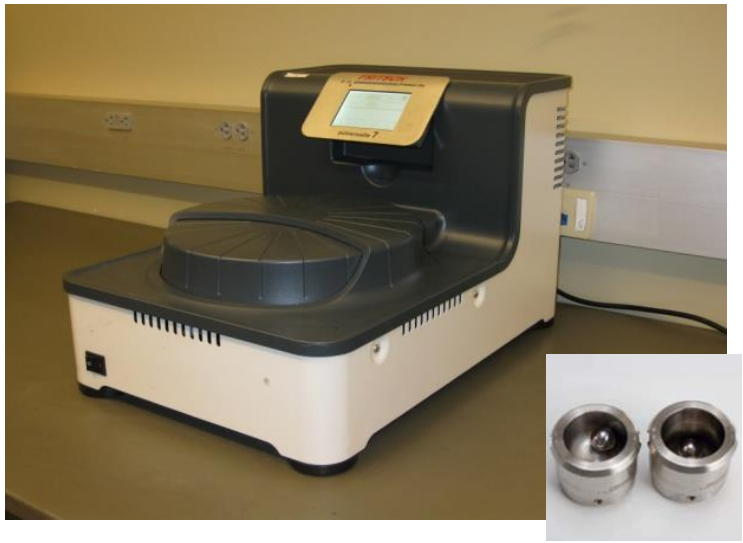

Figure 3-1 Fritsch P7 PL high energy planetary mill with tungsten carbide bowls and balls.

3.1.2. Hot press Densification

Direct hot press technique which is one of the methods in sintering of thermoelectric materials [5] was used to sinter the prepared powders. In this method (Figure 3-2 (a)), the powder is loaded

into a graphite die. In order to apply pressure, the powder is sandwiched between two graphite rods which is shown in Figure 3-2 (b). The die configuration heated up by passing a DC current though the powder which is under desired pressure. The pressure was applied by means of a hydraulic press. The effective press conditions are sintering temperature, holding time and applied pressure. The holing time is the time when the sample is held at the sintering temperature. For each specific material structure, all sintering parameters were optimized experimentally.

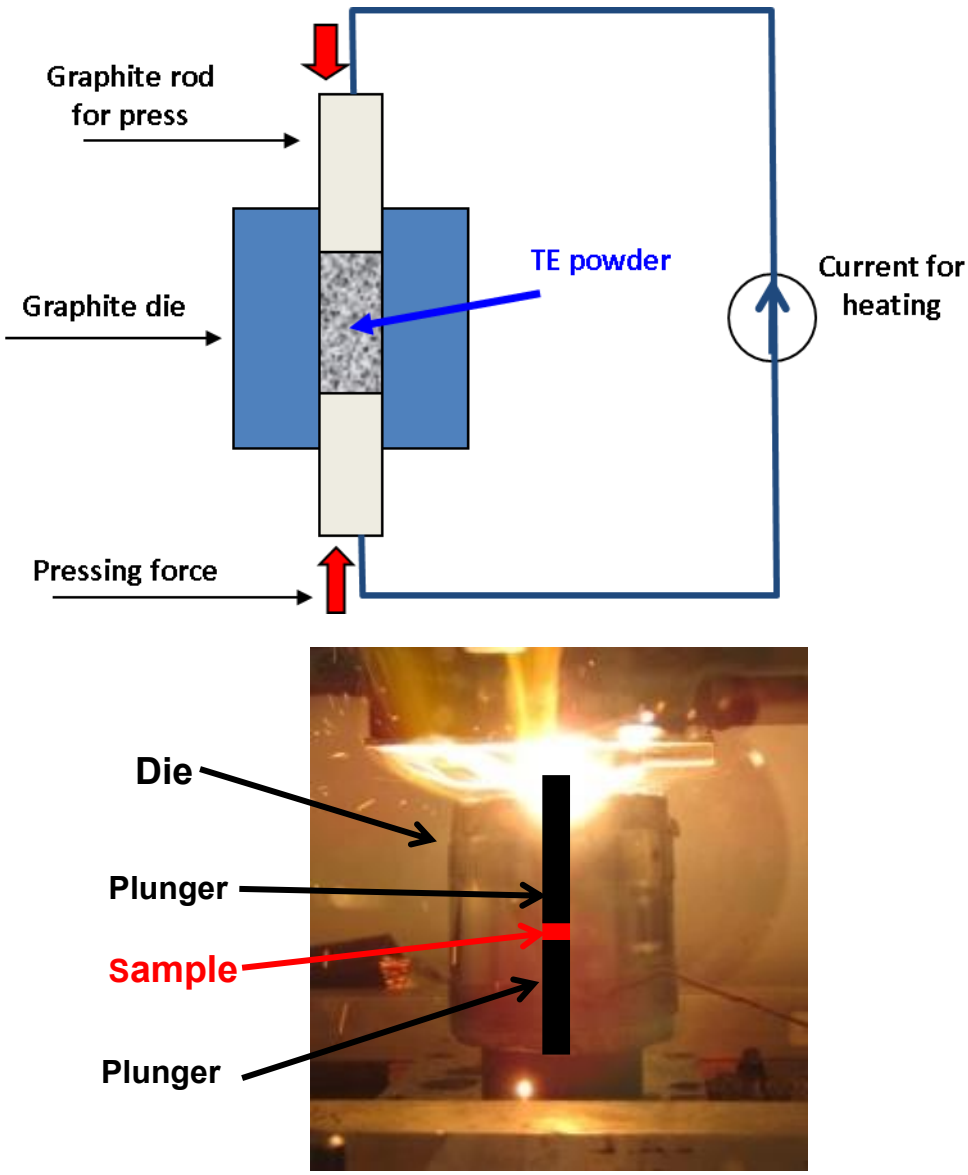

Figure 3-2 (a) Schematic hot press set up and (b) sample position in a die.

3.1.3. Thermoelectric Material characterization

Both milled powders and hot pressed samples were characterized by X-ray diffraction (Brucker AXS D8-Discover) with Cu K_α radiation, Scanning Electron Microscope (Hitachi S-4800), and Transmission Electron Microscope (JEOL JEM-2100). Energy Dispersive Spectroscopy (EDS) was employed to determine the composition and contamination levels (EDAX Apollo SDD detector). For most of the structures, the XRD data were recorded in the range of 2θ angles between 20˚ to 60˚. The identification of phases and the crystallite size were determined using the diffraction spectrum.

The sintered samples were cut into disks and rods for different type of measurements (Figure 3-3). The mass densities of the samples were measured using the Archimedes' principle. Seebeck coefficient and electrical conductivity of the samples were simultaneously measured in the temperature range of 300– 1273K with the four probe method using the commercially available equipment (Ulvac, ZEM-3). Thermal conductivity was measured from the disk samples of 2mm thick by laser flash method using Netzsch LFA 457.

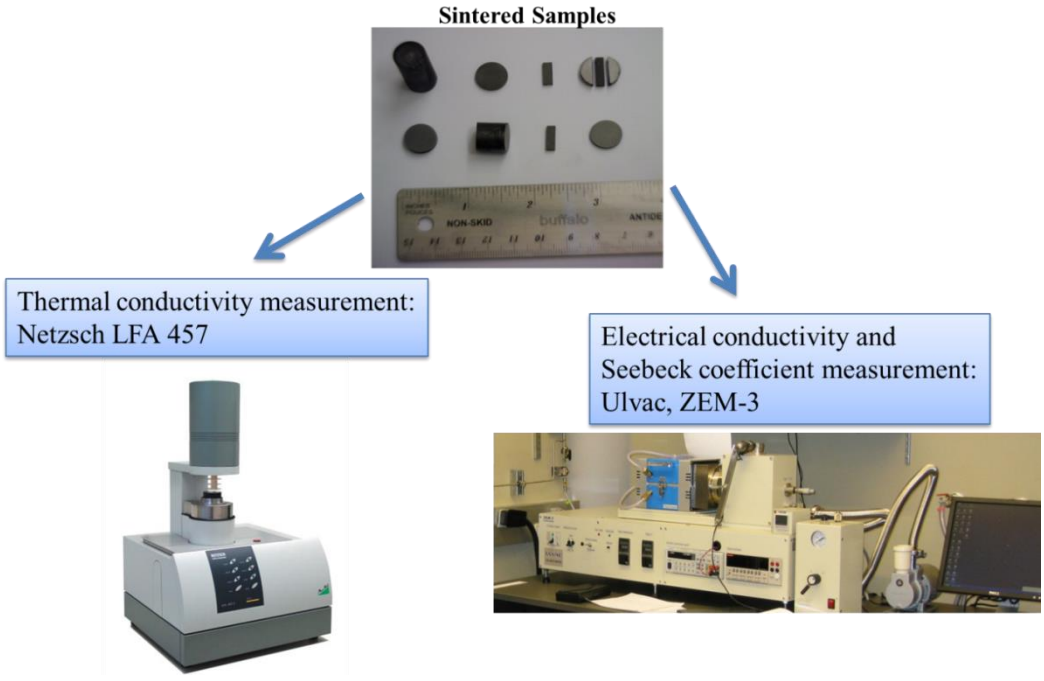

Figure 3-3 Sintered samples were cut into disk for thermal conductivity measurement and rod for electrical conductivity and Seebeck coefficient measurements.

3.1.4. Theoretical procedure

A code for theoretical modeling of TE material characterization has been developed in our group using Boltzmann equation with relaxation time approximation [6,7]. This code has been used to fit the experimental data with theory and extract more physical parameters and analyze the experimental results. The details of modeling calculations were described in the related sections in each chapter where the results for a specific material were explained. As it is shown in Figure 3-4 flow chart, the code is working based on the following procedure. According to

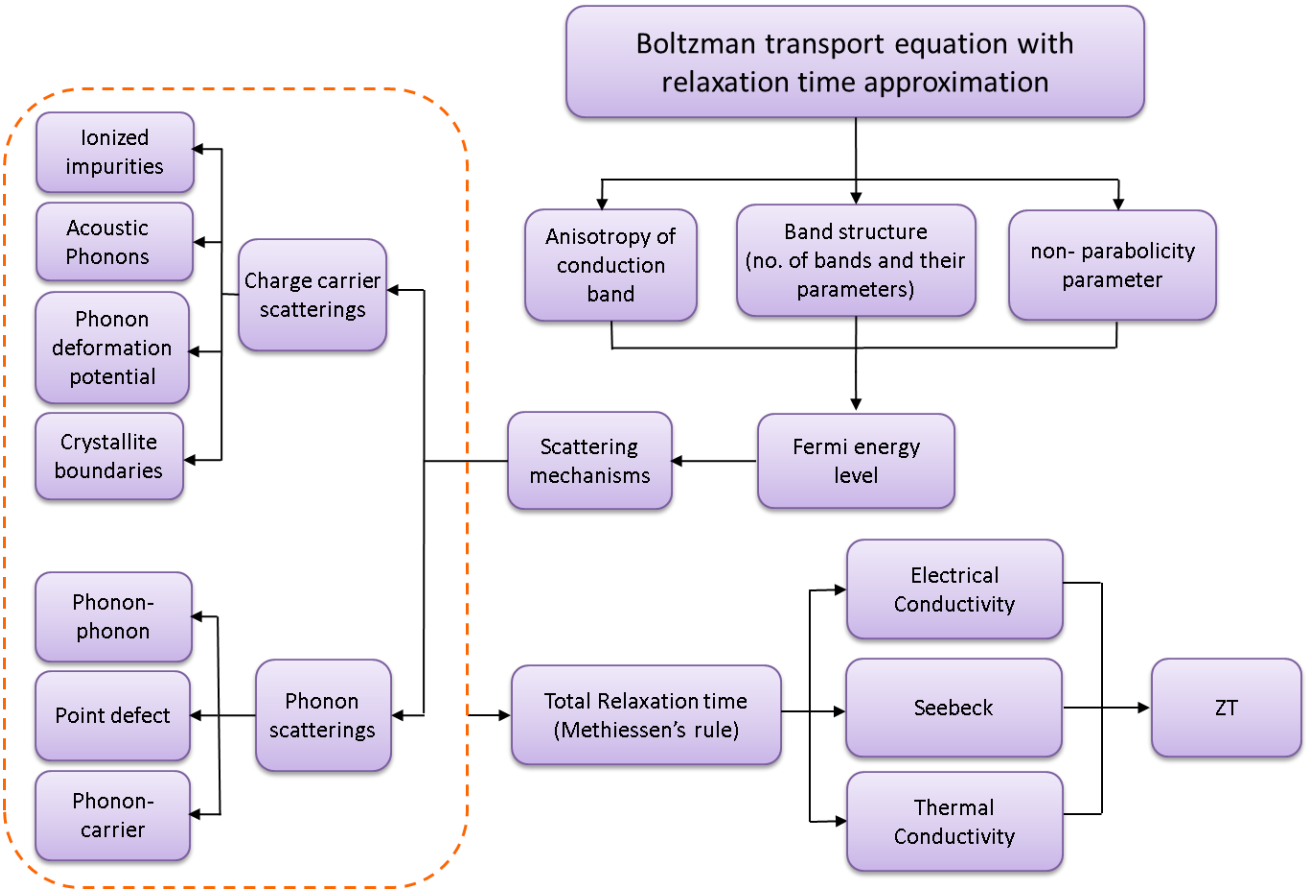

Figure 3-4 Theoretical modeling process flow determining TE properties of different material structure.

Boltzman equation, Fermi energy level and carrier concentration were calculated for specified doping level of desired material using the band structure parameters, anisotropy of conduction band and nonparabolicity parameters. The scattering mechanism contains two main groups:

charge carrier scatterings and phonon scatterings. Charge carrier scatterings include ionized impurities, acoustic phonons, phonon deformation potential and crystallite boundary scatterings. The phonon scatterings are due to phonon-phonon, point defect and phonon-carrier scatterings. Total relaxation time is calculated by Mathiessen's rule. Therefore, electrical conductivity, Seebeck coefficient, thermal conductivity, and ZT of desired structure can be calculated.

3.2. **Reference**

1 Bed Poudel, "A Study on Thermoelectric Properties of Nanostructured Bulk Materials", PhD Dissertation, Boston College, 2007.

2 C. Suryanarayana, Mechanical Alloying and Milling, Marcel Dekker, New York, 2004.

3 J. Schilz, M. Riffel, K. Pixius , H.-J. Meyer, Powder Technology 105 _1999. 149–154.

4 P. R. Soni, "Mechanical Alloying: Fundamentals and Applications", Cambridge Int. Science Publishing, Cambridge, 1999, ISBN 1898326568.

5 N.Savvides, H.J. Goldsmid, Hot-press sintering of Ge-Si alloys, Journal of Materials Science, 15 (1980) 594-600.

6 Zahra Zamanipour, Xinghua Shi, Arash M. Dehkordi, Jerzy S. Krasinski, Daryoosh Vashaee, Physica Status Solidi (b), Phys. Status Solidi A 209, No. 10, 2049–2058 (2012) / DOI 10.1002/pssa.201228102.

7 Payam Norouzzadeh, Zahra Zamanipour, Jerzy Krasinski, Daryoosh Vashaee, J. of Applied Physics, 112, 124308 (2012)

Chapter 4: Transport properties of nanostructured bulk thermoelectric p-type Silicon Germanium alloy

4.1. Introduction

Silicon Germanium (SiGe) has been one of the main thermoelectric materials for power generation at high temperatures above 800 ˚C. It was used in Radio Isotope Thermoelectric Generators (RTG's) powering NASA space-crafts since 1976 [1]. SiGe alloys possess high mechanical strength, high melting point, low vapor pressure and resistance to atmospheric oxidation [2]. Therefore, they are suitable for device applications at high temperatures. Improving the thermoelectric efficiency of SiGe alloys is especially interesting for industrial waste heat recovery, auto industry, and solar thermal power plants.

There have been many experimental research studies to improve thermoelectric figure-of-merit, ZT, of SiGe [1,3]. The maximum ZT of n-type bulk crystalline $Si_{0.8}Ge_{0.2}$ is ZT≅1 while the ZT of p-type bulk crystalline $Si_{0.8}Ge_{0.2}$ is ZT≅0.5 [1,4]. The main reason for the smaller ZT of p-type SiGe material compared with n-type SiGe is the smaller mobility of holes compared with electrons. Recently, there have been several studies to enhance the thermoelectric figure-of-merit of both n-type and p-type SiGe alloys [5,6,7,8,9,10,11,12]. In almost all these works the enhancement in ZT has been shown by reducing the thermal conductivity via nanostructuring. The scientific advantages of nanostructuring to enhance ZT are discussed in ref. [5]. In bulk nanostructured SiGe, the extra interfaces in the material enhance the phonon scattering. Since the phonon mean free path in SiGe is larger than that of charge carriers, such interfaces affect phonon transport more than transport of charge carriers [8]. Therefore, significant reduction of thermal conductivity is possible with small or no change in electrical conductivity.

The enhancement in ZT of nanostructured p-type SiGe was demonstrated in ref. [6]. It was shown that nanostructuring can result in ~50% enhancement in ZT compared to the best previously reported value for this material. The material was synthesized via mechanical milling and sintering approach. Subsequent works presented in refs. [7], and [10] on this material system confirmed the benefit of nanostructuring for enhancing ZT.

In previous studies of bulk nanostructured SiGe, the effect of material synthesis parameters on thermoelectric properties were barely discussed. As we will present in this study, the thermoelectric properties are highly sensitive to the process parameters and their precise optimization is required to improve ZT. As we will show the ZT of a nanostructured SiGe sample may degrade significantly without proper synthesis parameters.

The successful enhancement of ZT of nanostructured SiGe was followed by several theoretical studies. Refs. [8], and [9] explained the experimental data with model calculation and predicted ZT enhancement via nanostructuring. Although model calculations showed that further enhancement in ZT is possible with optimizing the crystallite size, germanium concentration, and doping concentration, in practice there are several other process parameters that have to be optimized to enhance ZT.

The purpose of this study is to show the importance of the synthesis parameters in making these structures. The data of several samples are selected from a large quantity of accumulated samples grown and studied in the last several years by the authors. The comparison of the data reveals the most important synthesis parameters affecting the electronic and thermal transport properties of these structures. Here we present the effect of mechanical milling and sintering conditions on the thermoelectric properties of nanostructured bulk p-type SiGe alloy. Variation of thermal and electrical properties with the average crystallite size, porosity, and doping concentration are studied. These are the main parameters in optimizing the materials morphology to enhance the thermoelectric figure-of-merit. Precise control of the milling and sintering conditions are required to optimize these parameters as we will discuss it in this chapter.

4.0. Experimental Procedures

Powder mixture of Silicon (>99.9%, Alfa Aesar), Germanium (>99.99% Alfa Aesar), and 2 at% boron (>99%, Alfa Aesar) as p-type dopant were loaded in Tungsten Carbide bowls. Powders

were milled in a planetary mill (Fritsch P7 PL) at 800 rpm under Argon atmosphere with ball-to-powder ratio of 8:1. The powders were mixed and reloaded into a bowl in periodic time intervals of a few hours to avoid sticking of the powder to the bowl.

The milling parameters for different samples are listed in Table 4.1. Here the milling time is the total run time excluding the pauses during the milling. Five minutes pause time was introduced after each ten minutes run to prevent overheating of the bowl. The centrifugal factor is defined as $F=R\omega^2/g$ in which R is the distance from the center of the disk to the center of the bowl, ω is the angular frequency of the sun-disk, and g is the gravitational acceleration. Another critical value for the milling condition is the ratio of the speed of the bowls (n) and sun-disk (N), i.e. n/N. This ratio sets the milling regime of impact, attrition, or combined. The mills had ratio of $n/N \cong 2$ which set a combined regime suitable for simultaneous mechanical alloying and size reduction [13].

In order to investigate the alloying process, samples were taken at different milling times for X-ray diffraction characterization. The powder was pressed in a cylindrical high strength graphite die with an internal diameter of 12.7 mm under 93 MPa pressure for 10 minutes followed by sintering at 1200 ˚C at the same pressure. The details of the sintering conditions are listed in Table 4.1. Here heating rate defines the rate of temperature increase in the unit of degree per minute. The holing time refers to the time when the sample is held at the sintering temperature. Samples 1, 2, 3, and 5 were held at 1200 ˚C for 6 minutes; however, there was no holding time for sample 4.

The sintered samples were cut into disks and rods for different measurements. The mass densities of the samples were measured using the Archimedes' principle. Both milled powders and hot pressed samples were characterized by X-ray diffraction (Brucker AXS D8-Discover) with Cu K_α radiation, Scanning Electron Microscope (Hitachi S-4800), and Transmission Electron Microscope (JEOL JEM-2100). Energy Dispersive Spectroscopy (EDS) was employed to determine the composition and contamination levels (EDAX Apollo SDD detector). The XRD data were recorded in the range of 2θ angles between 20˚ to 80˚. The identification of phases and the crystallite size were determined using the diffraction spectrum.

Seebeck coefficient and electrical resistivity were simultaneously measured in the temperature range of 300 K to 1273 K with the four probe method using the commercially available

equipment (Ulvac, ZEM-3). Thermal conductivity was measured from the disk samples of ~2 mm thick by laser flash method (Netzsch LFA 457).

4.1. Experimental Results

4.1.1. X-Ray Diffraction and Electron Microscopy Data

The XRD data taken from a processed powder and a hot pressed sample (sample 2) are shown in Figure 4-1. The powder spectrum shows diffraction lines which are located between Si (main-2θ=28.47˚) and Ge (main-2θ=27.29˚) lines. SiGe alloy makes a continuous solid solution, so the diffraction line from the alloy shifts from Si to Ge as the concentration of Ge is increased. The sharp line at main-2θ=28.28˚ indicates that alloying of $Si_{0.8}Ge_{0.2}$ is complete. A small peak close to 2θ=35.6˚ is seen for the powder which is not seen for the pressed sample. This peak matched with silicon oxide. This can be associated with the oxidation of the tested powder during the XRD measurement.

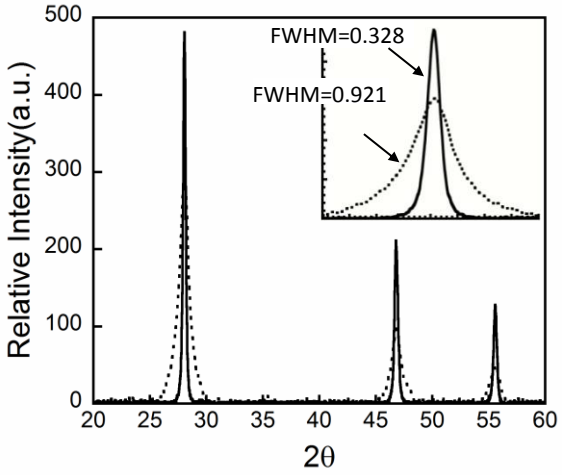

Figure 4-1: X-ray diffraction patterns of sintered sample 2 (solid line) and its powder (dotted line). Inset shows the corresponding peaks at 2θ≈28.28˚.

The inset in Figure 4-1 compares the broadening of the main diffraction line in the milled powder and the corresponding sintered sample. The average crystallite size is estimated as 25 nm for the sintered sample and 9 nm for its powder. This indicates that the crystallites grow during the sintering process.

The line broadening is created due to residual stress and the crystallite size. Since the crystallite sizes are small (10-30 nm), it is expected that the line broadening of the peak is dominated by the size of the crystallite rather than the residual stress.

The average crystallite size was calculated by commercial software (EVA 14, Bruker-AXS). The software uses a full pattern matching (FPM) of the XRD scan using an empirical model for the peak shape. The fitting of the scan is done by pseudo-Vigot functions. At the completion of the FPM model, the software calculates the crystallite size by the corrected Scherrer's formula for the instrumental broadening [14].

$$L = \frac{k.\lambda}{\cos\theta.\sqrt{U^2 - S^2}}$$

λ is the wavelength of the radiation, k is the Scherrer constant, a shape factor which is 0.89(ratio between the FWHM and the integral breath), $\sqrt{U^2 - S^2}$ is integral breath for Gaussian profile in which U is the FWHM of the unknown peaks and S is the instrument broadening in radian. Integral breath of the reflection is the corrected FWHM for crystallite size calculation by Scherrer equation.

Table 4.1 compares the calculated average crystallite sizes for the different samples.

The SEM and TEM images taken from the powder and the sintered sample are shown in Figure. 4-2. These images are similar to previously reported images from nanostructured SiGe alloys [6]. One can see that there is a distribution of crystallite sizes in the range of 10-500 nm. However, the large grains are made of smaller crystallites in the range of 10-20 nm. Comparing the crystallite size in the powder and the sintered sample, one can see significant crystallite growth due to sintering process.

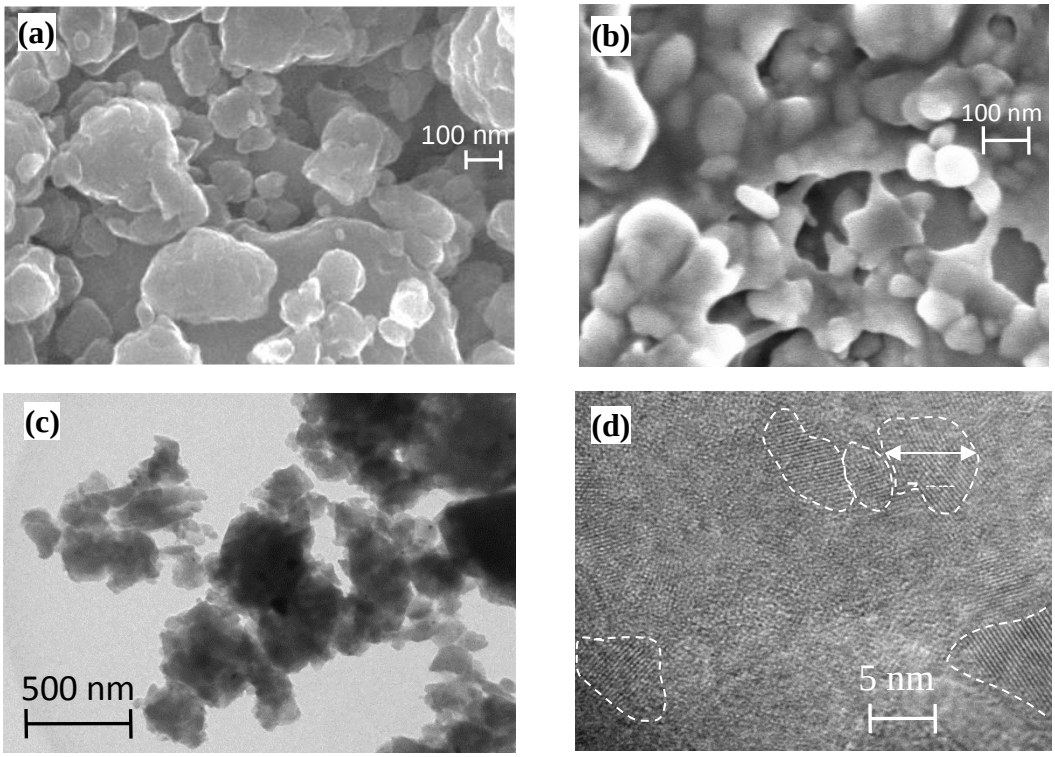

Figure. 4-2: SEM (a,b) and TEM (c,d) images of the SiGe powder (a,c,d) and the sintered sample (b).

4.1.2. Mass Density

The densities of different samples are shown in Table 4.1. In this manuscript, we refer to a sintered sample as "sample", and for powdered samples we use "powder". Sample 1 is $Si_{0.95}Ge_{0.05}$, and all other samples are $Si_{0.8}Ge_{0.2}$. The theoretical density of $Si_{0.8}Ge_{0.2}$ is 2.93 g/cm^3 and that of $Si_{0.95}Ge_{0.05}$ is 2.48 g/cm^3. One can see that samples 2, 3 and 4 have nearly 100% density and samples 1 and 5 have approximately 95% of theoretical density.

Table 4.1: Summary of the main characteristics of different sintered Si_xGe_{1-x} samples.

Sample ID	**1**	**2**	**3**	**4**	**5**
Composition (x)	0.95	0.8	0.8	0.8	0.8
Milling time (hour)	34	34	13	10	25
Centrifugal factor	72	72	72	72	72
Speed ratio, n/N	2	2	2	2	2
Holding time (min)	6	6	6	0	6
Heating rate (˚C/min)	171.4	291.5	257.1	285.7	266.7
Sintering temperature (˚C)	1200	1200	1200	1200	1200
Pressure (MPa)	93	93	93	93	93
Sample average crystallite size (nm)	22	25	29	31	33
Mass density (g/cm^3)	2.32	2.93	2.93	2.93	2.78

4.2. Thermoelectric Properties

Figure 4-3 shows electrical conductivity, Seebeck coefficient, thermal conductivity, and power factor of the samples versus temperature, and Figure 4 shows the figure-of-merit, ZT, of the samples as a function of temperature.

The temperature range is from room temperature to 1000 ˚C. Thermoelectric parameters of p-type SiGe crystalline bulk alloy used in RTG are also shown in the plots with solid lines for comparison [6].

These samples were selected from large quantity of accumulated samples grown by different synthesis parameters. The parameters listed in Table 4.1 such as the milling and sintering conditions were found to be close to optimum values. Sample 1 is an example of SiGe alloy with different composition ($Si_{0.95}Ge_{0.05}$) than the other four samples ($Si_{0.8}Ge_{0.2}$), which is selected to show as an example for the effect of variation in germanium concentration. The selected samples, which are grown under close to optimum conditions, still show large diversity in their thermoelectric properties. This indicates the high sensitivity of the thermoelectric properties to the variations in material composition and growth process parameters.

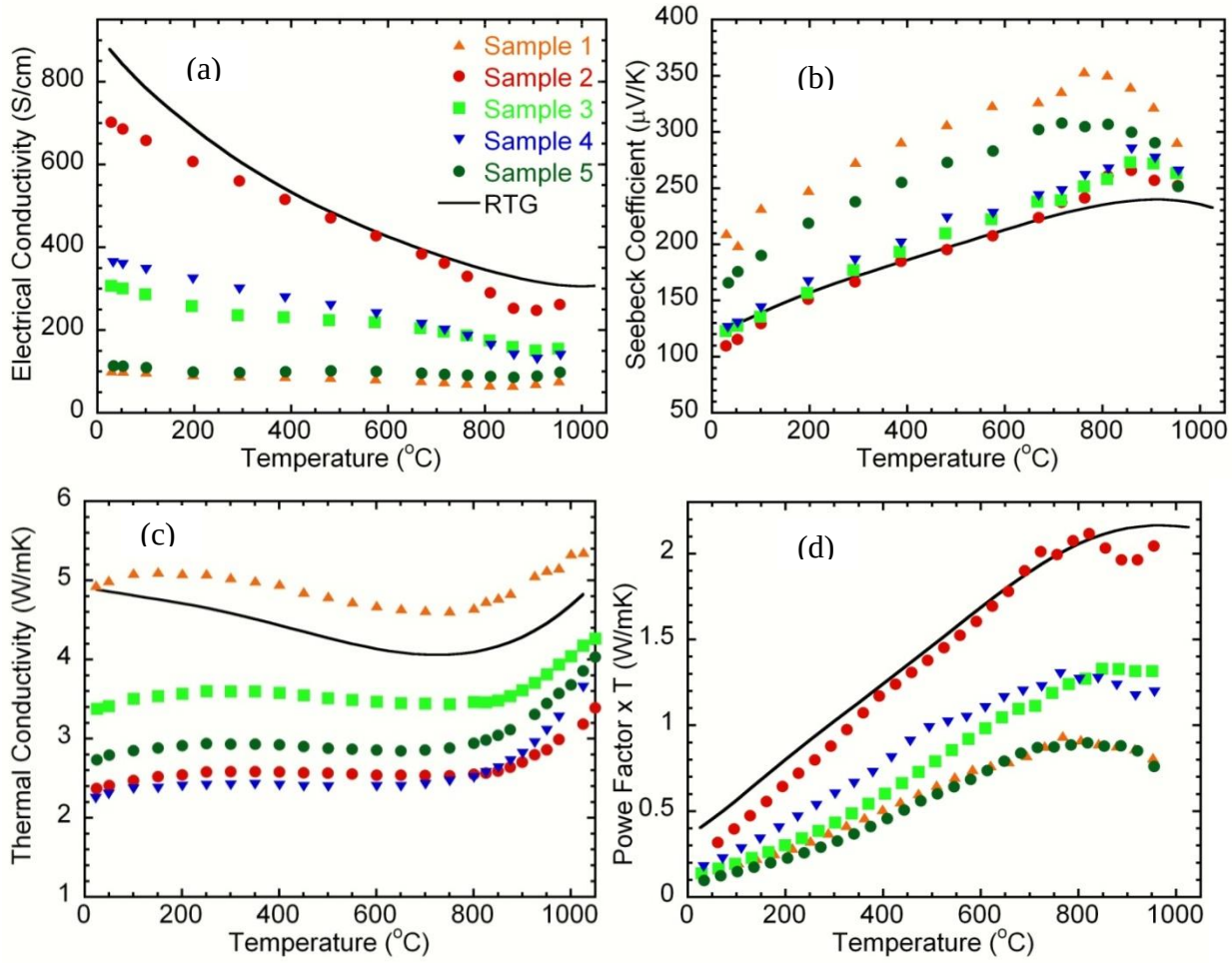

Figure 4-3: (a) Electrical conductivity, (b) Seebeck coefficient, (c) Thermal conductivity, and (d) Power factor times temperature of nanostructured bulk SiGe samples (symbols). For comparison the data for p-type SiGe bulk alloy used in RTG (solid lines) is also shown.

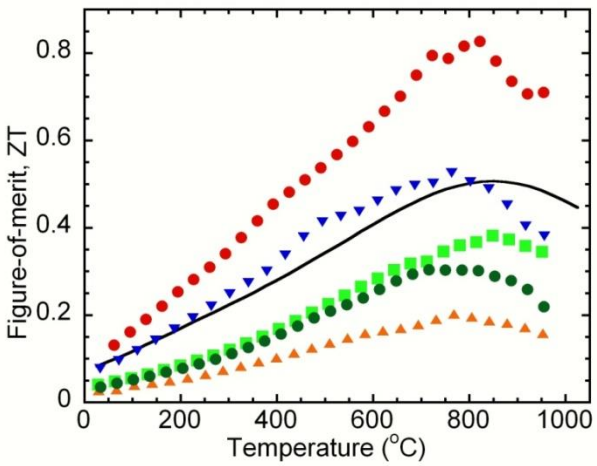

Figure 4-4: Thermoelectric figure-of-merit ZT of nanostructured bulk SiGe samples (symbols) compared with p-type SiGe bulk alloy used in RTG (solid line).

4.3. **Theoretical Modeling**

The electrical and thermal transport properties were calculated using the Boltzmann transport equation in relaxation time approximation framework. The model is explained in detail in ref. [8]. In brief, a three energy band model, including X and L symmetry points in conduction band and Γ point in valance band, was assumed for SiGe. The dominant scatterings for charge carriers were due to acoustic phonons, ionized impurities, deformation potential of optical phonons, and the crystallite boundaries. The Steigmeier and Abeles model was used for calculation of lattice thermal conductivity [15,16]. Three-phonon, charge carrier-phonon, point defect, and crystallite boundary scattering mechanisms were included in this calculation. The model for crystallite boundary scatterings of charge carriers and phonons are described in ref. [8]. Here coherent carrier scattering of charge carriers at independent grain boundary sites is modeled by a local disk shape potential. The scattering potential Pg is defined in cylindrical coordinate as $P_g = P_0 e^{-|z|/z_0}$ for $r < r_0$, and $P_g = 0$ for $r > r_0$, in which z is the direction perpendicular to the crystallite boundary, z=0 is the center of the disk, P_0 is a constant defining the strength of the crystallite boundary potential, and r_0 is the radius of the disk on the order of the charge screening length. The decaying exponential models the depletion of charge carriers at the crystallite boundary region. The TE characteristics of the nanostructured SiGe were calculated after incorporating the crystallite boundary scattering while keeping all other parameters unchanged.

Table 4.2 lists the carrier concentration, hall mobility, lattice and thermal conductivities of the samples at room temperature. For comparison, the properties of RTG sample are also shown.

Figure 4-5 show the model calculation for the thermoelectric properties of sample 2 and RTG versus temperature. A good agreement between the model and experimental data was achieved for both thermal and electrical properties. It was found that a crystallite size of 27 nm would fit the experimental data of sample 2, which is very close to the average crystallite size measured by X-ray diffraction for this sample. Figure 4-6 depicts the corresponding Hall mobility and hole mean free path (MFP). The hole MFP in RTG sample is estimated to be ~4.7 nm at room temperature. The corresponding value for the nanostructured sample is ~2.4 nm which is ~50% smaller than that of RTG. Similar trend observed for their Hall mobility at room temperature. However, the hole MFP at high temperature for both samples approaches ~ 2 nm. The difference between the Hall mobility of both samples is also reduced with temperature approaching 10 cm^2/Vs at 1000 ˚C.

Table 4.2: Comparison of selected room temperature properties of different samples.

Sample name	**Hole concentration ($\times 10^{20}/cm^3$)**	**Hall mobility (cm^2/Vs)**	**Lattice thermal conductivity (W/mK)**	**Electronic thermal conductivity (W/mK)**
Sample 1	1.2	6.5	4.5	0.1
Sample 2	2.9	17	1.8	0.5
Sample 3	3.0	7	3.2	0.2
Sample 4	3.0	8.1	1.9	0.3
Sample 5	1.6	5.1	2.7	0.1
RTG	1.6	37	4.4	0.6

The main reason for the different trend at high temperature compared with room temperature is that at room temperature the holes are dominantly scattered by crystallite boundaries; whereas, at

high temperature they are dominantly scattered by acoustic phonons which has similar strength in both samples. Since the high temperature hole mean free path is not yet dominated by crystallite boundary scattering, it is still possible to further decrease the crystallite size to reduce the thermal conductivity without significantly affecting the electrical conductivity.

The data of Table 4.2,

Figure 4-5, and Figure 4-6 in connection with the samples growth process parameters will be discussed in detail in the following sections.

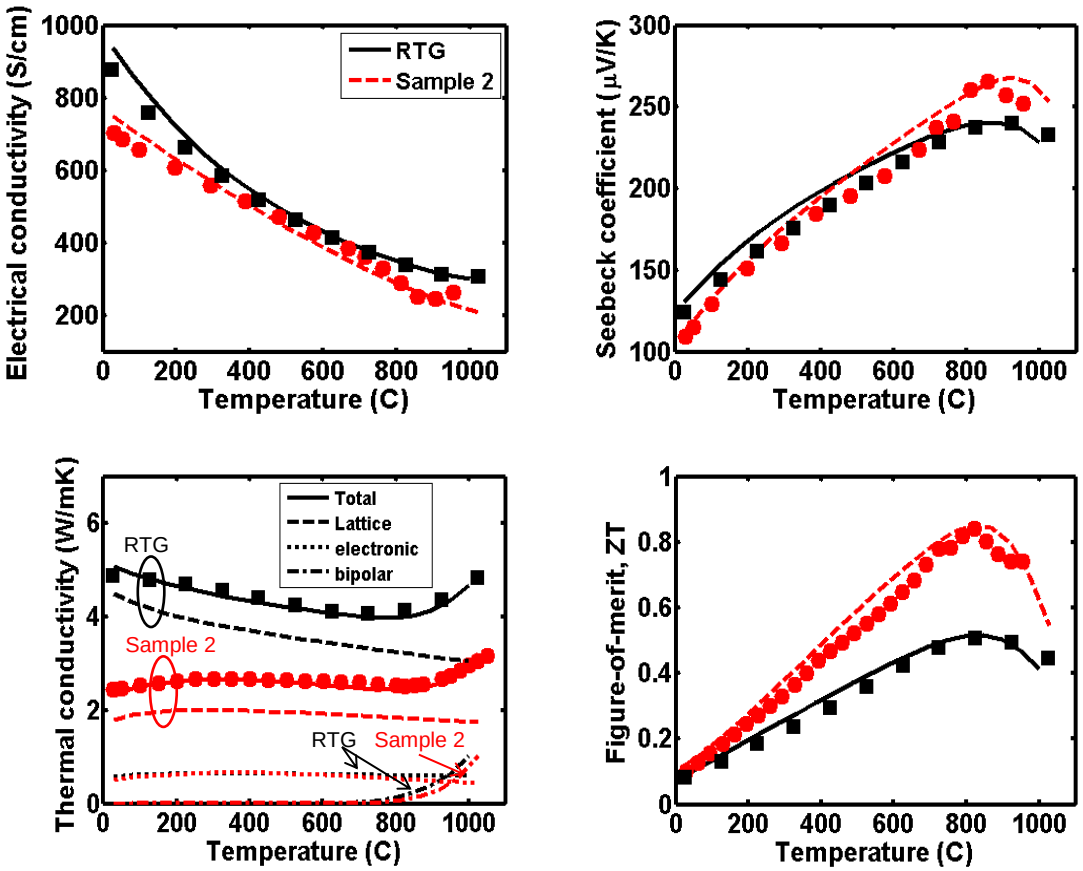

Figure 4-5 Comparison of calculated (lines) and experimental data (symbols) for thermoelectric properties of nanostructured SiGe (sample 2) and the RTG sample.

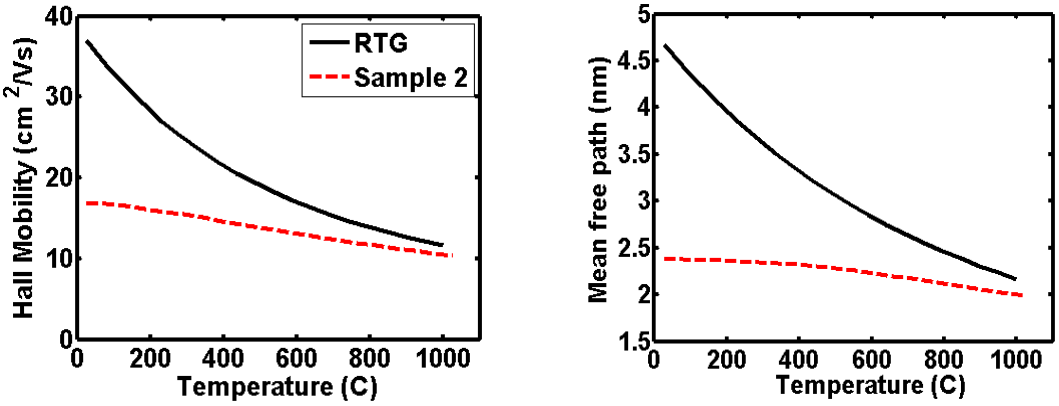

Figure 4-6 Comparison of Hall mobility and hole mean free path of nanostructured SiGe sample 2 and the RTG sample.

4.4. Discussion and Analysis

4.4.1. Growth Process Parameters

There are several important parameters that can affect the crystallite growth during sintering such as heating rate and holding time at sintering temperature. The rate of crystallites growth increases with temperature. Therefore, the press conditions must be well controlled, especially above 1000 ˚C, to make optimum structure in terms of the crystallite size, porosity, dopant activation, and the concentration of defects. Our experiments with many samples showed that if the sample is pressed with a short holding time, the electrical conductivity is often small. This can be due to the induced porosity and defect concentration. The effect of nanoscale porosity on thermoelectric properties of SiGe is discussed theoretically in ref. [17]. It was shown that in order to achieve high figure-of-merit, sample density must be high. In our work, although sample 3 and 4 are fully dense (100% of theoretical density), but their electrical conductivity is lower than that of sample 2 with same density. The similar Seebeck values of these three samples indicate that they have nearly equal carrier concentration. Therefore, the difference in electrical conductivity can be associated to the large concentration of crystallite interface defects in sample

3 and 4 compared with sample 2, which can reduce the charge carrier mobility. The crystallite boundary defects in these samples are often diverse consisting of amorphous phases, tilts, dislocations, twin boundaries, vacancy, or interstitial defects [6]. Although such defects can reduce the thermal conductivity by scattering phonons, they can also scatter charge carriers and reduce the electrical conductivity. To reduce the number of defects in the sample, the samples are typically sintered at a high temperature and are held at this temperature for a certain time, which we refer to as holding time in Table 4.1. Longer holding time reduces the defect density and provides better mechanical bonding of the crystallites. The holding temperature and time must be optimized to achieve good electrical conductivity while maintaining small crystallite sizes for minimum thermal conductivity to happen.

Two other important parameters that can affect the thermoelectric properties of the sintered samples are the pressure and the cooling rate after sintering. Our system allows maximum pressure of 93 MPa and this pressure was used in all our sintering processes. Smaller pressure may result in a porous sample. Although a porous sample can result in smaller thermal conductivity, our experiments show that the reduction in electrical conductivity in these samples is more severe. Therefore, porosity often results in smaller ZT, which confirms the previous theoretical study on porous SiGe [17].

The cooling rate which is the rate of cooling from the sintering temperature to about 600 ˚C might also affect the thermoelectric properties of the samples. We observed that the cooling rate does not have significant effect on the crystallite sizes. However, it can significantly affect the electrical conductivity due to the variation in the concentration of active boron atoms. At above 600 ˚C boron diffusion rate increases significantly [8]. At a small cooling rate boron atoms may diffuse and precipitate which would reduce the concentration of ionized boron acceptors in the lattice. This would reduce the hole concentration and consequently the electrical conductivity of the sample [18]. We studied three different conditions for the effect of cooling rate on dopant precipitation. In the first experiment, the die was air cooled after the sintering. This resulted in about 120 ˚C /min cooling. In the next experiment, the die was rapidly cooled with water resulting in about 240 ˚C /s. In the third experiment the pressed sample was heated to 1000 ˚C and slowly cooled to room temperature at a rate of approximately 30 ˚C /min. The samples of the first two experiments showed similar electrical conductivity. However, the sample of the third

experiment showed significant reduction in electrical conductivity due to the dopant precipitation. Therefore, air cooling was used for all other samples. The data plotted in Figure 4-3 and Figure 4-4 corresponds to the data measured after the first cooling process.

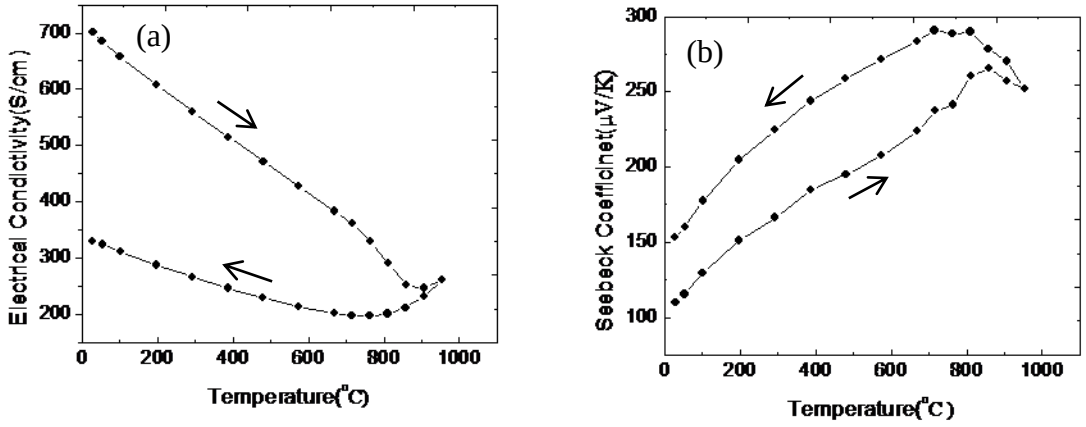

Fig 4-7: The effect of boron precipitation on electrical conductivity and Seebeck coefficient.

In order to further investigate the dopant precipitation, sample 2 was reset after the first measurement. The optimized reset process involves heating the sample to 1100 ˚C and holding it at this temperature for 20 minutes, followed by rapid cooling with quenching in water. After the reset process, the electrical conductivity and Seebeck coefficient were measured up to 1000 ˚C and measurements continued coming back to room temperature. The results are shown in Fig 4-7. Comparing the data of the heating cycle with that of the first measurement for electrical conductivity and Seebeck coefficient (Figure 4-3 (a) and (b)), one observes that both data are reproduced after resetting. In the cooling cycle, the electrical conductivity is significantly decreased. The reduction in electrical conductivity is accompanied by an increase in Seebeck coefficient, which is due to loss of active dopants by boron precipitation. The rest process proved that it is possible to reversibly activate boron atoms after their precipitation.

4.4.2. Electrical Conductivity and Seebeck Coefficient

In all the samples the electrical conductivity reduces with temperature. This is due to the reduction of carrier mobility caused by the increase of electron-acoustic phonon scattering at

high temperatures. At temperatures above 850 ˚C, a small increase in electrical conductivity is observed, which is due to the enhancement of intrinsic conduction at high temperatures.

A wide variation of electrical conductivity is observed for different samples. For example, at room temperature, sample 1 has the smallest electrical conductivity of approximately 100 S/cm while sample 2 has the largest value of approximately 700 S/cm. In order to understand such significant differences, it is helpful to compare the values of the Seebeck coefficients. A similar distribution but in an opposite direction in Seebeck values is also observed. This indicates that these variations are due to the concentration of charge carriers, which is in agreement with the data listed in Table 4.2.

The nominal boron concentration has been the same in all samples. The nominal boron concentration is the amount that is weighted and added to the powder for milling. However, the active boron concentration as we will discuss depends on the synthesis parameters.

Except for sample 4, the sintering conditions for all the samples have been similar. The only difference among these samples has been in their milling condition. The powder of sample 2, which has the highest electrical conductivity, has been milled at a higher energy compared with the powder of the other samples. This indicates the importance of the milling condition on doping concentration. It seems that at lower milling energy boron atoms are not homogeneously distributed in the lattice, which results in smaller carrier concentration.

The powder of sample 1 has been also milled with similar energy and time as sample 2. However, it has the smallest electrical conductivity and the largest Seebeck coefficient. This indicates that this sample has the smallest active dopant concentration (Table 4.2). It must be noted that the nominal boron concentration was 2% which is more than the equilibrium boron solubility limit (ESL) in SiGe. The ESL of boron in crystalline silicon is $9.25\times10^{22}\ exp(-0.73\ eV/kT)$ cm^{-3} [19]. This is nearly 10^{20} cm^{-3} at 1000 ˚C, which is ~0.2 at %. It is well known that the addition of germanium can increase the ESL of boron [20].Sample 2 ($Si_{0.8}Ge_{0.2}$) has higher germanium content than sample 1 ($Si_{0.95}Ge_{0.05}$). This shows that increasing the germanium content has enhanced boron solution in SiGe lattice.

It is further instructive to compare sample 2 with the RTG sample. The electrical conductivity of sample 2 is smaller than the RTG sample at room temperature. However, the difference in electrical conductivities is reduced at higher temperatures (T>400 ˚C). The Seebeck coefficient

of sample 2 is smaller than that of RTG sample at T<700 ˚C, which indicates sample 2 has higher ionized boron concentration. However, as depicted in Figure 4-6, the difference in their electrical conductivity at low temperature is mainly associated with the hole mobility. In RTG sample, the dominant hole scattering mechanism is ionized impurity scattering at room temperature and hole-acoustic phonon scattering at high temperatures. In sample 2, the dominant scattering mechanism is crystallite boundary scattering at room temperature and hole-acoustic phonon scattering at high temperatures. Therefore, the charge mobility in both samples is dominated by acoustic phonon scattering at high temperatures. Consequently, the difference in hole MFP of both samples is reduced with temperature as depicted in Figure 4-6, which agrees well with the fact that they both have similar electrical conductivity at high temperature.

At temperatures above 700 ˚C there is a sudden decrease in the electrical conductivity of sample 2. Such a behavior is not seen in the RTG sample. This drop in electrical conductivity can be related to the precipitation of ionized boron atoms at the crystallite boundaries in sample 2 [21,22,23]. The drop in carrier concentration has resulted in corresponding sudden increase in its Seebeck coefficient.

4.4.3. Thermal Conductivity

As shown in Figure 4-3-c, the thermal conductivity decreases with temperature. This is mainly due to the increase of phonon-phonon scattering with temperature [24] confirmed by the model calculation. However, above 800 ˚C the thermal conductivity starts to increase due to the ambipolar thermal conduction [25] as depicted in Figure 4-5.

The MFP of holes in highly doped p-type SiGe is about 2-5 nm (Figure 4-6). In contrast, the MFP of phonons is about 30-300 nm [8]. The larger MFP of phonons enables us to reduce the thermal conductivity in the nanostructured alloy without significantly affecting the electrical conductivity. For this purpose, the mean crystallite size of the alloy must be larger than the hole MFP and smaller than the phonon MFP.

Comparing the electrical and thermal properties of sample 2 with RTG, a significant reduction of thermal conductivity is observed without much decrease of electrical conductivity. The

electronic contribution to the thermal conductivity of sample 2 at room temperature is ~0.5 W/mK (dotted lines in Figure 4-6). The lattice thermal conductivity of sample 2 is ~1.8 W/mK, which is about half the value of the lattice thermal conductivity in the RTG sample (dashed lines in Figure 4-6).

It is expected that the lattice thermal conductivity is reduced with reducing the crystallite size due to the enhanced interfacial scattering [5,26,27,28,29]. However, as we will discuss the crystallite size is not always the only or the dominant parameter that affects the thermal conductivity as depicted in **Figure 4-8: Thermal conductivity of samples 1-5 at room temperature versus grain sizes.**Figure 4-8. This figure compares the thermal conductivity of several nanostructured SiGe samples versus their grain sizes.

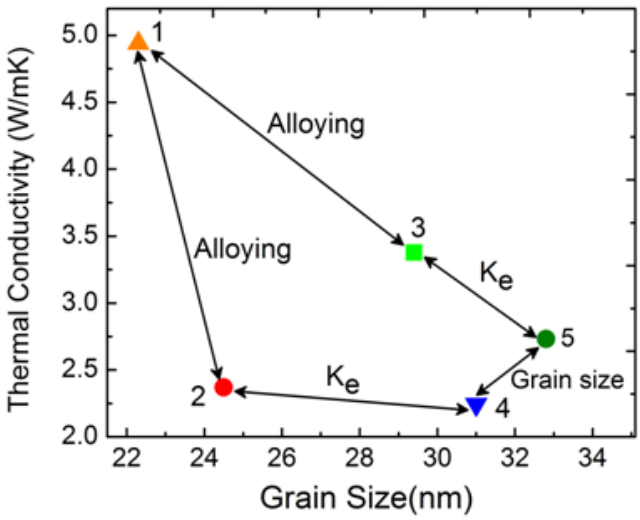

Figure 4-8: Thermal conductivity of samples 1-5 at room temperature versus grain sizes.

As can be seen in the thermal conductivity plot of

Figure 4-5, the lattice part of thermal conductivity is dominant at room temperature. However, at high temperature, the bipolar part of thermal conductivity becomes also important. Therefore, to study the effect of crystallite size, we compare the thermal conductivity of the samples at room temperature. Table 4.2 lists the calculated lattice and electronic thermal conductivities for

different samples. It is instructive to compare the thermal conductivity of selected samples (Figure 4-3 c) to study the effect of various parameters on thermal conductivity.

Sample 1 vs. others: Sample 1 has the highest thermal conductivity. The sample was prepared with same milling condition as sample 2, and the crystallite sizes are almost identical. However, sample 1 has much larger thermal conductivity. The composition of sample 1 is $Si_{0.95}Ge_{0.05}$ and all other samples are $Si_{0.8}Ge_{0.2}$. It indicates the strong effect of alloying in reducing the thermal conductivity [30,31]. The fact that the thermal conductivity in this nanostructured sample is not as small as those of other samples, shows that nanostructuring is not as effective as alloying in reducing the thermal conductivity [10].

Sample 2 vs. 3: The thermal conductivity of sample 2 (~2.4 W/mK) is significantly smaller than that of sample 3 (~3.4 W/mK). The difference, as listed in Table 4.2, is due to their different lattice thermal conductivity. This can be associated with the smaller average crystallite size in sample 2 compared with sample 3.

Sample 2 vs. 4: Sample 2 has the smallest average crystallite size of the samples. Although sample 4 has larger average crystallite size, it has smaller thermal conductivity compared with sample 2. Therefore, the crystallite size cannot explain the trend in their thermal conductivity.

Comparison of the Seebeck coefficient of the two samples shows that the carrier concentrations in the two samples are similar. Sample 4 is pressed at the same temperature and pressure as sample 2, but with no holding time. Therefore, the crystal defects in sample 4 are not annealed to similar level as in sample 2. The large density of defects has resulted in smaller lattice thermal conductivity in sample 4 (Table 4.2). In addition, the carrier mobility of sample 4 (8.1 cm^2/vs) is severely reduced due to the large density of defects at crystallite boundaries, which in turn results in smaller electronic thermal conductivity in this sample. Both effects have resulted in slightly smaller thermal conductivity in sample 4, but the reduction in electrical conductivity in this sample is severe resulting in smaller ZT. This again shows the importance of the holding time in the sintering process.

Sample 3 vs. 5: The average crystallite size in sample 3 is smaller than sample 5; however, sample 5 has smaller thermal conductivity. As listed in Table 4.2, this is due to both lattice and electronic thermal conductivity. Sample 5 has smaller mass density (2.78 g/cm^3) compared with sample 3 (2.93 g/cm^3), which results in smaller lattice thermal conductivity. Comparison of the

Seebeck coefficient of these two samples (Figure 4-3-b) indicates that sample 3 has larger carrier concentration (Table 4.2). Consequently, it has larger electrical conductivity and electronic thermal conductivity.

Sample 4 vs. 5: There are several factors that must be taken into consideration when comparing the thermal conductivity of these two samples: (a) Sample 4 has smaller average crystallite size than sample 5, which favors the reduction in thermal conductivity; (b) Sample 5 is porous with a density smaller than all other samples (~95% of full density). The higher density of sample 4 favors the increase in thermal conductivity; (c) Sample 4 is pressed with no holding time and sample 5 is pressed with six minutes holding time. Therefore, it is expected that sample 4 has larger lattice defect density than sample 5. This would in turn favor the reduction of thermal conductivity. The zero holding time for sample 4 has also resulted in smaller average crystallite size in this sample.

The fact that sample 4 has smaller thermal conductivity indicates that the effect of crystallite size and crystallite boundary defects is stronger than the effect of porosity in reducing the thermal conductivity [17].

In summary, the crystallite size is one of the parameters affecting the thermal conductivity. However, other parameters such as alloying, carrier mobility, carrier concentration, and sample porosity affect the thermal conductivity. These parameters are functions of growth process parameters such as milling and hot press conditions. Precise control of such parameters is necessary to attain an optimum structure.

4.4.4. Power Factor and Figure-of-Merit ZT

The thermoelectric power factor and the figure-of-merit ZT are shown in Figure 4-3-d and Figure 4-4, respectively. A significant enhancement in ZT of sample 2 (~60%) is observed compared to that of the RTG sample. The peak ZT is about 0.8 at 800 ˚C. Comparing the power factor of the two samples, they are similar, as expected from their similar electrical conductivity and Seebeck coefficient (Figure 4-3). The theoretical calculation of different components of the thermal conductivity and ZT of sample 2 compared with RTG is also shown in

Figure 4-5. The enhancement in ZT is mainly due to the reduction in lattice thermal conductivity. This indicates that the average crystallite size in this sample (i.e. ~25 nm) is smaller or comparable to the phonon MFP. The fact that the power factor is not affected by the crystallite boundary scattering indicates that the crystallite boundary scattering is not dominant for hole transport at high temperatures pertaining to similar hole mobility of sample 2 and RTG as depicted in Figure 4-6. This indicates that the average crystallite size (~25 nm) is much larger than the hole MFP in this sample (~2 nm) as shown in Figure 4-6.

4.5. **Conclusion**

The effect of mechanical alloying and sintering parameters on structural and thermoelectric properties of nanostructured bulk alloys of silicon germanium were investigated. The experimental data was compared with model calculation of electrical and thermal properties to identify the main parameters responsible to enhance ZT. The figure-of-merit ZT can reduce or decrease significantly depending on the synthesis parameters and their precise optimization is required to improve ZT. With optimizing the growth process parameters, we attained ZT>0.7 at 600-1000 ˚C with the peak ZT of 0.8 at 800 ˚C. Out of many synthesized nanostructured SiGe samples, the alloyed powder which made the sample with highest ZT was prepared by 34 hours of dry milling with BPR of 8:1 under Argon atmosphere at 800 rpm. The sintering parameters that resulted in highest ZT also included sintering temperature of 1200 ˚C, holding time of 6 min, heating rate of ~300˚C/min, and the press pressure of 93 MPa. Smaller sintering temperature, heating rate, or holding time can result in smaller crystallite size; however, it would decrease the charge carrier mobility, which results in smaller ZT. Model calculation showed that in the nanostructured sample the lattice thermal conduction still contributes to nearly 80% of thermal conduction. On the other hand, the charge carrier mobility and the mean free path for the nanostructured sample is still in the same range as that of the crystalline SiGe alloy at high temperature (>800 ˚C). Since the operating temperature of SiGe thermoelectric device is at this range of temperature, additional reduction in crystallite size should result in further enhancement of ZT by reducing the thermal conductivity without significantly affecting the carrier mobility.

4.6. **References**

[1] D.M. Rowe, CRC Handbook of Thermoelectrics, CRC-Press (1995)

2 J. P. Dismukes, L. Ekstrom, E. F. Steigmeier, I. Kudman, and D. S. Bears, J. Appl. Phys. 35(10), 2899 (1964).

3 D.M. Rowe, Thermoelectrics Handbook: Macro to Nano, CRC Press (2005)

4 Cronin B. Vining, William Laskow, Jack O. Hanson, Roland R. Van der Beck, and Paul D. Gorsuch, J.Appl.Phys. 1990, 69, 4333.

5 M.S. Dresselhaus, G. Chen, Z.F. Ren, J.-P. Fleurial, P. Gogna, M.Y. Tang, D. Vashaee, H. Lee, X. Wang, G. Joshi, G. Zhu, D. Wang, R. Blair, S. Bux, and R. Kaner, Proc. MRS Fall Meeting, Nov. 26-30, 2007, Paper No. U2.4, Boston, MA (Invited paper presented by M.S. Dresselhaus).

6 Joshi, Hohyun Lee, Yucheng Lan, Xiaowei Wang, Gaohua Zhu, Dezhi Wang, Ryan W. Gould, Diana C. Cuff, Ming Y. Tang, Mildred S. Dresselhaus, Gang Chen and Zhifeng Ren, Nano Lett., 2008, 8 (12), pp 4670–4674.

7 G.H. Zhu, H. Lee, Y.C. Lan, X.W. Wang, G. Joshi, D.Z. Wang, J. Yang, D. Vashaee, H. Guilbert, A. Pillitteri, M.S. Dresselhaus, G. Chen, and Z.F. Ren, Physical Review Letters, Vol. 102, 196803, 2009.

8 A. Minnich, H. Lee, X.W. Wang, G. Joshi, M.S. Dresselhaus, Z.F. Ren, G. Chen, and D. Vashaee, Physical Review B, Vol. 80, 155327, 2009.

9 Chandan Bera, M. Soulier, C. Navone, Guilhem Roux, J. Simon, S. Volz, and Natalio Mingo, J. Appl. Phys. 108, 124306 (2010); doi:10.1063/1.3518579.

10 Bux., J., P., R. Blair, P. Gogna, T. Caillat, R. Kaner, Mater. Res. Soc. Symp. Proc. Vol. 1166, 2009.

11 M.N. Tripathi and C. M. Bhandari, J. Phys.: Condens. Matter 15 , 2003, 5359-5370.

12 M Zebarjadi, G Joshi, G Zhu, B Yu, A Minnich, Y Lan, X Wang, M Dresselhaus, Z Ren, and G Chen, Nano Letters, 11 (6), 2225-2230.

13 P. R. Soni, Mechanical Alloying: Fundamentals and Applications, Cambridge Int. Science Publishing, Jan 1, 1999, ISBN 1898326568.

14 DIFFRACplus Basic Evaluation Package, EVA 14 user manual, Bruker AXS GmbH, Karlsruhe, Germany, 2008. Order no. DOC-M85-EXX002 V14.

15 J. Callaway, Phys. Rev., 113, 1046, 1959.

16 E. F. Steigmeier and B. Abeles, Physical Review 136, A1149 (1964).

17 H. Lee, D. Vashaee, D. Z. Wang, M. S. Dresselhaus, Z. F. Ren, and G. Chen, Journal of Applied Physics, 107, 094308 (2010).

18 V. S. Shukla and D. M. Rowe, Appl. Energy 9.2. 131–137 (1981).

19 S. Solmi, F. Baruffaldi, and R. Canteri, J. Appl. Phys. 69, 2135 (1991).

20 J. Adey, R. Jones, and P. R. Briddon, phys. stat. sol. (c) 2, No. 6, 1953–1957 (2005).

21 E. Landi, S. Guimaraes, and S. Solmi, Appl. Phys. A 44, 135-141 (1987).

22 A Armigliato, D Nobili, P Ostoja, M Servidori, S Solmi, Proceedings Electrochemical Society, V 77-2, Issue: Semicond. Silicon, 638-647 (1977).

23 Vining, C. B., "The Thermoelectric Properties of Boron-Doped Silicon and Silicon-Germanium in the as-Hot Pressed Condition", vining1988-1, Prepared for: United States Army, SLCET-PE, Fort Monmouth, New Jersey, JPL, Pasadena 1988.

24 D.P. White and P.G. Klemens, J. Appl. Phys. 71(9), 1992.

25 Geiger, F. E.; Cunningham, F. G., American Journal of Physics, Volume 32, Issue 5, pp. 336-342 (1964).

26 Yucheng Lan, Austin Jerome Minnich, Gang Chen, and Zhifeng Ren, Advanced Functional Materials 20 (2010) 357.

27 Xingzhe Wang, Yumei Yang, and Linli Zhu, J. Appl. Phys. 110, 024312 (2011).

28 Kim, P. et al.; Shi, L.; Majumdar, A.; McEuen, P. L. Physical Review Letters 87 (21) (2001).

29 Ju, Y. Sungtaek, Applied Physics Letters 87: 153106, (2005).

30 E. F. Steigmeier and B Abeles, Phys. Rev. v 136, 4A, A 1149-1155 (1964).

31 D.P. White and P G Klemens, J. Appl. Phys. 71 (9), 4258-4263 (1992).

Chapter 5 Boron precipitation effect on thermoelectric properties of nanostructured silicon germanium

5.1. Introduction

The carrier concentration in thermoelectric materials governs the electronic transport properties and must be optimized to reach the maximum ZT. The most commonly used dopants for $Si_{1-x}Ge_x$ alloys are phosphorous and arsenic for n-type and boron for p-type structures. The theoretical optimum carrier concentration in p-type $Si_{0.8}Ge_{0.2}$ is higher than the solid solubility limit of boron [1].The solid solubility limits are approximately 5×10^{20} cm^{-3} for boron and 1.5×10^{21} cm^{-3} for phosphorus in $Si_{0.8}Ge_{0.2}$ at 1200°C [2] and they both change with temperature [2,3]. As the temperature reduces, the solubility limits of the dopants also reduce and they precipitate out from the lattice resulting in reduction of the carrier concentration at lower temperatures. The reduction in carrier concentration can be so large that the reduction of the electrical conductivity cannot be compensated by the increase of the Seebeck coefficient; therefore, the net power factor and consequently the figure of merit decreases.

The active boron concentration, which is the ionized acceptor concentration, in bulk silicon or silicon-germanium alloy depends strongly on the kinetics of the precipitation process, the temperature history of the samples, and the solubility of boron [4,5,6,7].The precipitation of boron has been studied in highly doped bulk silicon [8,9]. It was concluded that boron precipitation is much slower and happens at higher temperatures compared with that of phosphorous and arsenic. The reversible nature of the precipitation and its effect on carrier concentration have been also investigated [10,11] and it was shown that the thermoelectric properties can be reset to their initial values by a proper heat treatment after each thermal cycling.

Several theoretical models have been developed to explain the precipitation kinetics of dopants in highly doped solutions. Among those models, conventional Lifshitz-Slyozov model could more

precisely describe the experimental data for precipitation of dopants in bulk crystalline silicon-germanium alloys [5]. This model assumes a critical radius for the initially precipitated particles. Particles smaller than the critical radius are dissolved into the lattice resulting in an increase of the carrier concentration. The process continues until all the small particles are dissolved. Particles bigger than the critical radius have the tendency to grow at a rate depending on the diffusion coefficient of the dopants. The precipitation rate and diffusion coefficient of boron versus temperature were calculated employing this model. The precipitation rate was estimated to have a maximum around 800 C [5]. Savvides et al [2] reported that the initial rate of precipitation cannot be explained by Liftshitz-Slyozov model as the precipitation rate follows a parabolic law until a critical time. This behavior was predicted by a soliton model [12]. Their experimental data [2] showed that the model is a more complete representation of the precipitation kinetics of boron in silicon germanium alloys.

Precipitation of dopants have been further reported in ion-implanted phosphorus [13], arsenic [14,15], and boron [16,17,18,19] in silicon. The diffusion and precipitation of boron implanted in Si has been described by Solmi et al [18,19]. Enhanced diffusion of boron during annealing after implantation in crystalline silicon, as well as nucleation, and growth of precipitated particles were modeled based on the classic thermodynamic laws. The enhanced diffusion of boron depends on temperature, depth, and boron concentration. Precipitation of boron immobilizes some fraction of dopants making the diffusion process complex. However at high temperatures (>900 C) significant time of annealing (more than 30 min) is necessary to reach the equilibrium conditions after which the diffusion process could be complete.

Nanostructured bulk silicon-germanium alloys have shown significant enhancement in thermoelectric figure-of-merit ZT compared with their crystalline or polycrystalline bulk structure [1,20,21]. The main effect of nanostructuring has been in reducing the thermal conductivity by introducing extra interfaces in the material as they scatter phonons [1,22,23,24,25,26,27].

Although dopants precipitation has been studied extensively in bulk $Si_{1-x}Ge_x$ alloys, there has been only a few reports on the precipitation of dopants in nanostructured bulk $Si_{1-x}Ge_x$. Minnich et al [23] reported that the precipitation of phosphorous dopants in n-type nanostructured thermoelectric silicon-germanium follows similar trend as in its crystalline form, which was evidenced by their similar carrier concentration versus temperature curves. A significantly large

drop of electrical conductivity was also reported by Zamanipour et al [1] in boron doped p-type nanostructured silicon-germanium after thermal cycling.

In this work, the effect of nanostructuring on boron precipitation in p-type $Si_{0.8}Ge_{0.2}$ was studied and compared with that of the polycrystalline structure. It was shown that, in contrast to the behavior of the phosphorous precipitation in n-type silicon-germanium [23], boron precipitates more strongly in nanostructured $Si_{0.8}Ge_{0.2}$. The increased precipitation of boron can be associated with the presence of extra interfaces and crystal defects at grain boundaries. The results are both theoretically and experimentally compared with that of the polycrystalline $Si_{0.8}Ge_{0.2}$ alloys. It was further shown that dopant diffusion becomes significant at temperatures above 600 C in both structures.

5.2. **Experimental procedures**

P-type silicon germanium alloyed powder was produced using high energy planetary ball milling. Pure elemental powders of Si (>99.9% Alfa Aesar), Ge (>99.99% Alfa Aesar), and Boron (>99% Alfa Aesar) with stoichiometric ratio of 78.4 at.% Si , 20 at.% Ge, 1.6 at.% B and tungsten carbide balls with ball-to-powder ratio of 8:1 were loaded into a tungsten carbide bowl. The bowl was sealed under argon atmosphere and milled in a planetary mill (Fritsch P7 PL) at 800 rpm for 34 hours. $Si_{0.8}Ge_{0.2}$ alloy phase formation was confirmed by X-ray diffraction (Brucker AXS D8-Discover) analysis. No other phases or contamination were found. The prepared $Si_{0.8}Ge_{0.2}$ alloy was then loaded into a graphite die for solidification. Using hot-press technique, the nanostructured sample was sintered at 1200 C for 6 minutes under 100 MPa pressure. The polycrystalline sample was prepared with a different procedure. Si, Ge and B powders with same stoichiometric ratio were milled for 5 hours in order to uniformly mix the powders. Subsequently the powder was melted in a BN crucible at 1450 C for one hour. Both samples were cut into rectangular rods and disks for different measurements. Electrical conductivity and Seebeck coefficient of both synthesized samples were measured using the commercially available equipment (ULvac, ZEM-3) and the thermal conductivity was measured by laser flash method (Netzsch LFA 457).

5.3. Experimental results and discussions

SEM image of some boron precipitate structures in a $Si_{0.8}Ge_{0.2}$ sample are shown in Figure 5-1. The precipitates are so large that they can be seen in micrometer scale imaging. Figure 5-1-shows a boron polycrystalline precipitate and Figure 5-1-b shows a boron whisker of approximately 1 mm long formed after precipitation.

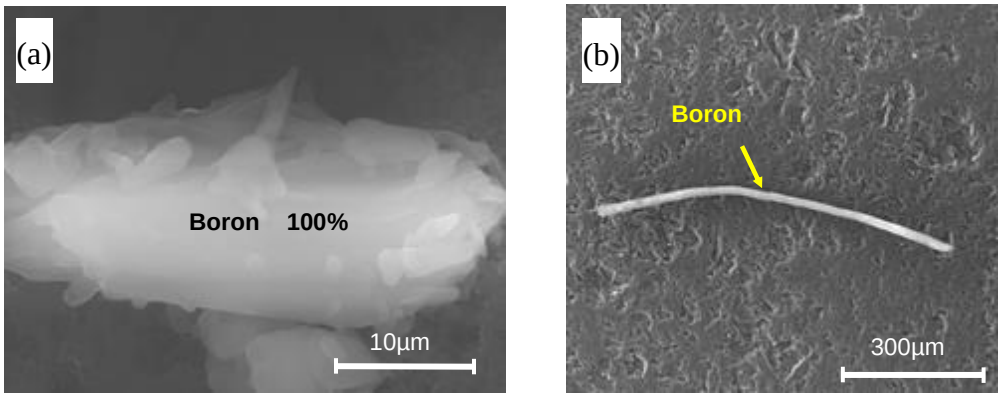

Figure 5-1: Boron precipitates in $Si_{0.8}Ge_{0.2}$ structure.

Figure 5-2 shows the experimental (symbols) and theoretical (lines) data of electrical conductivity (Figure 5-2a) and Seebeck coefficient (Figure 5-2b) as a function of temperature for both polycrystalline and nanostructured sample. In order to study the precipitation of active dopants, the measurements have been done first from room temperature to 900 C (heating cycle) and then from 900 C to room temperature (cooling cycle). The heating and cooling rates were approximately 8 C/min. As it is seen there is a significant difference in the electrical conductivity of polycrystalline and nanostructured sample over the entire temperature range. The Seebeck coefficient of the nanostructured sample is larger compared with that of the polycrystalline sample. Therefore, the small electrical conductivity of the nanostructured sample can be associated with its smaller carrier concentration.

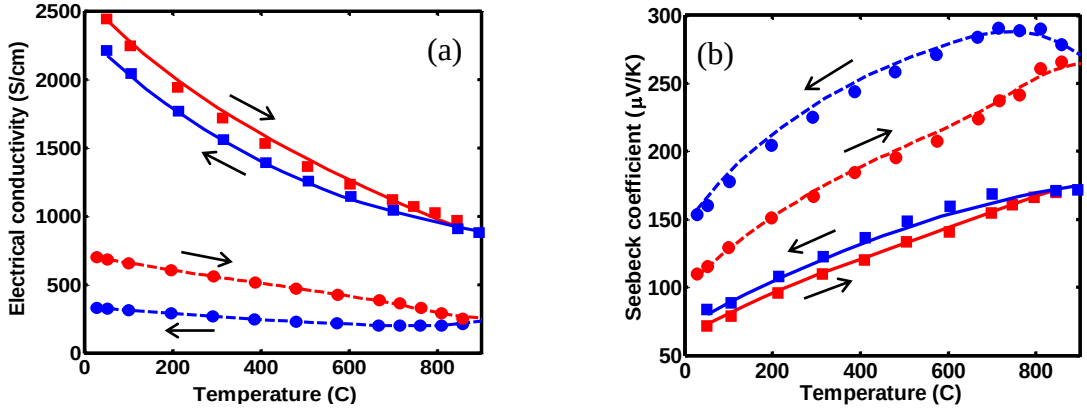

Figure 5-2: Electrical conductivity and Seebeck coefficient of melted (polycrystalline) (■) and nanostructured (●) $Si_{0.8}Ge_{0.2}$ for both heating (red in color) and cooling (blue in color) cycles. The theoretical data (solid lines for the melted $Si_{0.8}Ge_{0.2}$) and dashed lines for the nanostructured $Si_{0.8}Ge_{0.2}$ are also shown for comparison to the experimental data.

The effect of the boron precipitation can be seen in Seebeck coefficient and electrical conductivity plots for both samples when the heating cycle is compared with the cooling cycle. The room temperature electrical conductivity difference between the heating and cooling cycles for the polycrystalline sample is 234 S/cm while it is approximately 372 S/cm for the nanostructured sample. After the precipitation, the room temperature Seebeck coefficient has been increased by 12 μV/K and 46 μV/K for the polycrystalline and nanostructured samples, respectively. The increase in Seebeck coefficient indicates the reduction of carrier concentration. In both samples, there is a drop in carrier concentration when samples cool down to room temperature. The comparison shows that the boron precipitation is more significant in the nanostructured sample. We observed the increase of boron precipitation in the nanostructured sample even though it had smaller initial boron concentration compared with the polycrystalline structure. Since the only difference between the nanostructured and the polycrystalline sample is the increased number of defect concentration in the former one, this effect can be associated to the grain boundaries. As the density of crystallite boundaries increases, a higher number of boron atoms is trapped at the interfaces forming inactive boron particles. This trend was consistently observed in all nanostructured boron doped silicon germanium samples that we have grown.

5.4. Theoretical study

The electric properties of the polycrystalline and nanostructured $Si_{0.8}Ge_{0.2}$ were calculated using Boltzman transport equation. The modeling procedure is explained in detail in refs. [23,28]. Two conduction bands, one near X and one at L point, and one effective valence band were included in the theoretical modeling. The acoustic phonons, ionized impurities, deformation potential of optical phonons, and the crystallite boundaries are the dominant scattering processes considered here. The model for crystallite boundary scatterings of charge carriers is also described in refs. [23,28]. Here the carrier scattering of charge carriers at independent grain boundary sites is modeled by a local disk shape potential of the form $U_g=U_0\exp(-|z|/z_0)$ for $r<r_0$, and $U_g=0$ for $r>r_0$. z is the normal direction to the GB, z=0 is the center of the disk, U_0 is a constant defining the strength of the GB potential, and r_0 is the radius of the disk which is on the order of the charge screening length. The depletion of charge carriers at the interface is modeled by the decaying exponential function. The electrical characteristics of the nanostructured $Si_{0.8}Ge_{0.2}$ were calculated after incorporation of the GB scattering while keeping all other parameters unchanged.

The theoretical calculation of electrical conductivity and Seebeck coefficient versus temperature for both polycrystalline and nanostructured samples are shown in Figure 5-2 (solid lines for the polycrystalline and dashed line for the nanostructured). A satisfactory agreement between the model and experiment has been obtained for both electrical conductivity and Seebeck coefficient.

Figure 5-3-a shows the corresponding electron and hole concentrations as functions of temperature; solid and dashed lines show the carrier concentration for polycrystalline and nanostructured samples, respectively. In the nanostructured sample, the hole concentration is reduced during the cooling cycle more significantly than in the polycrystalline sample. The concentration of the electrons, which are the minority carriers, increases with temperature. However, it remains more than two orders of magnitude smaller than that of the holes even at high temperature. Therefore, the contribution of the minority carriers in electrical properties is negligible. An opposite trend is observed for the electron concentration as it increased during the cooling cycle. This is associated with the reduction of the Fermi energy due to boron

precipitation. With the increase of temperature, the Fermi energy moves up, closer to the mid gap and the concentration of the electrons increases due to thermal excitation.

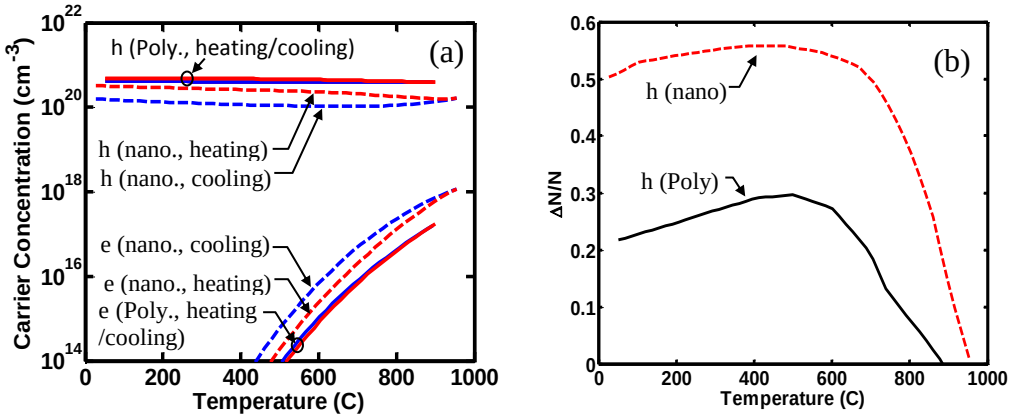

Figure 5-3: (a) electron (e) and hole (h) concentration versus temperature for both nanostructured (dashed lines) and polycrystalline (solid lines) samples for heating and cooling cycles (b) Normalized difference of the hole concentration between heating and cooling cycles versus temperature for both nanostructured (dashed lines) and polycrystalline (solid line) samples.

Figure 5-3-b shows the normalized difference of the hole concentration between the heating and the cooling cycles as functions of temperature for both samples. The hole concentration decreases rapidly as the sample cools down from 900 C to 600 C. The difference of the hole concentration between the heating and the cooling cycles at room temperature in the polycrystalline and the nanostructured sample is approximately 0.7×10^{20} cm^{-3} and 1.62×10^{20} cm^{-3}, respectively. The reduction of the hole concentration at room temperature in the nanostructured sample is approximately two times more than that of the polycrystalline sample. As discussed in the experimental section, this can be associated with the higher density of the interfaces in the nanostructured sample where boron atoms can be localized to form nucleation and growth of the precipitates. This observation is in agreement with previous studies of boron precipitation in highly doped crystalline [8,9] and amorphous silicon [9]. The kinetic study of boron deactivation in highly doped pre-amorphized silicon has shown that boron nucleation starts before the recrystallization of silicon because of high diffusivity of the boron atoms in amorphous silicon [9]. Therefore, very small aggregates of boron act as nucleation centers enhancing boron precipitation in the samples. On the other hand, if there are no aggregates of boron during the

recrystallization, precipitation is limited and it occurs much more slowly for the same amount of initial dopants.

Therefore, even though nanostructuring can enhance the thermoelectric figure of merit of silicon germanium, it also makes the material more unstable with respect to its transport properties and is not suitable for devices that undergo heating and cooling cycles. On the other hand, single crystalline or polycrystalline silicon germanium is more stable and can be used in applications with frequent thermal cycling.

5.5. **Conclusion**

The effect of precipitation on thermoelectric properties of nanostructured bulk p-type $Si_{0.8}Ge_{0.2}$ was studied. The experimental results show that the precipitation is higher in nanostructured sample compare with polycrystalline sample. Experimental data of electrical properties of both polycrystalline and nanostructured $Si_{0.8}Ge_{0.2}$ alloys were further compared to theoretical calculations by solving Boltzmann transport equation. The carrier concentrations for both structures were calculated from the measured Seebeck coefficient versus temperature during heating and cooling cycles and it was shown that boron precipitation in polycrystalline and nanostructured samples is approximately 20% and 50%, respectively, compared with its saturation level at 1200 C. Although nanostructuring can reduce the thermal conductivity and enhance the figure of merit, it causes instability in electric properties. Therefore, nanostructured $Si_{0.8}Ge_{0.2}$ alloys can work properly in high temperature applications where they do not undergo thermal cycling such as in RTGs in space craft, and single crystalline or polycrystalline $Si_{0.8}Ge_{0.2}$ alloy are more suitable for applications with frequent thermal cycling.

5.6. **References**

1 Zahra Zamanipour, Xinghua Shi, Arash M. Dehkordi, Jerzy S. Krasinski, and Daryoosh Vashaee, Phys. Status Solidi A 209, no. 10, 2049–2058 (2012).

2 N. Savvides, J. Appl. Phys. 54, 2402 (1983).

3 R. D. Nasby and E. L. Burgess, J. Appl. Phys. 43, 2908 (1972)

4 Vining, C. B., vining1988-1, Prepared for: United States Army, SLCET-PE, Fort Monmouth, New Jersey, JPL, Pasadena 1988.

5 V. S. Shukla, D.M. Rowe, Phys. stat. sol. (a) 66, 243 (1981)

6 N. Savvides, D.M. Rowe, J. Phys. D: Appl. Phys. Vol. 14, p.723-32, 1981.

7 V.S. Shukla, D. M. Rowe, Appl. Energy, vol 9, p. 131-137, 1981.

8 A. Armigliato, D. Nobili, P. Ostoja, M. Servidori, S. Solmi, Semiconductor Silicon 1977 (The Electrochem. Soc. Inc.,Princeton, NJ 1977) p. 638

9 E. Landi, S. Guimaraes, and S. Solmi, "Influence of Nucleation the Kinetics of Boron Precipitation in Silicon", Appl. Phys. A 44, i35-141 (1987)

10 Ekstrom. L., Dismukes. J. P. , J. Phys.Chem. Solids, Vol.27, p. 857, 1966.

11 D.M., Rowe, N. Savvides, J.Phys. D:, Appl. Phys., Vol.12, P.1613, 1979.

12 N. Gunther, in Proceedings of the 4th International Conference on Thermoelectric Energy Conversion, University of Texas at Arlington, March 10-12,1982, p. 89.

13 D. Nobili, A. Armigliato, M. Finnetti, and S. Solmi, J. Appl. Phys. 53, 1484 (1982).

14 D. Nobili, S. Solmi, A. Parisini, M. Derdour, A. Armigliato, Physical Review B, vol. 49, no. 4 ,pp. 2477-2483 , 1994.

15 D. Nobili, A. Carabelas, G. Celotti, S. Solmi: J. Electrochem.Soc. 130, 922-928,1983.

16 W. K. Hofker, H. W. Werner, D. P. Oosthoek, and H. A. M. de Grefte, Appl. Phys. 2, 265,1973.

17 H. Ryssel, K. Muller, K. Haberger, R. Henckelman, F.Jahnel: Appl. Phys. 22, 1980.

18 S. Solmi and F. Baruffaldi, J. Appl. Phys. 69 (4), 2135-2142, 1991.

19 S. Solmi, S. Valmorri, and R. Canteri, J. Appl. Phys. 77, 2400 (1995).

20 Giri Joshi, Hohyun Lee, Yucheng Lan, Xiaowei Wang, Gaohua Zhu, Dezhi Wang, Ryan W. Gould, Diana C. Cuff, Ming Y. Tang, Mildred S. Dresselhaus, Gang Chen and Zhifeng Ren, Nano Lett., 2008, 8 (12), pp 4670–4674

21 G.H. Zhu, H. Lee, Y.C. Lan, X.W. Wang, G. Joshi, D.Z. Wang, J. Yang, D. Vashaee, H. Guilbert, A. Pillitteri, M.S. Dresselhaus, G. Chen, and Z.F. Ren, Physical Review Letters, Vol. 102, 196803, 2009

22 M.S. Dresselhaus, G. Chen, Z.F. Ren, J.-P. Fleurial, P. Gogna, M.Y. Tang, D. Vashaee, H. Lee, X. Wang, G. Joshi, G. Zhu, D. Wang, R. Blair, S. Bux, and R. Kaner, Proc. MRS Fall Meeting, Nov. 26-30, 2007, Paper No. U2.4, Boston, MA (Invited paper presented by M.S. Dresselhaus).

23 A. Minnich, H. Lee, X.W. Wang, G. Joshi, M.S. Dresselhaus, Z.F. Ren, G. Chen, and D. Vashaee, Physical Review B, Vol. 80, 155327, 2009

24 Chandan Bera, M. Soulier, C. Navone, Guilhem Roux, J. Simon, S. Volz, and Natalio Mingo, J. Appl. Phys. 108, 124306 (2010); doi:10.1063/1.3518579.

25 S. K. Bux, R. Blair, G. P. Gogna, K. H. Lee, G. Chen, M. Dresselhaus, S. R. B. Kaner, and J.-P. Fleurial, Adv. Funct. Mater. 19, 1–8 (2009).

26 M.N. Tripathi and C. M. Bhandari, J. Phys., Condens. Matter 15 (20030 5359-5370.

27 M Zebarjadi, G Joshi, G Zhu, B Yu, A Minnich, Y Lan, X Wang, M Dresselhaus, Z Ren, and G Chen, Nano Letters DOI: 10.1021/nl201206d, (Web) May 2011

28 Zahra Zamanipour and Daryoosh Vashaee, J. Appl. Phys. 112, 093714 (2012).

Chapter 6 Phase heterogeneity effect on thermoelectric properties of nanostructured silicon germanium alloy

6.1. Introduction

The thermal behavior of $Si_{1-x}Ge_x$ alloys has been studied theoretically [1,2,3]. There are several parameters such as Ge concentration, doping concentration, and temperature which affect the thermal properties of this material system. Due to the strong phonon scattering by point defects resulted from alloying with Ge, its content plays an important role in lattice thermal conductivity [4,5,6]. While the increase of the Ge content up to approximately 50% decreases the lattice thermal conductivity, it also reduces the band gap that consequently increases the ambipolar diffusion part of the thermal conductivity. This part becomes comparable or higher than the lattice part of thermal conductivity at high temperature [1]. Previous experimental [5,7] and theoretical reports [3] have shown that the lattice thermal conductivity is approximately at its minimum value at 12% Ge content. Further increase of Ge concentration does not noticeably reduce the lattice thermal conductivity, but the ambipolar thermal diffusion increases significantly and dominates at high temperature. Nevertheless, $Si_{0.7}Ge_{0.3}$ and $Si_{0.8}Ge_{0.2}$ have been the most common material compositions studied and applied for thermoelectric power generation [8].

It can be concluded that precise knowledge of the structural phases of the synthesized $Si_{1-x}Ge_x$ alloy would help to analyze the experimental data and guide the experiments to adjust the process parameters for achieving the desired Ge concentration in the alloy. Therefore, in order to analyze and optimize the thermoelectric properties of the $Si_{1-x}Ge_x$ alloy, the Ge content must be precisely measured.

The X-ray diffraction (XRD) analysis has been the main characterization method for determining the alloy composition. However, since Si and Ge make continuous solid solution, the XRD lines

of the different phases overlap. The XRD data of nanostructured $Si_{1-x}Ge_x$ cannot precisely determine the phases due to the multiple numbers of unknown parameters such as the grain size, residual stress, instrumental broadening, and the phase heterogeneity. There has been little attention devoted to the phase determination of the nanostructured bulk $Si_{1-x}Ge_x$ thermoelectric alloys in the past. Differential thermal analysis (DTA) is one of the precise techniques that can show different transformations such as glass transitions, crystallization, melting and sublimation in materials. In DTA, the temperature of the sample is measured using a reference sample in the furnace while they are both receiving equal amount of heat. The area under the DTA peak gives the enthalpy change which is independent from the heat capacity of the material. Therefore, DTA can be recognized as a reliable and accurate method for phase structure identification, especially for solid solutions where the XRD data can be difficult to be interpreted due to the infinite number of possible phases that can be formed. It would be of interest to determine the phase structure of the synthesized nanostructured $Si_{1-x}Ge_x$ alloy and study the corresponding thermoelectric properties using DTA.

The aim of the this study was to identify the actual phase structure of the p-type nanostructured $Si_{0.8}Ge_{0.2}$ alloy synthesized via mechanical alloying and hot press sintering. XRD and DTA characterizations were performed on the synthesized material. Furthermore, the thermal properties along with electronic properties of the material were analyzed and compared with those of the single crystalline alloy. The analysis revealed phase heterogeneity in the sample, which was not detected in the XRD data. This phase heterogeneity was responsible for the changes in the thermoelectric properties of the material.

6.2. Experimental Procedure

Stoichiometric ratios of 80 at. %Si (99.9% purity), 20 at. % Ge (99.9% purity), and 1.6 at. % B (99.9% purity) were weighted and loaded into a tungsten carbide bowl with tungsten carbide balls under argon atmosphere. The powder was milled with Fritsch-P7 planetary ball mill for 10 hours at 1000 rpm with ball to powder ratio of three. The powder was collected and annealed in a quartz crucible at 1100 °C for 3 hours under argon atmosphere. The annealed powder was subsequently milled for approximately 60 hours with same milling condition. The powder was then filled into a graphite die with an internal diameter of 12.7 mm and was hot pressed at 1200 °C for approximately 6 minutes under 108 MPa. The pressed sample was cut into rods and disks

for thermoelectric properties measurements. The relative density of 93% of the theoretical density of $Si_{80}Ge_{20}$ ($2.93g/cm^3$) was achieved.

The sample was characterized by X-ray diffraction (XRD) using Brucker AXS D8-Discover with Cu Kα radiation and scanning electron microscope (SEM, Hitachi S-4800). Seebeck coefficient and electrical conductivity was measured simultaneously with four probe technique by commercially available equipment (Ulvac ZEM-3) and the thermal conductivity was measured by a laser flash apparatus (Netzsch LFA 457) from room temperature to 950 °C. The differential thermal analysis (DTA) and thermogravimetric analysis (TG) were accomplished in argon environment by Netzsch STA 449 F1. The temperature was increased 20 °C per minute from room temperature to 1550 °C.

6.3. **Results and Discussion**

The XRD analysis of the sample is shown in Figure 6-1(a). As Si and Ge make a continuous solid solution alloy, the $Si_{1-x}Ge_x$alloy XRD peaks are located between Si peaks (with the main peak at 2θ=28.47˚) and Ge peaks (with the main peak at 2θ=27.29˚). The spectrum shows a single peak between the corresponding two peaks of Si and Ge indicating the formation of a homogenous composition alloy. The average crystallite size was estimated using Sherrer's equation [9]. In this equation the instrument broadening was extracted and the residual stress of the sample was ignored. The average crystallite size of the sample was calculated to be 27nm.

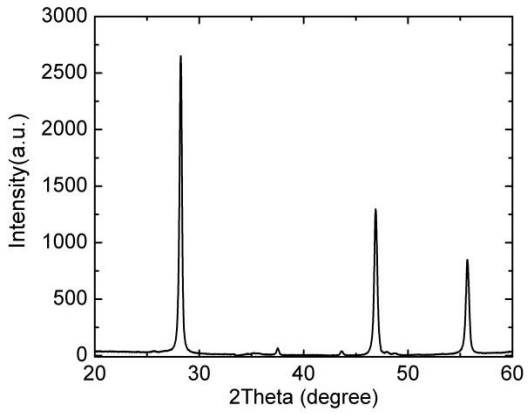

Figure 6-1 X-ray diffraction pattern of the nanostructured $Si_{0.8}Ge_{0.2}$.

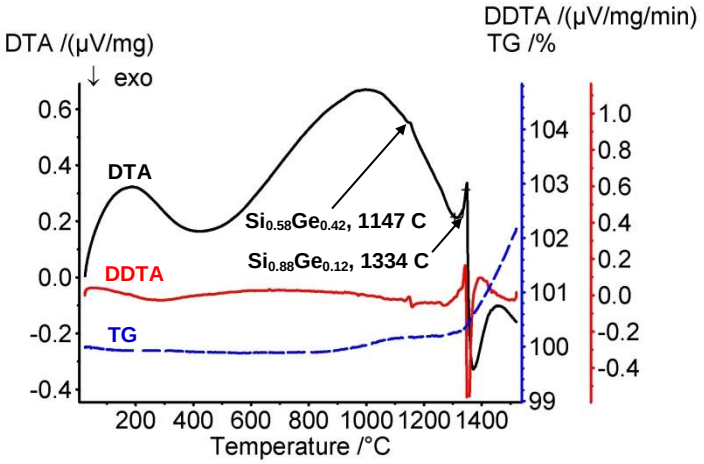

Figure 6-2 Differential thermal analysis (DTA), derivative of DTA (DDTA), and Thermogravimetry (TG) data of the sample.

Differential Thermal Analysis (DTA), derivative of DTA (DDTA), and Thermogravimetry (TG) of the sample are shown in Figure 6-2. The DTA and DDTA curves show two endothermic events attributed to liquation of two different phases. Considering the Si-Ge phase diagram [10] and the endothermic peaks observed in the DTA curve, it can be inferred that $Si_{0.88}Ge_{0.12}$ and $Si_{0.58}Ge_{0.42}$ alloys have been formed instead of the expected $Si_{0.8}Ge_{0.2}$ alloy.

It was hypothesized that the alloying to the nominal composition had not been completed after the last ball milling step. That is, the microstructure included a wide range of chemical compositions consisting of silicon and germanium. As a result of annealing at 1100 °C, liquation of Ge-rich alloy regions having solidus temperatures lower than 1100 °C produces a Ge-rich liquid and micro-segregated Si-rich solid regions. Since the initial powder mixture composition was Si-rich ($Si_{0.8}Ge_{0.2}$), the amount of Ge-rich regions is not considerable and no typical evidence of liquation like powder spoiling was observed. According to the phase diagram, all material formed within the composition range of $Si_{0.17}Ge_{0.83}$ to $Si_{0.5}Ge_{0.5}$ provide a solid co-existing with liquid of $Si_{0.17}Ge_{0.83}$ composition at 1100 °C. This solid-liquid mixture and the liquids formed due to liquation of alloys with the Si contents less than 17 at.% form a single-phase liquid with a content less than 17 at.% at 1100 °C. Clearly, solidification of the formed liquid leads to regions with a high Ge concentration with severe micro-segregation and inhomogeneity, due to the low solidus temperatures compared with the annealing temperature of at 1100 °C. The Ge content of these Ge rich regions is expected to reduce toward the equilibrium

ratio of $Si_{0.8}Ge_{0.2}$ by subsequent milling. However, even after a long milling, there may still remain phases deviated from the equilibrium value. During sintering at 1200 °C, similar liquation of Ge-rich alloy regions having solidus temperatures lower than 1200°C again may occur, forming another phase separation including a Ge-rich liquid and a Si-rich solid region. Finally, a typical dual-phase structure of $Si_{0.88}Ge_{0.12}$ and $Si_{0.58}Ge_{0.42}$ composition is developed. Such a heterogeneous phase was observed in the DTA data of many of our other hot pressed $Si_{0.8}Ge_{0.2}$ samples.

Although the TG graph of polycrystalline sample does not show any significant changes in mass in the whole temperature range, there is a small increase of mass after reaching the melting point. The mass increases approximately % 2-3 in temperatures higher than the melting point which may be associated to the oxidation of the sample. Due to the enhanced surface area in nanostructured sample, large amount of oxygen can be absorbed and react with the material increasing the mass at high temperatures.

It is difficult to detect the existence of the two phases of $Si_{0.88}Ge_{0.12}$ and $Si_{0.58}Ge_{0.42}$ from the XRD data as the diffraction peaks of these phases are close to those of $Si_{0.8}Ge_{0.2}$. The 2θ values for the diffraction lines of $Si_{0.88}Ge_{0.12}$ are 0.04-0.08 degrees more than those of $Si_{0.8}Ge_{0.2}$, and the 2θ values for $Si_{0.58}Ge_{0.42}$ are 0.13-0.24 degrees smaller. Therefore, their existence results in broadening of the $Si_{0.8}Ge_{0.2}$ lines, which makes it difficult to be distinguished from other sources of broadening such as residual stress, grain size, and the instrument. In addition, the phase heterogeneity of the alloy cannot be detected by Rietveld refinement either as Si and Ge can form a continuous solid solution; hence, many various phases can be formed that are unknown for this analysis. However, the data from the DTA would reveal the existing phases that can be input to the Rietveld refinement for further analysis.

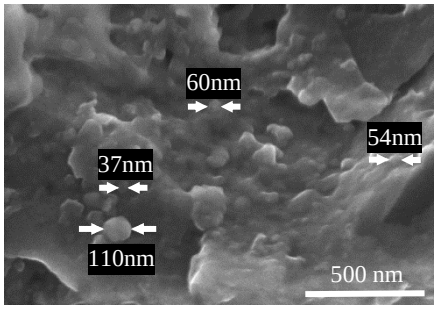

Figure 6-3: SEM micrograph of the nanostructured silicon germanium.

The SEM micrograph of the nanostructured sample is shown in Figure 6-3. The image indicates that the grain sizes in nanostructured $Si_{0.8}Ge_{0.2}$ have different sizes mostly in the range of 10-100 nm. The grain size plays an important role in charge transport properties affecting the thermal properties of the sample. The charge carrier mean free paths (MFP) in $Si_{1-x}Ge_x$ is in the range of 1-5 nm while the phonon MFP is mostly in the range of 1-100 nm [11,12]. It means that the grains in the nanostructured sample are larger than the charge MFPs and smaller than the phonon MFP. Therefore, the grain boundaries scatter phonons in a significantly higher rate than electrons. This effect reduces the thermal conductivity more than the electrical conductivity as shown in Figure 6-4(c).

Figure 6-4 shows the thermoelectric properties versus temperature for nanostructured sample. The thermoelectric properties of single crystalline $Si_{0.8}Ge_{0.2}$ [13] previously used in RTGs is also plotted for comparison. The room temperature electrical conductivity of the nanostructured sample is 560S/cm which is significantly lower than that of RTG sample. This can be associated with both lower carrier concentration and lower charge carrier mobility. However, this difference reduces at high temperatures due to the dominancy of the acoustic phonon scattering mechanism compared with the GB scattering [14]. Comparison of the Seebeck coefficient of the nanostructured sample with that of the RTG sample confirms that the nanostructured sample has lower carrier concentration.

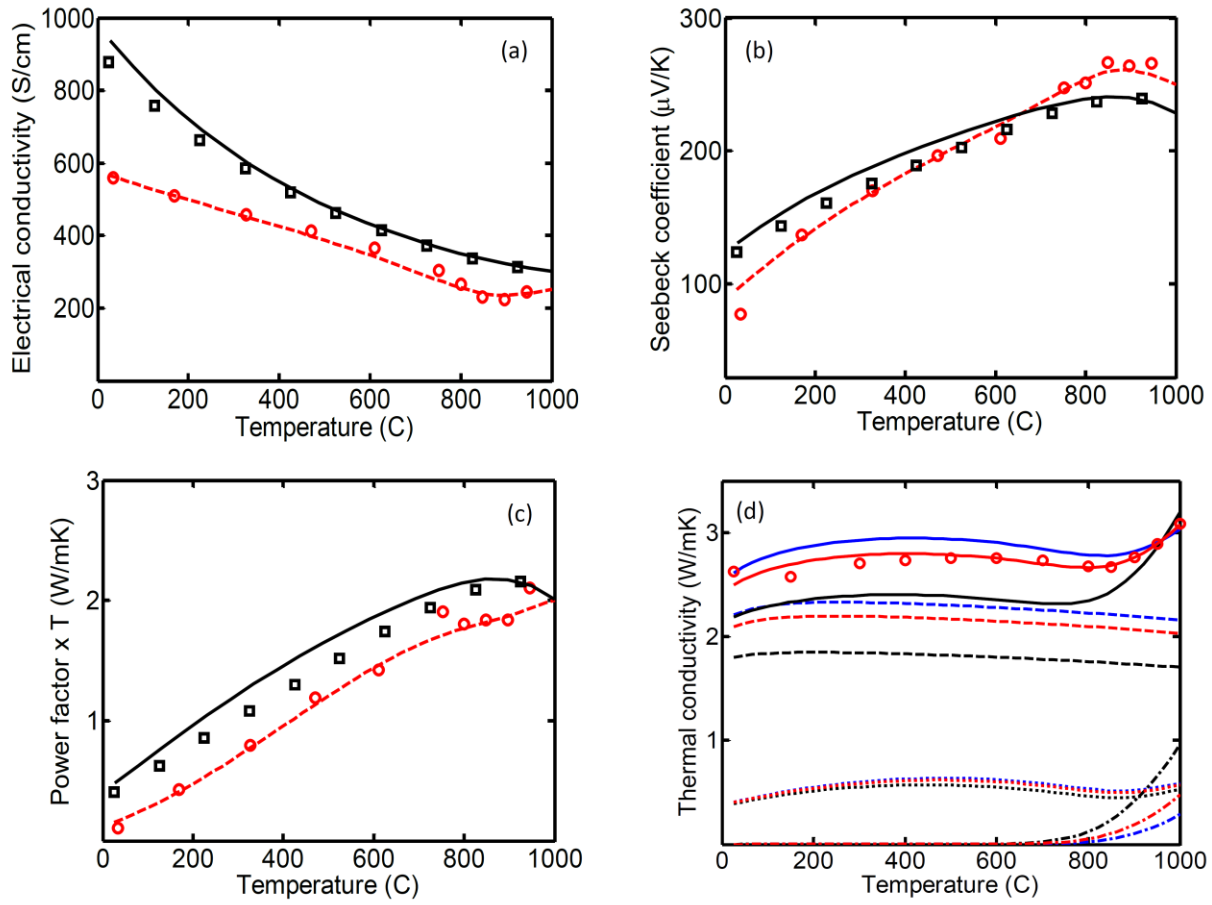

Figure 6-4: (a) Electrical conductivity, (b) Seebeck coefficient, (c) Power factor times temperature, and (d) Thermal conductivity versus temperature for nanostructured silicon germanium (circles) compared with single crystalline silicon germanium used in RTG's [13]. Symbols are experimental data and solid lines are the theoretical modeling.

Although nanostructuring process can reduce the thermal conductivity via the increase of the interfaces, it can also reduce the concentration of the active dopants and increase the thermal instability of the structure. It has been shown that nanostructuring leads to the precipitation of boron at the grain boundaries, which reduces the carrier concentration and consequently the electrical conductivity [14].

The increase of the thermal conductivity at high temperature is due to the ambipolar effect. It is seen that this effect is weaker in the nanostructured sample compared with that of the RTG sample. This can be associated with the effect of the existence of two different phases of $Si_{1-x}Ge_x$

in this sample. The dominant phase of $Si_{0.88}Ge_{0.12}$ has a larger band gap than $Si_{0.8}Ge_{0.2}$, which results in smaller ambipolar thermal diffusion.

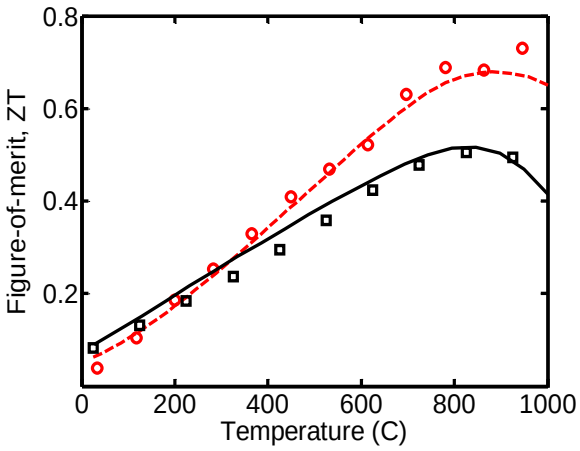

Figure 6-5 Figure-of-merit as a function of temperature measured for nanostructured silicon germanium (circles) compared with the single crystalline $Si_{0.8}Ge_{0.2}$ used in RTG's. Solid lines show numerical modeling data.

Temperature dependence figure-of-merits of both samples are shown in Figure 6-5. The maximum figure-of-merit is 0.7 at 950 °C for the nanostructured sample. The benefit of nanostructuring is obviously seen especially at high temperature ZT values, which is the operating temperature for this material system.

Theoretical modeling of the thermoelectric properties for both the nanostructured and crystalline samples are shown in Figure 6-4 and Figure 6-5 along with the experimental data. The modeling process is described in pervious works [11,14]. Here the same procedure with similar material parameters was followed to calculate the thermoelectric properties. As it is shown, there is a good agreement between the theoretical and experimental data. The fitting process of the Seebeck coefficient, electrical, and thermal conductivities leads to crystallite size and interface potential parameters. The experimental results were explained with the theory assuming the average grain size of 28 nm and grain boundary potential of 170 meV. It is noted that the fitting to the experimental data was possible when the combination of the two different phases of $Si_{0.88}Ge_{0.12}$ and $Si_{0.58}Ge_{0.42}$ were considered in the calculations. For this purpose, the thermoelectric properties of the mixed phase system were calculated from those of the individual phases using the following equations: $\sigma = x\sigma_1 + (1-x)\sigma_2$, $\kappa = x\kappa_1 + (1-x)\kappa_2$, $S =$

$x\sigma_1/\sigma S_1 + x\sigma_2/\sigma S_2$, in which σ_i, κ_i, and S_i are the electrical conductivity, thermal conductivity, and Seebeck coefficient of the different phases (i=1,2), respectively, and x is the volume fraction of $Si_{0.88}Ge_{0.12}$. x=0.73, which was calculated knowing that the starting materials were weighted according to $Si_{0.8}Ge_{0.2}$, i.e. 0.866x+0.55(1-x) = 0.779. 0.866, 0.55, and 0.779 are the Si volume fractions in $Si_{0.88}Ge_{0.12}$, $Si_{0.58}Ge_{0.42}$, and $Si_{0.8}Ge_{0.2}$, respectively. Combining the values of the Seebeck coefficient, electrical and thermal conductivity of $Si_{0.88}Ge_{0.12}$ and $Si_{0.58}Ge_{0.42}$ phases according to these equations could fit the experimental data of the nanostructured sample.

The thermal conductivity components for the nanostructured and RTG samples are shown in Figure 6-6. As it is shown In Figure 6-6(a), the lattice part of the thermal conductivity is larger in $Si_{0.88}Ge_{0.12}$. The effect of alloy scattering reduces the thermal conduction; hence, with more Ge content the lattice thermal conductivity decreases. The bipolar part of thermal conductivity of $Si_{0.58}Ge_{0.42}$ is higher than that of $Si_{0.88}Ge_{0.12}$ indicated by the higher slope of the thermal conductivity increase at high temperatures in this phase. Overall, it can be concluded that the presence of the dominant phase of $Si_{0.88}Ge_{0.12}$ alloy reduces the bipolar thermal conductivity, which is also observed in the thermal conductivity comparison of Figure 6-4(d).

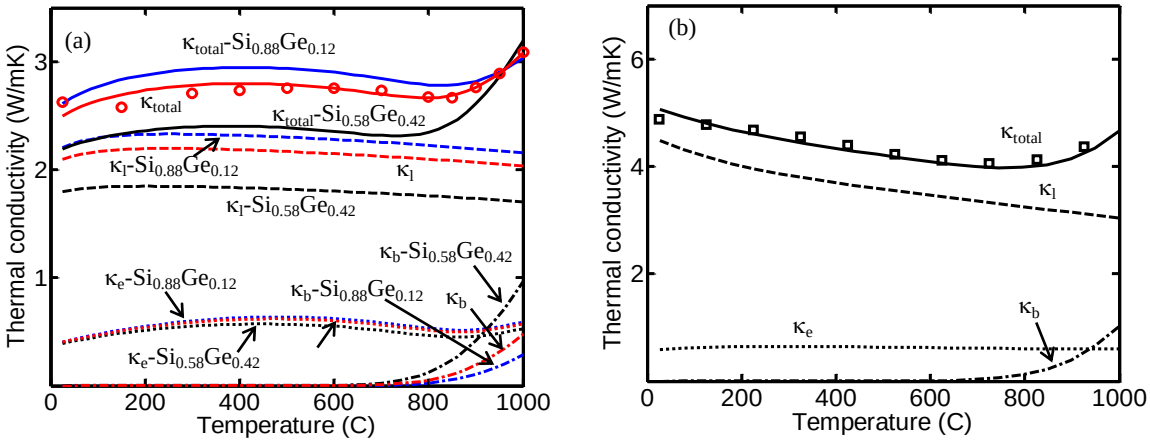

Figure 6-6: Thermal conductivity components for (a) nanostructured and (b) crystalline silicon germanium.

Figure 6-7 shows the comparison of the figure-of-merit, ZT, of the three different phases of $Si_{0.58}Ge_{0.42}$, $Si_{0.88}Ge_{0.12}$, and the $Si_{1-x}Ge_x$ composed of $Si_{0.88}Ge_{0.12}$ (73 vol %) and $Si_{0.58}Ge_{0.42}$ (27 vol %). The three compositions have approximately similar ZT at low temperatures (T<700 C). At higher temperature, the ZT variation is strongly affected by the bipolar thermal conductivity and the bipolar effect on Seebeck coefficient. The $Si_{0.88}Ge_{0.12}$ phase has larger ZT, which is mainly due to smaller bipolar effect resulted from its larger band gap. The ZT of the composite phase is between the ZT of the two constituent phases. This is in agreement with the previous theoretical predictions of the composite materials that the highest ZT of a composite material cannot reach to higher than the maximum ZT of the constituent components [15]. It should be noted that this prediction is based on classical theory and neglects the nanoscale effects in deriving this conclusion.

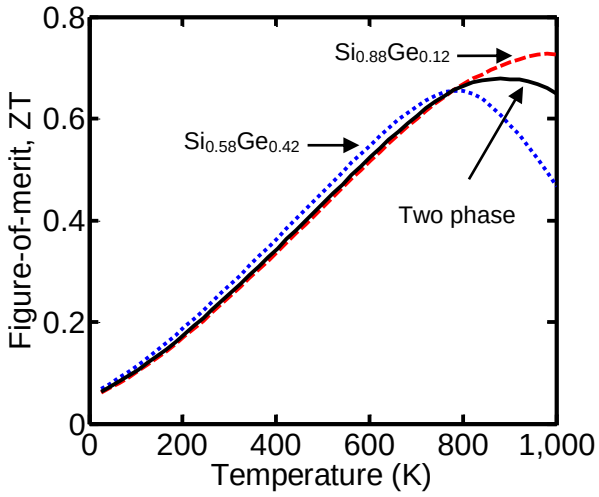

Figure 6-7: Thermoelectric figure-of-merit versus temperature for three compositions of $Si_{0.58}Ge_{0.42}$ (dotted), $Si_{0.88}Ge_{0.12}$ (dashed), and $Si_{1-x}Ge_x$ (solid) composed of $Si_{0.88}Ge_{0.12}$ (73 vol %) and $Si_{0.58}Ge_{0.42}$ (27 vol %).

6.4. **Conclusion**

Nanostructured thermoelectric $Si_{0.8}Ge_{0.2}$ alloy was synthesized via high energy ball milling and hot-press sintering. The thermal and transport properties of the prepared sample were studied and compared with the conventional $Si_{0.8}Ge_{0.2}$ alloy used in RTGs. The theoretical modeling based on Boltzmann transport equations in relaxation time approximation framework was fitted to the

experimental data. It was found that the Ge content has an essential role in thermoelectric properties of $Si_{1-x}Ge_x$ especially at high temperatures. In order to evaluate the actual phases developed in the $Si_{0.8}Ge_{0.2}$ structure, differential thermal analysis and thermogravimetery data of the synthesized sample were investigated in detail and compared with the X-ray diffraction data. We found that although x-ray diffraction results did not evidently show the presence of the different phases in the nanostructured sample, the DTA data taken over the temperature range of room temperature to 1500°C indicated the presence of two different phases, none of which being the anticipated $Si_{0.8}Ge_{0.2}$ phase. Even though the amount of Ge was 20 at. % in the starting material, the dominant phase was $Si_{0.88}Ge_{0.12}$ along with a small amount of $Si_{0.58}Ge_{0.42}$. The effect of the smaller Ge content in the former phase appeared in reducing the Seebeck coefficient and the thermal conductivity at high temperatures.

The DTA results were further studied by theoretical modeling. In order to fit the experimental data, a two component $Si_{1-x}Ge_x$ structure with x= 0.12 and x= 0.42 was assumed in the theoretical modeling. The agreement between the theory and experiment confirmed the presence of the two phases and signified the effect of the variation in Ge content. In $Si_{0.8}Ge_{0.2}$ alloy, at high temperature, the bipolar effect in the thermal conductivity and the Seebeck coefficient is significant. The bipolar effect decreases with the reduction of the Ge content due to its smaller band gap. However, the lattice thermal conductivity is also a function of the Ge content and is smaller for the phase with higher Ge content (up to approximately 50 at. % Ge [3]). Nevertheless, the reduction of the bipolar effect at high temperature is significantly more than the increase of the lattice part of the thermal conductivity when x increases above 0.12. Also, since different phases of $Si_{1-x}Ge_x$ have a similar crystal lattice structure with small deviation of the lattice constant, it is possible to make multicomponent $Si_{1-x}Ge_x$ structures with coherent grain boundary interfaces [16] that can improve phonon scattering while having minimal effect on the charge transport. Therefore, a multicomponent phase of the $Si_{1-x}Ge_x$ may provide a route for further improving the thermoelectric properties of this material system, which can be a subject for the future studies.

6.5. **References**

1 P.-E. Hellberg, S.-L. Zhang, F.M. d'Heurle, C.S. Petersson, J. Appl. Phys. 82 ,5773, 1997.

2 S.J. Kilpatrick, R.J. Jaccodine, P.E. Thompson, J. Appl. Phys. 81, 8018, 1997.

3 Jivtesh Garg, Nicola Bonini, Boris Kozinsky, and Nicola Marzari, Phys. Rev. Lett.106, 045901 (2011).

4 M.N. Tripathi and C. M. Bhandari, J. Phys.: Condens.Matter 15, 5359-5370, 2003.

5 B. Abeles, Phys. Rev. 131, 1906 (1963).

6 C. Bera, M. Soulier, C. Navone, Guilhem Roux, J. Simon, S.Volz, Natalio Mingo, J.App.Phys., 108,124306, 2010.

7 H. Stöhr and W. Klemm, Z. Anorg.Allg. Chem. 241, 304 (1954).

8 D.M. Rowe, CRC Handbook of Thermoelectrics, CRC-Press (1995).

9 Scherrer, P.GöttingerNachrichten Math.Phys.2, 98–100 (1918).

10 Olesinski, R.W., Abbaschian, G.J., in: "Binary Alloy Phase Diagrams", Second Edition, Vol. 2,T.B.Massalski (editor-in-chief), Materials Information Soc., Materials Park, Ohio, 1990.

11 Zahra Zamanipour, Xinghua Shi, Arash M. Dehkordi, Jerzy S. Krasinski, and Daryoosh Vashaee, Phys. Status Solidi A 209, No. 10, 2049–2058 (2012).

12 Nikhil Satyala, Daryoosh Vashaee, Appl. Phys. Lett.100, 073107 (2012).

13 Giri Joshi, Hohyun Lee, Yucheng Lan, Xiaowei Wang, Gaohua Zhu, Dezhi Wang, Ryan W. Gould, Diana C. Cuff, Ming Y. Tang, Mildred S. Dresselhaus, Gang Chen and Zhifeng Ren, Nano Lett., 2008, 8 (12), pp 4670–4674.

14 Zahra Zamanipour, Jerzy S. Krasinski, Daryoosh Vashaee, J.Appl.Phys., In press 2013.

15 D. J. Bergman and O. Levy, ,J. Appl. Phys., vol. 70, pp.6821, 1991.

16 Liu H., Zheng Z., Yang D., Ke X., Jaatinen E., Zhao J. C. and Zhu H. Y., , ACS Nano, 4 (10), pp 6219–6227 (2010).

Chapter 7 $Si_{0.8}Ge_{0.2}$ with embedded $CrSi_2$ Nano-inclusions

7.1. Introduction

The progress in enhancing ZT has been mainly followed in the direction of reducing the thermal conductivity via nanostructuring [1,2,3,4,5,6]. If the crystallite sizes in the nanostructured material are small compared with phonon mean free path and large compared with charge carrier mean free path, the thermal conductivity can be reduced more than the electrical conductivity resulting in enhancement in ZT [7,8]. The idea of reducing thermal conductivity via nanostructuring has resulted in enhancement of the ZT for p-type $Si_{0.8}Ge_{0.2}$ to ZT≅0.95 [9] and for n-type to ZT≅1.2 [10]. ZT enhancement in nanostructured silicon with a low concentration of germanium has been also reported due to the increased phonon scattering by nanograins and point defects [5].

Another direction to enhance ZT has been improving the power factor that can be done by enhancing the electrical conductivity and/or the Seebeck coefficient. This may be achieved by making a composite of different materials [11]. D. J. Bergman and L. J. Fel [12] developed an effective-medium theory to explain the thermoelectric properties of a composite material and concluded that the power factor of a composite of two materials can exceed that of the constituent component separately, but the highest ZT cannot reach to higher than the maximum ZT of each component. In their analysis the effect of crystallite boundary scattering was ignored in model calculations. However, it is known that phonons and charge carriers transport are influenced by crystallite boundary scattering especially when the size of the crystallites becomes comparable to their characteristic lengths. The Seebeck coefficient is expected to enhance due to energy filtering of hot carriers at the interface and under optimum conditions the enhancement in Seebeck coefficient can be greater than reduction in electrical conductivity, therefore, the thermoelectric power factor can enhance [6,13,14]. The enhancement of power factor has been

shown in composite structures embedded with nanoparticles such as $Si_{0.8}Ge_{0.2}$/Si [2] and InGaAs/ErAs [15].

The prospect of nanoparticle doping was also introduced with model calculation for silicide-SiGe alloy systems [16]. Several silicide-SiGe composite alloys were introduced that can potentially enhance ZT. However, no practical realization of these material systems was discussed. Here, we investigated the formation of nanostructured $Si_{0.8}Ge_{0.2}$ embedded with $CrSi_2$ nanoparticles. Both compounds of silicon germanium and chromium disilicides have shown large thermoelectric power factors. Silicon germanium has a larger band gap and smaller thermal conductivity than chromium disilicide which makes it better for thermoelectric application, especially at high temperature. However, chromium disilicide without any doping is a p-type material with larger electrical conductivity and thermoelectric power factor than doped silicon germanium [17]. $CrSi_2$ is one of the semiconductors that can be used at high temperature due to its high melting point (i.e. 1475°C) and thermal stability in air up to 1000°C [18,19]. $CrSi_2$ is a highly degenerate p-type semiconductor and its hole mobility is 100 times more than electron mobility [20]. However, the maximum reported ZT for $CrSi_2$ is only 0.2 at 600 °C [21]. The main limiting parameter in this material to achieve high ZT at high temperature is its small energy gap (i.e. 0.3 eV) that results in small Seebeck coefficient and large thermal conductivity due to the enhanced thermal carrier excitation at high temperature [17,22].

In this chapter, we present the results of investigation on thermoelectric properties of $Si_{0.8}Ge_{0.2}$ embedded with $CrSi_2$ nano-crystallite inclusions. The composite structure is formed by mechanical alloying of the elements and subsequent sintering. For comparison, nanostructured $Si_{0.8}Ge_{0.2}$ without $CrSi_2$ as a control sample was also synthesized with similar growth process parameters. Both structures were modeled and their thermal and electrical transport properties were studied in detail. It was shown that the composite of $Si_{0.8}Ge_{0.2}$-$CrSi_2$ suffers from the large interface potential barrier between the two material systems that prevents formation of an optimal material structure for large ZT to happen. The effects of nano-inclusions on electrical and thermal characteristics of the composite structure were discussed in detail and it was shown that there is no optimum size of $CrSi_2$ nano-inclusion that can enhance ZT.

7.2.Experimental Procedure

Elemental Si (99.9% purity), Ge (99.99% purity), B (99.9% purity) and Cr (99.9% purity) powders in stoichiometric ratio of 10 at.% of $CrSi_2$, and 90 at.% $Si_{0.8}Ge_{0.2}$ doped with 1.6 at.% B were weighted and loaded in a tungsten carbide bowl. In a separate bowl, elemental Si, Ge, and B powders were loaded in stoichiometric ratio of $Si_{0.8}Ge_{0.2}$ doped with 1.6% B. The bowls were hermetically sealed inside an argon (Ar) filled glove box and milled in Fritsch-P7PL planetary ball mill. The composite powder of $Si_{0.8}Ge_{0.2}$-$CrSi_2$ was milled for 46 hours with ball-to-powder-ratio (BPR) of 1.6 at 800 rpm and $Si_{0.8}Ge_{0.2}$ powder was milled for 42 hours with BPR of 4.6 at 1000 rpm. The powders were loaded in a graphite die with an internal diameter of 12.7 mm and sintered with hot-press at different pressures, sintering temperatures, and holding times as listed in Table 7.1.

Table 7.1: Sintering parameters

Sample ID	Material	Temperature (°C)	Holding time (min)	Pressure (MPa)
1	$Si_{0.8}Ge_{0.2}$	1200	6	93
2	$Si_{0.8}Ge_{0.2}$-$CrSi_2$	1200	6	108
3	$Si_{0.8}Ge_{0.2}$-$CrSi_2$	1200	1.5	93
4	$Si_{0.8}Ge_{0.2}$-$CrSi_2$	1100	6	93

The samples were cut into appropriate geometries for different characterizations. Electrical conductivity and Seebeck coefficient were measured with four probe method by means of commercially available equipment (Ulvac, ZEM-3). Thermal conductivity was measured by a laser flash apparatus (Netzsch LFA 457). The inaccuracy for the thermal conductivity measurement is <10%, and for electrical conductivity and Seebeck coefficient is <5%.

The milled powders and sintered samples were characterized by x-ray diffraction (Bruker AXS D8-Discover) with Cu Kα radiation. Phase formation and crystallite size were analyzed using the diffraction spectrum recorded in the range of 2θ angles between 20^o and 60^o. The structures of the sintered samples were imaged by Hitachi S-400 Scanning Electron microscope (SEM).

7.3. Results and Discussions

Figure 7-1 shows the XRD spectra taken from $Si_{0.8}Ge_{0.2}$-$CrSi_2$ composite powder at different milling times. The data from the sintered sample is also shown for comparison. In the spectra of the milled powder, Si, Ge, and Cr peaks are observed at both 3 and 20 hours of milling times. After 30 hours of milling, Si and Ge peaks disappeared, $Si_{0.8}Ge_{0.2}$ and $CrSi_2$ phases were formed, but the Cr peak was still observed. After 46 hours of milling, $Si_{0.8}Ge_{0.2}$ peaks corresponding to diffractions for (220) and (311) planes were reduced with the diffraction peak for (111) plane being dominant. This indicates the preferential orientation of crystallites along (111) direction during milling. Small Cr peak was still observed in the powder. However, the Cr peak completely disappeared after sintering as shown in the XRD spectra of the sintered sample. The diffraction peaks for (220) and (311) planes intensified after being sintered indicating the random orientation of the crystallites in the sintered sample. The area under $Si_{0.8}Ge_{0.2}$ and $CrSi_2$ peaks showed the intensity ratio similar to their stoichiometric ratio (i.e. 90:10). No other phases were observed.

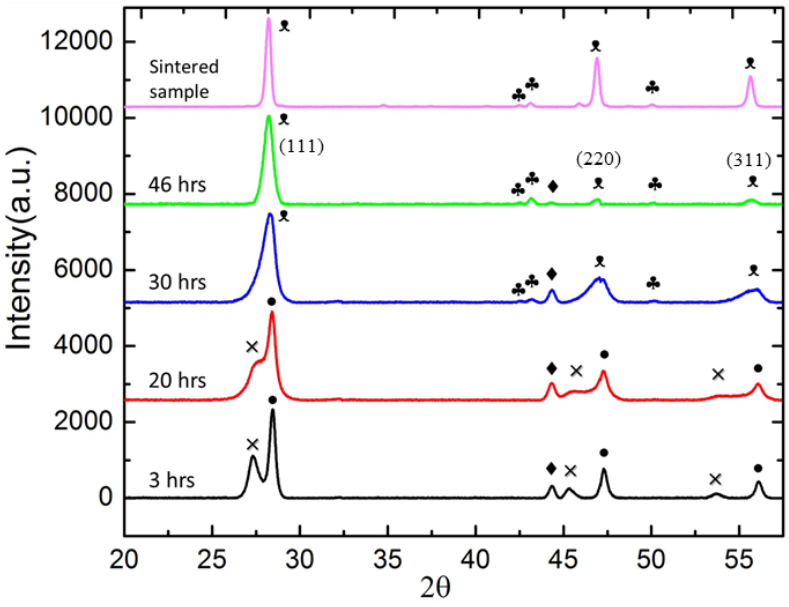

Figure 7-1: XRD spectra of the $Si_{0.8}Ge_{0.2}$-$CrSi_2$ powder at different milling times and that of the sintered sample 2. Different materials are marked by different symbols: Si (•), Ge (×), Cr (♦), $Si_{0.8}Ge_{0.2}$ (♠), $CrSi_2$ (♣).

Comparing the broadening of the peaks in the powder and sintered sample, one observes significant crystallite growth after sintering. The line broadening may be created due to both residual stress and the crystallite size. Since the crystallite sizes are small, it is expected that the line broadening of the peak is dominated by the size of the crystallites rather than the residual stress. The average crystallite size was estimated using commercial software (DiffracPlus EVA 14, Bruker-AXS). The software uses a full pattern matching (FPM) of the XRD scan based on an empirical model for the peak shape. The fitting of the scan was done by pseudo-Vigot functions. The average crystallite size was calculated by the corrected Scherrer's formula for the instrument broadening at the completion of the FPM model. The average crystallite size after extracting the instrument broadening for $Si_{0.8}Ge_{0.2}$ and $Si_{0.8}Ge_{0.2}$-$CrSi_2$ powders were 8 nm and 13 nm, respectively. The XRD analysis of the crystallite size is not accurate for large size grains (>100 nm). Therefore, the XRD analysis was not used to estimate the crystallite size of the sintered samples.

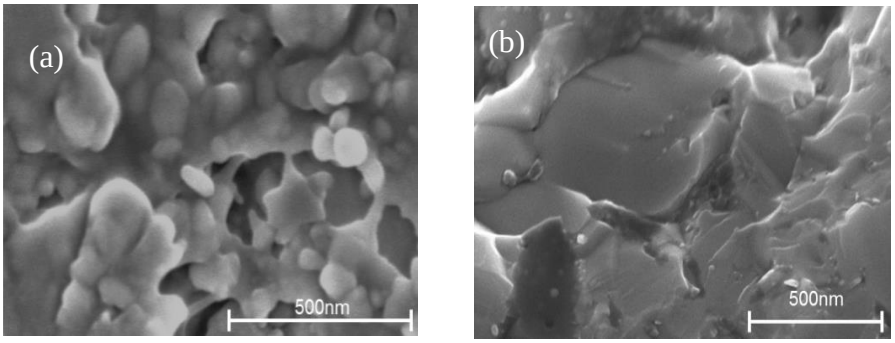

Figure 7-2: SEM images for (a) $Si_{0.8}Ge_{0.2}$ and (b) $Si_{0.8}Ge_{0.2}$-$CrSi_2$ composite sample 2. The composite sample consists of much larger crystallites than $Si_{0.8}Ge_{0.2}$ sample.

Figure 7-2 shows the SEM images for both $Si_{0.8}Ge_{0.2}$ and $Si_{0.8}Ge_{0.2}$-$CrSi_2$ composite sample 2. The average crystallite size in the composite sample is obviously larger than that in the $Si_{0.8}Ge_{0.2}$ sample. The SEM image observation revealed the order of crystallite size (i.e. ~20-50 nm in $Si_{0.8}Ge_{0.2}$ sample and ~200-700 nm in $Si_{0.8}Ge_{0.2}$-$CrSi_2$ composite sample 2) which as will be discussed in the next section has a vital role in transport properties.

Electrical conductivity, Seebeck coefficient, thermal conductivity, power factor, and figure-of-merit of all samples versus temperature are shown in Figure 7-3 and Figure 7-4. Although all composite samples have nearly similar Seebeck coefficient in the whole range of temperature,

their electrical and thermal conductivities show significant variation due to their different sintering conditions. The smallest electrical conductivity and thermal conductivity was obtained for sample 4 due to its lower sintering temperature (i.e. 1100°C) compared with sample 2 and 3. Sample 2 has slightly higher electrical conductivity which is due to its longer sintering time (i.e. six minutes).

The electrical conductivity of all samples reduces with temperature. Since the samples are highly doped, the carrier concentration does not significantly change with temperature and the electrical conductivity follows the mobility trend with temperature. As will be discussed in the next section, the slope of carrier mobility is effectively defined by characteristics of the charge carriers scattering by acoustic phonons which has a negative slope. At lower temperatures the descending slope is reduced due to the contribution of ionized impurity scattering in $Si_{0.8}Ge_{0.2}$ and nano-inclusion scattering in $Si_{0.8}Ge_{0.2}$-$CrSi_2$ structures.

Comparing the Seebeck coefficient of the composite samples with that of $Si_{0.8}Ge_{0.2}$, one observes that the composite samples have higher Seebeck coefficient in the whole tested temperature range. This indicates that the composite samples have smaller carrier concentration than $Si_{0.8}Ge_{0.2}$. This may be associated with the diffusion of boron into $CrSi_2$ phase resulting in smaller doping concentration in $Si_{0.8}Ge_{0.2}$.

The electrical conductivities of composite samples at room temperature are smaller than that of $Si_{0.8}Ge_{0.2}$ sample. The difference can be associated with the carrier mobility and concentration of the samples. However, the difference reduces with temperature. In a highly doped crystalline $Si_{0.8}Ge_{0.2}$ material, the dominant charge scattering mechanism at higher temperatures is due to acoustic phonons while the ionized impurity scattering is the most dominant one at room temperature. The effect of crystallite boundary scattering will be discussed further in the next section.

The smaller thermal conductivity and the larger power factor of sample 2 have resulted in its highest figure-of-merit ZT among the composite samples.

Comparing the power factor times temperature of sample 2 with that of $Si_{0.8}Ge_{0.2}$, one observes nearly 20% enhancement in power factor at 850°C. As it will be discussed in the next section, the main reason for enhancement of power factor in sample 2 is the increase of its charge carrier mobility. However, despite its larger power factor, the figure-of-merit plot shows that there is no

enhancement in ZT of the composite sample. As we will discuss in the next section, this is mainly due to the larger thermal conductivity of the composite sample compared with that of $Si_{0.8}Ge_{0.2}$ resulted from its larger average crystallite size.

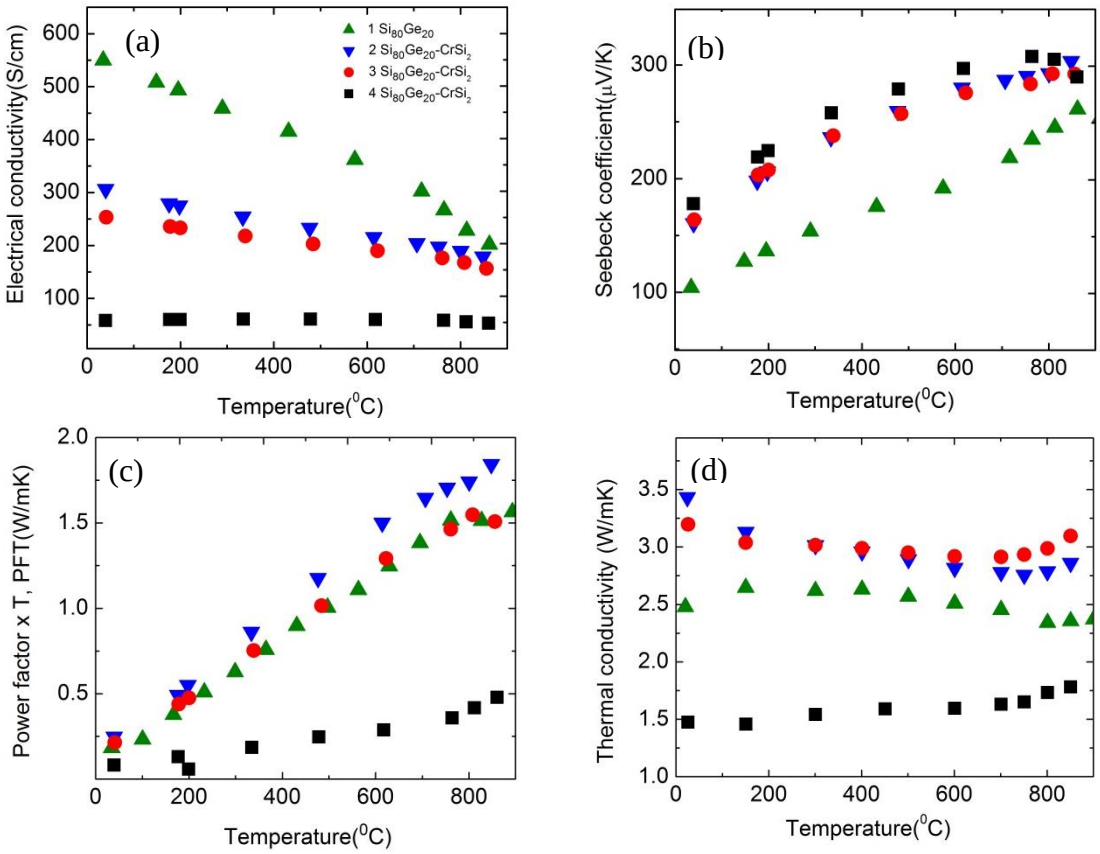

Figure 7-3 (a) Electrical conductivity, (b) Seebeck coefficient, (c) Power factor times temperature, and (d) Thermal conductivity Power factor times temperature of composite $Si_{0.8}Ge_{0.2}$-$CrSi_2$ samples compared with those of $Si_{0.8}Ge_{0.2}$ versus temperature.

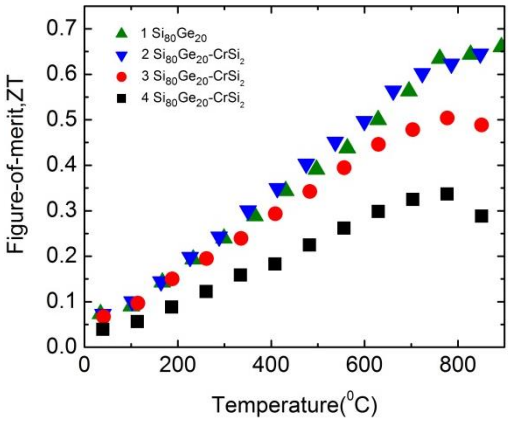

Figure 7-4 Figure-of-merit as a function of temperature for the composite $Si_{0.8}Ge_{0.2}$-$CrSi_2$ samples compared with that of $Si_{0.8}Ge_{0.2}$ sample.

7.4. Theoretical modeling and discussion

Using Boltzman transport equation with relaxation time approximation, the thermoelectric properties of sample 1 ($Si_{0.8}Ge_{0.2}$) and sample 2 ($Si_{0.8}Ge_{0.2}$ with $CrSi_2$ inclusion) were calculated and compared with experimental results. A three band model was assumed including one valence band and two conduction bands, one near the X point and one at the L point [23]. Band structure parameters for the conduction band and valence band were taken from ref. [24]. In this model, the parabolic band was corrected with a non-parabolicity parameter to account for deviation from parabolic band approximation which was necessary to fit the experimental data. The anisotropy of the conduction band was also taken into account through a mass tensor. Using the relaxation time approximation, the electrical conductivity, Seebeck coefficient, charge carrier mobility, mean free path, and electronic part of thermal conductivity were modeled. For charge carriers the scattering mechanisms due to ionized impurities, acoustic phonons, deformation potential of optical phonons, and the crystallite boundaries were taken into account. Other scattering mechanisms have negligible effect and can be reliably ignored in calculations [24]. The lattice thermal conductivity was calculated using Debye model and Boltzmann transport equation with relaxation time approximation [25,26]. Relaxation times were calculated for phonon-phonon, point defect, phonon-hole, and phonon-electron scattering mechanisms. The model parameters

for phonons were taken from ref. [24]. The modeling procedure was started with calculating the Fermi level, followed by computing different energy-dependent relaxation times for charge carriers and phonons. The doping concentration was estimated by fitting the experimental results for both $Si_{0.8}Ge_{0.2}$ and sample 2. The total relaxation time was calculated using Matthiessen's rule. The thermoelectric properties were finally calculated for the temperature range of 25 °C to 850°C.

Charge carrier scattering at $Si_{0.8}Ge_{0.2}$ crystallite interfaces was modeled by incorporating the additional GB scattering due to these interfaces. It was assumed that the carriers scatter coherently at independent grain boundary sites which are characterized by a local disk shaped potential following Ref. [26]. Since the screening and phase coherency lengths of the charge carriers are small compared with the size of the $Si_{0.8}Ge_{0.2}$ grains, carriers interact coherently only with a small region of the grain boundary in each scattering event. . Therefore, the grain boundary is divided into independent scattering sites resembling disk shaped potentials with cylindrical symmetry as depicted in Figure 7-5. In brief, a potential barrier with cylindrical symmetry in the form of $U(r,z)=U_c\exp(-z/z_c)\theta(r-r_c)$ was assumed at the interface, where z_c models the width of the space charge region and r_c models the lateral extension of the scattering potential. U_c is the strength of the potential barrier. θ is the Heaviside step function. In the composite sample charge carriers experience an extra scattering mechanism at the interface of $Si_{0.8}Ge_{0.2}$ and the embedded $CrSi_2$ crystallites.

The size of the nano-inclusions is comparable to the screening and phase coherency lengths of the charge carriers. As a result the carriers are scattered effectively by the whole spherical potential in each scattering event. Therefore, this scattering was modeled by a potential barrier with spherical symmetry in the form of $U(r)=U_s\exp(-r/r_s)$ as shown in Figure 7-5. U_s is the strength of the potential barrier and r_s models the width of the space charge region at the interface. The scattering rates were calculated using Born approximation for both potentials. U_c, U_s, r_c, r_s, and z_c were the fitting parameters in the model and were estimated by fitting the experimental data of electrical conductivity, Seebeck coefficient, and thermal conductivity.

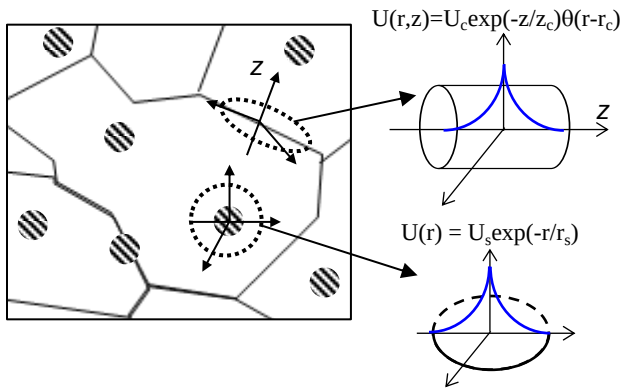

Figure 7-5: Schematic diagram of the crystallite and nano-inclusion interface scattering potentials. Nano-inclusions and crystallite interfaces were modeled with spherical and disk-shaped potentials with exponential decay in direction normal to the interface, respectively.

Phonon scattering at crystallite interfaces was modeled following standard methods [27,28,29]. In summary, crystallite boundaries can introduce three different types of scattering of phonons including regular reflection-refraction, diffusive scattering due to the corrugation of the GB, and Rayleigh scattering. It was found that a combination of reflection-refraction and diffusive scattering fits the experimental data.

Figure 7-6 shows the comparison of model calculations with the experimental results of thermoelectric properties of sample 1 and 2 versus temperature. A good agreement between the theory and experiment is observed over the entire range of the temperature.

The doping concentration was calculated from the data of Seebeck coefficient. The calculation requires several iterations to fit the Seebeck coefficient by adjusting the doping concentration. The average crystallite size and the interface potential are fitting parameters which affect both Seebeck and electrical conductivity with smaller effect on the former one. The crystallite size also affects the thermal conductivity. The fitting procedure starts with fitting roughly the Seebeck coefficient values by adjusting the doping concentration without considering the interface scatterings. In the next step, the average crystallite size and the interface potential scatterings were added to the model and their parameters were determined by fitting the experimental values of the electrical and thermal conductivities. At last, the calculated doping concentration was fine adjusted iteratively by tuning the fitting parameters so that electrical conductivity, Seebeck coefficient, and thermal conductivity are fitted over the entire range of temperature. To account for the grain size variation in the sample, a Gaussian distribution was

assumed for the grain sizes. The average GB scattering rate was calculated by summing over the scattering rates associated with the different grain sizes. The addition of interface scatterings affected the Seebeck coefficients which required recalculation of the estimated values of doping concentration. The iteration of fitting the experimental data of the three quantities of Seebeck coefficient, electrical and thermal conductivities converged to unique values for the average crystallite size and interface potential parameters. The interface potential U_c for the $Si_{0.8}Ge_{0.2}$ sample was estimated to be 130 meV. The estimated values for the interface potentials U_c and U_s in the composite sample were 150 meV and 500 meV, respectively. The average value of the crystallite sizes were determined to be 30 nm and 400 nm in $Si_{0.8}Ge_{0.2}$ and $Si_{0.8}Ge_{0.2}$–$CrSi_2$ samples, respectively. The estimated average crystallite sizes agree with the crystallites observed in the SEM image of Figure 7-2.

It was found that the crystallite boundary scattering enhances the Seebeck coefficient only slightly, which can be associated with the small boundary potentials that reduce the effect of energy filtering in these samples. To benefit from energy filtering mechanism, a large interface potential and a doping concentration which places the Fermi energy slightly ($2\text{-}3k_BT$) below the top of the potential barrier is required [13].

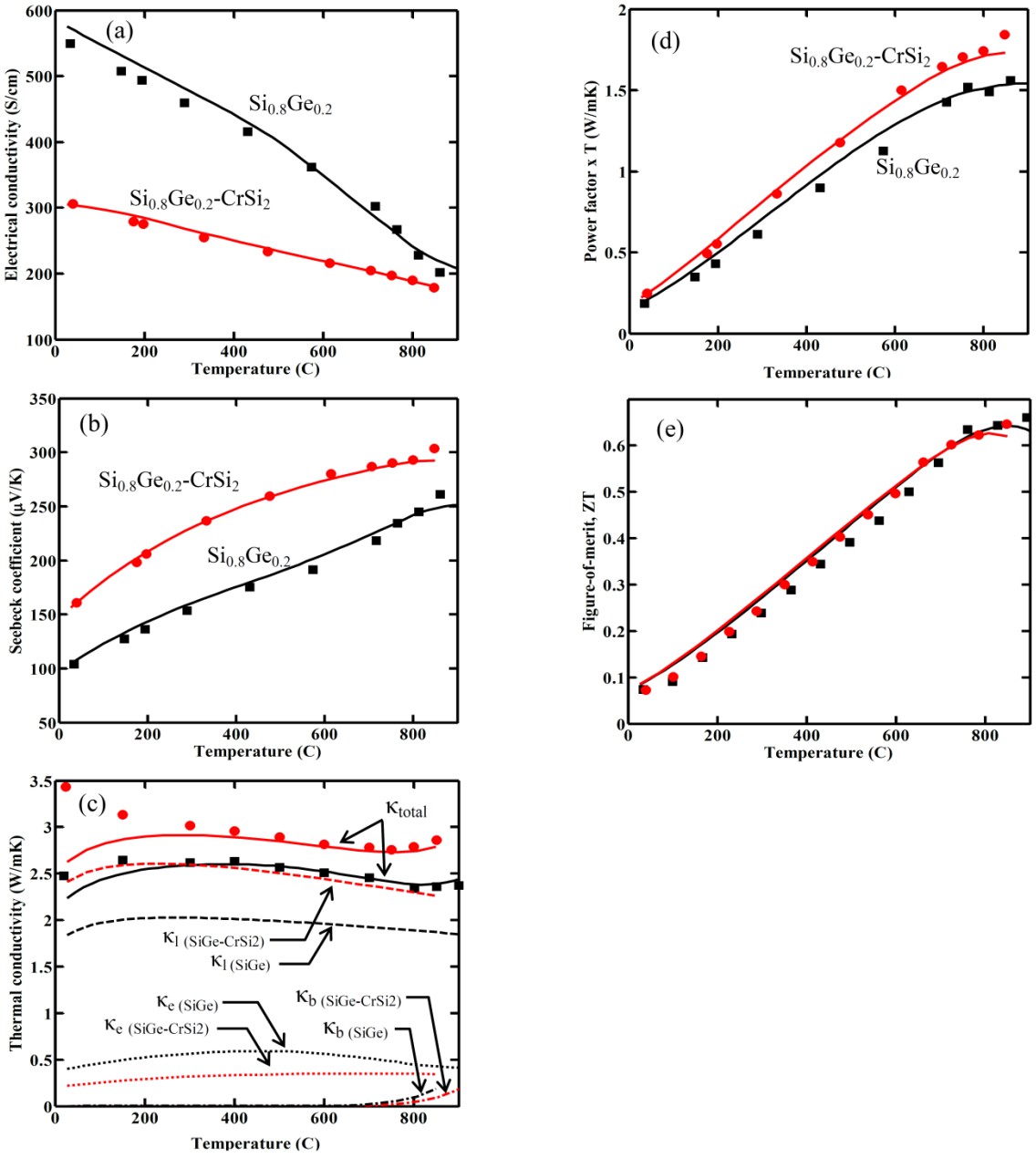

Figure 7-6: Comparison of the theoretical (lines) and experimental data (symbols) of thermoelectric properties of $Si_{0.8}Ge_{0.2}$ sample 1 (square, black) and $Si_{0.8}Ge_{0.2}$-$CrSi_2$ sample 2 (circle, red).

The calculated thermal conductivity components of both samples are shown in Figure 7-6-c. The total thermal conductivity is a result of three components due to lattice, charge carriers, and ambipolar diffusion. However, the lattice part contributes to approximately 80% of the total thermal conductivity. The lattice part of thermal conductivity in the composite sample is larger

than that of $Si_{0.8}Ge_{0.2}$ due to its larger crystallite size. The ambipolar diffusion is the smallest with increasing trend at high temperature, which remains negligible up to the highest measurement temperature.

Figure 7-7 illustrates the calculated carrier concentration (a), Hall mobility (b), hole mean free path (b), and Hall mobility components (c,d) for both samples as functions of temperature. Figure 7-7(a) shows that the composite sample has smaller carrier concentration than $Si_{0.8}Ge_{0.2}$, which can explain its larger Seebeck coefficient. The carrier concentration is much smaller than the nominal boron concentration of 1.6 at% which was added in the material. The solid solubility limit of boron depends on temperature and is approximately 0.2 at% at 1000°C [30]. The extra boron precipitates in the grains or at grain boundary regions [24,31,32]. It is also shown that the concentration of minority carriers (electrons) increase with temperature, which is responsible for a small increase in electrical conductivity, decrease in the slope of Seebeck coefficient, and increase in thermal conductivity at high temperatures.

Figure 7-7-b shows a different trend of Hall mobility for the two samples. While the Hall mobility of $Si_{0.8}Ge_{0.2}$ sample decreases monotonically with temperature (due to the dominancy of acoustic phonon scattering), the mobility of the composite sample shows an increasing trend with temperature from room temperature to ~250 °C and then a decreasing trend. The increasing trend of charge carrier mobility at lower temperature in the composite sample can be explained with the strong scattering of charge carriers by $CrSi_2$ nano-inclusions. Since the nano-inclusions scatter lower energy electrons more strongly, as the population of high energy charge carriers increases with temperature, the charge carrier mobility enhances with temperature up to 250 °C. Since the acoustic phonon scattering rate increases with temperature, the trend changes at 250 °C and the mobility decreases with temperature following similar trend as in $Si_{0.8}Ge_{0.2}$ sample.

Although the carrier mobility of the composite sample is larger than that of $Si_{0.8}Ge_{0.2}$, smaller carrier concentration resulted in a smaller electrical conductivity in this sample. $Si_{0.8}Ge_{0.2}$ has

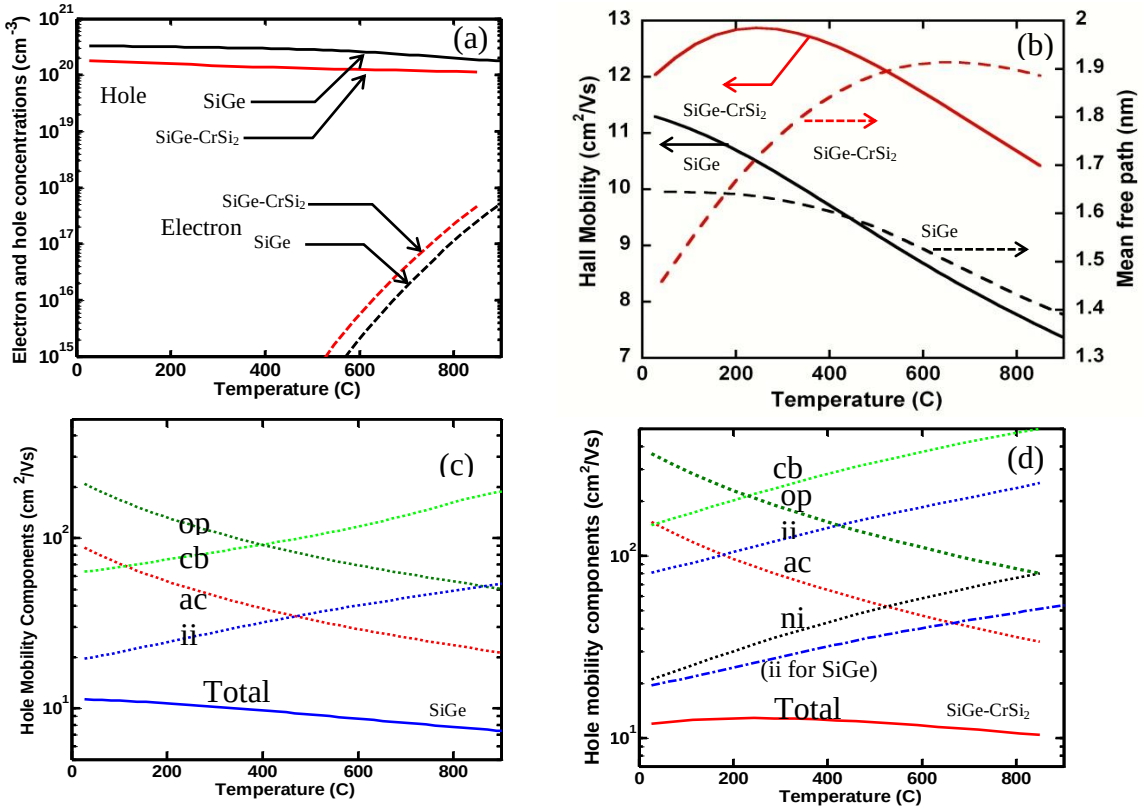

Figure 7-7: (a) Carrier concentration, (b) Hole mean free path (MFP) and Hall mobility for both $Si_{0.8}Ge_{0.2}$ sample 1 (black) and $Si_{0.8}Ge_{0.2}$-$CrSi_2$ sample 2 (red), and (c) and (d) Hall mobility components for $Si_{0.8}Ge_{0.2}$ and $Si_{0.8}Ge_{0.2}$-$CrSi_2$ composite, respectively. The ionized impurity component of $Si_{0.8}Ge_{0.2}$ structure is re-plotted in (d) for comparison with that of the composite structure.

higher carrier concentration than $Si_{0.8}Ge_{0.2}$-$CrSi_2$. The carrier concentration in both materials remains approximately constant with temperature (Figure 7-7-a). At low temperature, charge carrier mobility of $Si_{0.8}Ge_{0.2}$ is approximately similar to that of $Si_{0.8}Ge_{0.2}$-$CrSi_2$ (Figure 7-7-b) resulting in higher electrical conductivity of $Si_{0.8}Ge_{0.2}$. At high temperature, the charge carrier mobility in $Si_{0.8}Ge_{0.2}$-$CrSi_2$ is larger than that in $Si_{0.8}Ge_{0.2}$ compensating the effect of its lower carrier concentration. Therefore, the difference between the electrical conductivity of the two structures reduces with temperature.

The Hall mobility is calculated from the total relaxation time using Mattiessen's rule from the individual scattering rates. Different charge carrier scattering mechanisms including scattering by ionized impurities, acoustic phonons, optical phonons, and crystallite boundaries were

considered. In the composite sample, the crystallite boundary scattering consists of scatterings at $Si_{0.8}Ge_{0.2}$-$Si_{0.8}Ge_{0.2}$ and $Si_{0.8}Ge_{0.2}$-$CrSi_2$ interfaces.

In the $Si_{0.8}Ge_{0.2}$ sample the dominant scattering mechanisms are due to ionized impurities and acoustic phonons. In the composite sample, the dominant ones are the scatterings due to $CrSi_2$ nano-inclusions and acoustic phonons. The scattering rate from the $Si_{0.8}Ge_{0.2}$ crystallite interfaces is negligible in both samples (Figure 7-7-c and d). The smaller carrier concentration in the composite sample has significantly reduced the ionized impurity scattering component in this sample. However, the mobility is not proportionally enhanced, which is due to the additional scattering by $CrSi_2$ nano-inclusions in the composite sample. As shown in Figure 7-7-d, the $CrSi_2$ nano-inclusions in the composite sample are strongly scattering the charge carriers.

The hole mean free paths of both samples are also shown in Figure 7-7(b). It is shown that the MFP in both samples changes slightly with temperature remaining between 1-2 nm for the whole temperature range. The hole mean free path (MFP) in composite sample, following similar trend as hole mobility, increases with temperature and saturates to 1.9 nm at high temperatures. However, in $Si_{0.8}Ge_{0.2}$ sample MFP decreases monotonically with temperature and drops from ~1.6 nm at room temperature to ~1.4 nm at 900 °C. The increase in MFP of holes in composite sample is again due to the nano-inclusion scattering as discussed earlier for the mobility.

Figure 7-8 shows the prediction of the thermoelectric figure-of-merit versus the $CrSi_2$ nano-inclusions average radius for a fixed volume fraction of 6% (i.e. 10 % at.) at the temperature of 850 °C. It is seen that ZT is not a strong function of the nano-inclusion radius. At small size of radius, the nano-inclusions are the dominant charge carrier scatterers resulting in strong reduction in charge carrier mobility as shown in Figure 7-7-d. As the size of nano-inclusion increases above 10 nm, the ZT remains approximately constant. In this range, the nano-inclusion scattering is smaller than that of the acoustic phonons; therefore, the nano-inclusion size variation does not significantly affect the ZT. The maximum ZT is predicted to be ZT~0.62 for the grain size of approximately 4 nm.

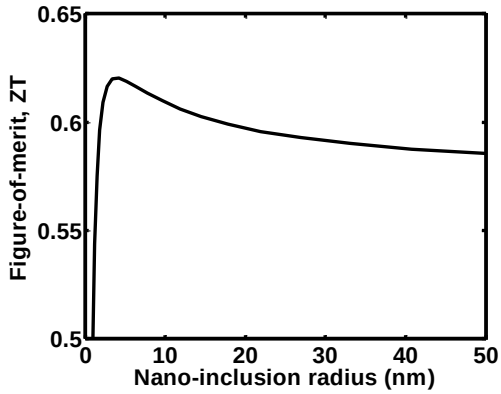

Figure 7-8: Thermoelectric figure-of-merit versus the average radius of the $CrSi_2$ nano-inclusions.

7.5. Conclusion

In summary, thermoelectric properties of p-type $Si_{0.8}Ge_{0.2}$ with 10 at.% of $CrSi_2$ nano-crystallite inclusion were studied. In order to compare the thermoelectric properties of the composite structure with $Si_{0.8}Ge_{0.2}$, both powders were synthesized by mechanical alloying and sintered by hot press method. Using the X-ray diffraction analysis, the phase formation and crystal structure of both powders were monitored. The sintering parameters were optimized to enhance the thermoelectric properties of the composite structure. Thermoelectric transport properties were measured from room temperature to 850 °C. It was shown that the thermoelectric power factor enhances by ~20% in the composite structure compared with $Si_{0.8}Ge_{0.2}$.

In order to understand the differences of the charge and phonon transport in the two material systems, using Boltzmann transport equation, the thermoelectric transport properties were modeled and fitted to their experimental value. The effect of crystallite boundaries and $CrSi_2$ nano-inclusions were modeled with cylindrical and spherical potential barriers, respectively. It was found that the charge carrier scattering by $Si_{0.8}Ge_{0.2}$-$Si_{0.8}Ge_{0.2}$ crystallite boundaries is negligible in both samples. For the case of $Si_{0.8}Ge_{0.2}$, the ionized impurity and acoustic phonons are the main scatterers at low (<450 °C) and high temperature, respectively. In the composite sample, the charge scattering from $CrSi_2$ nano-inclusions was dominant at lower temperature (<250 °C) and the acoustic phonon scattering was found to be dominant at higher temperatures.

The hole MFP in both samples remains in the range of 1-2 nm over the entire range of temperature. Since the $CrSi_2$ nano-inclusion scattering is dominant for charge carriers, the increase of their concentration does not enhance ZT due to same order reduction of the electrical and thermal conductivities. According to model calculations, the lattice part is the dominant component of thermal conductivity contributing 80% of the total thermal conductivity for both samples. The electronic part of thermal conductivity remains approximately constant at ~0.5 W/mk and ~0.2 W/mK for $Si_{0.8}Ge_{0.2}$ and $Si_{0.8}Ge_{0.2}$-$CrSi_2$, respectively. The ambipolar thermal diffusion remains negligible with slight increases as the temperatures increases above 800 °C for both samples.

The modeling data further indicates that the enhancement of power factor in $Si_{0.8}Ge_{0.2}$-$CrSi_2$ sample is not due to the hot carrier energy filtering and is mainly associated with its larger crystallite sizes. Theoretical calculation of ZT did not show a strong dependency on the average size of the nano-inclusions. The optimum average size of the nano-inclusions was determined to be approximately 4 nm. Smaller size of the nano-inclusions deteriorates ZT as they are dominant scatterers affecting the charge carrier mobility. At larger size of nano-inclusions the charge carrier scattering is dominated by acoustic phonons; therefore, ZT remains unchanged.

7.6.References

1 D.M Rowe, Thermoelectrics Handbook : Macro to Nano, CRC press, BocaRaton, FL, 2006.

2 M Zebarjadi, G Joshi, G Zhu, B Yu, A Minnich, Y Lan, X Wang, M Dresselhaus, Z Ren, G Chen, Nano Lett., vol. 11 (6), pp. 2225–2230, 2011.

3 M.S. Dresselhaus, G. Chen, Z.F. Ren, J.-P. Fleurial, P. Gogna, M.Y. Tang, D. Vashaee, H. Lee, X. Wang, G. Joshi, G. Zhu, D. Wang, R. Blair, S. Bux, and R. Kaner, , Proc. MRS Fall Meeting, Nov. 26-30, 2007, Paper No. U2.4, Boston, MA.

4 A. Minnich, D. Vashaee, and G. Chen, ,Proceedings of 2009 Inaugural US-EU-China Thermophysics Conference - Renewable Energy, May 28-30, 2009, Beijing, China.

5 G.H. Zhu, H. Lee, Y.C. Lan, X.W. Wang, G. Joshi, D.Z. Wang, J. Yang, D. Vashaee, H. Guilbert, A. Pillitteri, M.S. Dresselhaus, G. Chen, and Z.F. Ren, , Physical Review Letters, vol. 102, pp.196803, 2009.

6 D. Vashaee, A. Shakouri, J. Appl. Phys. Vol.101,pp.053719, 2007.

7 Nikhil Satyala and Daryoosh Vashaee, Appl. Phys. Lett. 100**,** 073107 (2012)

8 Nikhil Satyala and Daryoosh Vashaee, J. of Electronic Materials, Vol. 41, no. 6 (2012), 1785-1791.

9 Giri Joshi, Hohyun Lee, Yucheng Lan, Xiaowei Wang, Gaohua Zhu, Dezhi Wang, Ryan W. Gould, Diana C. Cuff, Ming Y. Tang, Mildred S. Dresselhaus, Gang Chen and Zhifeng Ren,, Nano Lett., vol.8 (12), pp. 4670–4674, 2008.

10 X.Wang, H.Lee, Y.C. Lan, G.H. Zhu, G. Chen, and Z. Ren, Appl.Phys. Lett., 93, 193121, 2008.

11 D. J. Bergman and L. J. Fel,,J. Appl. Phys., vol.85, pp.8205 , 1999.

12 D. J. Bergman and O. Levy, ,J. Appl. Phys., vol. 70, pp.6821, 1991.

13 D. Vashaee and A. Shakouri, Phy. Rev. Lett., Vol. 92, no. 10, pp. 106103-1, 2004.

14 M.Zebarjdi, K. Esfarjani, Z. Bian, and A. Shakouri, Nano. Lett., 11, 225-230, 2011.

15 J. M. O. Zide, D. Vashaee, G. Zeng, J. E. Bowers, A. Shakouri, A. C. Gossard, Physical Review B 74, 205335, 2006.

16 Mingo N, Hauser D, Kobayashi NP, Plissonnier M, Shakouri A., Nano Lett. 2009 Feb; 9(2):711-5.

17 T. Dasgupta, J. Etourneau, B. Chevalier, S. F. Matar, and A. M. Umarji, J. Appl. Phys. 103, 113516 (2008)

18 I. Nishida, , J. matt. sci. vol.7, pp.1119-1124,, 1972.

19 J. Ma, Y. Gu, L. Shi, L. Chen, Z. Yang, Y, Oian, ,J. Alloys Compd. Vol.376,pp. 176-179, 2004.

20 Shinoda, D.; Asanabe, S; Sasaki, Y, , J. Phys. Soc. Jpn., vol.19 (3),pp.269, 1964.

21 T. Dasgupta, A.M. Umarji, ,Journall of Alloys and Compd, vol.461, pp.292-297, 2008.

22 G. D. Mahan, J, AppL Phys, 65 (4), 1578-1583 (1989)

23 G.A.Slack and M.A. Hussain, , J.Appl.Phys. 70, 94(1991).

24 A. Minnich, H. Lee, X.W. Wang, G. Joshi, M.S. Dresselhaus, Z.F. Ren, G. Chen, and D. Vashaee, , Physical Review B, Vol. 80, 155327, 2009.

25 E.F . Steigmeier and B. Abeles, Phys.Rev. 136,A1149(1964).

26 Callaway,Phys.Rev. 113, 1046 (1959).

27 A. I. Hochbaum, R. Chen, R. D. Delgado, W. Liang, E. C. Garnett, M. Najarian, A. Majumdar, and P. Yang, Nature (London) 451, 163 (2008).

28 W. Kim, J. Zide, A. Gossard, D. Klenov, S. Stemmer, A. Shakouri, and A. Majumdar, Phys. Rev. Lett. 96, 045901 (2006).

29 Pomeranchuk, J. of Physics, VI, 6, 237, (1942)

30 S. Solmi, F. Baruffaldi, and R. Canteri, J. Appl. Phys. 69, 2135 (1991).

31 Zhaihui Gao; Zamanipour, Z.; Vashaee, D.; Green Technologies Conference, 2012 IEEE , vol., no., pp.1-4, 19-20 April 2012 doi: 10.1109/GREEN.2012.6200978.

32 Z.Zamanipour, X. Shi, A. M. Dehkordi, J. S. Krasinski and D. Vashaee, Phys. Status Solidi A, 1-10(2012).

Chapter 8 Nanostructured bulk p-type higher manganese silicide

8.1. Introduction

Nanostructuring has offered a new approach to enhance the efficiency of thermoelectric materials. $(Bi,Sb)_2Te_3$, Si_xGe_{1-x}, and Si bulk nanostructured materials have already shown enhanced ZT [1,2,3,4] due to the reduction in thermal conductivity (κ) without significantly affecting the thermoelectric power factor ($S^2\sigma$) [5,6,7]. On similar concepts, certain materials with higher power factors are expected to make good thermoelectric materials if they can be synthesized into nanostructured form. Since transition metal silicides have shown a good power factor for operating temperature range of 400-800 ºC, nanostructuring may help to improve their thermoelectric efficiency. Among them alloys of silicon and manganese with higher Si content such as $Mn_{11}Si_{19}$, $Mn_{15}Si_{26}$, $Mn_{27}Si_{47}$ and Mn_4Si_7 have shown power factor ($S^2\sigma$) approaching $\sim 2\times10^{-3}$ W/mK [1]. Higher manganese silicide (HMS) compounds make Chimney-ladder structures with a bandgap around 0.7 eV [1]. These compounds may also contain nano to micro-scale regions of manganese monosilicide (MnSi) which can reduce the thermal conductivity [7,8,9,10].

Large Seebeck coefficient, low resistivity, high oxidation resistance, and non-toxicity [11,12] make the HMS alloy a good candidate in thermoelectric device applications especially for mid to high temperature range devices. It is inexpensive and mechanically robust with lower density than Bismuth and Chalcogenide based alloys owing to the small density of Silicon. In comparison, alloys based on PbTe have shown enhanced thermoelectric figure-of-merit at medium temperature [13]. However, both Pb and Te are toxic. The non-toxicity, stability, and low cost of HMS make it a promising TE material especially for large scale energy harvesting applications.

Compound of $MnSi_{1.73}$ has been made via a powder metallurgical route [14] and characterized for its thermoelectric properties. $MnSi_{1.8}$ and $MnSi_{1.85}$ compounds have been also produced via mechanical alloying and pulse discharge sintering [15]. $MnSi_{1.7}$ powder has also been produced via gas atomization, which is appropriate for large scale production [16]. Compared with fabrication methods such as arc melting, induction heating, or conventional crystal growth methods, powder metallurgical methods have advantages for better structural homogeneity and smaller amounts of energy consumption [17].

In this work, we focused on mechanical alloying approach to produce thermoelectric alloys of $MnSi_x$ with different silicon contents ranging from x=1.73 to 1.77. The produced powders were sintered via the hot-press method to achieve nanostructured bulk structure. Their structural parameters and thermoelectric properties were characterized and discussed.

8.2. Materials and methods

8.2.1. Synthesis of HMS powder

The HMS powder was prepared from 100 mesh silicon and 325 mesh manganese powders from Alfa Aesar Co. with purity of 99.9% and 99.99%, respectively. The amount of each component was weighed in an argon-filled glove box for different compositions of $MnSi_x$ with x= 1.73, 1.75, and 1.77. The mixed powder with the tungsten carbon balls were loaded into tungsten carbide bowls and milled in planetary mill with ball to powder weight ratio (BPR) of five. Both Fritsch's planetary ball mills P6 (500rpm) and P7 (1000rpm) were used. The speeds are equal to centrifugal acceleration of about 22G and 86G, respectively, where G is the gravitational constant. All the powders were dry milled for approximately 50 hours. The milled powders were weighted and loaded into a graphite die with inner diameter of 12.7 mm. All three samples were sintered at 950 °C for 5 min under 108 MPa pressure. These milling and synthesis parameters were optimized by making and characterizing over two hundreds of different HMS samples.

8.2.2. Characterization

The cylindrical samples were cut into rectangular bars and circular discs for electrical resistivity and thermal conductivity measurements, respectively. To determine the thermoelectric

properties, the Seebeck coefficient (S) and electrical conductivity (σ) were measured from room temperature to 970 K using a ZEM system (ULVAC Riko Co.) equipped with a four probe contact measurement facility. The thermal conductivities were measured using the laser flash method with Netzsch's LFA 457 Micro Flash equipment.

The samples were structurally evaluated by performing scanning electron microscopy (SEM) using a Hitachi S-4800. X-ray diffraction (XRD) analysis was performed in the range of $20^o<2\theta<60^o$ using Bruker AXS D8 with Cu Kα radiation (λ =1.54056 Å).

To study the thermal behavior and melting point of the samples, differential thermal analysis (DTA, Netzsch, STA 449 F1 Jupiter®) was accomplished with heating rate of 20 K/min under flowing argon atmosphere in an alumina crucible.

8.3. Results and discussions

8.3.1. Structural analysis

The XRD patterns of the $MnSi_{1.75}$ powder milled at 500 rpm with different milling times are shown in Figure 8-1. It is shown that some small characteristic peaks of Mn and Si continuously decreased with milling time while the HMS peaks grow. The Mn and Si peaks diminished after approximately 12 hours of milling. It can be also seen that MnSi was present in the samples until 16 milling hours, which nearly vanished after 80 h of milling. At this point, all the major characteristic peaks of pure HMS appeared and were in good agreement with those reported by Karpinsky and Evseev [18]. When comparing the diffraction peaks, it is difficult to distinguish the real structure of HMS from the XRD data as the position of the peaks are weak functions of the exact composition of HMS. These observations can explain why the exact structure of HMS is rarely given in the literature. Compared with Zhou et al. who reported HMS composition variation resulted from oxidation of Mn and Si during milling [19], we did not observe any oxidation even in powders milled up to 80 hours.

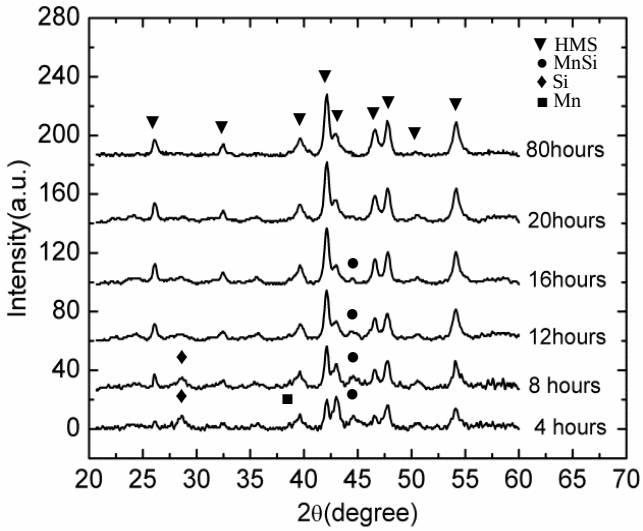

Figure 8-1: The XRD patterns of HMS powder after different milling times.

The XRD patterns of the hot pressed samples with three different HMS compositions were collected and shown in Figure 8-2 One can observe that the diffraction peak at 2θ=53.8° is shifted towards higher angles from $MnSi_{1.73}$ (red curve) to $MnSi_{1.77}$ (black curve). Moreover the relative intensities corresponding to this peak is considerably changed with the sample with highest Si content ($MnSi_{1.77}$) having the highest peak intensity. The XRD results indicate that three different composition of HMS were generated in the process.

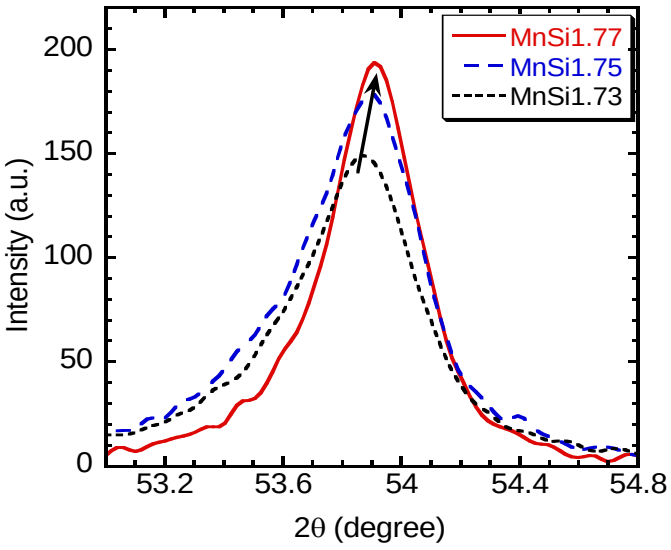

Figure 8-2 The diffraction peak at 2θ=53.8° degree for different HMS compositions

Figure 8-3 shows the SEM micrographs of the fracture surface of sintered $MnSi_{1.75}$ in three different magnifications. As can be seen here, voids of 5–200 μm in size in both intergranular and transgranular fractures were formed in the sample. The size of the primary grains ranged from 200 nm to 800 nm.

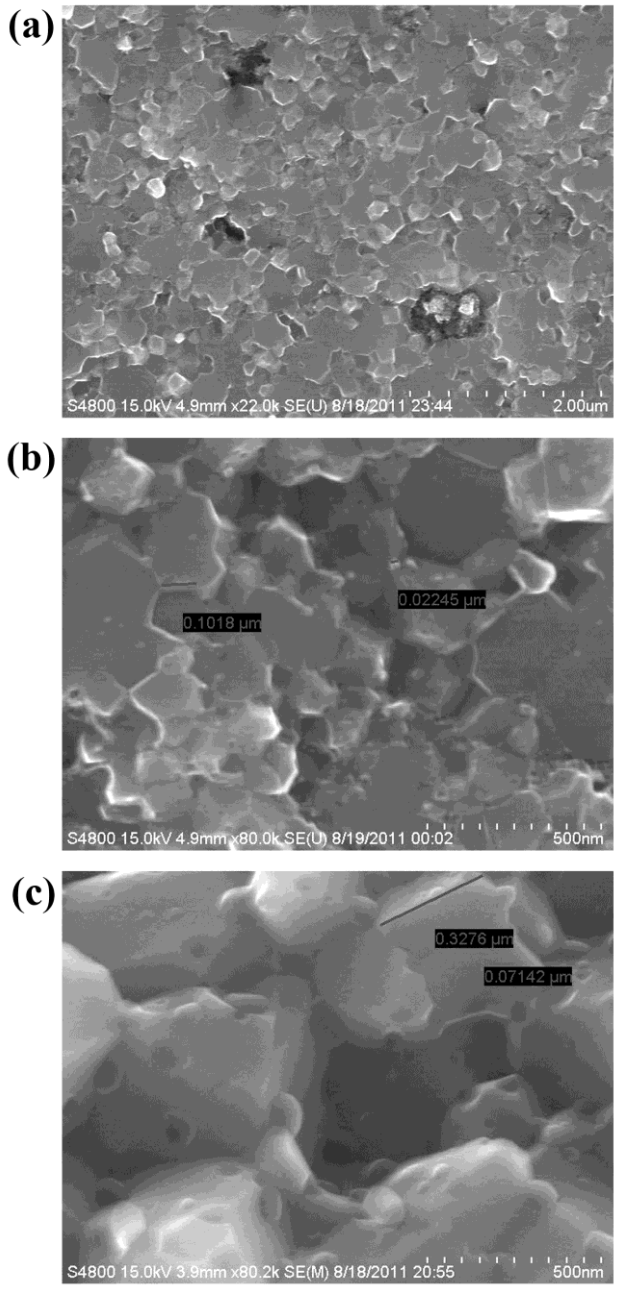

Figure 8-3 The SEM micrographs of sample $MnSi_{1.75}$ with different magnifications (a) ×22.0 k (b) ×80.0 k (c) ×80.2 k

Analyzing the DTA thermographs of the three different HMS compositions indicated no significant correlation between the main melting point within the range of our experiment (e.g. x=1.73, 1.75 and 1.77). According to the thermographs of different samples presented in Figure 8-4, a slight difference in melting point of different compositions was observed. The melting points are 1146.4, 1147.3 and 1149.0 °C for $MnSi_{1.73}$, $MnSi_{1.73}$ and $MnSi_{1.73}$, respectively. To the best of our knowledge there is no reporting data in this regard which indicates the melting point versus composition. Understanding of the physical reason for the small shift of melting point and the influence of Si on the structural properties needs to be investigated. Recently Borman et al. [20] introduced a theoretical description of melting point for nanostructured materials in the framework of a uniform approach using vacancy mechanism. In this framework the change of melting point with nanostructuring was described as a result of anharmonic oscillations of atoms. All in all, it seems that totally understanding the effect of Si on the structure and melting point of different samples from the bottom up is a daunting challenge.

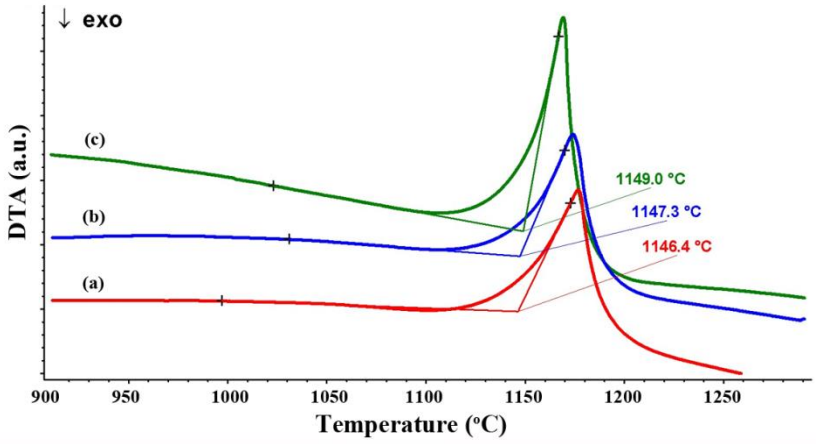

Figure 8-4 DTA thermographs of different $MnSi_X$ samples in the range of 900 to 1300 °C. (a) $MnSi_{1.73}$, (b) $MnSi_{1.75}$, and (b) $MnSi_{1.77}$

8.3.2. Effect of composition on thermoelectric properties

Figure 8-5 shows the temperature dependence of electrical conductivity for all three sintered $MnSi_{1.73}$, $MnSi_{1.75}$, and $MnSi_{1.77}$ samples. As shown in this figure, the electrical conductivity decreases with temperature.

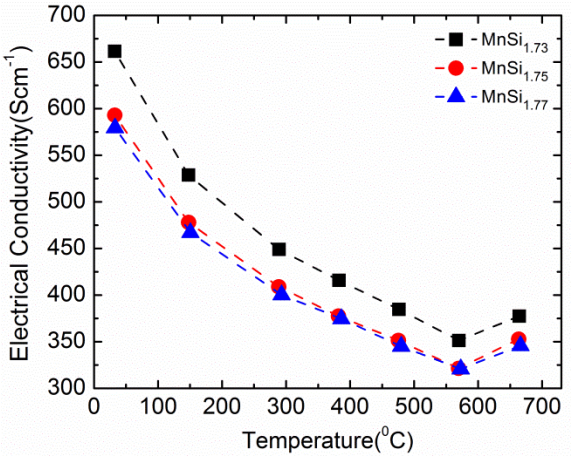

Figure 8-5 Electrical conductivity of different $MnSi_X$ samples versus temperature

Since the electron-acoustic phonon scattering rate increases with temperature, the charge carrier mobility decreases and consequently the electrical conductivity decreases. This decrease happens up to about 580^{0}C at which point by further increase of the temperature electrons, which are the minority carriers, are thermally excited and yield a small increase in electrical conductivity. Although this trend is similar in all semiconductors, the turning point depends on the band gap of the material [21,22,23]. Here, the electrical conductivity of $MnSi_{1.73}$ sample was slightly higher than $MnSi_{1.75}$ and $MnSi_{1.7}$ samples.

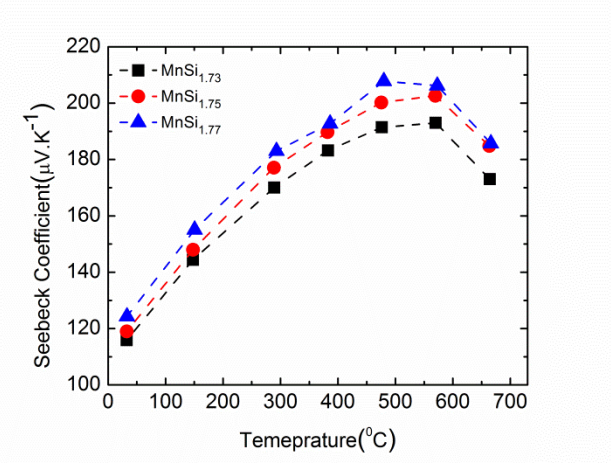

Figure 8-6 Seebeck coefficient trend of different $MnSi_X$ samples versus temperature

It is known that the charge carrier concentration and the grain boundary scattering both determine the Seebeck coefficient trends [3]. Seebeck coefficient versus temperature is shown in Figure 8-6 for all three samples. Seebeck coefficient in all samples increases up to 580^{0}C and then decreases at higher temperatures. It is seen that Seebeck coefficient trend is reversed compared with the temperature dependence of electrical conductivity (Figure 8-5).

Figure 8-7 shows the thermal conductivity of all three structures as a function of temperature. The thermal conductivity of the samples decreased with temperature up to about 500 °C. The initial reduction in thermal conductivity is due to the increase of phonon-phonon scattering which reduced the lattice part of thermal conductivity. However, the thermal conductivity increases rapidly as temperature increases above 500 °C. This is due to the enhancement of ambipolar thermal conduction. Ambipolar thermal conduction is a result of thermal excitation of electrons. Similar trend is reported in previous works [24]. HMS is known to have an indirect band gap of 0.77 eV [25], which is small compared with high temperature thermoelectric materials such as $Si_{0.8}Ge_{0.2}$. The thermal excitation of minority carriers enhances significantly at around 500 °C, which limits further increase of Seebeck coefficient and reduction of thermal conductivity. As a result the ZT has a turning point at around 500 °C with a decreasing trend at higher temperature as shown in Figure 8-9.

It is worth mentioning that the increment of silicon amount in HMS structure increased the electrical conductivity and decreased Seebeck coefficient. The power factor times temperature

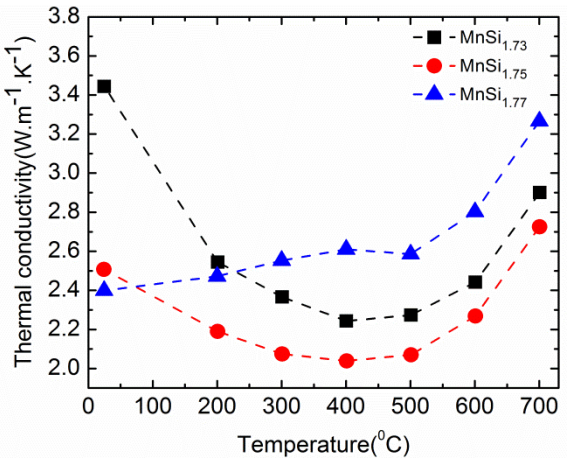

Figure 8-7 Thermal conductivity of different $MnSi_X$ samples versus temperature

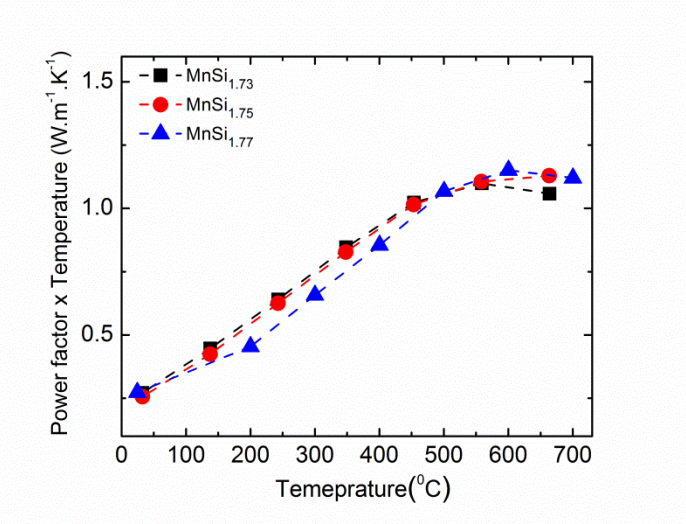

Figure 8-8 Power factor of different $MnSi_X$ samples versus temperature

(PFT) versus temperature for all compositions is shown in Figure 8-8. It can be seen that the power factor time temperature is approximately identical for all three different compositions with maximum value of 1.15 W/mK at 600 C. The figure-of-merit, ZT, of all sintered samples is shown in Figure 8-9. The ZT for all samples has a maximum around 600 °C after which it decreases. According to the ZT data versus temperature, it can be concluded that all three compositions have the optimum operation temperature range of 450°C to 650°C. $MnSi_{1.77}$ has the smallest ZT with the maximum value of 0.4 at 600C, which was due to the higher thermal conductivity of this structure. Among all compositions, $MnSi_{1.75}$ showed a maximum ZT of 0.55 at 600 °C.

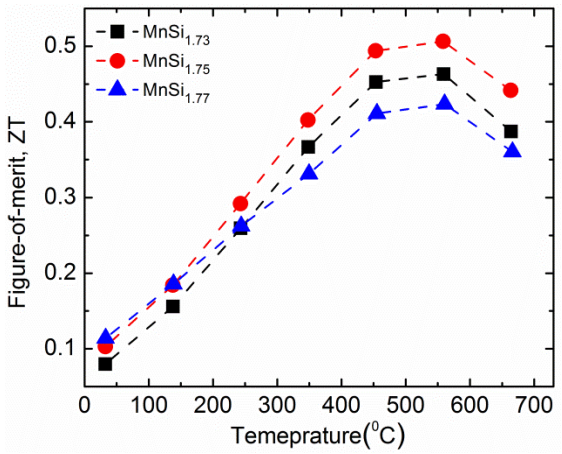

Figure 8-9 ZT of different $MnSi_X$ samples versus temperature

8.4. **Conclusion**

In this study, the microstructural and thermoelectric properties of different compositions of nanostructured bulk HMS ($MnSi_x$, x=1.73, 1.75 and 1.77) were investigated. It was found that the electrical conductivities of the three samples are similar with that of $MnSi_{1.73}$ nearly 10% larger than the other two compositions. The Seebeck coefficient increased with the increase in the Si content from peak value of ~190 μV/K for $MnSi_{1.73}$ to ~210 μV/K for $MnSi_{1.77}$. Although $MnSi_{1.77}$ has the maximum Seebeck coefficient, the power factor times temperature is approximately equal for all structures. Due to nanoscale grains, all tested material compositions showed smaller thermal conductivity than single crystalline HMS, which increased with the increase in the Si content. $MnSi_{1.75}$ showed the smallest thermal conductivity in the range of 2-2.7 W/mK. Overall, nanostructuring did not show significant improvement in ZT compared with that of traditional crystalline HMS. The different trends in thermal conductivity resulted in the highest value of ZT for $MnSi_{1.75,}$ which was 0.55, and the smallest value of ZT for $MnSi_{1.77}$, which was 0.4.

8.5. **References**

1 D.M Rowe, Thermoelectrics Handbook: Macro to Nano, CRC press, BocaRaton,FL,2006.

2 Poudel, Q. Hao, Y. Ma, Y. Lan, A. Minnich, B. Yu, X. Yan, D. Wang, A. Muto, D. Vashaee, X. Chen, J. Liu, M. S. Dresselhaus, G. Chen, Z. Ren, High-thermoelectric performance of nanostructured bismuth antimony telluride bulk alloys, B. Science, 320 (2008) 634- 638.

3 A. J. Minnich, X. Wang, H. Lee,1 M. S. Dresselhaus, Z.F. Ren, G. Chen, and D. Vashaee, Modeling study of thermoelectric SiGe nanocomposites, Physical Review B, 80 (2009) 15- 21.

4 S. K. Bux, R. G. Blair, P. K. Gogna, H. Lee, G. Chen, M. S. Dresselhaus, R. B. Kaner, and J. P. Fleurial, 19 (2009) 2445-2452.

5 D. Vashaee, A. Shakouri, Physical Review Letter, 92 (2004) 106103-1.

6 J. M. Zide, D. O. Klenov, S. Stemmer, A. C. Gossard, G. Zeng, J. E. Bowers, D. Vashaee, and A. Shakouri, Appl. Phys. Lett. 87 (2005) 112102.

7 M. C. Bost and J. E. Mahan, Journal of Electronic Materials, 16 (1987) 6-13

8 A. J. Zhou, T. J. Zhu, X. B. Zhao, S. H. Yang, T. Dasgupta, C. Stiewe, R. Hassdorf and E. Mueller, J. of Electronic Materials, 39 (2009) 2002.

9 K. Kakubo, Y. Kimura and Y. Mishima, Mat. Res. Soc. Symp. Proc. 646 (2001)

10 M. Umemoto, Z. G. Liu, R. Omatsuzawa and K. Tsuchiya, Materials Science Forum Vols. 343-346. (2000) and Journal of Metastable and Nanocrystalline Materials 8. 918-923 (2000)

11 S. Zhou, K. Potzger, G. Zhang, A. Mücklich, F. Eichhorn, N. Schell, R. Grötzschel, B. Schmidt, W. Skorupa, M. Helm, J. Fassbender, D. Geiger, Phys. Rev. B 75 (2007) 085203.

12 I. Kawasumi, M. Sakata, I. Nishida, K. Masumoto, J. Mater. Sci. 16 (1981) 355.

13 J. P. Heremans, V. Jovovic, E. S. Toberer, A. Saramat, K. Kurosaki, A. Charoenphakdee, S. Yamanaka, G. J. Snyder, Science, 321 (2008) 554-557.

14 Grob M. Riffel, U. Stohrer, Journal of Materials Research, 10 (1995), p. 34.

15 T. Itoh, M. Yamada, Journal of Electronic Materials. 38 (2009) 925-929.

16 H. Kleinke, Chemistry of materials, 22 (2010) 604-611.

17 S. Xinghua, Z. Zamanipour, A.M. Dehkordi, K.F. Ede, J.S. Krasinski, D. Vashaee, Green Technologies Conference, 2012 IEEE , pp.1-3.

18 O.G. Karpinsky, B.A. Evseev, Crystal structure of Mn4Si7, Izv. Akad. Nauk SSSR. Neorg.Mater. 5 (1969) 525-534.

19 A. J. Zhou, X. B. Zhao, T. J. Zhu, Y. Q. Cao, C. Stiewe, R. Hassdorf, E. Mueller, Journal of Electronic Materials, 38 (2009) 1072-1077.

20 V. D. Borman, p. V. Borisyuk, i. V. Tronin, v. N. Tronin, v. I. Troyan, m. A. Pushkin, o. S. Vasiliev, Int. J. Mod. Phys. B, 23 (2009) 3903-3911.

21 V.K. Zaitsev, D.M. Rowe (Eds.), CRC Handbook of Thermoelectrics, CRC Press, Boca Raton, FL (1995) 299.

22 M. Umemoto, Z.G. Liu, R. Omatsuzawa, K. Tsuchya, Mater. Sci. Forum. 918 (2000) 343-346.

23 Takahiro Yamada , Yuzuru Miyazaki, Hisanori Yamane, Thin Solid Films 519 (2011) 8524-8527.

24 Y.J.He, Q.R. Hou, Z.M. Wang, Y.B. Chen, Y.B., IEEE International Conference on Materials for Renewable Energy & Environment (ICMREE), 2 (2011) 1343-1345.

25 D. B. Migas, V. L. Shaposhnikov, A. B. Filonov, and V. E. Borisenko, N. N. Dorozhkin, Phys. Rev. B. 77 (2008) 1098-0121.

Chapter 9 Electrical contacts for higher manganese silicide

9.1. Introduction

Electrical contacts selection is very critical for highly efficient thermoelectric (TE) generators. In a conventional TE device, there are two metal contacts one at each end of the TE material. Since thermoelectric materials are usually doped to high concentration ($>10^{19}$ cm^{-3}), their electrical resistance is often small (~1-10 mΩ/cm). Due to the small resistance of the TE material, the device performance is sensitive to the ohmic contact resistance. For example, the electrical resistance of an HMS TE material with a thickness of 1 mm is typically ~5×10^{-4} Ωcm². Therefore, the ohmic contact resistance for an HMS TE device must be an order of magnitude smaller (i.e. $<5\times10^{-5}$ Ωcm²) so that the device performance is not reduced by the metal contacts.

In addition to low electrical contact resistance, the contacts should exhibit low thermal contact resistance. The contacts should also be mechanically and chemically stable in air without significant diffusion of the contact material into the TE material. The contacts should not degrade at working temperatures [1]. For practical thermoelectric applications, inexpensive, nontoxic materials with good physical-chemical reliability are desired.

In the past, the hot-side junctions were fabricated with a direct sintered contact [2,3,4,5]. These contacts were very stable, but exhibit high contact resistance. In this study, contacts were made by sintering of the metal or silicide powder, and the HMS powder together in one operation.

9.2. Experimental Procedures

9.2.1. Sample Preparation

The HMS and MnSi powders were prepared by mechanical alloying of elemental powders in planetary ball mills. 100 mesh silicon and 325 mesh manganese powders were obtained from Alfa Aesar Co. with purities of 99.9% and 99.99%, respectively. The average grain size of the

milled powder was about 200 nm. The remaining materials used in this study were obtained from Alfa Aesar and were used without milling. These powders included TiSi2 C54 with a phase purity of 99.5%, 325 mesh cobalt with a purity of 99.8%, 300 mesh nickel with a purity of 99.8%, 100 mesh chromium with a purity of 99%, 325 mesh titanium with a purity of 99.5%, and 250 mesh molybdenum with a purity of 99.9%.

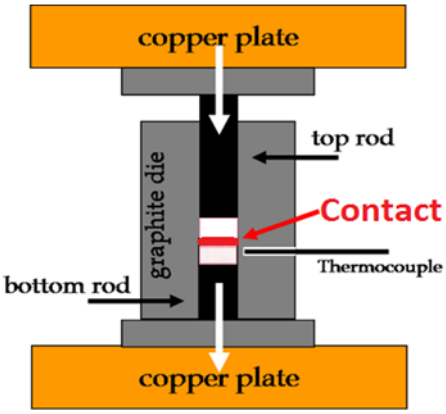

Figure 9-1 Sample sintering setup. The contact material is sandwiched between two layers of thermoelectric materials.

In order to test the properties of the metal contacts, a three layer structure or sandwich of HMS/contact material/HMS was fabricated. Figure 9-1 shows the sample setup schematically for sintering the contact structure. In a glove box filled with an argon atmosphere, HMS powder was weighed and loaded into a graphite die. Steel rods with very flat, smooth surfaces were used during the initial room temperature pressing cycles. The HMS powder was pressed at 93 MPa at room temperature for 10 minutes. Then the contact metal powder was loaded on top of the HMS layer and pressed at the same pressure at room temperature for 10 minutes. One more layer of HMS powder was loaded on top of the contact layer and the same pressure applied at room temperature for an additional 10 minutes. The pressing steps at room temperature were intended to create a good interface between the HMS and the contact materials. When the room temperature pressing was complete, the steel rods were replaced with graphite rods and the material was sintered at 950 °C for 5 minutes at 93 MPa. After allowing the system to cool down, the structure was removed from the graphite die. The samples were cleaned and polished

to obtain a sub 0.2 micron surface roughness for energy-dispersive x-ray spectroscopy (EDS) and x-ray diffraction (XRD) characterizations.

9.2.2. Measurement Methods

A four point probe resistivity measurement set up was used for measuring the metal or silicide/HMS contact resistance. The contact resistance was estimated from the plot of the resistance versus the distance between the voltage sensing probes. The experimental set up for measuring the contact resistivity and a sample result are shown in Figure 9-2. The sample and the measurement probes were inside an infrared furnace controlled by a computer for automated measurement of the contact resistance over a temperature range of 20 – 700 °C.

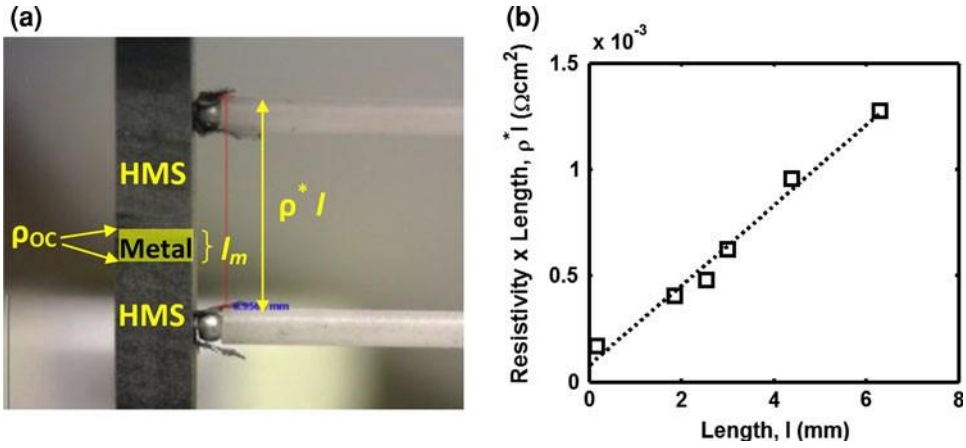

Figure 9-2 (a) Photograph of an HMS/contact/HMS sample with probes, and (b) an example plot to determine the contact resistance.

The total resistance (R[Ω]) between the two probes is the sum of the resistances of the HMS (R_{HMS} [Ω]), the contact resistance (R_{oc}[Ω]), and the metal resistance (R_m [Ω]):

$$R = R_{HMS} + R_{oc} + R_m \tag{9.1}$$

$$R = \rho \frac{l - l_m}{A} + \frac{2\rho_{oc}}{A} + \rho_m \frac{l_m}{A} \tag{9.2}$$

$$\rho^* l = \rho(l - l_m) + 2\rho_{oc} + \rho_m l_m \tag{9.3}$$

where ρ [Ωcm] is the electrical resistivity of the thermoelectric material, ρ* [Ωcm] is the effective electrical resistivity between the two probes at a distance of l $[cm]$, ρ_{oc} [Ωcm^2] is the ohmic contact resistance, A [cm^2] is the cross sectional area of the sample, and l_m [cm] is the thickness of the metal contact.

ρ^* and l were measured at a constant temperature using variable spacing four-point probes. $\rho^* l$ was plotted as a function of $l - l_m$ and fit to a straight line, which was extrapolated to find $\rho^* l$ at $l - l_m = 0$. Fig 2(b) shows an example plot. According to Eq.3, the contact resistance, $\rho_{oc} = \frac{1}{2}(\rho^* l - \rho_m l_m)$ at $l - l_m = 0$. Since the resistivity of the metal is very small compared to the contact resistivity, Eq.3 can be further approximated by $\rho_{oc} = \frac{1}{2}\rho^* l$ at $l - l_m = 0$.

In order to examine thermal stability, the structures were heated to 700 °C under argon atmosphere and held for either 5 h or 29 h, then cooled down to room temperature for characterization.

9.3. **Results and Discussions**

Co, Ni, Mo, Cr and Ti were investigated in this study because they are inexpensive and have large work functions [6]. Structures of HMS/metal/HMS were prepared for each of the metals and subjected to EDS and XRD examination. The EDS data were collected along a line that crossed and was perpendicular to one of the HMS/metal interfaces. The XRD data were collected for both HMS phases and for the metal phase of each sandwich at points that were one hundred micrometers from an HMS/metal interface.

Figure 9-3 (a) shows the EDS results for an HMS/Co interface. Traces of Mn and Si in the Co region of Figure 9-3(a) indicate that HMS diffused into the Co region. No diffusion of Co into the HMS region was observed. In Figure 9-3(b), regions I and III correspond to the HMS phases while region II corresponds to the Co layer. The XRD data shows the formation of CoSi in the Co region that can be attributed to the diffusion of Si atoms into the Co layer and a reaction with Co, which formed a brittle layer with poor contact strength. Similar results were observed for Cr, Mo, and Ti.

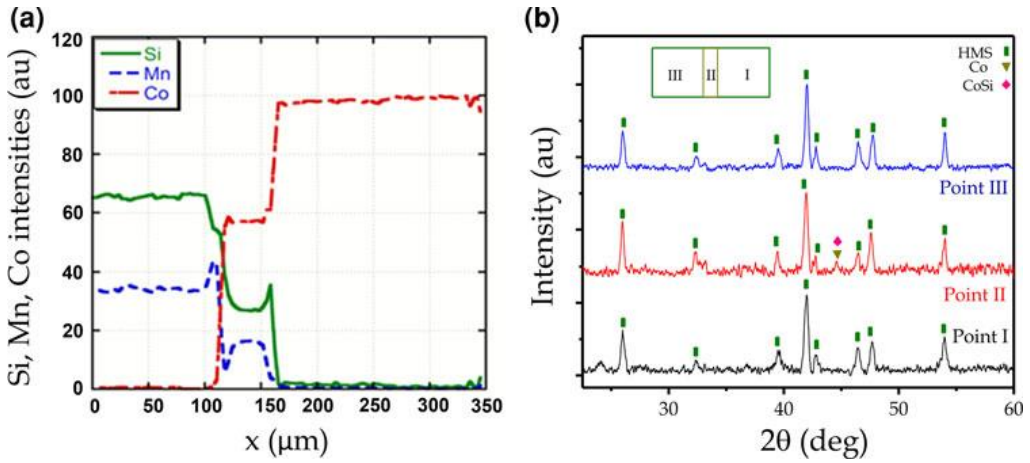

Figure 9-3 (a) EDS data for a Co/HMS contact (b) XRD results for a Co/HMS electrical contact.

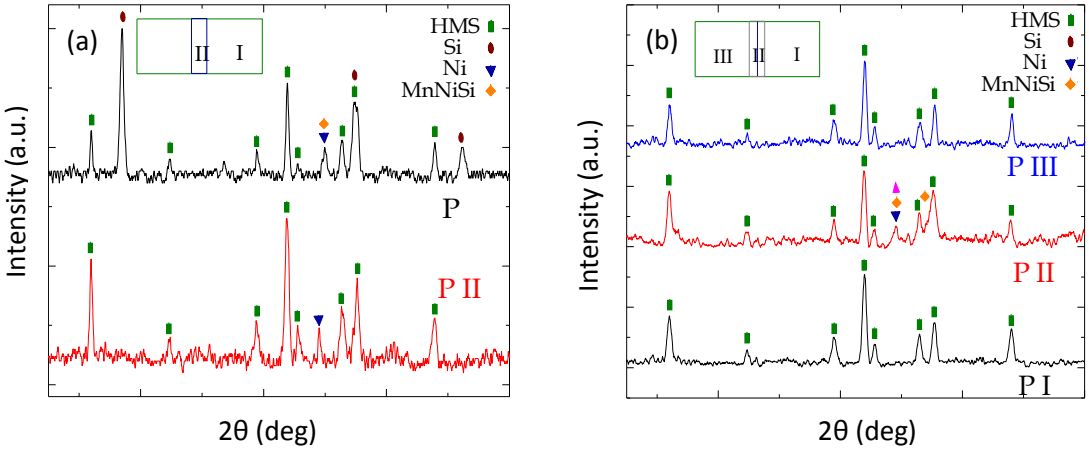

Figure 9-4 (a) XRD data for a Ni/HMS electrical contact, (b) XRD data for a Ni/HMS contact with Cr layer as a diffusion barrier.

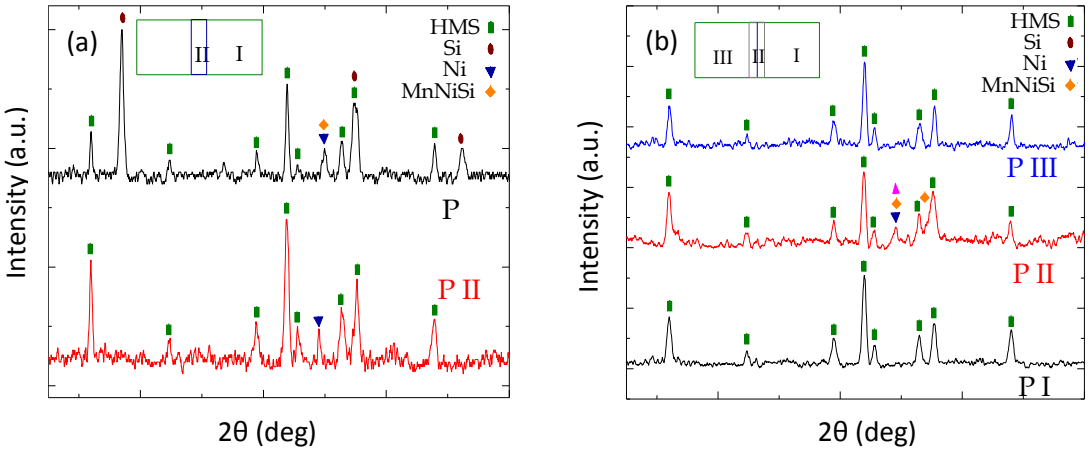

Figure 9-4 (a) shows the XRD results for the HMS/Ni/HMS configuration. Regions I and II correspond to HMS and Ni layers, respectively. Diffusion of Ni into the HMS layer was observed evidenced by the presence of elemental Ni and MnNiSi in the HMS layer. The data also indicates that HMS had diffused into the Ni layer.

In order to determine if Cr could act as an effective diffusion barrier, an HMS/Cr/Ni/Cr/HMS structure was prepared and examined with XRD. Figure 9-4(b) shows the results. Regions I, II, and III correspond to the HMS, Cr/Ni/Cr, and HMS layers, respectively. The XRD line, labeled P II, was taken at the mid-point of the Ni layer and shows that a Ni-Cr alloy had formed. Interestingly, no diffusion of Ni or Cr was observed into the HMS region. Diffusion of HMS into the Ni layer was observed. However, this is not of concern since the electrical conductivity of Ni, even with HMS present, is very high and would not be expected to affect the performance of a device. These data show that Cr is an effective deterrent to diffusion of Ni into HMS in an HMS/Ni system.

Although the diffusion between HMS and Ni can be significantly reduced by a Cr layer, Cr reacts with HMS at high temperatures to form a fragile layer between the Cr and HMS. Therefore, the use of a Cr layer is not a good solution for a device that must operate at high temperatures.

Other metal barrier systems were examined: Cr as a barrier layer for Co, and Ti as a barrier layer for Ni and Co. These three systems have a mismatch of coefficients of thermal expansion

resulting in mechanically weak contacts after thermal cycling. Therefore, none of the pure metals demonstrated satisfactory performance as a contact material for HMS.

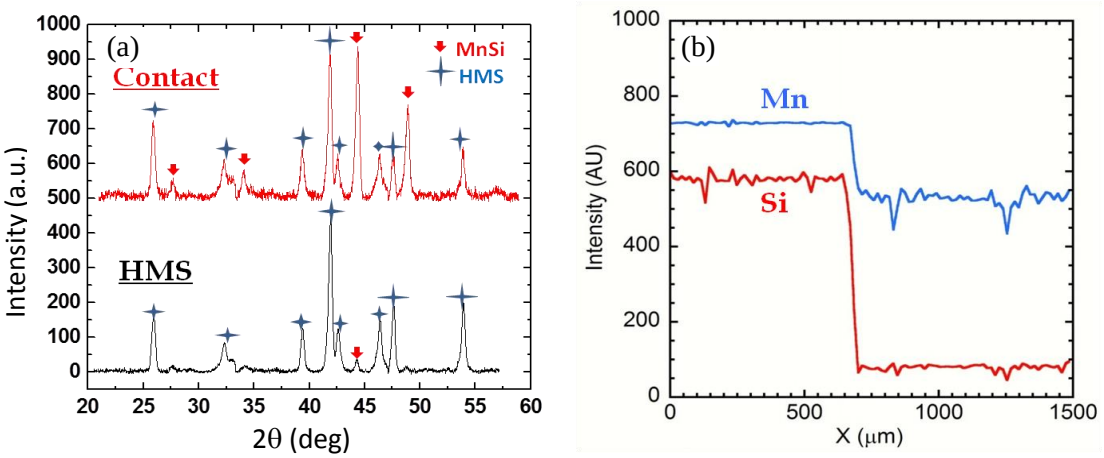

Figure 9-5 (a) XRD and (b) EDS data for and MnSi/HMS electrical contact.

Figure 9-5 shows XRD and EDS data for a structure in which MnSi was the contact material. Note should be made that the starting HMS powder had a small amount of MnSi, which shows in the bottom curve of

Figure 9-5 (a). However, the magnitude of the MnSi peak is small and shows that there was no significant diffusion of MnSi into the HMS layer. The top curve of

Figure 9-5 (a) shows that a significant amount of HMS diffused into the MnSi contact layer. As noted above, diffusion of HMS into the contact region is not of concern due to the large electrical conductivity of the contact layer. EDS results from the interface area (

Figure 9-5 (b)) shows that the interface between the HMS and MnSi layers is sharp indicating very little diffusion of the MnSi into the HMS layer.

Figure 9-6 (a) shows the contact resistance versus temperature for a MnSi/HMS structure. The resistance ranges from 10^{-4} to 1.2×10^{-4} Ωcm^2 for temperatures in the range of 20 °C to 700 °C, which is acceptable for bulk thermoelectric elements. The extrapolated resistivity measurements

for different temperatures converge to within ~0.1 μΩcm^2, as seen in Figure 9-6 (b), which is indicative of a good measurement.

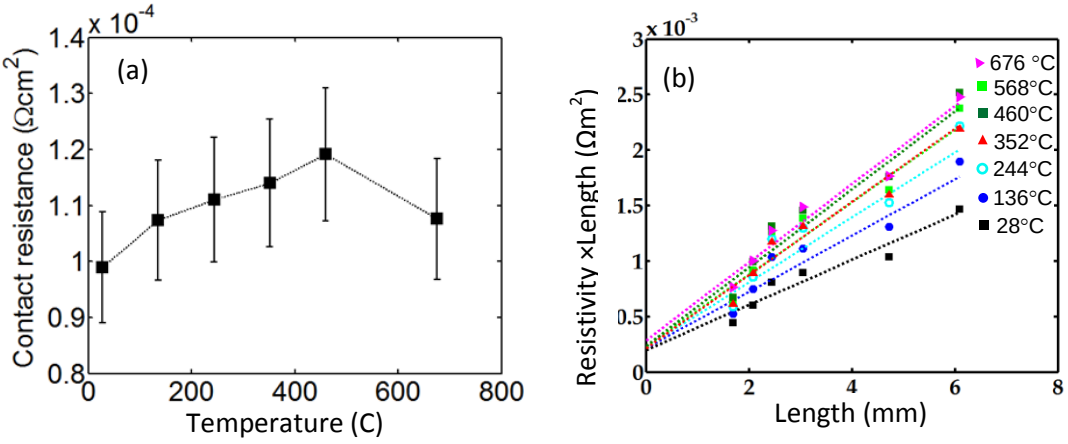

Figure 9-6 (a) Electrical contact resistance versus temperature for MnSi/HMS structure, (b) MnSi/HMS electrical contact resistance lines at different temperatures.

Figure 9-7 shows the EDS data after the thermal stability tests for an MnSi contact structure across the interface region for 5 h (Figure 9-7 (a)) and 29 hours (b) of annealing at 700 °C. The border between the MnSi and HMS regions is still sharp after each high temperature heating test.

Figure 9-8 illustrates contact resistance versus temperature after 29 h at 700 °C for MnSi system. The MnSi contact resistance ranged between 10^{-5} to 3×10^{-4} Ωcm^2 for temperatures between room temperature to 700 °C. In addition, the contact resistance decreased with temperature until it reached a value with order of magnitude 10^{-5} Ωcm^2 at T = 400 °C to 700 °C, which is the nominal operating temperature of HMS thermoelectric devices.

Comparing the contact resistance versus temperature before (Figure 9-6 (a)) and after (Figure 9-8) annealing shows two different trends at low and high temperature. While the high

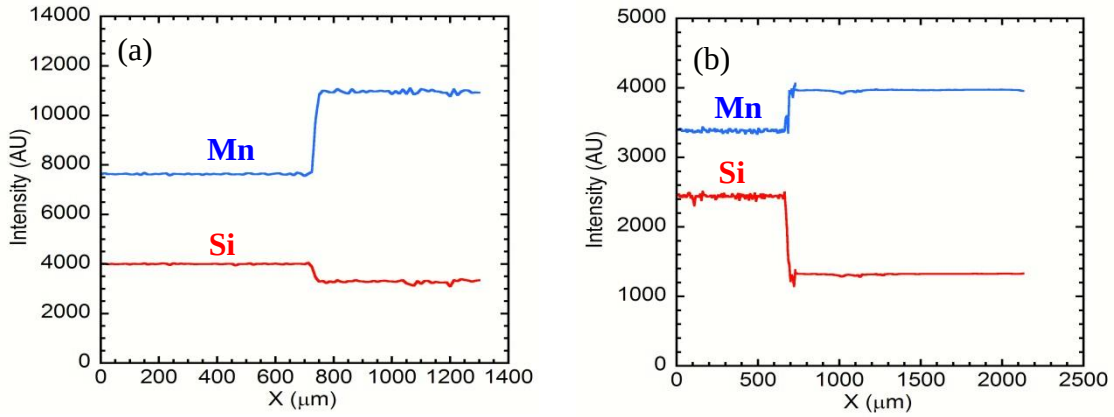

Figure 9-7 EDS data for the MnSi/HMS interface after (a) 5 h and (b) 29 h at 700 °C.

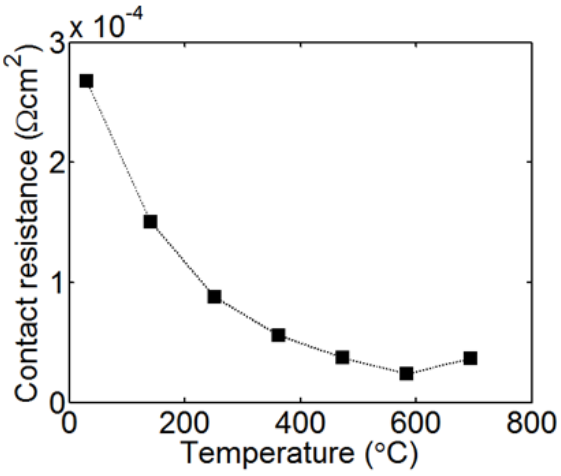

Figure 9-8 Electrical contact resistance for MnSi/HMS structure after 29 h 700 °C.

temperature contact resistance has reduced after annealing; the contact resistance at low temperature has increased. This difference may be explained by the fact that carrier concentration and energy gap in HMS are functions of defects such as stacking faults. It is known that such defects reduce the energy gap and increase the carrier concentration in HMS [7]. Before annealing a large density of defects is expected to exist at HMS/MnSi contact resulting in smaller energy gap and large carrier concentration at the interface. After annealing many of such defects are expected to be annealed. Therefore, the Schottky barrier at HMS/MnSi contact is increased after annealing resulting in larger contact resistance at low temperature. The reduction of contact resistance with temperature in Figure 9-8 follows the expected trend in a Schottky contact. In contrast, the contact resistance before annealing is approximately constant

versus temperature (Figure 9-6(a)). This indicates that the contact resistance is not limited by Schottky barrier as expected by the effect of the large density of defects in reducing the barrier potential. Due to the large density of crystal defects at interface, the contact resistance is dominated by physical defects such as vacancies, dislocation, tilts, etc. Figure 9-9 shows XRD results on α-$TiSi_2$/Higher Manganese Silicide electrical contact. The diffusion between α-$TiSi_2$ and Higher Manganese Silicide is not detectable.

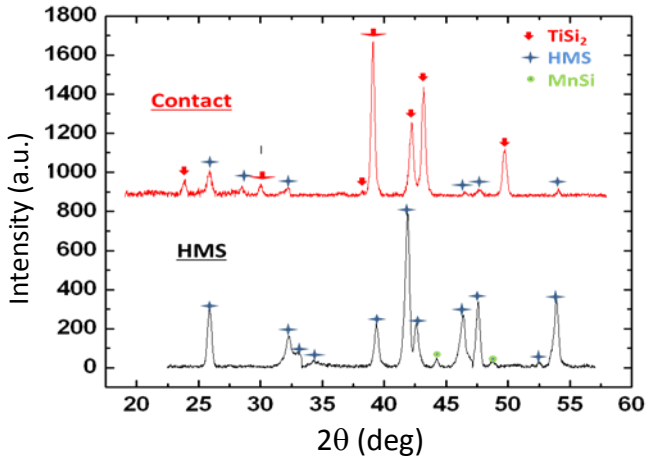

Figure 9-9 XRD results for an α-$TiSi_2$/HMS electrical contact. No diffusion of α-$TiSi_2$ into HMS was detected.

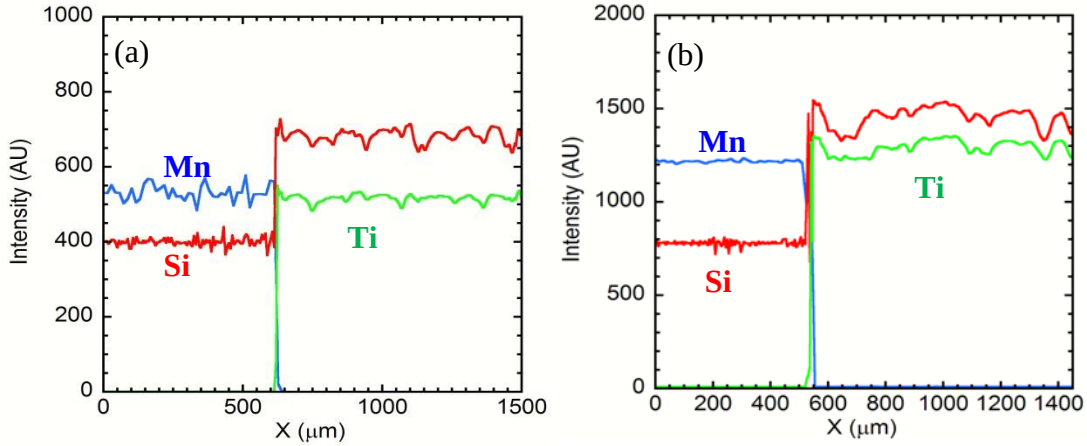

Figure 9-10 (a) EDS results for an α-$TiSi_2$/HMS electrical contact after (a) 5 h and (b) 29 h at 700 °C.

Figure 9-10 (a) and Figure 9-10 (b) show EDS data for an α-TiSi2/HMS electrical contact after heating to 700 °C for 5 h and 29 h, respectively. The interfaces, after heating, are sharp indicating negligible or no diffusion between the layers in the contact structure.

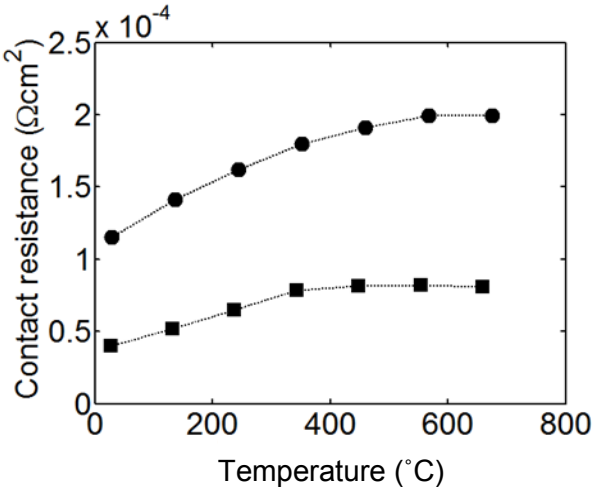

Figure 9-11 Contact resistance in a α-$TiSi_2$/HMS structure before (squares) and after (circles) 29 h at 700°C.

Figure 9-11 gives α-$TiSi_2$/HMS contact resistance versus temperature before and after the structure was heated to 700 °C for 29 h. After heating, the contact resistance ranged between 10^{-5} and 2×10^{-4} Ωcm^2 over a temperature range of 20 °C to 700 °C. The higher contact resistance after heat treatment can be related to grain coarsening at high temperature that can increase the density of vacancies at the interface. The long time stability of the contact at high temperature requires further study.

In order to further enhance the performance of MnSi and $TiSi_2$ contacts, MnSi and $TiSi_2$ were milled to powders of approximately 50 nm in size and used to make contact structures. Figure 9-12 shows the contact resistance for a nano grained MnSi/HMS and α-$TiSi_2$/HMS structures versus temperature. The contact resistance for MnSi/HMS structure ranged from 10^{-5} to 10^{-6} Ωcm^2 over a temperature range of 20 °C to 700 °C. This is approximately one order of magnitude less than the previous results for a MnSi/HMS contact (Figure 9-6). The SEM image

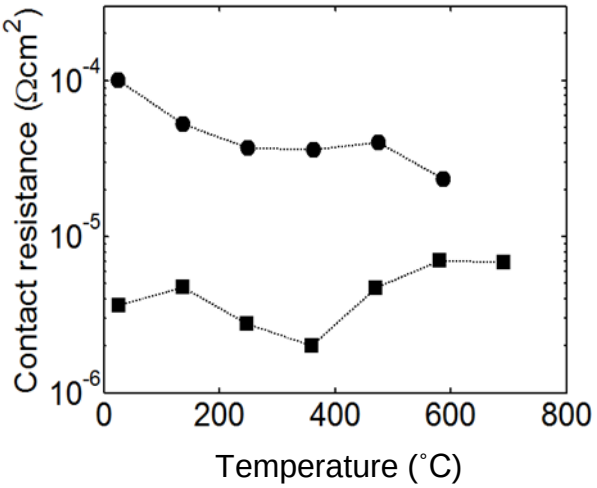

Figure 9-12: The nano MnSi/HMS (squares) and the nano α-$TiSi_2$/HMS (circles) contact resistance versus temperature.

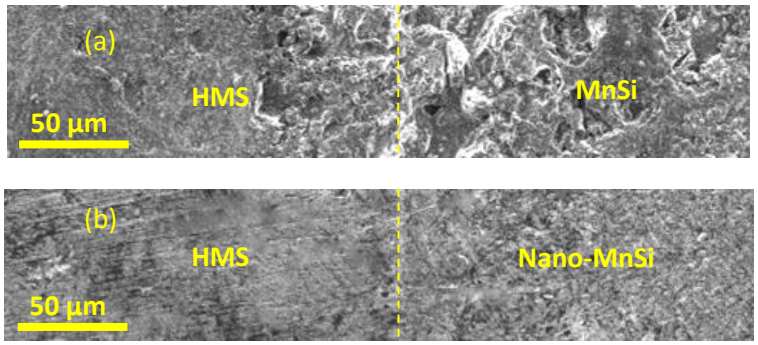

Figure 9-13: (a) The Scanning electron microscope (SEM) picture on (a) HMS/MnSi (b) HMS/nano-MnSi interface.

of the nano contact (Figure 9-13) has clearer border and is less porous contact interface than the large grain contact. The nano α-$TiSi_2$/HMS contact resistance is also shown in Figure 9-12 ranging from 10^{-4} to 10^{-5} Ωcm^2 for the temperature range of 20 °C to 700 °C. The contact resistance is again approximately an order of magnitude smaller at high temperatures than the previous results for an α-$TiSi_2$/HMS contact (Figure 9-11).

9.4. **Conclusions**

Different metals including Co, Ni, Cr, Ti, Mo, MnSi, and α-$TiSi_2$ were investigated as contacts for HMS thermoelectric devices. The elemental metals did not have proper mechanical and chemical stability. In contrast, α-$TiSi_2$ and MnSi can make practical electrical contacts for their low contact resistance, strong mechanical bonding, chemical stability as well as thermal stability.

Nano-grained MnSi and α-$TiSi_2$ contacts were further tested and showed improved contact conductance for the as pressed samples compared with their large grained ones. The long time stability of the nano-grained contacts at high temperature requires further study.

9.5. **References**

1 N. I. Erzin and N.V.Makov, Appl. Solar Energy 1,33 (1965).

2 K. Uemura, Y. Mori, T. Imai, I. Nishida, S. Horie, and M. Kawaguchi, in Proc. 8th ICTEC, Nancy, France ,151 (1989).

3 U. Stohrer, R. Voggesberger, G. Wagner, and U. Birkholz, Energy Convers. Mgmt. 30,143 (1990).

4 T. Nakajima, M.Suzuki, and J.Ohta, in Proc.16th IECEC 2013 (1981).

5 U. Stohrer, R. Voggesberger, G. Wagner, and U. Birkholz, in Proc. 8th ICTEC, Nancy, France,130 (1989).

6 CRC Handbook of Chemistry and Physics, 78th Edition, edited by DR Lide, CRC Press,BocaRaton, p 12-115 (1997).

7 D. B. Migas, V. L. Shaposhnikov, A. B. Filonov, and V. E. Borisenko, Phys. Rev. B, 77,075205 (2008).

Chapter 10 Enhancement of Thermoelectric Figure of Merit in n-type Silicon Germanium-Iron Silicide Composite Alloy

10.1. Introduction

The optimized composite structure is the other approach to enhance the power factor which was proposed in 1991 [1] and later [2] an effective-medium theory has been developed to calculate the power factor of a composite of two different thermoelectric materials. It was proved theoretically that the power factor of a composite of two materials can be increased in respect to that of each individual materials, but the maximum ZT of the composite cannot be enhanced to a higher value that that of each component materials. In these model calculations, the effect of crystallite boundary scattering was not included. Some experimental studied on different thermoelectric materials have shown power factor enhancement for other materials such as Si/ Si0.8Ge0.2 [3], InGaAs/ErAs [4,5], Bi/Cu [6], Bi/Ag [7].

The promising nanocomposite alloys with nanoparticle doping approach was introduced with model calculation specifically for silicide-SiGe composite alloys [8]. Few investigations have been accomplished experimentally. In our previous work, we studied $CrSi_2$ nano-inclusions embedded in $Si_{0.8}Ge_{0.2}$ [9,10].The enhancement of power factor in $Si_{0.8}Ge_{0.2}$-$CrSi_2$ structure was due the enhancement in charge carrier mobility. Here we investigated the composite structure of $Si_{0.8}Ge_{0.2}$ and $FeSi_2$. Both have shown high Seebeck coefficient.

Low temperature $FeSi_2$ possessing orthorhombic lattice structure is beta (β) phase which exhibits thermoelectric characteristics [11,12,13,14]. Due to its small energy gap, thermal stability and corrosion resistance β-$FeSi_2$ has been considered as a thermoelectric material for temperature range of 500-900 K [14]. The other considerations are low price and abundance of this compound which make it more interesting for large scale energy harvesting applications.

The main challenge to enhance the figure of merit of β-$FeSi_2$ is that the ratio of electrical conductivity to thermal conductivity (σ/k) of β-$FeSi_2$ is low comparing with other thermoelectric

materials. This ratio is about 2500 V-2K for a p-type β-FeSi2 alloy, while it is about > 60,000 V-2K for a Bi2Te3 structure [15]. The β-$FeSi_2$ has larger thermoelectric power factor than SiGe [15], and thermal conductivity of nanostructured SiGe is low, therefore a composite structure of SiGe and β-$FeSi_2$ may enhance the thermoelectric properties respect to those of individual structures.

Investigation on the n-type bulk nanostructured $Si_{0.88}Ge_{0.12}$-$FeSi_2$ is presented in this paper. The

Synthesized composite structures are formed by mechanical alloying and sintering procedures. A small percentage of silver has been used in composite structure to enhance electrical binding. In order to provide a comparison, a composite structure without silver was also synthesized with same growth parameters as for composite structures. The thermoelectric properties of all samples were studied and analyzed accurately. The results showed a significant enhancement in figure of merit in composite structures.

10.2. **Experimental Procedure**

$Si_{0.88}Ge_{0.12}$ and $FeSi_2$ powders were alloyed and nanostructured by high energy mechanical ball milling, separately. Stoichiometric ratio of Si (99% purity), and Ge (99.99%) with 2 at. % P (99.9% purity) as dopant element were weighted and loaded in a tungsten carbide bowl. The bowl was sealed inside an Ar filled glove box and milled in Fritsch-P7PL planetary ball mill. Similarly, $FeSi_2$ powder were prepared with stoichiometric ratio of Si (99% purity), Fe (99.99% purity) with 1.6 at. % Co as dopant element. Three different composite powders were prepared: $Si_{0.88}Ge_{0.12}$-5%$FeSi_2$, $Si_{0.88}Ge_{0.12}$-5%$FeSi_2$-2.5% Ag, and $Si_{0.88}Ge_{0.12}$-5%$FeSi_2$-5%Ag. All the powders were milled in Fritsch-P7PL planetary ball mill under Ar atmosphere at 1000 rpm for 50 hours.

The powders were loaded in graphite dies with an internal diameter of 12.7 mm and sintered at different sintering temperature, holding time and pressures. We have made 4 composite structures with different composition and sintering structures which are presented in Table 10.1.

Table 10.1 Sintering parameters of different structures

Sample ID	Material	Sintering Temperature (˚C)	Holding time (min)	Pressure (MPa)
1	$Si_{0.88}Ge_{0.12}$-5%$FeSi_2$	1170	0	138
2	$Si_{0.88}Ge_{0.12}$-5%$FeSi_2$-2.5% Ag	1050	0	138
3	$Si_{0.88}Ge_{0.12}$-5%$FeSi_2$-2.5%Ag	1000	15	138
4	$Si_{0.88}Ge_{0.12}$-5%$FeSi_2$-5%Ag	1000	15	138

The milled powders and sintered samples were characterized by x-ray diffraction (Bruker AXS D8-Discover). The structure of sintered samples was characterized by a Hitachi S-400 scanning electron microscope (SEM).

10.3. **Experimental Results and Discussions**

The XRD data of sample 3 is shown in Figure: **10-1**. The peaks for $Si_{0.88}Ge_{0.12}$, $FeSi_2$ and Ag are observed in the spectra. It is shown that there are no other phases or any contamination in the composite structure. The average crystallite size of this sample was calculated by commercial software (DiffractPlus EVA 14, Brucker-AXS) which uses a full pattern matching (FPM) of the XRD data based on empirical model for the peak shape and pseudo Vigot functions for the fitting the data. In these calculations, corrected Scherrer's formula for the instrument broadening was used to estimate the average crystallite sizes. The estimated crystallite size for the sample 4 was 31nm.

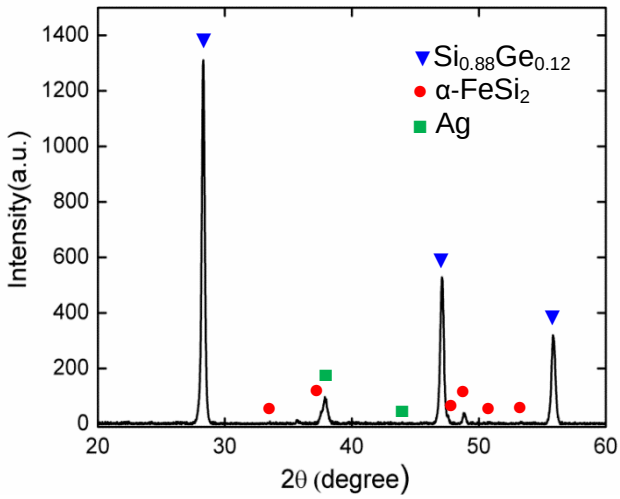

Figure: 10-1 XRD spectrum of the composite sample 4 (Si0.88Ge0.12-5%FeSi2-2.5%Ag)

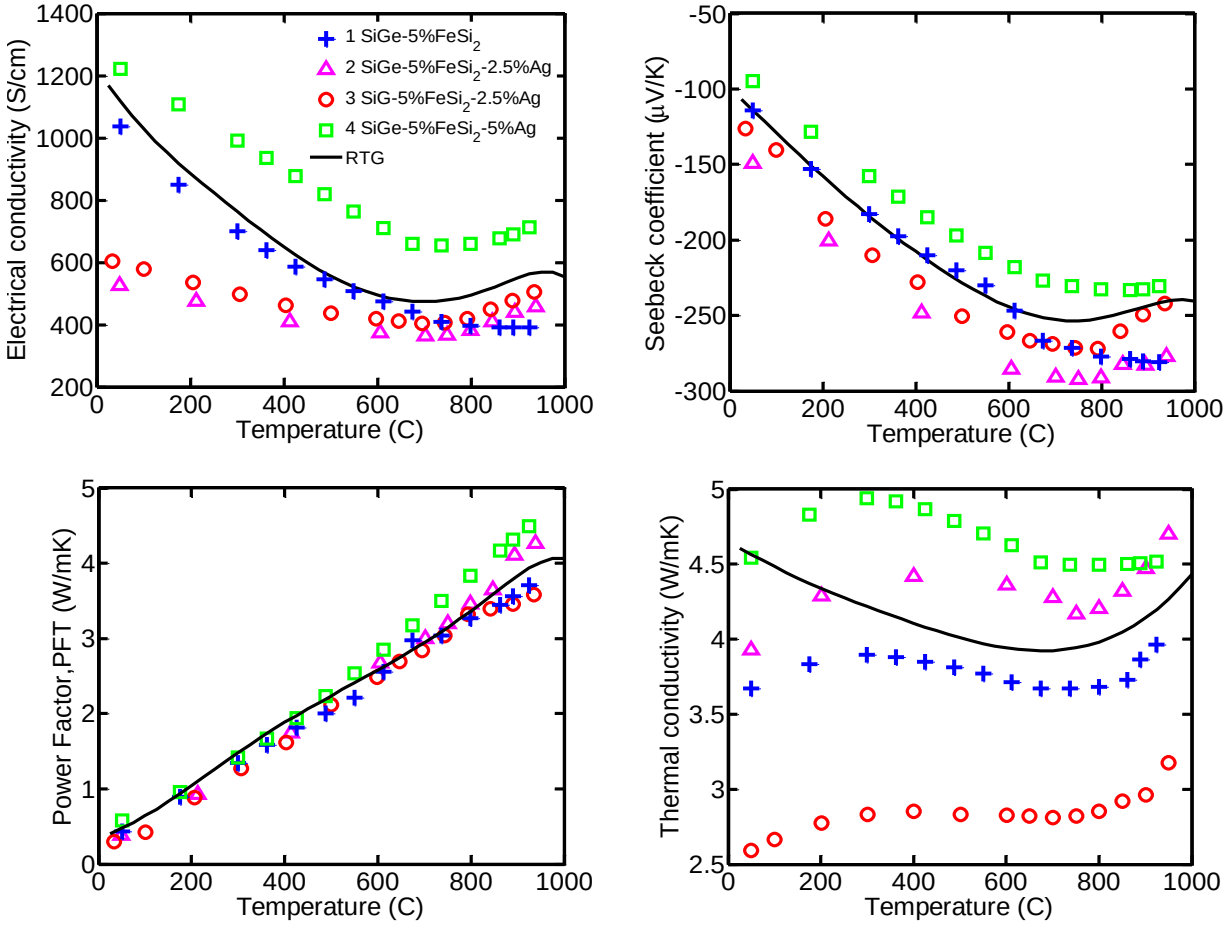

Figure 10-2: (a) Electrical conductivity, (b) Seebeck coefficient, (c) Power factor times temperature, (d) thermal conductivity of synthesized composites.

Figure 10-2 shows the (a) electrical conductivity, (b) Seebeck coefficient, (c) Power factor, and (d) thermal conductivity of all synthesized composite samples compared to those of crystalline SiGe used in RTG's as a function of temperature. Composite 4 has higher electrical conductivity at in whole temperature range. The 5% silver has been used in this sample structure which is the highest silver percentage.

Seebeck coefficient confirms that sample 4 has higher carrier concentration which is due to silver amount. Adding silver was supposed to provide better bonding of crystallites, because it has lower melting point (~ 900°C) respect to SiGe and $FeSi_2$. Hence at the sintering temperatures, Ag is melted and diffuses between grain boundaries and makes a better electrical contact.

The reduction of electrical conductivity in all samples with temperature is due to the decrease in carrier mobility originates from increasing electron-acoustic phonon scatterings with temperature. The small increase in electrical conductivity of all samples was observed at temperatures above 800°C which was resulted from increase in intrinsic carrier concentration.

Electrical conductivity and Seebeck coefficient of sample 1 and RTG sample are very close together. It is observed that although both samples have almost same electrical conductivity at low temperatures, in composite structure the intrinsic carrier effect at high temperatures was reduced.

Increasing trend of Seebeck coefficient with temperature shows increasing carrier concentration at higher temperature and a small decrease above 800°C indicating intrinsic minority carrier concentrations which has Seebeck coefficient with opposite sign of major carriers. The sample 2 has the higher Seebeck coefficient all over the temperature range which is due to lower carrier concentration at this sample.

At low temperatures up to 400 °C, the power factor times temperature (Figure 10-2-c) is almost the same for all composite structures, while it differs at high temperatures. The highest power factor is 4.5 W/mK belongs to sample 4. Other samples have almost identical power factor.

The thermal conductivity decreases with temperature due to the increase of phonon-phonon scattering with temperature. The increase of thermal conductivity at high temperatures above 800°C is the result of ambipolar thermal conductivity. A wide variation of thermal conductivity

is observed for different composite structures. Sample 4 has the highest and sample 3 has the lowest thermal conductivity among all samples over whole temperature range.

Composite structure without silver (sample 1) has lower thermal conductivity compared to that of RTG sample which is due to nanostructuring effect in composite sample. In addition, this sample was pressed with no holding time which reduced crystallite size growth and phonon scatterings are higher in this sample reducing the thermal conductivity. Sample 4 has higher thermal conductivity compared with that of RTG sample due to high concentration of silver. Sample 3 has lowest thermal conductivity. Although sample 4 was pressed at same sintering temperature as sample 3, it has higher thermal conductivity due to higher silver concentration. Therefore, it can be seen that only optimized silver amount can reduce thermal conductivity by providing lower sintering temperature.

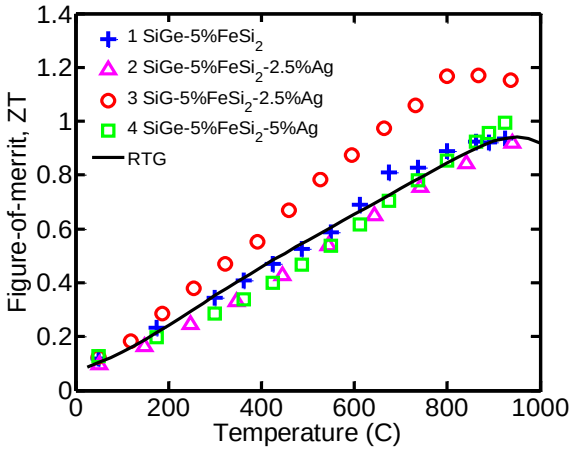

Figure 10-3 Figure of merit versus temperature for all synthesized composite structures.

The figure of merit of all synthesized samples is shown in Figure 10-3 as a function of time. Sample 1, 2, 4 have almost same figure of merit all over temperature range. The maximum figure of merit is ~1.2 belongs to sample 3 which is a good ZT compare to previously published papers on SiGe alloys.

10.4. **Conclusions**

N-type SiGe composites with 5% at $FeSi_2$ were synthesized and studied. The samples were synthesized by hot pressing of the milled powder. The samples were characterized by X-ray diffraction analysis. Thermoelectric properties of the synthesized structures were measured and compared with that of crystalline SiGe used in RTGs. In order to increase electrical conductivity, different amount of silver (0, 2.5% at, 5% at) were added to $Si_{0.88}Ge_{0.12}$-$FeSi_2$ composite alloy. Silver melted and filled the spaces between grains resulting lower sintering temperature. Sample with 5% silver showed the largest electrical conductivity and thermal conductivity; however, the figure of merit did not show any improvement. The 2.5% at silver was the optimum amount for silver as it maintained the electrical conductivity while thermal conductivity was reduced. Figure of merit of 1.2 at 950C was achieved which is about 20% enhancement compared to crystalline SiGe.

10.5. **References**

1 D. J. Bergman and O. Levy, J. Appl. Phys. 70, 6821 (1991).

2 D. J. Bergman and L. J. Fel, J. Appl. Phys. 85, 8205 (1999).

3 M. Zebarjadi, G. Joshi, G. Zhu, B. Yu, A. Minnich, Y. Lan, X.Wang, M. Dresselhaus, Z. Ren, and G. Chen, Nano Lett. 11(6), 2225–2230(2011).

4 J. M. O. Zide, D. Vashaee, G. Zeng, J. E. Bowers, A. Shakouri, and A. C.Gossard, Phys. Rev. B 74, 205335 (2006).

5 Je-Hyeong Bahk, Zhixi Bian, Mona Zebarjadi, Parthiban Santhanam, Rajeev Ram,and Ali Shakouri, Appl.Phys. Lett., 99, 072118 (2011).

6 Tsutomu Kanno, Satoshi Yotsuhashi, Akihairo Sakai, Kouhei Takahashi, and Hideaki Adachi, Appl.Phys.Lett., 94, 061917 (2009).

7 J. P. Hermans, and C.M. Jaworski, Appl.Phys. lett., 93, 122107 (2008).

8 N. Mingo, D. Hauser, N. P. Kobayashi, M. Plissonnier, and A. Shakouri, Nano Lett. 9(2), 711–715 (2009).

9 Zahra Zamanipour and Daryoosh Vashaee, J. Appl. Phys. 112, 093714 (2012).

10 Z. Zamanipour and D. Vashaee, Green Technologies Conference, IEEE, April 2012.

11 M. Ito and Y. Takiguchi, Materials Transactions, Vol. 46, No 7, (2005), pp. 1497-1501.

12 T. KOJIMA, , phys. stat. sol. (a) 111, 233 (1989).

13 U. Birkholz, E. Grop, and U. Stohrer, CRC Handbook of Thermoelectric, 1995.

14 A. Heinrich, H. Griessmann, G. Behr, K. Ivanenko, J. Schumann, H. Vinzelberg, Thin Solid Films 381,287-295(2001).

15 H.Y. Chen, X.B. Zhao, T.J. Zhu, Y.F. Lu, H.L. Ni, E. Mu¨ller, A. Mrotzek, Intermetallics 13,704–709 (2005) .

Chapter 11 Ultrafast pump-probe technique for thermal and electrical characterization of low-dimensional devices

11.1. Introduction

The development of high speed and small dimensional devices such as microelectronic, optoelectronic and microelectrochemical devices need understanding the ultrafast carrier dynamics and the limitations of the physical properties in semiconductor materials. As the dimensions of a system shrink, the mechanical, electrical and thermal properties of the system are not obey their bulk complements definitions [1]. The fundamental studies require understanding the fast microscopic processes which happen on a picosecond or even femtosecond time scale in low dimensional devices. The process such as momentum and energy relaxation and mechanisms such as carrier-carrier scattering, intervalley and intravalley scattering, optical phonon scattering, and carrier diffusion have been investigated theoretically and experimentally to understand the nanoscale physical properties of such low dimensional devices[2].

The thermal management is a serious concern for advanced nanoscale devices [3]. In some cases such as computer processors [4] and semiconductor lasers [5], generated heat must be taken away from system in an efficient way, so these systems need high thermal conductivity. In some other cases, such as thermoelectric materials used for solid state cooling systems, low thermal conductivity is needed. On the other side macroscopic heat transfer laws may not valid in macro/nano scale dimensions and challenges arise in thermal properties measurement of such systems such as temperature, thermal conductivity, and thermal conductance between material layers.

To explain the significance of understanding detailed thermal properties in low dimensions, the thermal properties in thermoelectric material is considered. As it is mentioned in previous

chapters, in order to enhance the conversion efficiency of thermoelectric devices, thermal conductivity of such devices must be reduced. The performance of a thermoelectric material is based on figure of merit $ZT=S^2\sigma T/\kappa$, where S, σ, T, and κ are the Seebeck coefficient, electrical conductivity, temperature, and thermal conductivity[6]. One of the major approaches to enhance the figure of merit of TE materials is thermal conductivity reduction. It is shown that the nanostructured materials can have much lower thermal conductivity due to reduction in lattice thermal conductivity by increasing the interface density [7,8,9,10,11].Therefore understanding the heat transfer phenomena at nano-scale dimensions is vital to develop and improve the performance of thermoelectric devices. The other important parameter of interest is the interface thermal conductance which degrades the performance of materials such as polycrystalline diamond, semiconductor superlattices, multilayer thin films, and nanostructured composites [12,13].

Availability of ultrafast lasers led to develop the photoexcitation techniques which are essential methods for investigations of the ultrafast processes in low dimensional devices. The most common method is pump-probe technique [2,14,15]. The short pulse duration of the laser pulses provides high temporal resolution tracking of the dynamical process. Probing the processes in femtoseconds to nanoseconds time scale is possible by this technique. Pump-probe technique was used to understand carrier dynamics [16,17], non-equilibrium phonon generation by hot carriers [18,19,20], and electron-phonon couplings[21,23]. In addition, pump-probe technique was used for thermal transport probing by Paddock's group [14] for the first time. Their experiments was continued and developed by Maris et al [15,22], Norris et al [23], Cahill [12,24], and Schmidt [25,26,27]. Figure 11-1 shows the schematic diagram of pump probe technique. In this technique, a laser pulse (pump pulse) is used to excite the material. This excitation makes some changes in optical properties of the material such as reflectivity, absorptivity or transitivity. The second laser beam (probe beam) measures the changes of the variation in optical properties in the exposure sample. The probe light can be delayed respect to pump beam by variation of optical path, so that the probe beam can measure the processes dynamically during their progress. The probe beam is much weaker than pump pulses to minimize its effect on the sample. When the probe measures the time dependent reflectivity of the sample, the technique is called Transient Thermoreflectance (TTR) and monitoring the absorption changes of the sample is called Transient Absorption (TA).

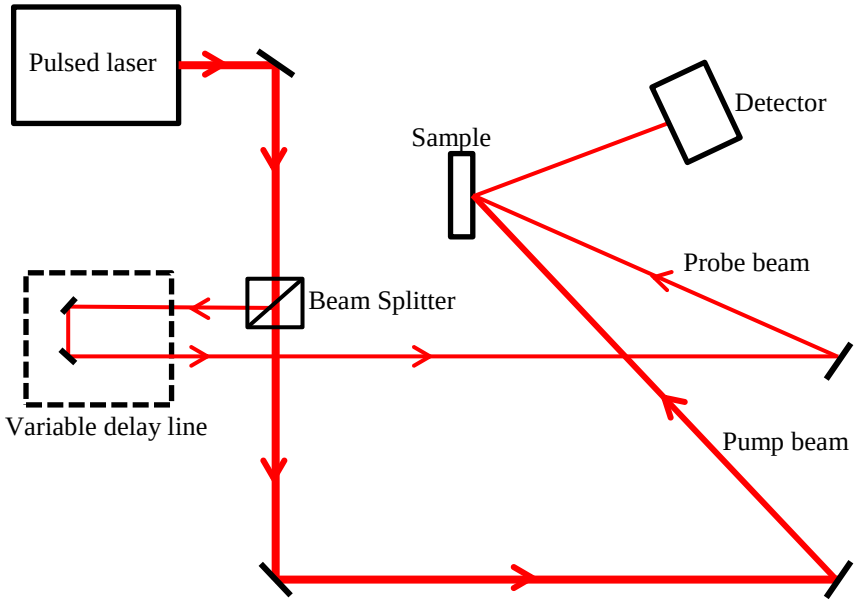

Figure 11-1 Schematic diagram of pump- probe technique

In this part of the research program, a new pump-probe design developed for two purposes: first, measurement of thermal properties of thin films and nanowires. In addition, existing theory of thermal transport modeling in pump-probe method for cross plane and in plane thermal conductivity measurements has been extended to measure the thermal conductivity in three directions which can be applied for anisotropic materials such as nanowires. The isothermal boundary solution is derived as well. Second, using the multi-purpose optical design enables studying the dynamical processes of hot carriers relaxation, phonon generation and relaxation, and carrier-phonon couplings in different semiconductors.

11.2. Thermal transport in ultrashort laser exposure

In pump-probe method, the samples are coated with a thin layer of metal (Figure 11-2). This metal layer absorbs the laser beam and converts it into thermal energy. The other role of the metal layer is that it acts as a temperature sensor. The temperature change on sample is monitored from the temperature dependent reflectivity of metal layer. The typical thickness of metal layer is 70-100 nm.

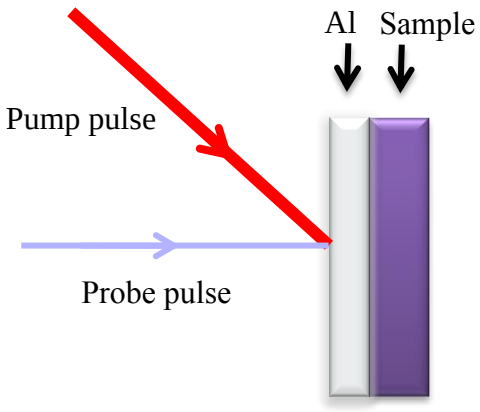

Figure 11-2 Thin metal layer (70-100nm) coated on sample acts as a heater and temperature sensor

The interaction of ultrashort laser pulses with submicron metal film cannot be explained by the classical diffusion model which was developed first by Fourier [28]. Thin films are typical examples of nanostructured materials and their thermal transport is a complex phenomenon that must be considered as nanoscale process with a more detailed expression of individual heat carriers.

When the laser pulses are exposed to the sample, photons are absorbed by metal film. Laser beam thermalizes free electrons in metal layer via electron-electron scattering and generates nonequilibrium hot electrons. The electrons relax to equilibrium with the lattice by the emission of phonons (electron-phonon scattering). Since the pulse duration is short compared to electron-phonon energy transfer time, there exists a temperature difference between nonequilibrium electrons and phonons [29,30]. It is proven that the ballistic motion contributes to heat transport in fs time scale [31].The heat transport velocity is in the order of Fermi velocity which is about 10^6 m/s. The other process which must be considered is the collisions between hot electrons and electrons around Fermi level. The hot electrons diffuse into deeper parts of the metal. The diffusion length depends on electron-phonon interaction which reduces the electrons temperature. Electron mean free path commonly is in 50-100nm range [32], the ballistic electrons will be distributed uniformly through metal layer in 100-200 fs time range, and within 500fs electron population can be described by a well-defined electron temperature [29,31]. The electron temperature can be 2-3 orders of magnitude higher than that of the lattice reaching

several thousand degrees Kelvin above the equilibrium. This is due to the smaller electron heat capacity to that of the lattice.

The thermal transport process can be described by the two-temperature model (TTM) [33]. Depending on the excitation energy above Fermi level, thermal equilibrium of hot electrons takes several hundred femtoseconds. As it is mentioned, there is a temperature difference between electrons and lattice. Therefore the physical situation can be described by two different temperatures: electron temperature, T_e, and lattice temperature, T_l. Time dependent thermal relaxation and sample depth are modeled by two coupled diffusion equations, one describing the thermal conduction of the electrons and the other one explaining the thermal conduction of the lattice. The equations are connected by a parameter called the electron-phonon coupling constant, G. This parameter indicates the transfer energy between two systems. TTM equations proposed by Anisimov et al and it is described in different papers such as in [29,33]. The equilibrium time between two populations was estimated by TTM model is about 1-100ps which was verified by reported experimental data [34,35].

The diffusion of the phonons across the interface is very slow compared to the thermal transport within the thin metal film. Using this fact, Capinski et al [22] estimates the time constant for the temperature to become uniform inside the film. The time constant can be calculated for this process in an insulated metal film as: $\approx \frac{d^2}{\pi^2 D}$, where d is the thickness of the film and D is the thermal diffusivity of the film. For 100nm thick Al film, D= 0.45 $cm^2\ s^{-1}$, τ is 23ps at 300K.

11.3. **Thermoreflectance Coefficient**

The reflectivity of metal film varies with temperature through thermoreflectance coefficient. The change of the reflection coefficient for each degree of surface temperature change is called thermoreflectance coefficient, $(\Delta R/R)K^{-1}$. This coefficient depends on electronic structure of material and photon energy. The typical value of thermoreflectance for common metals such as Al, Au, Cu, Ta, Pt is on the order of 10^{-4}-10^{-5} K^{-1}[36,37,38,39]. Figure 11-3 shows the thermoreflectance spectra of Al, Pt and Ta. The absorbance coefficient of these metals is shown in Figure 11-4. Aluminum has high thermoreflectance coefficient among metals with a peak around 800 nm. And it is the common metal used in pump probe technique when the probe beam

peak is at 800nm. In our system, the central wavelength of pump beam is 800nm and for the probe beam is 400nm. It should be noticed that in the systems which have different pump and probe

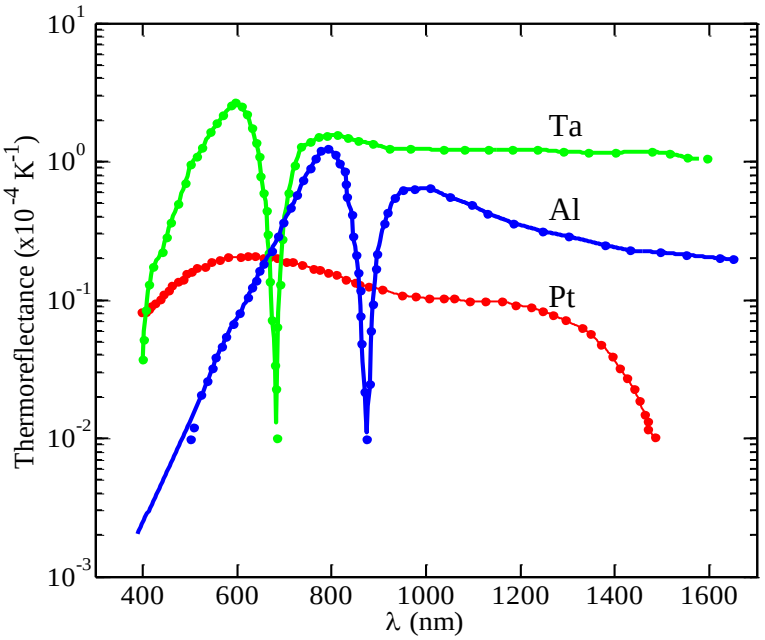

Figure 11-3 Thermoreflectance spectrum for Al, Pt, and Ta at room temperature [39].

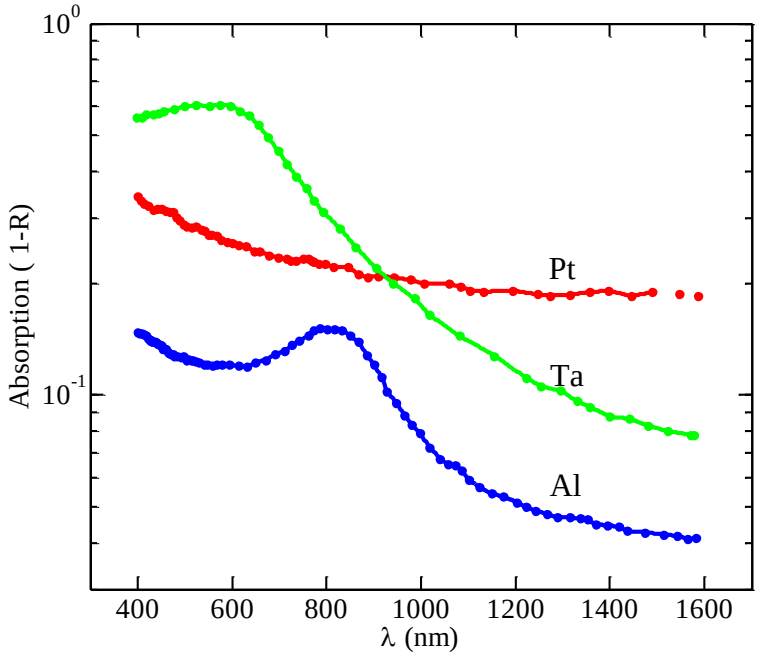

Figure 11-4 Absorption coefficients for Al, Pt, and Ta at room temperature [39].

wavelengths such as our system, instead of thermoreflectance coefficient, the maximum changes in reflectivity must be considered to select the proper metal coating, because the maximum changes in reflectivity is desirable for output signal of the system.

The maximum changes in reflectivity depend on the thermoreflectance coefficient of the metal layer as well as the absorption of the pump beam by the metal layer. In order to consider the maximum changes in reflectivity, we define a parameter as figure of merit which is estimated by the absorbed energy at pump wavelength times thermoreflectance coefficient at probe wavelength (= $(1-R_{pump})*(\Delta R/R)_{probe}$). In our system, for example, figure of merit is calculated by the absorbed energy at 800nm times thermoreflectance coefficient at 400nm, $(1-R_{800nm})*(\Delta R/R)_{400nm}$. According to the thermoreflectance coefficient and absorption data in Figure 11-3 and Figure 11-4, the figure of merit for Al, Pt and Ta were calculated to be $3*10^{-3}$, $1.8*10^{-2}$, and $3*10^{-2}$ respectively. Therefore for our experimental set up, we can have maximum detectable changes in reflectivity and more accurate data when we coat the samples with Ta.

11.4. Thermal Conductance

The absorbed energy is transferred from metal coating to the substrate by Phonon-phonon scatterings. If the sample is electronically conductive, the other possible mechanism in heat transport is electron-electron collisions. The extensive studies of both cases have been accomplished in previous reports [40,41,42].

The thermal transport across the interface is modeled with a parameter which is called thermal interface conductance, G. When the heat flux across the interface is f and temperature difference across the interface is $\Delta\theta$, then G, thermal conductance is given by $G=f/\Delta\theta$. There is no general approved modeling to calculate thermal conductance in nanoscale range. One of the difficulties is that a single temperature definition is not valid for different groups of phonons. At the interface, the energy spectrum of local phonons is different from that of arriving phonons. The measured value of equilibrium temperature is a local energy density and cannot show only the incoming phonons energy at interface. On the other side, the equilibrium temperature which can be measured experimentally is a measure of the local energy density and does not reveal the energy of only the phonons arriving to the interface. Therefore temperature in thermal transport

modeling must be explained with more attention. The other parameters such as bulk disorder, imperfections in physical contact between the two materials have also considerable influence.

Thermal conductance between different materials has been measured with pump-probe technique by Cahill et al [12,39,43] and Capinski et al [26,27]. Typical thermal conductance is in the order of 30 MW/m^2K for two dissimilar materials and 400 MW/m^2K for metal-metal interfaces.

11.5. Thermal Transport in Substrate

Phonon-phonon collisions and also electron-electron collisions in case of electronically conductive materials are the main thermal transport mechanisms in the substrate. Since the traditional Boltzman equation cannot explain these phenomena in nanoscale range, other theoretical approaches are developed which were described in details by Cahill [3]. Phonon wavelengths distributed from atomic dimensions to the size of the sample, but most of the heat is transferred by the phonons with wavelength of a few nanometers. The relaxation time of the phonons in crystalline solids such as silicon are in the order of 100ps [44].

In this work, the metal films will thermalize within a few tens of picoseconds, and phonon diffusion in a crystalline substrate would take about 100 ps. Hence, the equations used in the following sections for thermal transport modeling are valid in the time scale more than ~100ps.

11.6. References

1 Gang Chen, "Nanoscale Energy Transport and Conversion", Oxford University Press, New York, 2005.

2 Andreas Othonos, Journal of applied physics, vol. 83, no. 4, 1998.

3 David G. Cahill, Wayne K. Ford, Kenneth E. Goodson, Gerald D. Mahan, Arunava Majumdar, Humphrey J. Maris, Roberto Merlin, and Simon R. Phillpot, Journal of Applied Physics, 93(2):793-818, 2003.

4 David G. Cahill, Kenneth Goodson, and Arunava Majumdar, , Journal of Heat Transfer, 124(2):223-241, 2002.

5 Gang Chen, Annual Review of Heat Transfer, 7:69, 1996.

6 D.M Rowe, Thermoelectrics Handbook: Macro to Nano, CRC press, Boca Raton, FL, 2006.

7 M.S.Dresselhaus, G. Chen, M.Y. Tang, R. Yang, H. Lee, D. Wang, Z. Ren, J. fleurial, P. Gogna, Advanced Materials, vol. 19, pp.1043-1053, 2007.

8 G. Chen, Phys. Rev. B, 57(23):14958{14973, Jun 1998.

9 X. B. Zhao, S. H. Yang, Y. Q. Cao, J. L. Mi, Q. Zhang, T. J. Zhu, J. Electron. Mater. , 2009, 38, 1017.

10 R. Venkatasubramanian, E. Siivola, T. Colpitts, B. O'Quinn, Nature2001, 413, 597.

11 Q. Zhang, J. He, X. B. Zhao, S. N. Zhang, T. J. Zhu, H. Yin, T. M. Tritt, J. Phys. D: Appl. Phys.2008, 41, 185103.

12 Ruxandra M. Costescu, Marcel A. Wall, and David G. Cahill, Phys. Rev. B 67, 054302 (2003).

13 R. M. Costescu, D. G. Cahill, F. H. Fabreguette, Z. A. Sechrist, S. M. George, Science, vol. 303, 2004.

14 C. A. Paddock and G. L. Eesley, J. Appl. Phys. 60, 285, 1986.

15 W. S. Capinski and H. J. Maris, Rev. Sci. Instrum. 67, 2720, 1996

16 H. M. van Driel, Phys. Rev. B 19, 5928 ~1979.

17 W. Potz and P. Kocevar, Phys. Rev. B 28, 7040 ~1983.

18 D. von der Linde, J. Kuhl, and H. Klingenberg, Phys. Rev. Lett. 44, 1505,1980.

19 J. C. Tsang, J. A. Kash, and S. S. Jha, Physica B & C 134B, 184,1985.

20 J. A. Kash, J. C. Tsang, and J. M. Hvam, Phys. Rev. Lett. 54, 2151,1985.

21 T. Q. Qiu and C. L. Tien. Short-pulse laser heating on metals, International Journal of Heat and MassTransfer, 35(3):719-726, 1992.

22 W. S. Capinski, H. J. Maris, T. Ruf, M. Cardona, K. Ploog, and D. S. Katzer, Phys. Rev. B, 59(12):8105-8113, 1999.

23 Pamela M. Norris, Andrew P. Ca_rey, Robert J. Stevens, J. Michael Klopf, Jr. James T. McLeskey, and Andrew N. Smith.. volume 74, pages 400-406,AIP, 2003.

24 David G. Cahill, Review of Scienti_c Instruments, 75(12):5119-5122, 2004.

25 Aaron J. Schmidt, Xiaoyuan Chen, and Gang Chen, Rev. Sci. Instrum. 79, 114902 (2008)

26 Aaron Schmidt, Matteo Chiesa, Xiaoyuan Chen, and Gang Chen, Rev. Sci. Instrum. 79, 064902 (2008).

27 Aaron J. Schmidt, Ramez Cheaito, and Matteo Chiesa, Rev. Sci. Instrum. 80, 094901 (2009).

28 Jean Baptiste, Joseph Fourier, The University Press, Cambridge, UK, 1878.

29 R. W. Schoenlein, W. Z. Lin, J. G. Fujimoto, and G. L. Eesley, Phys. Rev. Lett., 58(16):1680-1683, Apr 1987.

30 Rafal Jasiak, Ultrafast electron dynamics and decoherence in metallic nanostructures, University of Strasbourg, 2011.

31 S. D. Brorson, J. G. Fujimoto, and E. P. Ippen, Phys. Rev. Lett., 59(17):1962-1965, Oct 1987.

32 N.W. Ashcroft and D. Mermin. Solid State Physics, Holt Rhinehart, New York,1976.

33 J. Hohlfeld, S.S. Wellershoff, J. Gdde, U. Conrad, V. Jhnke, E. Matthias, Chemical Physics, 251, 237–258, 2000.

34 J. G. Fujimoto, J. M. Liu, E. P. Ippen, and N. Bloembergen, Phys. Rev. Lett., 53(19):1837-1840, Nov 1984.

35 H. E. Elsayed-Ali, T. B. Norris, M. A. Pessot, and G. A. Mourou, Phys. Rev. Lett., 58(12):1212-1215, Mar 1987.

36 W. J. Scouler, Physical Review Letters, vol.18, no.12, 1967.

37 R. Rosei and D. W. Lynch, Phys.Rev. B, 5(10):3883-3894, May 1972.

38 M.G. Burzo, P.L. Komarov, and P.E. Raad, Components and Packaging Technologies, IEEE Transactions on Components, Packaging and Manufacturing Technology, 28(1):39{44, March 2005.

39 R. B. Wilson, Brent A. Apgar, Lane W. Martin, and David G. Cahill, Vol. 20, No. 27 / OPTICS EXPRESS 28830, 2012.

40 E. T. Swartz and R. O. Pohl, Rev. Mod. Phys., 61(3):605{668, Jul 1989.

41 Gang Chen, Oxford University Press, New York, pp. 180-185, 2005.

42 Ronggui Yang, Gang Chen, Marine Laroche, Yuan Taur, J. Heat Transfer 127(3):298-306 (2005).

43 Bryan C. Gundrum, David G. Cahill, and Robert S. Averback, Physical Review B (Condensed Matter and Materials Physics), 72(24):245426, 2005.

44 A. Henry and G. Chen, Journal of Computational and Theoretical Nanoscience, 5(12): 141-152, 2008.

Chapter 12 A new Experimental set up for pump-probe technique

12.1. Introduction

The pump and probe system has been developed during the years of employing this optical method for thermal transport measurements. Paddock and Eesley [1] fabricated the pump-probe system in 1986. Their system utilized two synchronously pumped dye lasers to pump and probe the sample at 633nm and 595nm, respectively. The laser repetition rat was 246 MHz with pulse with of 6 ps. The next system built by Capinski and Maris [2] had several enhancement. They used a single dye laser with wavelength of 632nm, repetition rate of 76 MHz and shorter pulse width of 0.2ps. The other improvement was that they used an optical fiber after delay stage to transfer the probe beam which minimized the errors from probe beam misalignment and divergence of the beam along the delay stage. This set up enabled study of thermal diffusion and acoustic phenomena. Cahill and his group [3,4] and later Schmidt [5] built an improved system utilizing a Ti: sapphire laser for pump and probe beams with a central wavelength of 790nm, 150fs pulse width and repetition rate of 80 MHz. High repetition rate provides higher signal to noise ratio because of two reasons. First is that high repetition rate enables to modulate the pump beam at high frequency which reduces 1/f noise and second one is that shot-to-shot noise is averaged. Therefore, small temperature changes can be detected in such systems. Their delay line was 2.1 m optical path difference providing 7ns delay time. An integrated CCD camera has been for viewing the sample and beam spots, and inductive resonators in series with the photodiode detector has been used to enhance signal to noise ratio by a factor of 10 or more [3,6,7]. The other features of Schmidt [5] system were: they used second harmonic generator to obtain frequency-doubled pump beam which reduces considerably the optical noise and also allowed them to use a simplified coaxial geometry where pump and probe beams were focused on the

sample. In addition, they have used an expanded probe beam which reduces divergence over the delay stage length.

Our designed and implemented pump-probe system utilizes an ultrafast Ti: sapphire laser with central wavelength of 790nm, pulse width of ~10fs. This Ti: sapphire laser has two outputs with different repetition rates: main output with 80MHz and dumped output with 2 MHz. In this chapter detailed description of the fabricated system is explained. Our system is designed with improved features respect to previous pump-probe systems. One of the essential improvements is providing longer delay time. Our delay line has 8m optical path equivalents to 24 ns delay time. Longer delay time enables measuring the very low thermal conductivity systems as well as providing higher resolution of delay time steps. The system designed to provide ultrashort pulse width. During beam pass across the optical system, the pulse width of the beam will be expanded due to group velocity dispersion when the beam passes through optical components with glass medium. Therefore, at the sample position, the pulse width is more than ~10fs. In order to avoid pulse width broadening, optical components with minimum thickness were used. In addition, we have used reflective lenses with curved mirrors combination instead of ordinary glass lenses. Moreover, using prism pair compensator which is be explained in more detail later in this chapter compensates the pulse width broadening and produces short pulse width as ~10fs. The ultrashort pulse is necessary to study the electron-phonon interactions.

In this chapter, our new optical design is presented. This novel set up is designed such that the pulse width has minimum expansion along the whole optical path. Other than pulse width expansion, we considered different issues such as power loss, laser spot size and shape, and probe polarization. In each step of design change, we avoid some of the errors. The detailed optical system and components are explained here, and then instrumentation details and measurement system are described.

12.2. Optical set up

Figure 12-1 shows the schematic diagram of our initial design for pump-probe set up. This system uses a Ti:sapphire laser (Cascade-5 KMLabs Inc.) which emits pulses of 8-100 fs with repetition rate of 80MHz.The optimum average power in mode locked mode is 300mW provides

~3.7nJ/pulse. The dumped beam output of this laser provides lower repetition rate of 2MHz gives average power of 80-100mW and ~30nJ/pulse. The central wavelength is around 790nm with optimum bandwidth of 100-110nm. The laser beam special distribution is near TEM_{00} with divergence of < 1.0 mrad and horizontal polarization. The wavelength spectrum of the laser and its Fourier transform are shown in Figure 12-2 .

The spectrum was obtained from spectrometer provided inside the laser enclosure. The Fourier transform gives a rough estimation of the pulse width. The accurate pulse width measurement requires advanced techniques such as interferometric autocorrelation or frequency–resolved optical grating [8,9,10]. For thermal conductivity measurement, it is not necessary to have an accurate pulse width, but for the second phase of this project, ultrafast carrier dynamics studies, pulse width will be measured by interferometric autocorrelation method by an autocorrelator from Femtochrome Research Inc.

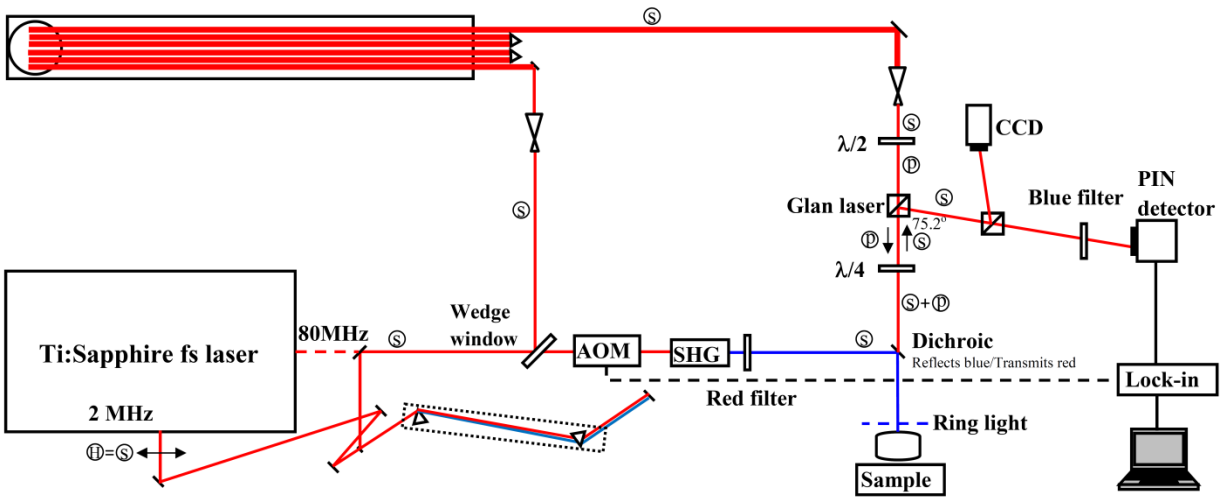

Figure 12-1 Schematic diagram of the initial design of pump-probe system

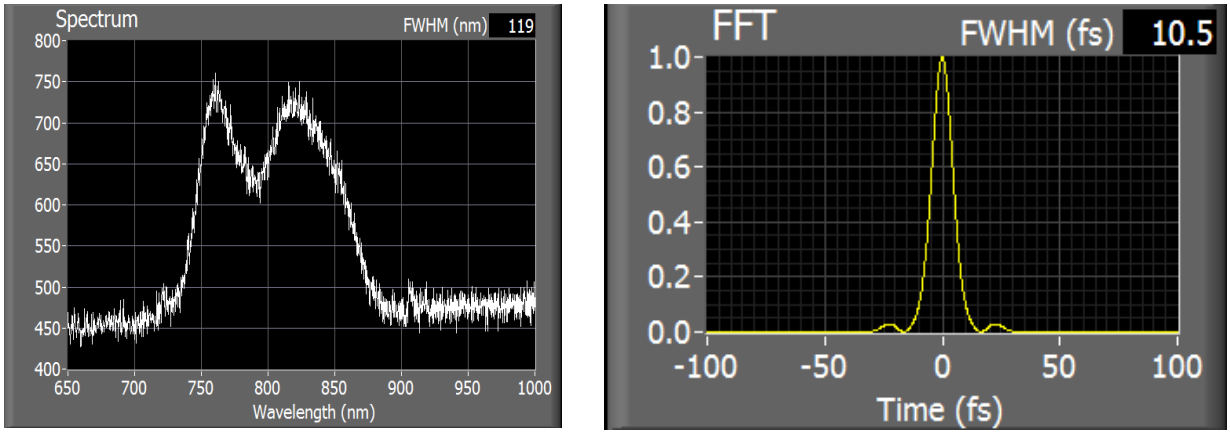

Figure 12-2 Laser beam spectrum and its Fourier transform. The band width is ~110-120nm and pulse duration is about 10fs.

In the first design, the 80MHz beam output goes directly to the wedge window. Only the dumped beam output (2MHz) passes through the prism pair compensator. Before continue the design explanation, the alignment procedure of prism pair compensator is described in detail.

As it is shown in Figure 12-1, the prism pair compensator consists of two prisms and two mirrors. The beam hits near the tip of the first prism in the upper 1/3 of the prism. The first prism is rotated to the minimum deviation angle. In this angle the reflection loss is minimized. When the prism is rotated in a direction, the beam moves in the same direction until the minimum deviation is reached. At this point the beam reverses directions. The beam should pass near the tip of the 2nd prism without being clipped. The second prism also is rotated to the minimum deviation position. A mirror is replaced after the second mirror to reflect the beam back toward the prisms. The reflected beam is aligned to be lower than the input beam. After the reflected beam passes through the 1st prism, it is reflected from peak off mirror positioned below the input beam. The 2nd prism and mirror are in a movable stage (Figure 12-3) so that the distance between two prisms is adjustable to get the maximum compensation.

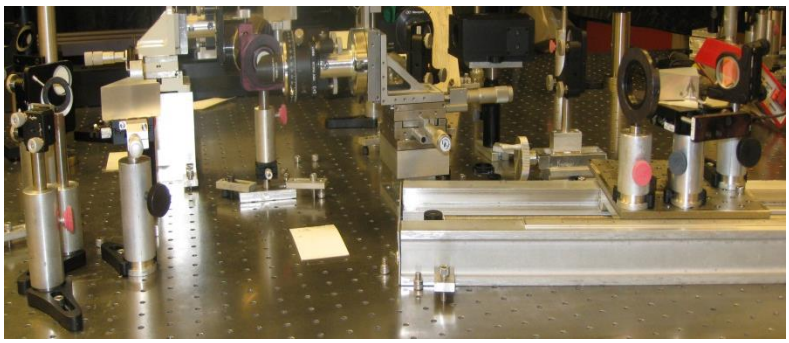

Figure 12-3 Prism pair compensator set up. The second prism and mirror are in a movable stage.

The compensated beam was directed to the main beam position using a movable 45° AOI mirror. The main beam or the dumped beam divided into two parts by a wedge window. In order to avoid the effect of the surface reflections on the transmitted beam, the wedge window (with wedge angle of 2°) is used instead of flat window. The wedge window with the 45°angle of incidence (AOI) reflects 10% of the beam which was allocated for the probe beam. The thickness of the wedge window is minimum available thickness of 3mm to avoid pulse width broadening. The wedge window has antireflection coating to eliminate any reflection from the second surface of the window and minimize the power loss.

The pump beam must not reach to the detector. One of the approaches is that the pump and probe beams are send onto the sample at different angles so that the reflected pump and probe beam can be separated spatially [11,15,23]. The other method is using a beam block and polarization to separate the pump beam reflection [3]. But these methods are suspicious to have a reflection of pump beam into the detector due to scattering into different angles and polarizations because of the roughness of the sample. Also precise overlap of the two beams is very difficult using different angles to focus the beams onto the sample. Therefore, in these approaches the pump beam reflection is not completely avoidable to reach the detector.

In our system, we adapted to Schmidt system [5] which utilized a second harmonic generator (SHG) and a co-axial geometry to have precise pump and probe beam overlap and avoid any optical noise from the pump beam in the detected signal. The pump beam is directed onto the SHG crystal to change the wavelength of the pump beam to second harmonic wavelength. Here we have used a bismuth triborate (BiB3O6-BIBO) crystal (8*8*0.09 mm^3). The thickness is

considered to be minimized to avoid pulse width broadening but the conversion efficiency from 800nm to 400nm in the system becomes as low as 1%. Therefore most of the pump power lost in the conversion.

In order to avoid the huge loss of pump beam after SHG, we changed the design. In the second design which is shown in Figure 12-4 schematically, there are two fundamental changes. First, both main beam and dumped beam passed through the prism pair compensator. In this way the pulse width of the main beam also can be compensated to desired ultrashort fs pulses. The main beam and dumped beam is designed to be exchanged using a movable mirror. Second, beam passes through the SHG before separating the pump and probe beams. This minimizes the power loss due to SHG. The beam passes through second harmonic generator, so that output has both second harmonic beam with the center frequency of 400nm and also the incident beam as loss power. Therefore, after SHG, both beam separated and the main beam (800nm) is used as pump beam and the second harmonic beam as probe beam. In this way, instead of having a power loss from SHG, we have used this loss as pump beam. The beams are separated by a dichroic mirror (cold mirror) in 45° AOI which reflects the 400nm and transmits the 800nm beam.

In order to focus the beam onto the SHG crystal and collimate the output beam, two 90°off axis parabolic (OAP) mirrors with following characteristics:

1- OAP1: Parent Focal length (PFL) of 25.4 mm, Effective Focal Length (EFL) of 50.8 mm
2- OAP2: PFL of 59.7 mm, RFL of 119.4 mm

Using mirror instead of lens has this advantage that we could avoid the pulse width broadening. The output beam spot is so sensitive to the beam alignment. Therefore, the xyz stage and rotating holders are used for the off axis parabolic mirrors alignment. The output beam diameter can be varied by changing the distance of the second off axis parabolic mirror from the crystal.

The magnification of output beam from the collimating OAP is 2.4 (= 12/5). It means that the separated probe beam is already expanded to maximum reasonable size and beam spot will have minimum divergence when it travels through the delay line. A blue filter is used to eliminate any 800nm light from the probe beam and a red filter is used to eliminate 400nm beam from pump beam.

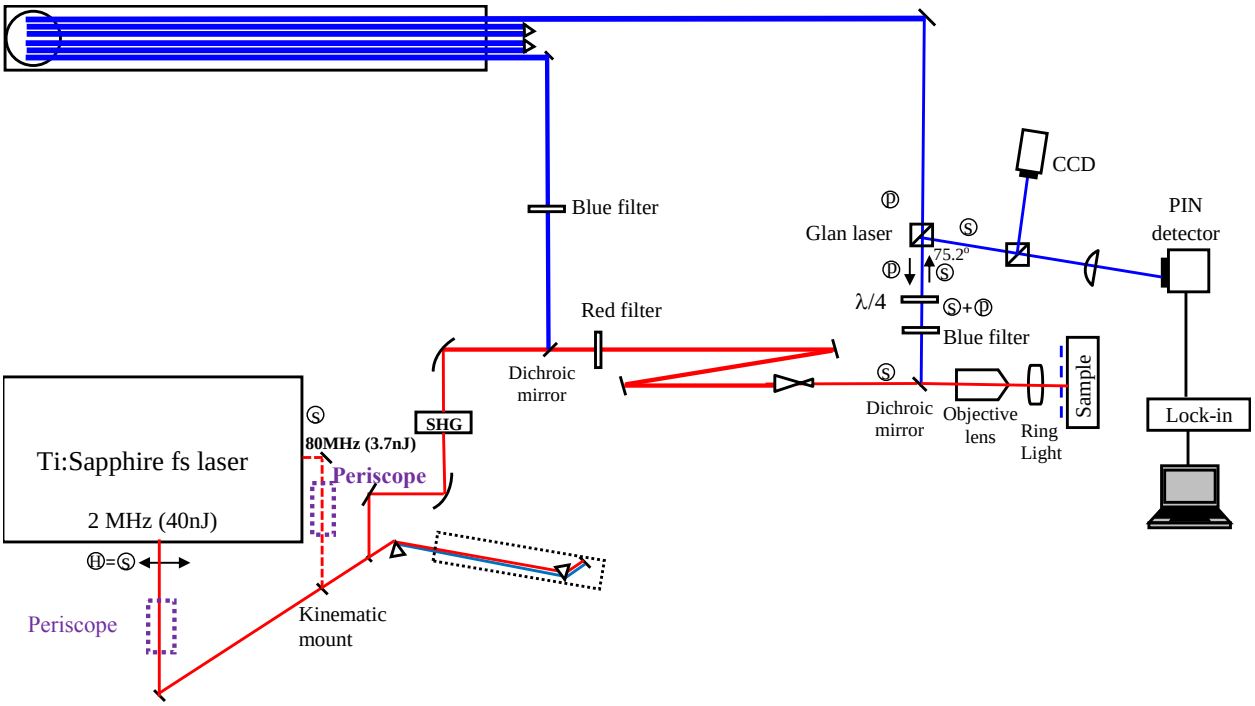

Figure 12-4 Schematic diagram of the second optical design. Pump and probe beam are separated after second harmonic generation with minimum power loss.

In our system, the probe beam passes through the delay line. The delay line is designed to generate 8m optical path difference which corresponds to 24 ns delay time. The delay line, as it is shown in Figure 12-5, consists of a delay stage with 1.2m length (Newport linear stage IMS1200LM-SA), cube corner mirror (retroreflector) and 2 pairs of 90° mirrors with two solid posts angled 60° vertically. The sketch of the delay line and real set up are shown in Figure 12-6. The post with 60 degree angle is made to transfer the beam vertically and also 90 degree angle between each pairs of mirrors is adjusted to reflect the beam back to the cube corner. The posts are designed and machined precisely. The 6-pass beam alignment between cube corner mirrors and 2 external pairs of mirrors is very difficult and needs time and effort. The incoming beam must be aligned such that the position of the output beam does not change during the delay stage movement. In order to make this happen, alignment of beam through each pass must be done precisely. The beam alignment on each mirror and the reflections were aligned when the stage was in front of the stage and end of the stage. This procedure is done step by step for each mirror

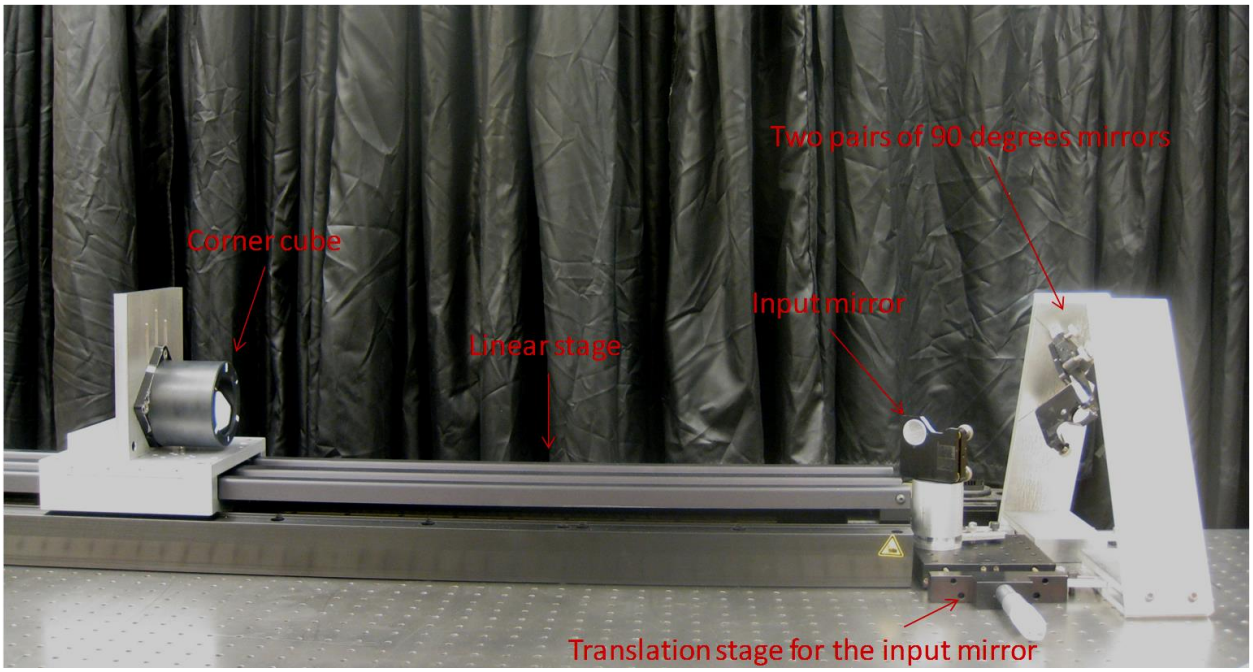

Figure 12-5 Delay line structure. Our 6-pass delay line provides 24ns delay time between pump and probe beam.

and the position and angle of the beam is corrected by moving the cube cornet back and forth in the stage repeatedly. After perfect alignment of the beam in the output of the delay line, it is adjusted in far distance with stage movement.

The common beam expanders/compressors use lenses which increase the pulse width of the beam and are not proper in ultrashort system design. Instead of using lens combination beam expander/compressor, we have used reflective mirrors combination. After the delay line, probe beam is compressed 0.64 times and collimated by pairs of 90° off axis parabolic mirrors:

1- OAP3: PFL of 59.7 mm, EFL of 119.4 mm
2- OAP4: PFL of 38.1 mm, EFL of 76.2 mm

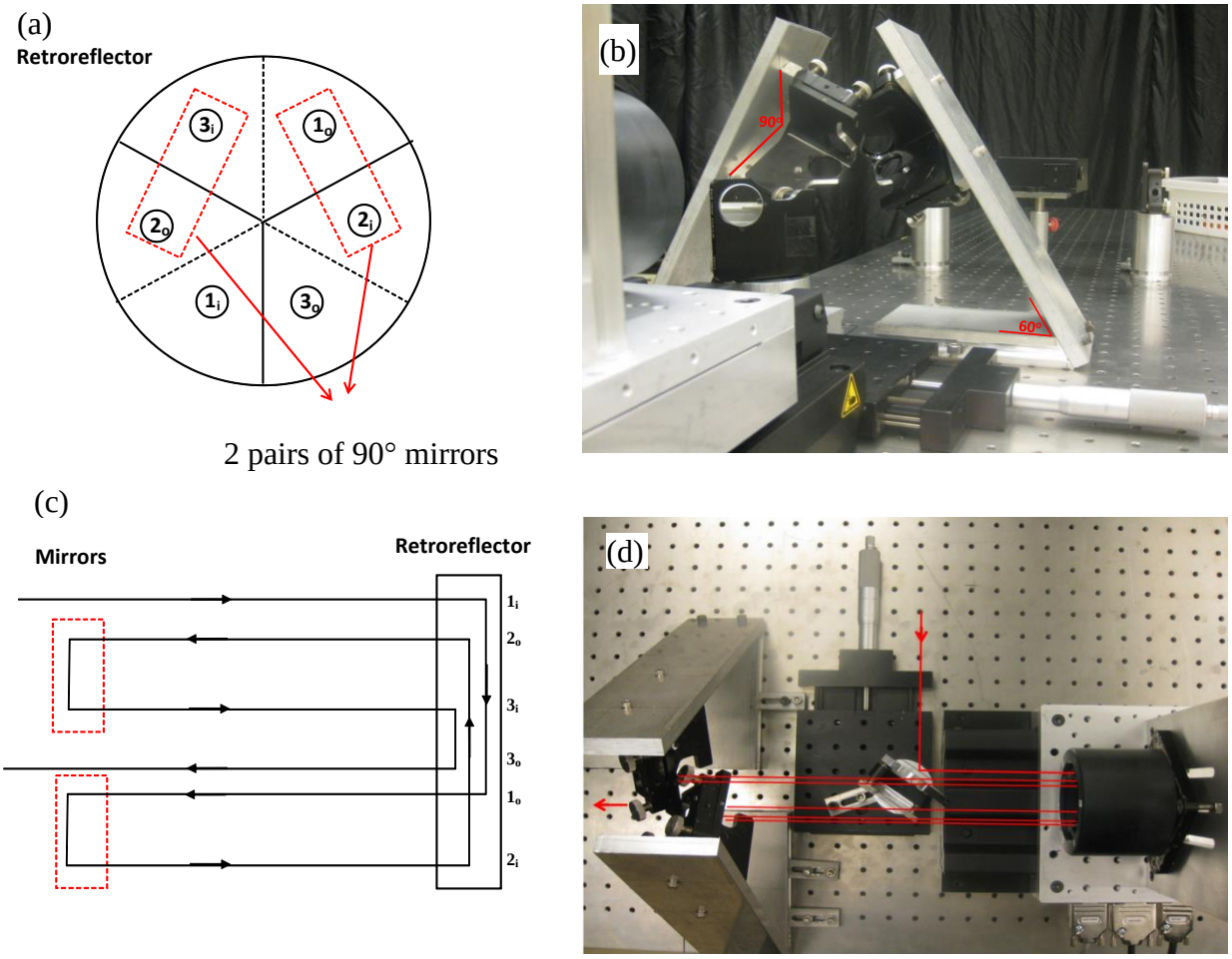

Figure 12-6 (a) Schematic design and (b) picture of delay line mirrors position respect to the retroreflector (cube corner mirror). (c) Sketch and (d) picture of 6-pass beam between retroreflector and mirrors.

After compression, probe beam passes through a glan laser beam splitting/combining which transmits p polarization beam and reflects the s polarized beam with angle of 75.2 respects to the incident beam. We need the glan laser to separate the reflected probe beam from sample. The beam with p polarization passes through the glan laser. λ/4 retarder makes circular polarization. Therefore, after that, the probe beam has p and s polarization components which are perpendicular to each other.

After making an optical matching path for pump beam to compensate the path difference between probe and pump beam, the pump beam spot size also is reduced to 0.25 times using a reflective beam expander/compressor (Thorlabs BE04).

Using a dichroic mirror (cold mirror) which transmits 800nm beam and reflects 400nm at 45° AOI, both beams are aligned to have maximum overlap and directed into a long-working distance 36× objective lens to focus the beam spots on the sample. The reflected probe beam from the sample is aligned to reflect back to the glan laser by dichroic mirror. The s-polarization component of the reflected probe beam is reflected from glan laser at 75.2° which is focused onto a high speed PIN detector (Thorlabs DET36A) with rise time of ~14ns. A blue filter is used before glan laser to avoid entering any reflected pump beam into the detection line. The Pine diode is connected to the lock-in amplifier to amplify the detected signal. A lock-in amplifier made by Zurich Instruments (HF2LI, 50MHz, and 210 Msa/s) was used in the system.

In detection path a removable mirror inserted to reflect the beam into a CCD camera as a microscope to view the sample in detail. It is also applicable to see the overlapping of pump and probe beams. In order to measure the beam spots of both beams, the CCD camera is used with knowing the distance of the objective lens to the CCD. The spot measurement can be done by Knife-edge method.

The final design of optical set up is shown in Figure 12-7. The main change is adding a window and detector to sample the probe beam intensity after the second pairs of off axis parabolic mirrors. The detected signal is used as baseline and subtracted from the main signal. Therefore the variation of intensity due to delay stage is removed from the main signal.

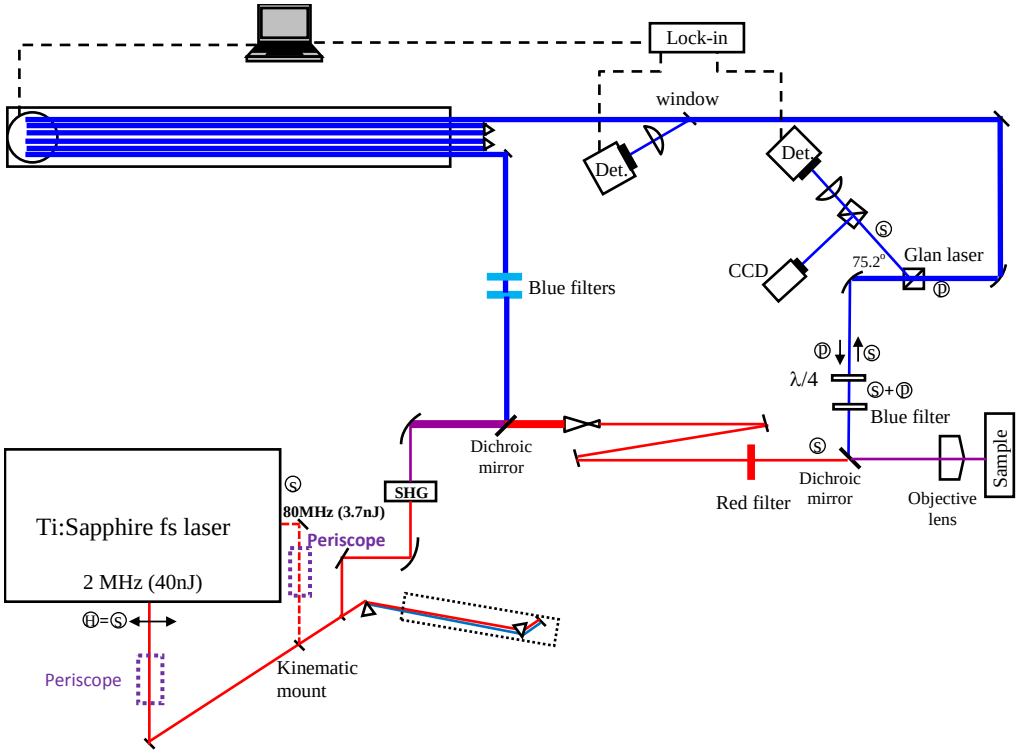

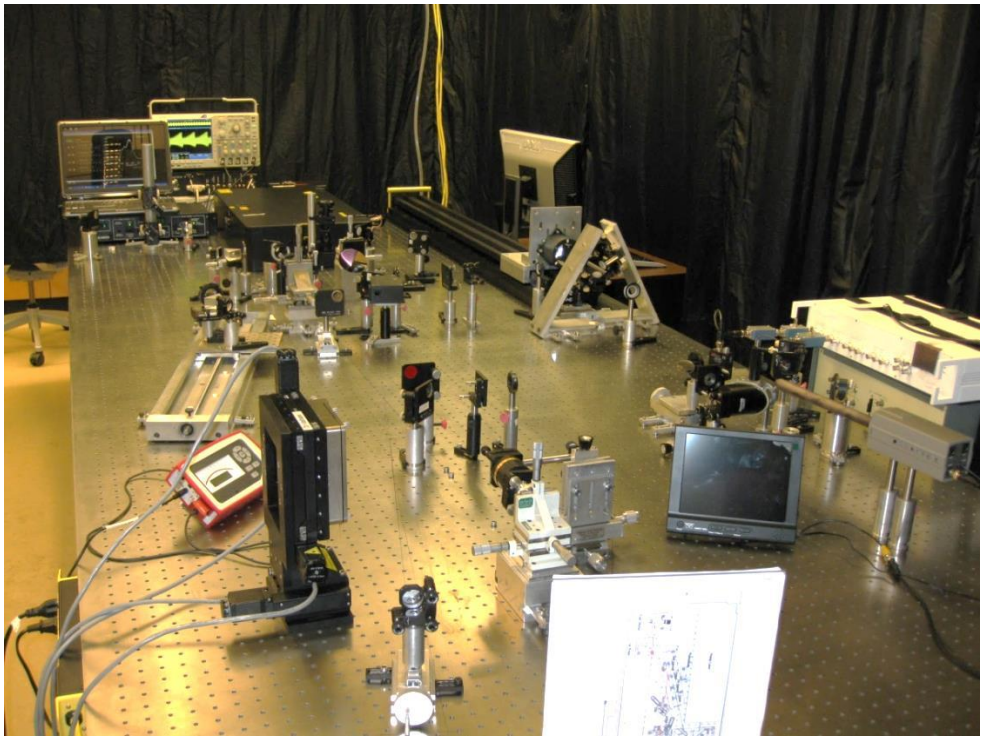

Figure 12-7 Final version of optical design.

12.3. **Beam Spot measurement**

In order to calculate the energy density absorbed by a sample, the beam waist must be known. The beam waist w_0 (beam diameter = $2w_0$) of the focused beam on the sample position was measured with a knife-edge technique [12,13,14]. The experimental set up is shown in Figure 12-8. Both pump and probe beams are focused at the sample position into the smallest beam size of $2w_0$. A razor blade mounted on a x-y stage positioned instead of sample and the blade cuts the laser beam horizontally or vertically by moving its stage in x or y position. The passing beam is focused by a lens onto the photodiode detector which is connected to the lock-in amplifier. The signal is collected as a function of the razor blade position. Step size for collecting the data is 10μm. The cross section intensity distribution of a laser beam with Gaussian profile is given by [14]:

$$I(x,y) = \frac{2A_0}{\pi w_0^2} \exp\left(-\frac{2x^2 + 2y^2}{w_0^2}\right) \qquad (12.1)$$

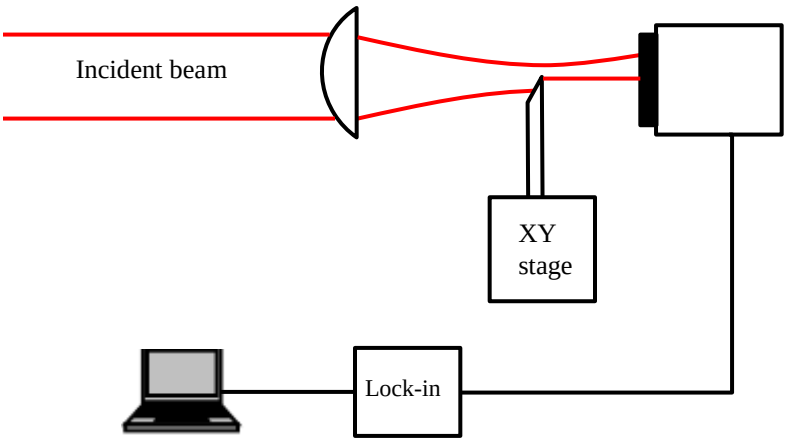

Figure 12-8 Schematic diagram of the knife edge technique to measure the beam spot

where A_0 is the total laser power, x and y are the cross sectional coordinates, and w_0 is the $1/e^2$ point of the beam radius. If the razor blade motion is in the x direction, the total intensity at the detector is given by:

$$I(x) = \frac{2A_0}{\pi w_0^2} \int_{-\infty}^{\infty} dy \exp\left(\frac{-2y^2}{w_0^2}\right) \int_{-\infty}^{\infty} \mathrm{dx} \exp\left(\frac{-2x^2}{w_0^2}\right) \qquad (12.2)$$

Taking the derivative of the resulting curve gives the intensity profile in the x direction. The collected data is fit then to the Gaussian profile to find the $1/e^2$ spot size.

12.4. **Instrumentation**

Using proper electronic elements are necessary to achieve precise measurement in such optical system. In our set up the main instruments are: the PIN photodiode to detect the optical pulses, lock-in amplifier to detect and amplify the desired signal.

As it is mentioned before the thermoreflectivity coefficients are on the order of 10^{-4} or less. Therefore the probe reflected beam is very weak signal which is buried into different noise signals and also large DC background component of reflection. The best instrument to obtain a weak signal from high level of noise is using a lock-in amplifier which is based on phase sensitive detection principle. Along with the input signal, a reference signal is provided. The amplifier then responds only to the portion of the input signal that occurs at the frequency with a fixed phase relationship. In our set up we have used lock-in amplifier made by Zurich Instruments (HF2LI, 50MHz, and 210 Msa/s).

The lock-in amplifier detects the signal in very narrow bandwidth. The reference signal is a square wave, thus the output signal can be consist of all the odd harmonics of the reference signal. In order to eliminate the higher harmonics from the main signal, we have used an inductor following Schmidt set up [25]. The inductor can generate a resonant filter with the photodiode at the reference frequency and increase the signal intensity by a factor of 10 or more [15]. The photodiode is considered as a current source in parallel with a capacitance. The inductor is inserted in series between photodiode and lock-in amplifier and it was tuned to cancel the capacitance at the reference frequency. This forms a series LC circuit with highly damping by the lock-in amplifier input impedance. This capacitance in our photodiode is 40 PF and we have used a variable impedance of 1-50 kΩ.

12.5. **Noise sources**

Different sources of noise can reduce the signal to noise ratio of the system. In order to have a precise measurement, the noise level must be minimized. Thermal fluctuations generate Johnson noise and discrete nature of electric charge produces shot noise. The dominant noise source in photodiode is shot noise. This noise in the probe beam is $(2e/I)^{0.5}$ where e is electron charge and I is the photocurrent produced by the diode.

Pink noise or 1/f noise is the main source in the system. This spectral noise arises in electronic devices due to a direct current. The bandwidth of lock-in measurement was set to …which gives signal fluctuation of …. And our measurement is in the order of 10^{-5}-10^{-4}. Therefore, the signal to noise ratio is sufficient for the measurements. At frequencies below 2MHz the 1/f noise fluctuations becomes ~ $10^{-6}/(Hz)^{0.5}$. In this case, the signal is measurable with smaller bandwidth of lock in amplifier which causes slower lock-in time constant.

12.6. **References**

1 C. A. Paddock and G. L. Eesley, J. Appl. Phys. 60, 285, 1986.

2 W. S. Capinski and H. J. Maris,"Improved apparatus for picosecond pump-and-probe optical measurements", Rev. Sci. Instrum. 67, 2720, 1996.

3 D.G. Cahill, W. K. Ford, K. E. Goodson, and Majumdar, J. Heat Transfer, 124, 223, 2002.

4 D.G. , W.K. Ford, K.E. Goodson, G. D. Mahan, A. Majumdar, H. J. Maris, R. Merlin, and S. R. Phillpot, J.Appl. Phys., 93, 793, 2003.

5 Aaron Schmidt, Matteo Chiesa, Xiaoyuan Chen, and Gang Chen, Rev. Sci. Instrum. 79, 064902 (2008).

6 K. E. O'Hara, Xiaoyuan Hu, and David G. Cahill, Journal of Applied Physics, 90(9):4852-4858, 2001.

7 D.G. Cahill, Review of Scientic Instruments, 75(12):5119-5122, 2004.

8 F. Salin, P. Georges, G. Roger, and A. Brun, Applied Optics, Vol. 26, Issue 21, pp. 4528-4531 (1987).

9 Melanie T. Asaki, Chung-Po Huang, Dennis Garvey, Jianping Zhou, Henry C. Kapteyn, Margaret M. Murnane, Optics Letters, Vol. 18, Issue 12, pp. 977-979 (1993).

10 Ryuji Morita, Masakatsu Hirasawa, Naoki Karasawa, Satoru Kusaka, Naoya Nakagawa, Keisaku Yamane, Liming Li, Akira Suguro, and Mikio Yamashita, Measurement Science and Technology, 13(11):1710-1720, 2002.

11 A.J.Sabbah and D.M.Riffe, Physical Review B 66, 165217,2002.

12 Amaud, J. A., W. M. Hubbard, G. D. Mandville, B. de la Claviere. E. A. Franke. and J. M.Franke. 197 1. Appl. Opt. 10,2775.

13 Skinner, D. R., and R. E. Whitcher, 1972, J. Phys. E 5, 237.

14 Suzaki, Y., and A, Tachibana, 1975, Appl. Opt. 14,2809

15 K. E. O'Hara, Xiaoyuan Hu, and David G. Cahill, Journal of Applied Physics, 90(9):4852-4858, 2001.

Chapter 13 Thermal transport modeling and data analyzing

13.1. Introduction

In pump-probe technique, extracting thermal properties data of the sample required is accomplishes with comparing the recorded experimental data to the modeling data of the heat transport of the system. In this comparison, the unknown properties of interest such as thermal conductivity of the sample, thermal conductance between two layers are considered as free parameters and adjusted to minimize the differences between the modeling data and the experimental data. The modeling procedure can be divided into two parts. First part is to obtain the relation between output of the lock-in amplifier and the detected probe beam. In this step, the resulted function is given in terms of the impulse response or frequency response of the system. The excitation process must be modeled as a linear time-invariant (LTI) system. The second part is finding the thermal response of the system. The heat flow in layered structures regarding to the effect of radial heat flow, anisotropic heat flow and thermal interface conductance are analyzed in details in this chapter. The 3 dimensional heat flow analysis in layered structure is calculated This new approach in pump-probe technique enables to have a reliable technique for thermal properties measurement of strong anisotropic materials such as nanowires. In the following sections, the whole modeling procedure is discussed in details. Moreover, the isothermal boundary condition solution as well as adiabatic boundary condition is derived.

13.2. Modeling the thermal system as LTI

We describe our thermal system as a LTI system. Theory of LTI systems is commonly used in many fields, especially signal processing and control systems [1]. This assumption implies that we can use all the mathematical tools for LTI systems, such as superposition, convolution, and simple conversion between the time and the frequency domains. The temperature of the system,

for example, obeys superposition if the temperature changes are small enough that the physical properties of the system remain constant [2]. Moreover, the thermoreflectance coefficient must be linear versus temperature over the working temperature range of the system. In addition, the temperature increase resulted from a single pulse and the steady state accumulation of heat is on the order of a few kelvins or smaller. Therefore the linearity assumption is valid in our thermal system and it enables using convenient way to deal with heat transfer problems, especially in time varying heat input systems such as periodic heat in case of our pump-probe system. It is verified that by changing the input power, the measured signal linearly varied. According to mentioned reasons, we can use LTI assumption and apply the mathematical tools in our modeling following Schmidt's approach [3]. The output of the lock-in amplifier is modeled in two ways, in terms of the impulse response, h(t) and in terms of the frequency response, H(ω). The impulse response is suitable for numerical solutions, while frequency response is appropriate when frequency domain analytical solution for the temperature is known.

13.3. **Lock-in amplifier Output Signal**

A lock-in amplifier is a device that can extract a signal with a known reference signal from an extremely noisy signal. By using phase sensitive detection concept, very narrow bandwidth filtering can be achieved, which enables very weak signal to be measured from a noisy signal as it is shown in Figure 13-1.

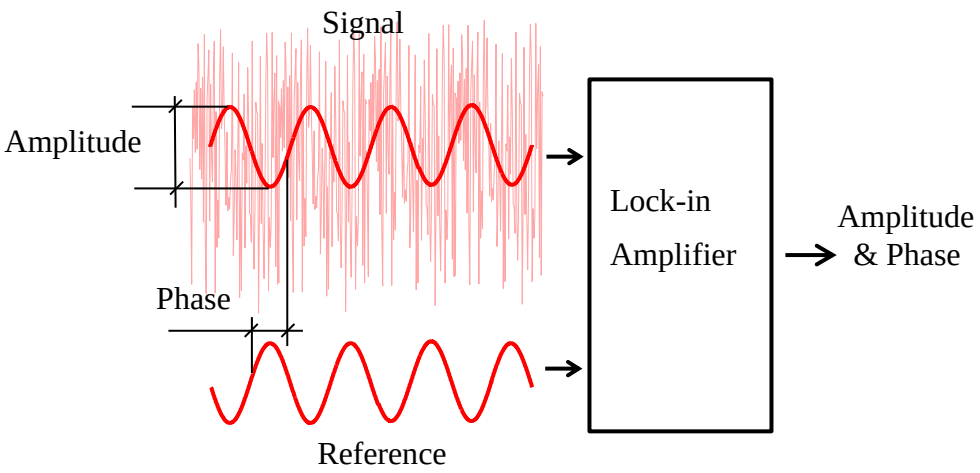

Figure 13-1 Lock in amplifier can measure weak signals buried in noise [4].

The signal is amplified in the lock-in and multiplied by the reference with a phase sensitive multiplier. The output of the multiplier contains a zero frequency component proportional to the amplitude and phase of the signal at the reference frequency and some higher frequency components. When the output of multiplier is passed through a low pass filter, the higher frequency signals are removed. Therefore, the output of the lock-in amplifier for a reference signal $e^{i\omega_0 t}$ can be written as:

$$\text{Output signal} \equiv Ae^{i\phi} = Z(\omega_0) \qquad (13.1)$$

where A is the amplitude, ϕ is the phase of the lock-in amplifier and $Z(\omega)$ is the transfer function. The system response will be appeared in amplitude and phase of the lock-in amplifier and both of them will be function of the delay time between the pump and probe pulses and the physical properties of the sample. The reference frequency, ω_0, will be taken from pump pulse. The transfer function is a function of the thermal response of the system and pump and probe beam properties. This function will be derived for the current system in the following sections.

The lock-in amplifier has two output readings: in-phase component, X, and out-of-phase component, Y. In-phase component is a composition of the cosine components of the signal, and out-of-phase component is a composition of the sine components of the signal. The magnitude of the signal is obtained from $(X^2+Y^2)^{1/2}$ and the phase from $\tan^{-1}(Y/X)$.

13.4. Measured signal in terms of impulse response

In order to derive the thermal response of the system, first consider the response of the system to a series of modulated pulses. The modulation function is assumed to be sinusoid. The square wave can be divided into its Fourier components, and because the system is linear, response to each component can be considered independently. The lock-in amplifier amplifies only some components in a very narrow band around the modulation frequency. Therefore we take into account only the fundamental component of the modulated beam. The small effect of other components is removed using the inductive filter between photodiode and locked-in amplifier, as

it is mentioned in section 11.4. The DC offset also can be ignored, as it is rejected by the lock-in amplifier. DC offset is the result of quasi-steady state of the system after a short period of time.

In our system we have two different frequency options: 2MHz if we use dumped beam output of the laser and 80MHz if we used mode locked beam output of the laser. The pulse width is about 10fs and it is very shorter than the heat transfer time scale. Hence, in the modeling each laser pulse is an impulse with energy Q and we use a delta function for each pulse.

A demonstration of the modulated heat input pulse with 80MHz is shown in Figure 13-2 in time domain and frequency domain. The heat impulse produces temperature change in the sample which is shown in Figure 13-3. As it is demonstrated, surface temperature does not vanish before the next heating impulse arrives.

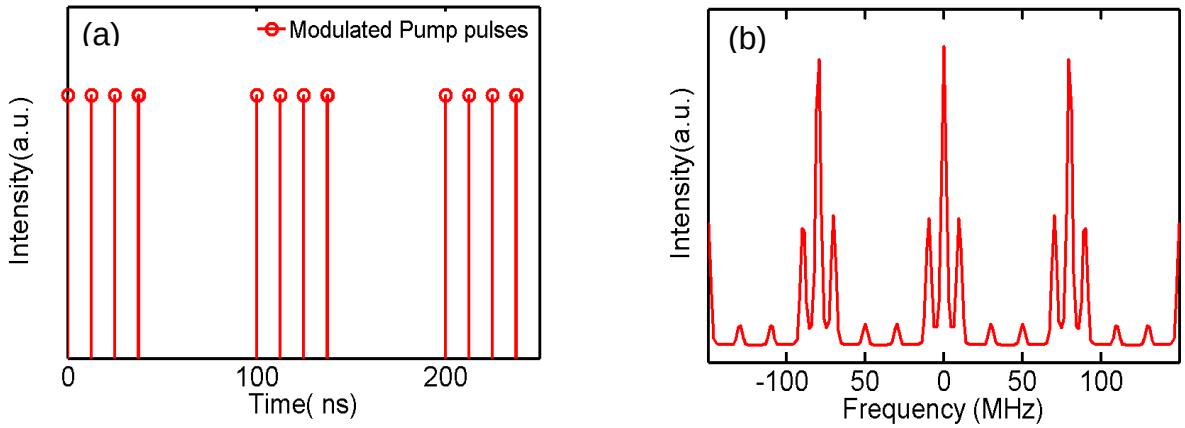

Figure 13-2 Demonstration of modulated pump beam (80MHz) with a square signal (10MHz) in (a) time domain, (b) frequency domain.

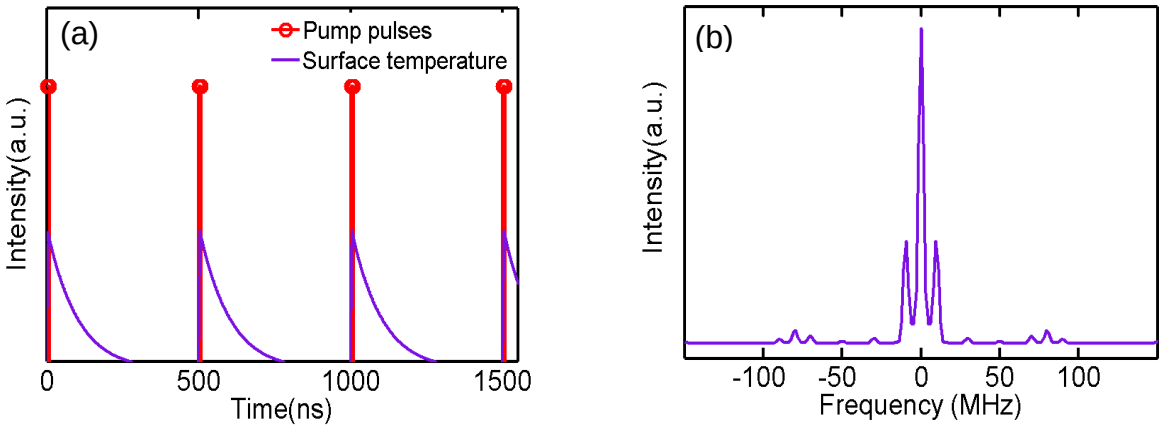

Figure 13-3 Surface temperature variations of the sample due to pump beam exposure: (a) Time domain (b) frequency domain. Temperature decay does not die away before next pulses arrives

The probe pulses with a variable delay time (τ) respect to the pump pulses hit the sample. The delay time varies with the optical path difference between pump and probe pulses which is provided by moving the delay stage. The reflected probe beam from the sample is directed into the photodiode for detection. The probe pulses samples the surface temperature which is illustrated in Figure 13-4. The only component of the probe signal at the reference frequency will be recorded by the lock-in amplifier. All other frequency components of the probe signal will be ignored by lock-in amplifier. Figure 13-5 shows a representation of the recorded signal by lock-in amplifier. The amplitude and phase of the reflected probe beam are recorded at each delay time.

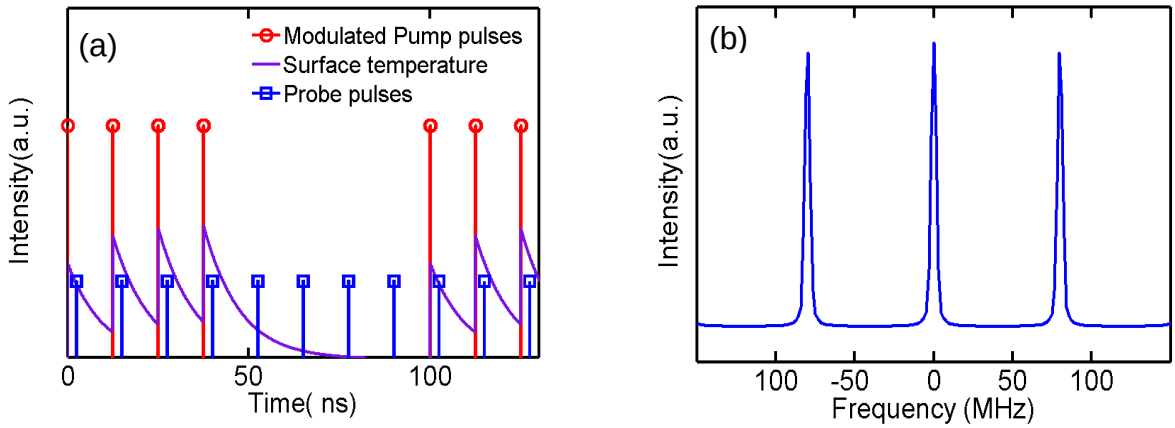

Figure 13-4 Probe pulses in (a) time and (b) frequency domain representation received at the sample. The probe beam is delayed respect to the pump pulses.

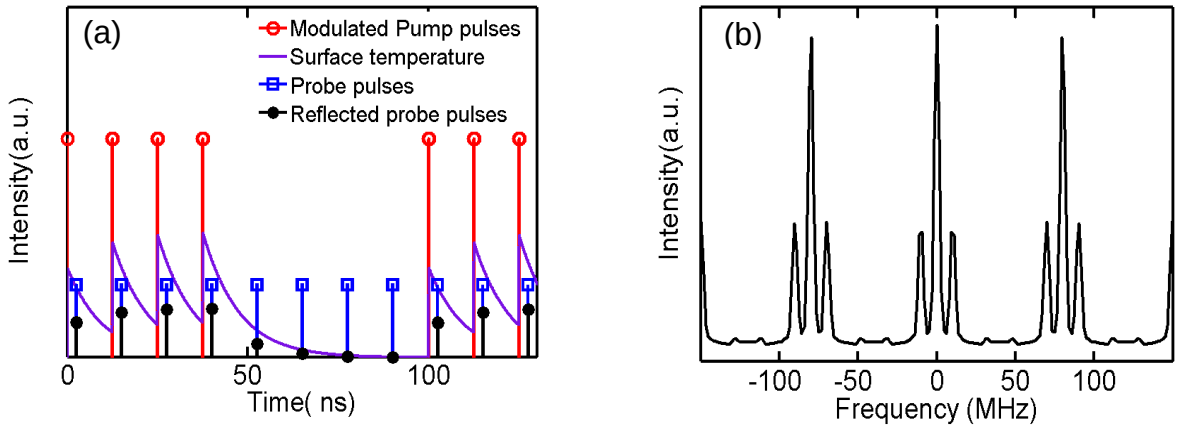

Figure 13-5 Reflected probe beam (a) time and (b) frequency domain representation.

In our 2MHZ experiments, pump pulses are not modulated. Similar demonstration of pump pulses, probe pulses, surface temperature and detected probe reflection beam are shown in Figure 13-6, Figure 13-7, Figure 13-8, and Figure 13-9.

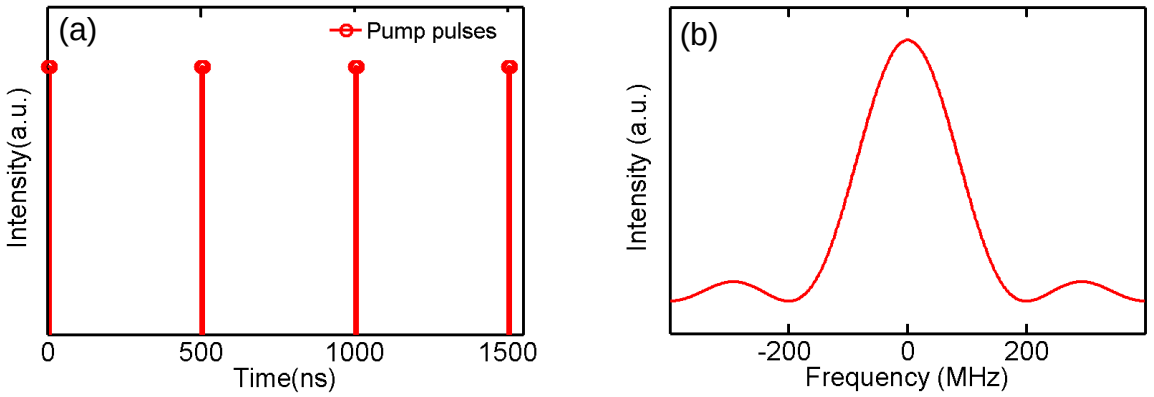

Figure 13-6 Pump pulses with 2MHz frequency illustration in (a) time domain, and (b) frequency domain.

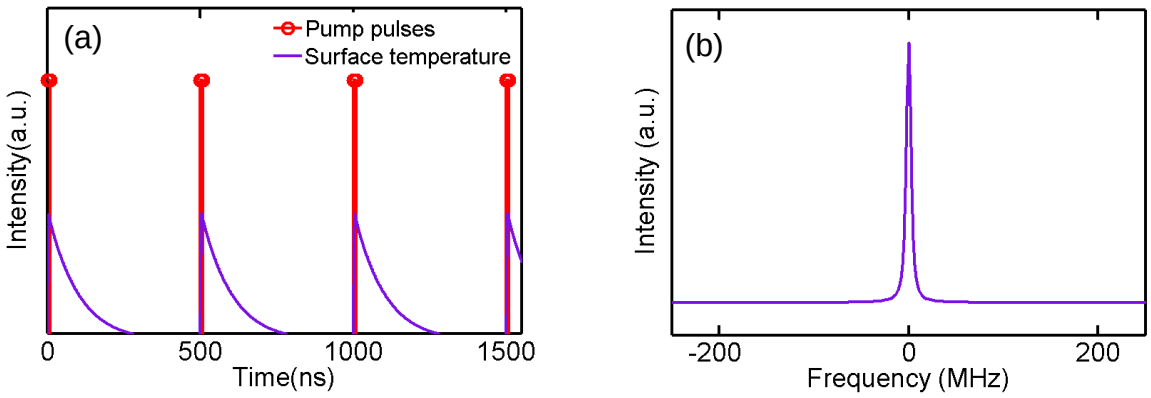

Figure 13-7 Surface temperature change due to pump beam irradiation: (a) Time domain, (b) Frequency domain.

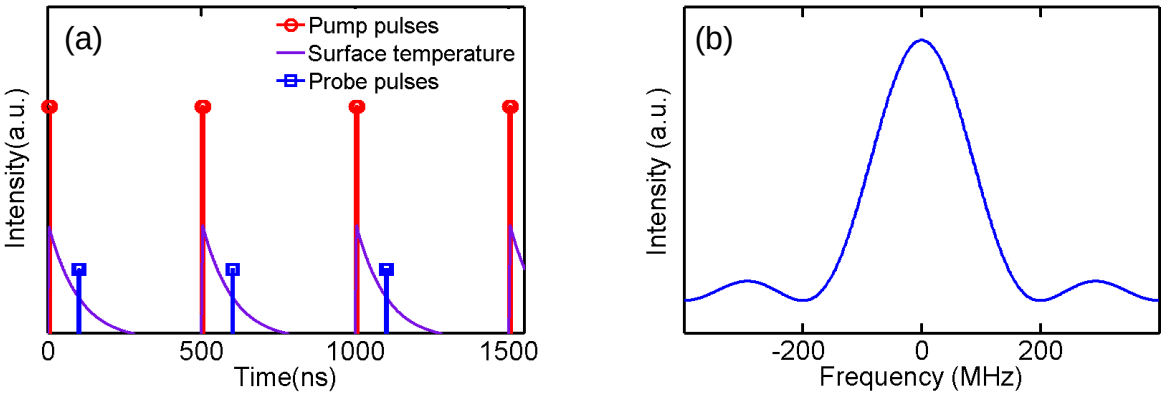

Figure 13-8 (a) Schematic demonstration of pump (2MHz), probe and surface temperatures in time domain, (b) Frequency domain sketch of probe beam.

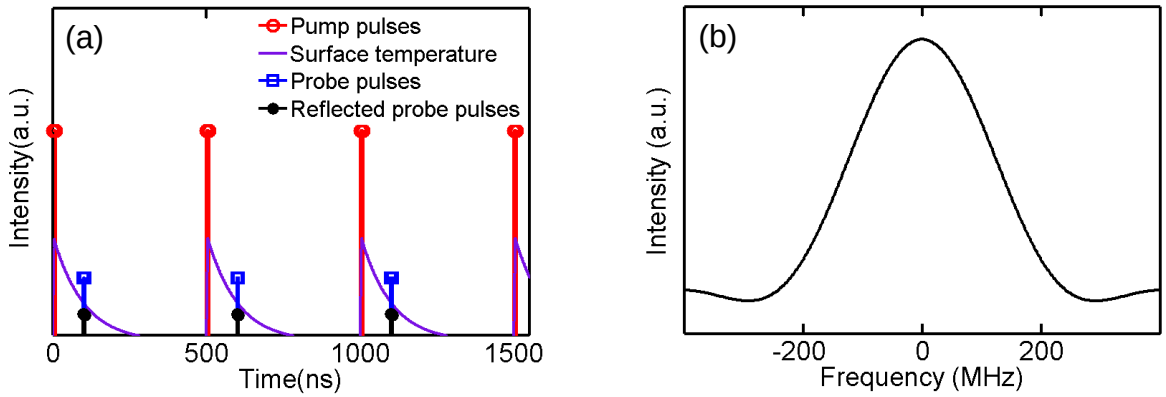

Figure 13-9 (a) Time domain reflected probe beam demonstration along with pump, probe and surface temperature. (b) Frequency domain illustration of reflected probe beam.

13.5. Time domain Lock-in amplifier transfer function

In order to model the thermal response of the system, first we derive an expression for the reflected probe beam intensity in the time domain. Then its Fourier transform is obtained and the frequency component at the modulation frequency is extracted, because the output of lock in amplifier will be the thermal response at this frequency.

It is noted that each pump pulse can be assumed as a heat impulse. First, an heat impulse Qδ(t) which is a heat impulse with strange Q at very short time hits the sample. The temperature response of the system to this heat impulse is supposed to be Q h (**r**,t), where h (**r**,t) is the unit impulse response with unit of (temperature/energy), **r** is the special coordinate, t is the time and Q is the energy of the impulse. In our system, heating source q(t) is the pump beam which can be written as:

$$q(t) = \frac{1}{2}\left(1 + e^{i\omega_0 t}\right)\sum_{m=-\infty}^{\infty} Q_{pump}\delta(t - mT - T_0), \qquad (13.2)$$

where ω_0 is the modulation frequency, T is the time between pulses (laser period), T_0 is an arbitrary time offset between t=0 and the time when the first pulse arrives, and Q_{pump} is the energy per pulse of the pump beam.

The temperature response to a heat input which is time dependent, q(t), is given by the convolution [25]:

$$\theta(\boldsymbol{r},t) = q(t) * h(\boldsymbol{r},t) = \int_{-\infty}^{\infty} q(t')h(\boldsymbol{r},t-t')dt', \quad (13.3)$$

and for the pump-probe system, Since the lock in-amplifier will amplify the periodic part with frequency ω_0, we only write the periodic component of heat input:

$$q(t) = e^{i\omega_0} \sum_{m=-\infty}^{\infty} Q_{pump}\delta(t-mT-T_0), \quad (10.4)$$

According to equation (10.2), the surface temperature of the system is:

$$\theta(\boldsymbol{r},t) = Q_{pump} \int_{-\infty}^{\infty} e^{i\omega_0 t} \sum_{m=-\infty}^{\infty} \delta(t'-mT-T_0)h(\boldsymbol{r},t-t')dt', \quad (13.5)$$

Using:

$$\int_{-\infty}^{\infty} f(x)\delta(x-x_0)dx = f(x_0), \quad (13.6)$$

the surface temperature is then given by:

$$\theta(\boldsymbol{r},t) = Q_{pump} \sum_{m=-\infty}^{\infty} e^{i\omega_0(mT+T_0)} h(\boldsymbol{r},t-mT-T_0), \quad (13.7)$$

The probe beam hits the sample after a delay time, τ and the reflected probe beam is detected by photodiode and lock-in amplifier. The reflected probe beam is proportional to the surface temperature of the sample, Therefore, it can be expressed by $\beta\theta P(t)$, where β is a constant includes the thermoreflectance coefficient of the sample and electronics gain and P(t) is the probe beam. The probe beam can be written as:

$$P(t) = \sum_{n=-\infty}^{\infty} Q_{probe}\delta(t-nT-T_0-\tau), \quad (13.8)$$

Where Q_{probe} is the energy per pulse of the probe beam, τ is the delay time between pump and probe pulses. The reflected probe beam can be written as:

$$z(t) = \beta\theta(t) \sum_{n=-\infty}^{\infty} Q_{probe}\delta(t-nT-T_0-\tau\ , \quad (13.9)$$

Inserting $\theta(t)$ gives:

$$z(t) = \left(\beta Q_{pump}Q_{probe} \sum_{m=-\infty}^{\infty} e^{i\omega_0(mT+T_0)} h(\boldsymbol{r},t-mT-T_0) \right) \times$$

$$\sum_{n=-\infty}^{\infty} \delta(t-nT-T_0-\tau), \quad (13.10)$$

The special variable, r, is ignored here, since we are looking at a fixed position in the impulse response. Taking Fourier transform of equation (13.10),

$$Z(\omega) = \int_{-\infty}^{\infty} z(t) e^{-i\omega t}\, dt =$$

$$\beta Q_{pump} Q_{probe} \sum_{m=-\infty}^{\infty} \sum_{n=-\infty}^{\infty} e^{i\omega_0 (mT+T_0)}\, h(nT + T_0 + \tau - mT - T_0) e^{-i\omega(nT+T_0+\tau)}, \quad (13.11)$$

Changing variable m to q such that q=n-m, we have:

$$Z(\omega) = \beta Q_{pump} Q_{probe} \sum_{n=-\infty}^{\infty} \sum_{q=-\infty}^{\infty} e^{i\omega_0 ((n-q)T+T_0)}\, h(qT + \tau) e^{-i\omega(nT+T_0+\tau)} \quad , \qquad (13.12)$$

by rearrangement:

$$Z(\omega) = \beta Q_{pump} Q_{probe} \sum_{q=-\infty}^{\infty} e^{-i\omega_0 (-qT+T_0)}\, h(qT + \tau) \sum_{n=-\infty}^{\infty} e^{i\omega_0 nT}\, e^{-i\omega(nT+T_0+\tau)}$$

$$= \beta Q_{pump} Q_{probe} \sum_{q=-\infty}^{\infty} e^{-i\omega_0 (-qT+\tau)}\, h(qT + \tau) \sum_{n=-\infty}^{\infty} e^{i\omega_0 (nT+T_0+\tau)}\, e^{-i\omega(nT+T_0+\tau)}, \quad (13.13)$$

The second sum in equation (12.13) (sum over n), can be modified to:

$$A(\omega) = e^{i(\omega_0-\omega)(T_0+\tau)} \frac{2\pi}{T} \sum_{n=-\infty}^{\infty} \delta(\omega_0 - \omega + \frac{2\pi n}{T}), \qquad (13.14)$$

For n≠0 , $\frac{2\pi n}{T}$ in $\omega = \omega_0 + \frac{2\pi n}{T}$ is much greater than the modulation frequency, therefore, all the delta functions at frequencies $\omega = \omega_0 + \frac{2\pi n}{T}$ for n≠0 are outside of the lock-in amplifier pass band, consequently transfer function can be approximated to:

$$Z(\omega) = \frac{\beta Q_{pump} Q_{probe}}{T} \sum_{q=0}^{\infty} e^{-i\omega_0 (qT+\tau)} h(qT + \tau) 2\pi\delta(\omega_0 - \omega)\,, \qquad (13.15)$$

Since for t<0, h(t)≡0, q takes positive values. Taking inverse Fourier transforms to obtain the signal function in time domain:

$$z(t) = Z(\omega_0) e^{i\omega_0 t}, \qquad (13.16)$$

where:

$$Z(\omega_0) = \frac{\beta Q_{pump} Q_{probe}}{T} \sum_{q=0}^{\infty} h(qT + \tau)\,, \qquad (13.17)$$

$Z(\omega_0)$ is the transfer function of the lock-in amplifier at modulation frequency. As it is seen from the equation, transfer function is a function of the energy of the pump and probe pulses,

period of the laser beam, and delay time. The thermal response of the system (h(t)) in time domain must be replaced in the transfer function. The output of the lock-in amplifier should be compared with this equation and minimize the error between model and experimental data.

In some heat transfer problems, analytical solutions are convenient to derive in the frequency domain. In such conditions, it is desired to have the transfer function (equation (13.17) in frequency domain which is called thermal frequency response. This function was given by Schmidt [25]:

$$Z(\omega_0) = \frac{\beta Q_{pump} Q_{probe}}{T^2} \sum_{k=-\infty}^{\infty} H(\omega_0 + k\omega_s) \exp(ik\omega_s \tau), \qquad (13.18)$$

where ω_0 is the reference frequency and $\omega_s=2\pi/T$. Equation (13.18) is mathematical equivalent of equation (13.17) and they are Fourier transform of each other as it is expected in a LTI system. In the following sections, the thermal frequency response of the system, H(w) will be derived for one dimension, radial, and 3-dimension heat flow in layered structures.

13.6. Accumulation effects

As it mentioned, Ti: sapphire laser used in our system has two outputs: an 80 MHz output and 2MHz dumped beam output. In our experiments we have mainly used dumped beam output. The 80MHZ average output power is about 300mW and energy of each pulse is about 4nJ/pulse while the dumped beam average power is about 100mW and energy of each pulse is 50nJ/pulse. The time between laser pulses for 80MHz is about 12.5 ns and for 2MHz is about 500ns.

If the time between pulses is not long enough for system to go to the equilibrium condition, Reflectivity change, ΔR (t), does not originate entirely from a single pump, since the pump pulse has not fallen to a negligible value by the time the next pulse arrives. This accumulation effect was first considered by Capinski et al [15] in one dimensional transient thermoreflectance (TTR) technique. Later, Schmidt et al [3] reported that how accumulation effect leads to radial transport effects. It is mentioned that although pulse accumulation complicated the system analysis, it also makes time-domain thermoreflectance method as a powerful tool by allowing two length scales to be probed simultaneously. In their work, the transfer function has been derived in two time limits: first in the limit that the time between pulses, T, becomes infinite:

$$\lim_{T\to\infty} \frac{\beta Q_{pump} Q_{probe}}{T} \sum_{q=0}^{\infty} h(qT + \tau) e^{-i\omega_0 (qT+\tau)} = \frac{\beta Q_{pump} Q_{probe}}{T} h(\tau) e^{-i\omega_0 \tau} \qquad (13.19)$$

at very long times, h(qT+τ) is zero for all terms where q≠0. In this case, thermal transfer function reduces to the impulse response as a function of delay time, τ. As it is expected, the amplitude of the signal is proportional to the energy of a single pulse and the phase shift is the delay time multiplied by the modulation frequency.

The other time limit is when the T is close to zero:

$$\lim_{T\to 0} \frac{\beta Q_{pump} Q_{probe}}{T^2} \sum_{q=0}^{\infty} e^{-i\omega_0 \tau} h(qT+\tau) T = \frac{\beta Q_{pump} Q_{probe}}{T^2} H(\omega_0) \qquad (13.20)$$

In this case, transfer function approaches to the frequency response, which is the steady periodic response at modulation frequency.

In cases when the decay time of the system is not much longer or shorter than the pulse period, the output signal has elements of both the impulse response and the steady frequency response. Most of the thermal conductivity measurements are in this intermediate range of time.

When the effect of one pulse vanishes before the next pulse arrives, there is no accumulation effect and heat transfer is considered as one dimensional. The thermal penetration depth $L = \sqrt{\alpha t}$ is in the range of 30-300nm for most of the materials with a decay time of 10ns. The penetration depth in this case is so smaller than spot sizes which are typically in the range of 10-100μm. Therefore, the radial effect of heat transfer can be ignored. The other case is when the effect of one pulse does not vanish fully and having accumulation effect. Thermal penetration depth for thermal wave can be calculated by $L = \sqrt{2\alpha/\omega_0}$ where ω_0 is the modulation frequency. With 10MHz modulation, the thermal penetration depth will be in the range of 200nm-2μm. In system with 80MHz pulse frequency, the accumulation effect exists and the radial heat flow analysis must be considered for thermal properties measurements.

In our system, with dumped beam exposure (2MHz), laser period is 500ns. In most of the material systems, even in low thermal conductive materials, temperature decays completely in few ns time scale which is much shorter than the pulse period (500ns). Therefore, we do not have accumulation effect in our system using 2MHZ output. This system is the unique set up in this aspect among pump-probe previous designs. The absence of accumulation effect will increase the accuracy of extracted data.

13.7. Heat transfer in layered structures

Heat flow through layered structures in one dimensional isotropic media has been described in several publications [2,5] and the solution is applied for TTR method by Cahill [6]. The solution was extended for radial effects using Hankel transformation by Schmidt et al [3]. In previous works, one dimensional solution is solved for only adiabatic boundary condition. In this section, the solution for one dimensional conduction by Carslaw and Jaeger [7] for layered structures will be extended to three dimensional solutions for anisotropic media with adiabatic boundary condition. In addition, the isothermal solution for 3d isotropic and anisotropic media will be extracted and the results will be compared with adiabatic boundary conditions. This extended numerical solution enables us to measure the thermal conductivity and thermal conductance of strong anisotropic media such as nanowires. The isothermal solution provides more accurate solution for the systems with non-isolated sample.

13.7.1. One dimensional heat transfer

One dimensional heat flow in layered structure was analytically solved in "Conduction of heat in solids" by Carslaw and Jaegar [7]. The temperature, θ_t, and heat flux, f_t, on the top side of a single layer material with heat flow in z direction are related to the temperature, θ_b, and heat flux, f_b, on the bottom side by the following matrix:

$$\begin{bmatrix}\theta_b\\ f_b\end{bmatrix} = \begin{bmatrix}\cosh(qd) & \frac{-1}{\sigma_z q}\sinh(qd)\\ -\sigma_z q\sinh(qd) & \cosh(qd)\end{bmatrix}\begin{bmatrix}\theta_t\\ f_t\end{bmatrix}, \tag{13.21}$$

where d is the layer thickness, σ_z the cross-plane thermal conductivity, and $q^2 = i\omega/\alpha$, ω is the frequency of thermal source oscillation, and α is the thermal diffusivity. This solution can be extended for multiple layers of different materials by multiplying the matrices for each layer:

$$\begin{bmatrix}\theta_b\\ f_b\end{bmatrix} = M_n M_{n-1} \dots M1 \begin{bmatrix}\theta_t\\ f_t\end{bmatrix} = \begin{bmatrix}A & B\\ C & D\end{bmatrix}\begin{bmatrix}\theta_t\\ f_t\end{bmatrix}, \tag{13.22}$$

$$M = M_n M_{n-1} \dots M1 = \begin{bmatrix}A & B\\ C & D\end{bmatrix} \tag{13.23}$$

where M_1 is the matrix for the top layer and M_n is the matrix for bottom layer. We call the matrix M as layers matrix. Assuming adiabatic condition for the bottom surface of nth layer or

supposing the nth layer as semi-infinite, temperature flux of the last layer is zero, f_b=0, hence, $C\theta_t+Df_t=0$ and the surface temperature can be calculated by :

$$\theta_t = \frac{-D}{C} f_t \qquad (13.24)$$

13.8. Thermal interface conductance

As it is discussed in section 11.4, there is a thermal conductance at the interface of two materials due to electronic impedance, interface quality or contamination. The thermal conductance (G) is defined as $G=f/(\theta_2-\theta_1)$, where f is the heat flux across the interface and θ_1 and θ_2 are the temperatures on each side of interface. In order to use interface conductance equation with equation (12.22), it can be written in matrix form of:

$$\begin{bmatrix}\theta_2 \\ f\end{bmatrix} = \begin{bmatrix}1 & G^{-1} \\ 0 & 1\end{bmatrix}\begin{bmatrix}\theta_1 \\ f\end{bmatrix} \qquad (13.25)$$

Therefore, thermal conductance coefficient can be included where the layers matrix (M) is calculated. This enables the modeling analysis to extract the thermal conductance between different layers of the sample.

13.8.1. Radial heat transfer

As it is mentioned in section accumulation effect description, in a system with accumulation effect, the heat transfer system is not in one dimension. Therefore, the heat transfer must be analyzed radially. Equation (13.24) can be extended to radial heat flow. As the laser spots have cylindrical symmetry, a zero-order Hankl transform can be used to simplify the equations [7]. The Hankel transform of θ (r) is given by [8]:

$$\overline{T}_r = \mathcal{H}[T(r)] = \int_0^\infty rJ_0(kr)T(r)dr \qquad (13.26)$$

Where k is the transform variable, r is the radial coordinate variable and J0 is the zero-order Bessel function of the first kind. The heat equation in cylindrical coordinate is:

$$\rho c \frac{\partial \theta}{\partial t} = \frac{\sigma_r}{r}\frac{\partial}{\partial r}\left(r\frac{\partial T}{\partial r}\right) + \sigma_z \frac{\partial^2 T}{\partial z^2}) \qquad (13.27)$$

Where ρ is the density, c is the specific heat, and σ_r and σ_z are the radial and cross-plane thermal conductivities, respectively.

Taking the Hankel transform of equation (13.27) gives:

$$\rho c \frac{\partial \bar{T}}{\partial t} = -\sigma_r k^2 \bar{T} + \sigma_z \frac{\partial^2 \bar{T}}{\partial z^2} \tag{13.28}$$

Applying Fourier transform ($\partial/\partial t \leftrightarrow i\omega$) of the equation (12.28) gives:

$$\rho c i\omega c \bar{T}(\omega) = -\sigma_r k^2 \bar{T}(\omega) + \sigma_z \frac{\partial^2 \bar{T}(\omega)}{\partial z^2} \tag{13.29}$$

If q is defined as:

$$q^2 = \frac{\sigma_r k^2 + \rho c\, i\omega}{\sigma_z} \tag{13.30}$$

Then the equation (12.29) can be reduced to:

$$\frac{\partial^2 \bar{T}(\omega)}{\partial z^2} = q^2 \bar{T}(\omega) \tag{13.31}$$

which is the one dimensional heat equation in frequency domain. Therefore, the solution is described in previous section for the one dimensional equation can be used here with new q as is defined by equation (13.30).

In our system, heat flux at the top boundary of the layers (f_t) is a Gaussian distribution with power of A_0 and $1/e^2$ radius w_0:

$$I(x,y) = \frac{2A_0}{\pi w_0^2} \exp\left(\frac{-2r^2}{w_0}\right), \tag{13.32}$$

In the calculations, we need f_t in frequency domain. Therefore taking Fourier transform of (12.32) gives:

$$f_t \equiv I(k) = A_0 \exp\left(\frac{-k^2 w_0^2}{8}\right), \tag{13.33}$$

The surface temperature in special transform domain is given by inserting f_t into equation (12.24):

$$\bar{T}(\omega, k) = -\frac{D}{C} A_0 \exp\left(\frac{-k^2 w_0^2}{8}\right), \tag{13.34}$$

where C and D are the matrix elements from equation (13.23). Taking the inverse Hankel transform give the surface temperature in real space:

$$T(\omega,r) = \int_0^\infty kJ_0(kr)\left(-\frac{\mathrm{D}}{\mathrm{C}}\frac{A_0}{2\pi}\exp\left(-\frac{k^2w_0^2}{8}\right)\right)dk, \quad (13.35)$$

The thermal response of the system in frequency domain, H(ω), is given by the weighted average of surface temperature by the coaxial probe beam. The probe beam distribution is a Gaussian distribution (equation 13.32) with power of A_1 and $1/e^2$ radius of w_1. The thermal response of the system will be:

$$\mathrm{H}(\omega) = \int_0^\infty \left(\frac{2\mathrm{A}_1}{\pi \mathrm{w}_1^2}\right)\exp\left(\frac{-2\mathrm{r}^2}{\mathrm{w}_1^2}\right)2\pi\mathrm{r}\mathrm{d}\mathrm{r}\int_0^\infty \mathrm{k}\mathrm{J}_0(\mathrm{k}\mathrm{r})\left(-\frac{\mathrm{D}}{\mathrm{C}}\right)\exp\left(\frac{-\mathrm{k}^2\mathrm{w}_0^2}{8}\right)\mathrm{d}\mathrm{k}, \quad (13.36)$$

and by some rearranging and calculating one of the integrals, it can be reduced to:

$$H(\omega) = \frac{A_0A_1}{2\pi}\int_0^\infty k\left(-\frac{D}{C}\right)\exp\left(\frac{-k^2(w_0^2+w_1^2)}{8}\right)dk \quad (13.37)$$

The thermal response equation is inserted into transfer function equation (13.17) and is solved numerically.

13.8.2. Three dimensional heat transfer

In order to apply TDTR method for thermal conductivity measurement of an anisotropic media, heat flow problem should be solved in three dimensions. Starting with heat equation in Cartesian coordinate [2]:

$$\rho c\frac{\partial T}{\partial t} = \sigma_x\frac{\partial^2 T}{\partial x^2} + \sigma_y\frac{\partial^2 T}{\partial y^2} + \sigma_z\frac{\partial^2 T}{\partial z^2}, \quad (13.38)$$

where T, ρ, c, σ_x, σ_y, and σ_z are the surface temperature, density of the layer, specific heat, the thermal conductivities in x, y, z directions, respectively. In order to simplify the equation and convert it to an equation similar to one dimensional heat equation, Fourier transform can be used respect to time and x and y [9]. Applying Fourier transforms to equation (12.26) respect to x and y gives:

$$\rho c\frac{\partial \bar{T}}{\partial t} = -\sigma_x k_x^2\bar{T} - \sigma_y k_y^2\bar{T} + \sigma_z\frac{\partial^2 \bar{T}}{\partial z^2}, \quad (13.39)$$

where $\bar{T} = \bar{T}\left(t, k_x, k_y, z\right)$, and k_x and k_y are the transform variables. In order to transfer the equation from time domain into frequency domain, another Fourier transform respect to time is applied:

$$i\omega\rho c\bar{T} = -\sigma_x k_x^2 \bar{T} - \sigma_y k_y^2 \bar{T} + \sigma_z \frac{\partial^2 \bar{T}}{\partial z^2}, \tag{13.40}$$

where $\bar{T} = \bar{T}\left(\omega, k_x, k_y, z\right)$. Rearranging the equation (13.28) gives:

$$\frac{\partial^2 \bar{T}}{\partial z^2} = q^2 \bar{T} \tag{13.41}$$

where

$$q^2 \equiv \frac{i\omega\rho c + \sigma_x k_x^2 + \sigma_y k_y^2}{\sigma_z}, \tag{13.42}$$

Equation (13.41) is similar to the one-dimensional heat equation in the frequency domain with q^2 defined as equation (13.30).

Therefore, equations (13.21) to (13.24) are valid here with new q^2 from equation (13.42).

Heat flux (pump beam exposure) at the top boundary (f_t) is a 2 dimensional Gaussian spot with power A_0 and $1/e^2$ radius of w_{0x} and w_{0y} in x and y direction:

$$I(x,y) = \frac{2A_0}{\pi w_{0x} w_{0y}} \exp\left(\frac{-2x^2}{w_{0x}}\right) \exp\left(\frac{-2y^2}{w_{0y}}\right), \tag{13.43}$$

Taking the Fourier transforms respect to x and y:

$$f_t \equiv I(k_x, k_y) = A_0 \exp\left(-\frac{w_{0x}^2 k_x^2 + w_{0y}^2 k_y^2}{8}\right), \tag{13.44}$$

Inserting the f_t into equation (13.24), the surface temperature in special transform domain is obtained as:

$$\bar{T}\left(\omega, k_x, k_y\right) = -\frac{D}{C} A_0 \exp\left(-\frac{w_{0x}^2 k_x^2 + w_{0y}^2 k_y^2}{8}\right), \tag{13.45}$$

The surface temperature of the system in real space is given by the inverse Fourier transform of $\bar{T}\left(\omega, k_x, k_y\right)$ respect to k_x and k_y:

$$T(\omega, x, y) = \frac{1}{(2\pi)^2} \int_{-\infty}^{+\infty} \int_{-\infty}^{+\infty} \left(\frac{-D}{C}\right) A_0 \exp\left(-\frac{w_{0x}^2 k_x^2 + w_{0y}^2 k_y^2}{8}\right) \exp(ik_x x) \exp\left(i k_y y\right) dk_x dk_y, \tag{13.46}$$

The thermal response of the system in frequency domain, H (ω), is given by the weighted average of equation (13.46) by the coaxial probe beam with radius w_1. The probe beam distribution can be written as a two dimensional Gaussian beam function, same as pump beam:

$$I(x,y) = \frac{2A_1}{\pi w_{1x} w_{1y}} \exp\left(\frac{-2x^2}{w_{1x}}\right) \exp\left(\frac{-2y^2}{w_{1y}}\right), \quad (13.47)$$

Therefore, the frequency domain response of the system will be:

$$H(\omega)=\int_{-\infty}^{+\infty}\int_{-\infty}^{+\infty}\left\{\left[\frac{2A_1}{\pi w_{1x} w_{1y}} \exp\left(\frac{-2x^2}{w_{1x}}\right) \exp\left(\frac{-2y^2}{w_{1y}}\right)\right] \times \right.$$

$$\left.\left[\frac{1}{(2\pi)^2}\int_{-\infty}^{+\infty}\int_{-\infty}^{+\infty}\left(\frac{-D}{C}\right) A_0 \exp\left(-\frac{w_{0x}^2 k_x^2 + w_{0y}^2 k_y^2}{8}\right) \exp(ik_x x) \exp(i k_y y)\, dk_x dk_y\right]\right\} dxdy, \quad (13.48)$$

Rearranging and calculating two spatial integrals respect to x and y simplify the equation to:

$$H(\omega) = \frac{A_0 A_1}{(2\pi)^2}\int_{-\infty}^{+\infty}\int_{-\infty}^{+\infty}\left(\frac{-D}{C}\right) \exp\left(-\frac{(w_{0x}^2 + w_{1x}^2)k_x^2 + (w_{0y}^2 + w_{1y}^2)k_y^2}{8}\right) dk_x dk_y \quad (13.49)$$

H (ω) is the frequency response function. Inserting this function into transfer function (equation 13.18) will give full description of our thermal system output which should be detected in the lock-in amplifier.

13.8.3. Heat transfer in layered structures using isothermal boundary condition

The expressed analytical solution was solved for adiabatic condition. However, if there last layer is not insulated, the sample will be in isothermal condition especially in small layer thicknesses. In order to obtain the analytical solution for isothermal condition, we suppose that the temperature of bottom layer is in heat sink temperature, T_0. Therefore, there is no temperature change on the bottom layer; implying new boundary condition, $\theta_b = T_0$, in equation (13.23) gives:

$$A\theta_t + Bf_t = T_0 \quad (13.50)$$

and the surface temperature can be obtained by:

$$\theta_t = \frac{T_0}{A} - \frac{B}{A} f_t, \quad (13.51)$$

a. Radial heat flow

It is noted that the thermal response of the system for radial heat transport was analyzed in adiabatic condition [3,6]. Using the isothermal boundary condition (equation (13.51)) and following the same calculation procedure which is explained in previous sections: the heat flux from top layer is:

$$f_t \equiv I(k) = A_0 \exp(-\frac{k^2 w_0^2}{8}), \quad (13.52)$$

Inserting this equation into equation (12.51) gives the surface temperature in special transform:

$$\bar{T}(\omega, k_x, k_y) = \frac{T_0}{A} - \frac{B}{A}\frac{A_0}{2\pi}\exp\left(-\frac{k^2 w_0^2}{8}\right), \quad (13.53)$$

Where B and A are the matrix elements from equation (13.22). Taking Hankel transform gives T(r) which is the surface temperature in real space:

$$T(r,\omega) = \int_0^\infty k J_0(kr)\left(\frac{T_0}{A} - \frac{B}{A}\frac{A_0}{2\pi}\exp\left(-\frac{k^2 w_0^2}{8}\right)\right) dk, \quad (13.54)$$

And the thermal response of the system, H (ω), is the weighted average of equation (13.42) by the coaxial probe beam with radius ω_1:

$$H(\omega) = \int_0^\infty 2\pi r dr\left(\frac{2A_1}{\pi w_1}\right)\exp\left(\frac{-2r^2}{w_1^2}\right)\left(\int_0^\infty k J_0(kr)\left(\frac{T_0}{A} - \frac{B}{A}\frac{A_0}{2\pi}\exp\left(-\frac{k^2 w_0^2}{8}\right)\right) dk\right), \quad (13.55)$$

Taking integral respect to r, the final thermal response equation is:

$$H(\omega) = A_1 \int_0^\infty k\left(\frac{T_0}{A}\exp\left(-\frac{k^2 w_1^2}{8}\right) - \frac{B}{A}\frac{A_0}{2\pi}\exp\left(-\frac{k^2(w_0^2 + w_1^2)}{8}\right)\right) dk, \quad (13.56)$$

b. Strong anisotropic heat flow

The thermal response of anisotropic material systems in isothermal condition is calculated using isothermal boundary condition, equation (12.39), and following calculation procedure from equations (12.31) to (12.37):

According to equation (12.39) and (12.32), the surface temperature in special transform domain is given by:

$$\bar{T}(\omega, k_x, k_y) = \frac{T_0}{A} - \frac{B}{A}A_0 \exp\left(-\frac{w_{0x}^2 k_x^2 + w_{0y}^2 k_y^2}{8}\right), \quad (13.57)$$

and its equivalent in real space will be Fourier transform respect to k_x and k_y:

$$T(\omega,x,y) =$$

$$\frac{1}{(2\pi)^2}\int_{-\infty}^{\infty}\int_{-\infty}^{\infty}\frac{T_0}{A}\exp(\mathrm{ik_x x})\exp(\mathrm{i\,k_y y})\,\mathrm{dk_x dk_y} +$$

$$\frac{1}{(2\pi)^2}\int_{-\infty}^{+\infty}\int_{-\infty}^{+\infty}\left(\frac{-\mathrm{B}}{\mathrm{A}}\right)\,\mathrm{A_0}\,\exp\left(-\frac{\mathrm{w_{0x}^2\,k_x^2}+\mathrm{w_{0y}^2\,k_y^2}}{8}\right)\exp(\mathrm{ik_x x})\exp(\mathrm{i\,k_y y})\,\mathrm{dk_x dk_y}, \qquad (13.58)$$

In order to obtain thermal response of the system in frequency domain, the weighted average of equation (12.58) by the coaxial probe beam with radius w_1 is calculated:

$$\mathrm{H}(\omega) = \int_{-\infty}^{+\infty}\int_{-\infty}^{+\infty}\left\{\begin{array}{c}\left[\frac{2\mathrm{A_1}}{\pi \mathrm{w_{1x}\,w_{1y}}}\exp\left(\frac{-2\mathrm{x}^2}{\mathrm{w_{1x}}}\right)\exp\left(\frac{-2\mathrm{y}^2}{\mathrm{w_{1y}}}\right)\right]\times \\ \left[\int_{-\infty}^{+\infty}\int_{-\infty}^{+\infty}\frac{1}{(2\pi)^2}\frac{T_0}{A}\exp(\mathrm{ik_x x})\exp(\mathrm{i\,k_y y})\,\mathrm{dk_x dk_y}\right]\end{array}\right\}\mathrm{dxdy} +$$

$$\int_{-\infty}^{+\infty}\int_{-\infty}^{+\infty}\left\{\left[\frac{2\mathrm{A_1}}{\pi \mathrm{w_{1x}\,w_{1y}}}\exp\left(\frac{-2\mathrm{x}^2}{\mathrm{w_{1x}}}\right)\exp\left(\frac{-2\mathrm{y}^2}{\mathrm{w_{1y}}}\right)\right]\times\right.$$

$$\left.\left[\frac{1}{(2\pi)^2}\int_{-\infty}^{+\infty}\int_{-\infty}^{+\infty}\left(\frac{-\mathrm{B}}{\mathrm{A}}\right)\,\mathrm{A_0}\exp\left(-\frac{\mathrm{w_{0x}^2\,k_x^2}+\mathrm{w_{0y}^2\,k_y^2}}{8}\right)\exp(\mathrm{ik_x x})\exp(\mathrm{i\,k_y y})\,\mathrm{dk_x dk_y}\right]\right\}\mathrm{dxdy}, \qquad (13.59)$$

With calculating two spatial integrals respect to x and y, the equation (12.59) will be reduced to:

$$H(\omega) = \frac{T_0\,A_1}{(2\pi)^2}\int_{-\infty}^{+\infty}\int_{-\infty}^{+\infty}\frac{1}{A}\,\exp\left(-\frac{\mathrm{w_{1x}^2\,k_x^2}+\mathrm{w_{1y}^2\,k_y^2}}{8}\right)\mathrm{dk_x dk_y} +$$

$$\frac{A_0 A_1}{(2\pi)^2}\int_{-\infty}^{+\infty}\int_{-\infty}^{+\infty}\left(\frac{-D}{C}\right)\exp\left(-\frac{(w_{0x}^2+w_{1x}^2)k_x^2+(w_{0y}^2+w_{0y}^2)k_y^2}{8}\right)\mathrm{dk_x dk_y}, \qquad (13.60)$$

13.9. **References**

1 Alan V. Oppenheim and Alan S. Willsky S. Hamid. Signals and System, Prentice Hall, 2nd edition, 1996.

2 H. S. Carslaw and J. C. Jaeger. Conduction of Heat in Solids. Oxford University Press, New York.

3 Aaron J. Schmidt, Xiaoyuan Chen, and Gang Chen, Rev. Sci. Instrum. 79, 114902 (2008)

4 Website: http://www.ni.com/white-paper/5613/en, 'How to Measure Small Signals Buried in Noise Using LabVIEW and Lock-In Amplifier Techniques'.

5 A. Feldman, High Temp. - High Press. 31, 293, 1999.

6 David G. Cahill, Review of Scientific Instruments, 75(12):5119-5122, 2004.

7 H. S. Carslaw and J. C. Jaeger. Conduction of Heat in Solids. Oxford University Press, New York, 1959, pp. 109-112.

8 Aaron Schmidt, Matteo Chiesa, Xiaoyuan Chen, and Gang Chen, Rev. Sci. Instrum., 79, 064902 (2008).

9 H. S. Carslaw and J. C. Jaeger. Conduction of Heat in Solids. Oxford University Press, New York, 1959, pp. 455-464.

Chapter 14 Conclusion and Future Work

14.1. Conclusion

In this PhD dissertation several thermoelectric materials based on silicide alloys were investigation in detail. The results of these investigations are briefly described in this section.

At first, the nanostructured silicon germanium was synthesized and studied in detail. Nanostructured silicon germanium thermoelectric materials prepared by mechanical alloying and sintering method have recently shown large enhancement in figure-of-merit, ZT. The fabrication of these structures often involves many parameters whose understanding and precise control is required to attain large ZT. In order to find the optimum parameters for further enhancing the ZT of this material, we synthesized and studied both experimentally and theoretically different nanostructured p-type SiGe alloys. The effect of various parameters of milling process and sintering conditions on the thermoelectric properties of the grown samples were studied. The electrical and thermal properties were calculated using Boltzmann transport equation and were compared with the data of nanostructured and crystalline SiGe. It was found that the thermal conductivity not only depends on the average crystallite size in the bulk material, but also it is a strong function of alloying, porosity, and doping concentration. The Seebeck coefficient showed weak dependency on average crystallite size. The electrical conductivity changed strongly with synthesis parameters. Therefore, depending on the synthesis parameters the figure-of-merit reduced or increased by ~60% compared with that of the crystalline SiGe. The model calculation showed that the lattice part of thermal conductivity in the nanostrcutured sample makes ~80% of the total thermal conductivity. In addition, the model calculation showed that while the room temperature hole mean free path in the nanostructured sample is dominated by the crystallite boundary

scattering, at high temperature the mean free path is dominated by acoustic phonon scattering. Therefore, the thermal conductivity can be further reduced by smaller crystallite size without significantly affecting the electrical conductivity in order to further enhance ZT.

In the next set of experiments, we studied the effect of boron precipitation in highly doped p-type silicon germanium alloys. In particular, we studied boron precipitation process and its effect on electronic properties of p-type bulk nanostructured silicon germanium ($Si_{0.8}Ge_{0.2}$) compared with large grain polycrystalline $Si_{0.8}Ge_{0.2}$. The structures were synthesized and their thermoelectric properties were measured versus temperature during heating and cooling cycles. The experimental data showed stronger temperature variation of Seebeck coefficient, carrier concentration, and conductivity in the nanostructured $Si_{0.8}Ge_{0.2}$ compared with the polycrystalline form indicating stronger boron precipitation in this structure. The electrical properties of both samples were calculated using a multi-band semi-classical model. The theoretical calculations confirm that the increase of boron precipitation in the nanostructured $Si_{0.8}Ge_{0.2}$ is responsible for its higher thermal instability. Since the thermoelectric properties of the nanostructured sample degrade as a result of thermal cycling, the material is appropriate only for continuous operation at high temperature without cooling.

In a new set of experiments, we studied the effect of phase heterogeneity in silicon germanium alloy. In this study, our detailed examination of the nanostructured bulk $Si_{0.80}Ge_{0.20}$ alloy synthesized by mechanical alloying and hot-press methods revealed that the alloy composition can unintentionally deviate from its nominal value. The phase deviation is difficult to be detected with x-ray diffraction due to the continuous solid solution characteristics of the Si-Ge alloy. Differential thermal analysis (DTA), in particular, showed that the synthesized nanostructured bulk $Si_{0.80}Ge_{0.20}$ alloy was a composition of two unintentional phases. The dominant phase was $Si_{0.88}Ge_{0.12}$ with admixture of $Si_{0.58}Ge_{0.42}$ in a much lower concentration. The two-phase structure is difficult to be detected in XRD analysis and is often neglected. Thermoelectric properties of $Si_{1-x}Ge_x$ significantly depend on the Ge content in the synthesized alloy. The thermoelectric properties of the synthesized material were studied experimentally and theoretically. The comparison of the data of the mixed phase nanostructured alloy with

those of the single phase $Si_{0.80}Ge_{0.20}$ alloy showed enhancement in Seebeck coefficient and reduction in thermal conductivity of the former material. It was found using model calculations that these differences are due to the existence of the $Si_{0.88}Ge_{0.12}$ phase in the two-phase structure that results in the reduction of the bipolar diffusion part of the thermal conductivity and the bipolar effect in the Seebeck coefficient at high temperature. The results can stimulate a new route for enhancing the thermoelectric properties of silicon germanium alloy based on multicomponent material design.

In another attempt, in order to study the effect of metal inclusions in silicon germanium alloy, P-type nanostructured bulk $Si_{0.8}Ge_{0.2}$ and $Si_{0.8}Ge_{0.2}$ composites with $CrSi_2$ nano-crystallite inclusions were synthesized via sintering approach. The composite structure showed power factor enhancement compared with nanostructured $Si_{0.8}Ge_{0.2}$ alloy. The experimental data for both structures were modeled with solving the multiband Boltzmann transport equation in the relaxation time approximation for charge carriers and phonons. The $Si_{0.8}Ge_{0.2}$ crystallite boundary scattering was modeled by a cylindrical potential barrier at the interfaces and the effects of $CrSi_2$ nano-inclusions were modeled by spherical potential barriers in the $Si_{0.8}Ge_{0.2}$ lattice. The model calculations revealed that the enhancement in power factor is not an effect of hot carrier energy filtering, but it is due to the enhancement in charge carrier mobility in the composite structure. The analysis of charge carrier mobility components showed that while in nanostructured $Si_{0.8}Ge_{0.2}$ the ionize impurities and acoustic phonons are dominant scatterers, in the composite structure the scattering by $CrSi_2$ nano-inclusions and acoustic phonons are dominant. The optimum size of the $CrSi_2$ nano-inclusions for enhancing ZT was predicted with the characteristic that ZT drops rapidly when the crystallite size decreases, but it changes slowly as it is increased above its optimum value.

The next set of experiments was concentrated around higher manganese silicide (HMS) thermoelectric alloy. P-type higher manganese silicide has attracted considerable interest due to its remarkable thermoelectric properties and potential applications at intermediate and high temperature TE devices. In this study, a series of nanostructured bulk p-type HMS materials with different compositions of $MnSi_x$ (where $x = 1.73$, 1.75 and 1.77)

were synthesized via mechanical ball milling and hot-press sintering. The X-ray diffraction analysis of the synthesized materials showed that increasing the Si contents yields to a slight shift to higher diffraction angles. The increase in Si content further resulted in a decrease in electrical conductivity and increase in Seebeck coefficient. The power factor of $MnSi_{1.77}$ was higher than those of $MnSi_{1.73}$ and $MnSi_{1.75}$ with the latter two being approximately identical. However, the lowest thermal conductivity was achieved in $MnSi_{1.75}$ and resulted in the highest figure-of-merit among all the compositions.

In another set of experiments, five metals with large work functions including Co, Ni, Cr, Ti, and Mo and two silicides including MnSi and $TiSi_2$ were examined to determine the best contact material for the thermoelectric material higher manganese silicide (HMS). Three-layer structures of HMS/contact/HMS were prepared in a sintering process. The contact resistance was measured versus temperature. The structures were subjected to x-ray diffraction (XRD) and energy-dispersive x-ray spectroscopy (EDS) examination. Thermal stability of the structures was determined by heating the samples to 700 °C for different time intervals. The pure metals failed to make reliable contacts due to poor mechanical and chemical stability at high temperatures. In contrast, the metal silicides (MnSi and $TiSi_2$) showed superior chemical and mechanical stability after the thermal stability test. The observed contact resistance of MnSi and $TiSi_2$ was within the range of practical interest (10^{-5} - 10^{-4} Ωcm^2) over the entire range of investigated temperatures (20 °C - 700 °C). The best properties were found for the nano grained MnSi for which the resistance of the contact was as low as 10^{-6} Ωcm^2.

In another very interesting set of experiments, we achieved enhancement of the thermoelectric figure of merit (ZT) in the bulk composite structure of $(Si_{0.88}Ge_{0.12})_{0.925}$-$(FeSi_2)_{0.05}$-$Ag_{0.025}$ doped with phosphorous. The ZT of crystalline single phase n-type silicon germanium is about one at about 950 C. The composite structure showed a ZT of about 1.2 at 950 C, which was primarily due to the reduction in thermal conductivity while maintaining the thermoelectric power factor. The effect of addition of different amount of silver was investigated. It was found that among different silver percentage

examined, 2.5% at silver allowed lower sintering temperature to maintain the electrical conductivity while the thermal conductivity was reduced. Consequently, 5% $FeSi_2$ in SiGe with addition of 2.5% at silver enhanced the ZT.

In efforts to build an optical characterization tool, a new pump-probe design and its implementation were developed for two purposes. The first goal was the measurement of thermal properties in thin films and nanowires. The theory of the thermal transport used in pump-probe method for cross plane and in plane thermal conductivity measurements was developed and extended to measure the thermal conductivity in three directions which can be applied for strong anisotropic materials such as nanowires. Second, using the multi-purpose optical design we aimed to study the dynamical processes of hot carriers relaxation, phonon generation and relaxation, and carrier-phonon couplings in different semiconductors.

Our new optical design was presented. This novel set up was designed such that the pulse width has minimum expansion along the whole optical path. Other than pulse width expansion, we considered different issues such as power loss, laser spot size and shape, and probe polarization. The detailed optical system and components were explained, and the instrumentation details and measurement system were described.

On the theoretical calculation of the heat flow in the pump-and-probe experiment, the heat flow in layered structures including the effect of the radial heat flow, the anisotropic heat flow and the thermal interface conductance were analyzed in details. The heat flow calculations were extended for three dimensional heat transfer. In addition, the solutions considering the isothermal boundary conditions were derived.

14.2. **Future Directions**

The traditional way of thinking for enhancing TE properties is not likely to make any new dramatic changes and novel ideas are needed for promising and exciting results. For

example, most recent advances in bulk thermoelectrics have been achieved by using different techniques of reducing the thermal conductivity. [1,2,3,4,5,6]. However, when the lattice thermal conductivity becomes comparable to (or smaller than) electronic thermal conductivity, the enhancement in ZT becomes less significant. In order to further improve the ZT, one has to increase the power factor simultaneously while reducing the thermal conductivity.

We discussed a new approach based on nanocomposites that can potentially result in significant nonlinear enhancement of the TE power factor, along with reduction of the thermal conductivity. The idea builds upon our observation of enhancement of the TE power factor in some of our nanocomposite structures.

This concept is a nanoscale effect that happens only if the energy distribution function of the carriers does not relax to that of the bulk material in the grain. This state of electronic properties requires grain size of sub-10 nm in most thermoelectric materials, which is often difficult to attain in bulk structures using conventional sintering methods.

Our experience with growing and testing over thousands of samples in the last several years indicates that a conventional hot pressing approach, such as direct DC current heating or spark plasma sintering, cannot yield the optimized nanoscale features. The main reason is that during the sintering time the grains grow and nanoscale features broaden or diminish within the process. Reducing the sintering time does not help either, as the material is not properly sintered; thus, results in low carrier mobility. Therefore, the material often has grains larger than 10-20 nm in size at best.

Experimentally, a new synthesis method is highly desired to generate nanocomposites with sub-10 nm crystallites. The challenge in any experimental method for this purpose will be controlling the nanoscale features in terms of size and distribution in the material.

It is also critical that material structure and composition is designed properly to achieve the intended enhancement of TE power factor. Therefore, it is important to combine the

experimental efforts with theoretical calculations so that one can explain the interplay between different properties of the material in the range that electrons and phonons enter the non-equilibrium domain of transport at nano-scale.

As such, the immediate natural extension of the presented PhD research is to focus on experimental and theoretical investigation of the influence of interface disturbance of the energy spectra on charge transport in nanocomposite bulk structures. Along with the experimental efforts, the incoherent transport of electrons and phonons using theoretical calculations should be investigated in detail to provide means to analyze and understand the experimental data and to give direction to design and realize such material structures.

On the optical characterizations, the experimental investigation of the non-linear nanocomposite materials can be combined with ultrafast optical pump-and-probe experiments to probe the non-equilibrium phase of the charge carrier dynamics and to better understand the experimental results.

14.3. **Reference**

1 R. Venkatasubramanian, E. Siivola, T. Colpitts & B. O'Quinn, Nature 413, 597-602 2001.

2 J. Androulakis, K. F. Hsu, R. Pcionek, H. Kong, C. Uher, J. J. D'Angelo, A. Downey, T. Hogan, M. G. Kanatzidis, Advanced Materials, Volume 18 Issue 9, Pages 1170 – 1173, 2006.

3 K. F. Hsu, S. Loo, F. Guo, W. Chen, J. S. Dyck, C. Uher, T. Hogan, E. K. Polychroniadis, M. G. Kanatzidis, Science 6 February 2004: Vol. 303. no. 5659, pp. 818 - 821.

4 X.W. Wang, H. Lee, Y.C. Lan, G.H. Zhu, G. Joshi, D.Z. Wang, J. Yang, A.J. Muto, M.Y. Tang, J. Klatsky, S. Song, M.S. Dresselhaus, G. Chen, and Z.F. Ren, Applied Physics Letters, Vol. 93, 193121 (1-3), 2008.

5 Y. Ma, Q. Hao, B. Poudel, Y. Lan, B. Yu, D. Wang, G. Chen, and Z. Ren, Nano Letters, Vol. 8, No. 8, pp. 2580-2584,2008.

6 Kanishka Biswas, Jiaqing He, Ivan D. Blum, Chun-I Wu, Timothy P. Hogan, David N. Seidman, Vinayak P. Dravid, Mercouri G. Kanatzidis, Nature 489, 414–418, 2012 doi:10.1038/nature11439.

VITA

Zahra Zamanipour

Candidate for the Degree of

Doctor of Philosophy

Thesis: NANOSTRUCTURED THERMOELECTRIC MATERIALS AND OPTICAL METHOD FOR THERMAL CONDUCTIVITY MEASUREMENT

Major Field: Electrical engineering

Biographical:

Education:

Completed the requirements for the Doctor of Philosophy in Electrical engineering at Oklahoma State University, Tulsa, Oklahoma in July, 2013.

Completed the requirements for the Master of Science in Physics at Sharif University of Technology, Tehran, Iran in 1998.

Completed the requirements for the Bachelor of Science in Physics at Amirkabir University of Technology, Tehran, Iran in 1996.

Experience:

Thermoelectric materials, Material characterization, Lasers and optical systems.